



Pilkington Library

Author/Filing Title LI, P

Accession/Copy No.

FOR REFERENCE ONLY
040147119

Vol. No. Class Mark

0401471195



BADMINTON PRESS
18 THE HALFCROFT
SYSTON
LEICESTER LE7 1LD

**3-D SURFACE MODELLING OF THE HUMAN BODY
AND 3-D SURFACE ANTHROPOMETRY**

by


LI, Peng

A Doctoral Thesis

Submitted in partial fulfilment of the requirements for the award of Doctor of
Philosophy of the Loughborough University

November 1996

©by Li, Peng 1996

 LOUISIANA	
Date	July 97
Class	
Adm No	060147119

Synopsis

This thesis investigates three-dimensional (3-D) surface modelling of the human body and 3-D surface anthropometry. These are two separate, but closely related, areas. 3-D surface modelling is an essential technology for representing and describing the surface shape of an object on a computer. 3-D surface modelling of the human body has wide applications in engineering design, work space simulation, the clothing industry, medicine, biomechanics and animation. These applications require increasingly realistic surface models of the human body. 3-D surface anthropometry is a new interdisciplinary subject. It is defined in this thesis as *the art, science, and technology of acquiring, modelling and interrogating 3-D surface data of the human body*. Three essential components in this definition, namely: data collection, modelling and interrogation of the human body surface, present a wide interaction in several technologies. In particular, this indicates that 3-D surface modelling of the human body requires surface scan data to enhance and improve the generation of human models; 3-D surface anthropometry requires surface modelling technique to model and represent the surface scan data, and to fulfil data interrogation.

Research into 3-D surface modelling in this thesis is concerned with generic and anthropometry-based surface modelling. The application of non-uniform rational B-spline (NURBS) is explored in establishing a generic modelling method. A skinning technique is employed to interpolate a number of cross-sections which are specially selected for representing the human body shape. A parameterisation method for the surface interpolation is designed to achieve a more accurate and smoother surface model with regard to the curve fitting process of cross-sections in which a non-uniform distribution and variant number of interpolated data points in each cross-sectional curve are unavoidable. Non-uniform B-spline form provides a convenient computational approach in the proposed parameterisation method.

Automatic data editing and curve-fitting is desirable for building a geometric model of the human body from raw scanned data. When a torso model is required (for example, in clothing design) trimming arms from raw data is an essential but time-consuming data editing and curve fitting task. An automatic method for arm trimming and filling the void

data is developed in association with the editing and approximation of the raw scanned data. A tensor-product scheme is proposed and implemented for surface approximation.

Anthropometry based surface modelling is devoted to creating a parametric surface model of the human torso from traditional anthropometric measurements (e.g. length, width and girth). A parametric surface model is more representative of the human body but difficult to modify with simple dimensional measurements. A reference body approach is developed to support the generation of a parametric surface. The modification of a surface model of the human torso is implemented on a basis of modifying key cross-sections. The shape of a cross-sectional curve is associated to simple dimensional measurements, and modification rules are heuristic. Therefore certain knowledge about body shape could improve the generated model. This is explored from shape classification of the human body. Shape classification of cross-sections of the human body is presented by hierarchical cluster analysis, which is viewed as a necessary step to improve the reference body model.

In the area of 3-D surface anthropometry, this thesis focuses on three essential aspects: calibration and error analysis of digital camera systems in the data collection stage, fundamental methods to acquire the location of feature points (anatomical landmarks) from the scanned data, and general methods for data interrogation. Important areas related to applications of CCD (Charge Coupled Device) and Newvicon® cameras in 3-D vision tasks, including the stability of a camera-frame grabber system, the location of the image centre and image processing methods are examined in this thesis. Two kinds of calibration methods of camera systems are evaluated, both from simulated and real data. Their performances under a variety of noises and initial value settings are investigated.

The identification and location of the key feature points is an essential measurement task in 3-D surface anthropometry. In this thesis, a method to modify the LASS (Loughborough Anthropometric Shadow Scanner) for acquiring the grey-scale image is developed and an associated location method of feature points is derived. The accuracy of measurement from the method is verified by comparing co-ordinate measurement result with a Co-ordinate Measuring Machine. Application of feature point location, as well as other higher-order measurements, including circumference, area and volume calculation are presented. Functional decomposition for creating a 3-D surface anthropometry software tool kit is given.

Acknowledgements

This research was completed in the HUMAG Research Group, Department of Human Sciences, Loughborough University and was funded by Courtaulds Lingerie (Daintifyt).

I would like to thank Professor Peter R.M. Jones, my supervisor who made my Ph.D. study possible, and for his supervisory role during my studies and research work over the past years. His advice, encouragement and enthusiasm in all aspects of my study has been beyond value. He is also a very respectable friend of my family. Thanks also to Professor Ray Meddis (now moved to Essex University) who was my Director of Research.

I am most grateful to Mr. David Gilliland, Ms. Jackie Fulford-Smith and Mr. David Reade of Courtaulds Lingerie, not only for their financial support, but also for many stimulating and challenging discussions throughout the project. Their eagerness for exploiting new technologies and persistent support were invaluable to the completion of this research.

Part of the work, described in Chapter 4, was funded by Kennett & Lindsell Ltd. I would like to thank Mr. Len Boxall for his support and encouragement.

Within the Department of Human Sciences, I would like to thank all staff for their help and advice, particularly from the general office and supporting staff. Much of the experimental work would not have been possible without the skilful and valuable assistance of Jeff Read, mechanical engineer in the Department. To Dr. Gordon West (retired) who gave me valuable help in understanding his original software and hardware which drove and made up the LASS system. Dr. Katherine Brooke-Wavell provided help and advice in running the LASS system and passed on much of her experiences.

There are many people in other departments of this university which I would like to be acknowledged, in particular, Dr. Jim Chandler, the Department of Civil Engineering who introduced me to photogrammetry, Dr. J. Petzing, the Department of Mechanical Engineering for the loan of a CCD camera for evaluation, Mr. J. Singh, the Department of Manufacturing Engineering to measure feature points with CMM.

Finally, the support from my family is invaluable. My wife, Jianqiu spent considerable time reading my manuscript. I thank her for her love, support and patience. I also would like to thank my parents-in-law for their support during my writing-up.

TABLE OF CONTENTS

TABLE OF CONTENTS.....	v
LIST OF FIGURES	x
LIST OF TABLES.....	xiii
ABBREVIATIONS	xv

CHAPTER ONE

INTRODUCTION	1
1.1 RESEARCH SCOPE	3
1.1.1 3-D surface modelling of the human body	4
1.1.2 3-D surface anthropometry	5
1.2 OVERVIEW OF THE THESIS	6

CHAPTER TWO

THREE DIMENSIONAL SURFACE ANTHROPOMETRY AND SURFACE MODELLING OF THE HUMAN BODY: AN OVERVIEW.....	7
2.1 INTRODUCTION TO 3D SURFACE ANTHROPOMETRY	7
2.1.1 Evolution of anthropometry	7
2.1.2 Traditional anthropometry	8
2.1.3 3D surface anthropometry	9
2.2 DATA ACQUISITION AND REDUCTION	10
2.2.1 Stereophotogrammetry.....	11
2.2.2 Moiré fringes	13
2.2.3 Structured light method	14
2.3 APPLICATIONS OF 3D SURFACE ANTHROPOMETRY AND DATA INTERROGATION	16
2.3.1 Medical application.....	17
2.3.2 Engineering design/ergonomics application	19
2.3.3 Clothing design/size survey application.....	19
2.3.4 Other application.....	20
2.3.5 Data interrogation method	21
2.4 3-D SURFACE MODELLING OF THE HUMAN BODY	21
2.4.1 Surface modelling of the human body with engineering design accuracy	23

2.4.2 Anthropometry-based modelling of the human body	24
2.5 SUMMARY.....	26

CHAPTER THREE

3-D SURFACE MODELING OF THE HUMAN BODY	27
3.1 TENSOR-PRODUCT APPROACH OF PARAMETRIC SURFACE INTERPOLATION AND ITS APPLICATION IN HUMAN BODY MODELLING.....	27
3.1.1 The basic definition of non-uniform rational B-spline curve and surfaces.....	27
3.1.2 Curve interpolation.....	29
3.1.3 Tensor-product surface interpolation : skinning approach.....	31
3.1.4 Surface interpolation of the human body	34
3.2 APPROXIMATION OF RAW SCANNED DATA.....	46
3.2.1 Curve approximation of raw data by linear least-square method.....	47
3.2.2 Surface approximating by tensor-product representation	50
3.3 PRE-PROCESSING METHODS OF RAW SCANNED DATA	52
3.4 SUMMARY.....	53

CHAPTER FOUR

ANTHROPOMETRY BASED SURFACE MODELLING	55
4.1 ANTHROPOMETRY-BASED PARAMETRIC SURFACE MODEL.....	56
4.1.1 Selection of anthropometric data.....	56
4.1.2 Method of shape modification.....	60
4.2 SHAPE CLASSIFICATION OF CROSS-SECTION OF THE HUMAN BODY	67
4.2.1 Shape classification of silhouette of the human body	68
4.2.2 The classification of cross sections	68
4.2.3 Representation of reference body	80
4.3 RELATIONSHIP BETWEEN WIDTH, DEPTH AND CIRCUMFERENCE OF A CROSS SECTION.....	81
4.4 SUMMARY.....	83

CHAPTER FIVE

3-D MEASUREMENT TASK-I: CALIBRATION OF DIGITAL CAMERA SYSTEMS	84
5.1 MODELLING A DIGITAL CAMERA SYSTEM.....	84
5.1.1 Ideal geometric model of a camera system.....	85

5.1.2 Distortion factors: Lens geometry and interior orientation of a camera.....	88
5.1.3 Other distortion factors.....	91
5.2 CALIBRATION METHODS OF THE DIGITAL CAMERA SYSTEM: AN OVERVIEW	92
5.2.1 Calibration of the interior parameters.....	93
5.2.2 Calibration of the exterior parameters.....	94
5.2.3 Hybrid calibration methods	98
5.4 EVALUATION OF CALIBRATION METHODS.....	102
5.4.1 Non-linear optimisation method.....	102
5.4.2 Improvements of Tsai's method.....	105
5.4.3 Simulation tests of three calibration methods.....	108
5.4.4 Discussions.....	117
5.5 PRACTICAL CALIBRATION OF A DIGITAL CAMERA SYSTEM	117
5.5.1 Camera system.....	117
5.5.2 Stability test of frame grabber, Newvicon® and CCD cameras	119
5.5.3 Design of a test bench and control field.....	123
5.5.4 Physical calibration of image centre.....	123
5.5.5 Analytical calibration of the digital camera system.....	124
5.5.6 Discussion	126
5.6 SUMMARY.....	127

CHAPTER SIX

3-D MEASUREMENT TASK-II: LOCATING FEATURE POINTS IN 3D

SCANNED SURFACE DATA.....	128
6.1 LOCATION OF FEATURE POINTS IN 3D SURFACE ANTHROPOMETRY.....	128
6.2 MODIFYING LASS SYSTEM TO CAPTURE GREY-SCALE IMAGE	129
6.2.1 Structure and principle of the LASS system	129
6.2.2 Comparison and selection of modification methods	130
6.3 RAY-TRACING METHOD TO MAP 2D POINTS TO 3D SURFACE.....	134
6.3.1 Basic ray-projection equation and ray-tracing method	135
6.3.2 Searching a solution from a large surface.....	142
6.3.3 Case study	145
6.4 ERROR ANALYSIS OF THE DIRECT MAPPING METHOD FOR FEATURE POINT LOCATION.....	148
6.4.1 Camera position error.....	148

6.4.2 Projected co-ordinate error	150
6.4.3 Error analysis related to surface approximation	152
6.4.4 Verification of mapping accuracy	153
6.5 AN APPLICATION OF LOCATED FEATURE POINTS: SURFACE TRIMMING	154
6.5.1 Introduction to surface trimming.....	154
6.5.2 Surface trimming of raw scanned data	155
6.6 SUMMARY.....	160

CHAPTER SEVEN

THE MATHEMATICS AND SOFTWARE STRUCTURE OF 3D SURFACE

ANTHROPOMETRY	161
7.1 ONE-DIMENSIONAL MEASUREMENT	162
7.1.1 The measurement of length.....	162
7.1.2 The measurement of circumference.....	163
7.2 TWO-DIMENSIONAL MEASUREMENT	165
7.2.1 The area of a planar closed curve	165
7.2.2 The area of a surface.....	166
7.3 THREE-DIMENSIONAL GEOMETRIC MEASUREMENT	166
7.3.1 Volume between two planar sections.....	166
7.3.2 Volume between two surfaces.....	167
7.4 APPLICATION EXAMPLES OF THE HIGHER DIMENSIONAL GEOMETRIC MEASUREMENT	168
7.4.1 Surface area measurement of breast tissue	168
7.4.2 Volume calculation of breast tissue.....	169
7.4.3 Conclusion.....	169
7.5 SOFTWARE STRUCTURE OF 3-D SURFACE ANTHROPOMETRY.....	170
7.5.1 Data import and export	171
7.5.2 Data editing and modelling	172
7.5.3 Anthropometric measurements and data interrogation.....	172
7.5.4 Special modelling functions	173
7.6 SUMMARY.....	174

CHAPTER EIGHT

CONCLUSIONS AND FUTURE WORKS.....

8.1 RESULTS AND LIMITATIONS.....	176
----------------------------------	-----

8.1.1 3-D surface modelling of the human body	176
8.1.2 Anthropometry based surface modelling.....	177
8.1.3 3-D surface anthropometry	178
8.2 FUTURE WORK	180
REFERENCES	181
APPENDIX A: MATHEMATICS	193
APPENDIX B: PUBLICATIONS.....	198
APPENDIX C: EVALUATION AND COMPARISON OF CALIBRATION METHODS	228

LIST OF FIGURES

Figure 1- 1. 3-D surface modelling and 3-D surface anthropometry.....	3
Figure 2- 1. Stereo vision to measure human face (Duncan & Mair 1983).....	12
Figure 2- 2. Moiré fringe image of a live body, from Takasaki [1973].....	13
Figure 2- 3. Four representations of the human body, from Calvert et al.[1993]	22
Figure 2- 4. Polygon form of the 'Fourth Men' [Fetter 1982]	23
Figure 3- 1. A B-spline curve and its control points.	29
Figure 3- 2. Two-steps of skinning method: surface control point and cross-sectional curves	33
Figure 3- 3. Format of LASS shape matrix.....	34
Figure 3- 4 Eight key levels of the human torso	35
Figure 3- 5. Distribution of interpolated data points at (a) chest section;(b) hip section.....	40
Figure 3- 6. Effect of parameterisation: (a) surface interpolation without relocation of cross-sectional data; (b) surface interpolation with the relocation method, 16 points case;.....	40
Figure 3- 6. (c) surface interpolation with relocation by the angle average, 32 points; (d) surface interpolation with the new relocation method, 32 points.	41
Figure 3- 7. Wireframe form of data distribution: (a) from the angle average method; (b) the original curve fitted data	41
Figure 3- 7. (c) the side view of data from the relocation method; (d) the back view of data from the relocation method; (e) the cross-sectional view of 16 point data from the relocation method; (f) the cross-sectional view of 32 point data from the relocation method	41A
Figure 3- 8. (a) error of angle average method at chest section; (b) error of new parameterisation method at chest section; (c) error of 16 points and 32 points interpolation of new parameterisation method at chest section; (c) error of 16 points and 32 points interpolation of new parameterisation method at hip section	42
Figure 3- 9. (a) cross-sectional data with arm ; (b) cross-sectional data after deleting arm.	48
Figure 3- 10. Incorrect fitting of arm gap.....	49
Figure 3- 11. Radial curve of a cross-section, the horizontal axis is angle space	49
Figure 3- 12. Cross-sectional view of arm trimming with trimmed arm image superimposed on the raw data	51
Figure 3- 13. (a) raw scanned surface; (b) a surface with refilled data gap by curve approximation.....	51
Figure 3- 14. A surface with refilled data gap by tensor-product approximation	51

Figure 4- 1. Illustration of anthropometric measurement	58
Figure 4- 2. Key measurements from front view and side view	59
Figure 4- 3. (a) A cross section and (b) its shape vector	61
Figure 4- 4. Relationship between depth measurement and shape vector	63
Figure 4- 5. Two shape vectors with different Width/Depth ratio	64
Figure 4- 6. Anthropometry input panel.....	66
Figure 4- 7. A re-generated body surface	66
Figure 4- 8. Body growth and sections change (size 12 with size 22 superimposed)	
(a) Front and side view.....	69
(b) Cross sectional view	70
Figure 4- 9. Typical radial shape curves	72
Figure 4- 10. Dendrogram of hierarchical clustering	76
Figure 4- 11. Dendrograms of the clustering at maximum hips section	
(a) Polynominal fitting method	78
(b) Fourier descriptor method.....	79
Figure 4- 12. Two locations of extreme and corresponding curve shapes.	81
 Figure 5- 1 Three co-ordinate systems of a camera model	86
Figure 5- 2. Tilted photo plane in a world co-ordinate system.....	89
Figure 5- 3. Lens distortions: a) radial distortion; b) tangential distortion.	90
Figure 5- 4. Flowchart of the non-linear optimisation method.....	105
Figure 5- 5. The flowchart of the improved Tsai's method.	108
Figure 5- 6. Camera and world co-ordinate systems	109
Figure 5- 7. Projection error and estimated parameter error in the RDO method and Tsai's	
method with different lens distortion coefficient k_1 : (a) prjerr curves; (b) Z_c error curves	112
Figure 5- 7. (c) ω error curves; (d) k_1 error curves	113
Figure 5- 8. Effect of noise level for three calibration methods: (a) prjerr curves; (b) Z_c error	
curves.....	115
Figure 5- 8. Effect of noise level for three calibration methods: ((c) ω error curves; (d) k_1 error	
curves.....	116
Figure 5- 9. Photograph of LED calibrator	120
Figure 5- 10. (a) x pixel fluctuation of a frame grabber.....	122
(b) x pixel fluctuation of a CCD camera.....	122

(c) x pixel fluctuation of a Newvicon camera.....	122
Figure 6- 1. Block diagram of the LASS system.	131
Figure 6- 2. An additional imaging system to the LASS.	135
Figure 6- 3. Ray/surface intersection.....	136
Figure 6- 4. Containment relationship of a point in a triangular area	140
Figure 6- 5. Ray/quadrilateral mesh intersection.....	142
Figure 6- 6. Visible and non-visible intersection.....	143
Figure 6- 7. Search space of a body surface a) height constraint; b) angle constraint.	146
Figure 6- 8. Case of feature point location: (a) labelling of feature marks in the image window; (b) mapped 3-D co-ordinates of the feature marks in the raw scanned surface.	147
Figure 6- 9. Error of ray/surface intersection.....	152
Figure 6- 10. Scanning line trimming of a surface.....	157
Figure 6- 11. Non-integral co-ordinate relationship between a trimming polygon and underlying surface	158
Figure 6- 12. Trimming vector and its IntersectionsLists.....	160
Figure 7- 1. Diagram of Graham scan: a) polygon P and its internal point q b) doubly-link list of Graham scan.....	164
Figure 7- 2. Area of a polygon.	166
Figure 7- 3. Volume between two cross-sections.....	167
Figure 7- 4. Breast boundary definition from cross-sectional data	168
Figure 7- 5. Software functions of 3D surface anthropometry	171

LIST OF TABLES

Table 4- 1. Example of some anthropometric measurements.	53
Table 4- 2. Comparison of differences (MEAN and SD) of anthropometric measurements between raw scans and recreated bodies from 15 female subjects (Unit: mm).....	67
Table 4- 3. Descriptive statistics of the feature values of polynomial fitting.....	77
Table 4- 4. Regression equations of Depth, Width and Girth.....	82
Table 5- 1. Simulation result of iterative improvement of Tsai's method	107
Table 5- 2. Two tests of non-linear method under different p_1, p_2	111
Table 5- 3. Pixel stability statistics.....	121
Table 5- 4. Practical calibration of camera systems	125
Table 6- 1. X error of ray/plane intersection from two calibration methods.....	149
Table 6- 2. Co-ordinate values of seven points from two measurement methods.....	153
Table C- 1. Default camera parameters	228
Table C- 2. Two tests of non-linear method under different p_1, p_2 and with k_1 varies	228
Table C- 3. Test of the RDO method via. different k_1	229
Table C- 4. Test of Tsai's method with different k_1	230
Table C- 5. Initial value conditions of the non-linear method.....	231
Table C- 6. Initial value conditions of the RDO method ($k_1=0.0000001$ and noise level =0.5 pixel).....	231
Table C- 7. Tsai's method under variation of principle points u_0, v_0	232
Table C- 8. Response of the non-linear method to different noise levels	233
Table C- 9. Response of the RDO method to different noise levels	235
Table C- 10. Response of Tsai's method to different noise levels	237
Table C- 11. Effect of noise distribution at 0.5 pixel level to the RDO method	238
Table C- 12. Effect of noise distribution at 0.5 pixel level to Tsai's method	239
Table C- 13. Effect of control point distribution to the RDO method (camera position at (-8, 10, 1100))	240

Table C- 14. Effect of control point distribution to Tsai's method (camera position at (-8, 10, 1100)) 240

Table C- 15. Effect of camera orientation for the RDO method..... 242

Table C- 16. Calibration results using data from the thin lens formula 243

ABBREVIATIONS

3-D	- three-dimensional
AP	- Additional Parameters
ASP	- American Society of Photogrammetry
CAD	- Computer Aided Design
CCD	- Charge Coupled Device
CMM	- Co-ordinate Measuring Machine
DLT	- Direct Linear Transformation
IGES	- Initiative Graphics Exchange Standard
LASS	- Loughborough Anthropometric Shadow Scanner
LED	- Light Emitted Diode
LS	- Least square
NURBS	- Non-Uniform Rational B-Spline
RMS	- Root Mean Square
mm	- millimetre
prjerr	- RMS of 3D-2D projection errors

CHAPTER ONE

INTRODUCTION

Three-dimensional (3-D) surface modelling of the human body and 3-D surface anthropometry are two separate, but closely related, areas. 3-D surface modelling of the human body has wide applications in engineering design, workplace simulation, the clothing industry, medicine, biomechanics and animation. There is an increasing need from science and engineering-oriented applications for models of the human body. To this end, the anthropometric and real surface shape data are required to be incorporated into the surface modelling process in order to obtain a more realistic representation of the human body. 3-D surface anthropometry has stemmed from this need. It is concerned with the collection, processing and interrogation of surface data of the human body. 3-D surface anthropometry, on the other hand, needs methods developed in 3-D surface modelling to reduce, model and interrogate the measured data. 3-D surface modelling of the human body and 3-D surface anthropometry are two closely interlaced areas.

One ultimate goal of 3-D surface modelling of the human body is to provide a representative form of the human figure. The computerised 3-D model of the human body attempts to provide the shape and size of the human body in an environment in which the interaction of the human body and its external world can be simulated and evaluated in a computer. In this way, the figure of the human body can be integrated into engineering design, analysis and manufacturing application. 3-D surface modelling is receiving increasing attention in human body modelling because it can generate a more realistic and more accurate geometric model than other forms. 3-D surface modelling of the human body is mainly concerned with:

1. Geometric modelling, which includes approximation and reduction of the raw measured data, selection of the approximation function, tackling different data sets (trunk, limb, etc.) and “stitching” them into one model;
2. Feature modelling, which studies methods of relating a surface model to key anthropometric measurements and other application features, retrieving, averaging and comparing 3-D body shape according to key features;

3. Physical and functional modelling, which discusses how to alter the geometric model of the human body under different external conditions, such as postural change, movement, force action, and how to simulate human behaviour from a series of surface shape changes, for example, standing, seating, loading and lifting.

Clearly, the accurate acquisition of raw data is crucial in achieving realistic modelling of the human body surface. This is addressed by 3-D surface anthropometry. In order to measure the surface shape and size of the human body, efforts have been put into the development of the automatic 3-D imaging device to measure the human body surface [Takasaki, 1970; Frobin and Hieholzer, 1983; Jones, West, Harris & Read, 1989; Uesugi 1991; Vannier, Pilgram, Bhatia, Brunsten & Commey, 1991; Rioux, 1992; Cyberware, 1996]. 3-D surface scanning systems and other measurement methods and systems have been invented. However, the processing of the raw data is a complex task [Jones, Li, Brook-Wavell & West, 1995, Nurre, Whitestone, Hoffmeister & Burnsides, 1995]. Methods are required to register, to reduce and to approximate the scanned data before they can be utilised. 3-D surface anthropometry is developed to address these aspects. Three principal topics in 3-D surface anthropometry are:

1. Data collection, which includes: basic methods to acquire the surface data and feature points, their hardware and software implementation, as well as accuracy evaluation and systems calibration;

2. Data modelling, which includes: editing and approximation of the data to produce a generic model of the human body together with its surface components;

3. Data interrogation, which includes: basic anthropometric measurement from the raw data or computerised geometric model of the human body; definition, identification and extraction of landmarks from the scanned data; average and comparison of a bulk of scanned data, higher dimensional geometric measurements and complex surface analysis, etc.

As mentioned earlier, research in 3-D surface modelling of the human body and 3-D surface anthropometry are interlaced. The relationship between them have been diagrammatically shown in Figure 1-1. 3-D surface modelling provides a useful tool for data modelling and interrogation in 3D surface anthropometry. Data modelling in 3-D anthropometry needs the help of the geometric modelling in 3-D surface modelling to fit and

reduce the raw data. In addition, 3-D surface modelling of the human body requires anthropometric data to widen its applications.

1.1 Research Scope

This research programme explored the methods and techniques for 3-D surface modelling of the human body and 3-D surface anthropometry. Research into 3-D surface modelling is concerned with generic and anthropometry-based surface modelling. Research into 3-D surface anthropometry is concerned with co-ordinate measurement of feature landmarks and data interrogation methods of the human body.

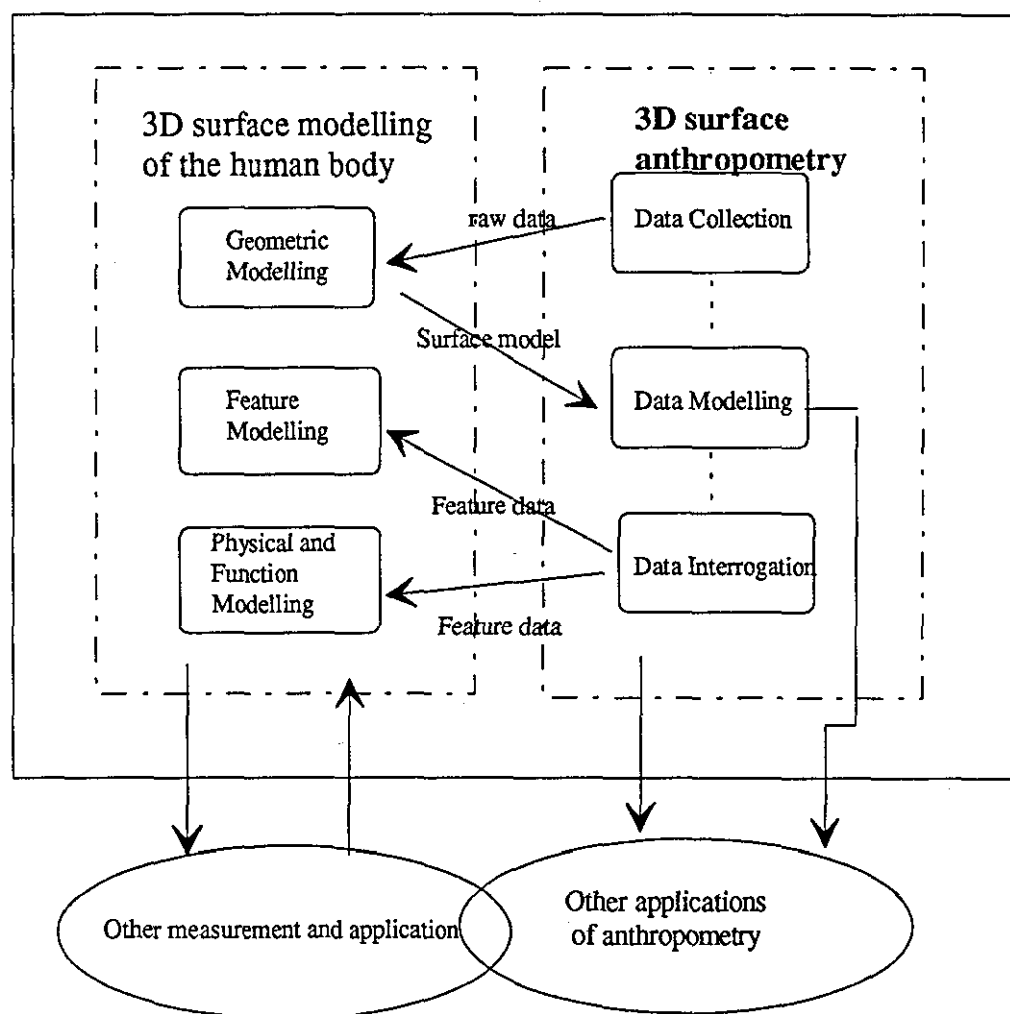


Figure 1- 1. 3-D surface modelling and 3-D surface anthropometry

1.1.1 3-D surface modelling of the human body

3-D surface modelling in this thesis is confined to generic surface modelling methods of raw scanned data, an automatic data editing method and anthropometry-based surface modelling of the human body.

A generic surface modelling method is used for approximating and reduction of the raw scanned data and for achieving a more concise representation of the human body. The application of non-uniform rational B-spline (NURBS) is explored in establishing a generic modelling method. A skinning technique is employed to interpolate a number of cross-sections which are specially selected for representing the human torso shape. A parameterisation method for the surface interpolation is designed to achieve a more accurate and smoother surface model with regards to the curve fitting process of cross-sections in which a non-uniform distribution and variant number of interpolated data points in each cross-sectional curve are unavoidable.

Automatic data editing and curve-fitting is desirable for building a geometric model of the human body from raw scanned data. When a torso model is required (for example, in the clothing design) trimming arms from raw data is an essential but time-consuming data editing and curve fitting task. An automatic method for arm trimming and filling the void data is developed in association with the editing and approximation of the raw scanned data. A tensor-product computational scheme is proposed and implemented for surface approximation.

Anthropometry-based surface modelling is important due to the limited availability of 3-D surface scanning devices. 3-D surface scanning of the whole human body is still expensive and the scanned data are difficult to access. Existing anthropometric data, which are presented in linear measurement form (length, width and girth), are available and have been widely applied in various design work. Anthropometric data have been incorporated into some human body modelling packages in which the human model is represented by simple geometric primitives [Dooly 1982, Das and Sengupta 1995]. However, the parametric surface model which can be controlled by anthropometric measurement has not been reported. This thesis innovates an anthropometry-based surface modelling method which can modify and constrain a surface model of the human body by using linear measurements.

1.1.2 3-D surface anthropometry

In the area of 3-D surface anthropometry, this thesis focuses on three essential aspects: calibration and error analysis of camera systems in the data collection stage, fundamental methods to acquire the location of feature points (anatomical landmarks) from LASS scanned data, and general methods for data interrogation.

Photogrammetrists have investigated the calibration of camera systems for a considerable time [Brown 1970, Faig 1975, Wong 1995]. However, cameras used in 3-D vision and scanning systems are digital. That is, the quality of a camera and lens, data acquisition method and storage media of images, and the range of measurement are different from those in traditional photogrammetry. This thesis examines important areas related to applications of CCD (Charge-Coupled-Device) and vidicon cameras in 3-D measurement tasks, including the stability of a camera-frame grabber system, location of image centre and image processing methods. Two kinds of calibration methods of camera systems are evaluated both from simulated and real data. Their performances under a variety of noise and initial value settings are investigated.

The identification and location of the key feature points is an essential measurement task in 3-D surface anthropometry. This task is defined as a zero-order measurement problem in the thesis. Higher-order complex measurements (distance, area, volume measurement and higher-order surface characteristics) are based on the zero-order measurements. Automatic feature extraction has been investigated in machine vision areas. However, the surface of the human body is featureless compared with mechanical parts. Moreover, many key anatomical landmarks are invisible from the scanned surface profile. The automatic feature location from scanned surface data is inappropriate. Only grey-scale colour image or high resolution scanning of the object surface would be suitable for locating the anatomical landmarks with the help of artificial marks. In this thesis, a method to modify the LASS (Loughborough Anthropometric Shadow Scanner) for acquiring a grey-scale image is developed and an associated location method of feature points is derived. Application of feature points location, as well as other higher-order measurements including circumference, area and volume calculation, are presented. An analysis for creating a 3-D surface anthropometry software tool kit is given.

1.2 Overview of the thesis

The thesis is organised as follows:

Chapter 1 is a brief introduction to the subject of the research programme and provides an overview of the thesis.

Chapter 2 reviews the methods used and problems existing in 3-D surface anthropometry and 3-D body modelling.

Chapter 3 discusses NURBS based interpolation method, its application in modelling the human body, and the application of curve and surface approximation in automatic editing and smoothing of raw scanned data.

Chapter 4 addresses the anthropometry-based surface modelling, shape analysis and classification methods of cross-section data.

Chapter 5 reviews principal calibration methods for 3-D vision based measurement systems.

Chapter 6 describes extensive experiments on two types of calibration methods and evaluates Newvicon® and CCD cameras with respect to their adequacy for 3-D measurement tasks.

Chapter 7 develops a method for locating feature points from scanned data and its application in surface trimming of raw scanned data.

Chapter 8 discusses the mathematical foundations for data interrogation methods in 3-D surface anthropometry and illustrates a software structure for 3-D surface anthropometry tool kit.

Chapter 9 concludes the research programme and discusses further research related to 3-D body modelling and 3-D surface anthropometry.

Note: In the following chapters, *3-D body modelling* is interchangeable with *3-D surface modelling of the human body*.

CHAPTER TWO

THREE DIMENSIONAL SURFACE ANTHROPOMETRY AND SURFACE MODELLING OF THE HUMAN BODY: AN OVERVIEW

This chapter briefly reviews the 3-D surface anthropometry and 3-D surface modelling of the human body. 3-D surface anthropometry is a newly developing subject. It is an interdisciplinary science and is involved with vast and diverse applications. This thesis is mainly concerned with accurate geometric measurement and representation of the human body. Therefore, the methods of acquiring and representing the surface shape of the human body as well as the methods of interrogating the body model are at the centre of this review.

2.1 Introduction to 3D surface anthropometry

As a newly developing discipline 3D surface anthropometry covers a broader scope, from data acquisition to data interrogation of the human body surface. This section reviews the evolution of anthropometry, its engineering applications, and the main features of 3-D surface anthropometry.

2.1.1 Evolution of anthropometry

Anthropometry is defined in The Oxford English Dictionary (Second edition 1989) as: *'the measurement of the human body with a view to determine its average dimensions, and the proportion of its parts, at different ages and in different races or classes'*. It specifies three basic elements in anthropometry:

1. measuring geometric/physical dimensions of the human body;
2. data processing methods which contain mainly averages and proportions;
3. dealing with a group of people.

This definition is suitable for the *anthropological anthropometry* in which the dimension/size difference of the human body is mainly related subjects' ages, races and classes. On the other hand, the *engineering anthropometry*, largely developed after World War II, emphasizes the application of anthropometric data in engineering design, fitness evaluation of equipment for the intended user population, and workplace evaluation. Engineering anthropometry is defined as: *"the application of scientific physical measurement methods to human subjects for the development of engineering design*

standards and specific requirements and for evaluation of engineering drawings, mock-ups, and manufactured products for the purpose of assuring suitability of these products for the intended user population" [Roebuck, Kroemer & Thomson, 1975, page 6]. Engineering anthropometry is a bi-direction technology. On the one hand, it provides data of the human body for engineering design and analysis. On the other hand the requirement from engineering practice is stimulating and driving new methods and technologies to be invented and employed to measure the human body. Nowadays, engineering anthropometry has become an essential branch of human engineering [Green, Self, and Ellifritt, 1995].

The 3-D measurement technology of the human body surface has revolutionary influences among the important developments in engineering anthropometry. It is broadening the application scope of anthropometry, as well as requiring new methods and techniques to handle the measurement data, and to deliver the computational results. This results in the advent of a new era of anthropometry -- *3-D surface anthropometry*. 3-D surface anthropometry is a new stage of engineering anthropometry, but it does not mean to completely replace traditional anthropometry. At the current stage, 3-D surface anthropometry is still an assistant technology for anthropometric applications or dedicated to a relative small scale, precise measurement tasks.

2.1.2 Traditional anthropometry

Traditional anthropometry has two main features. Firstly its measurement tools are manually operated and designed to take 'linear' or distance measurements only. For example, it utilises a stadiometer for height measurement, a sliding calliper for length measurement and tape for circumference measurement. Secondly, its data processing methods are largely limited to statistics. Because of the above features, traditional anthropometry is easy to practise but labour intensive, especially if a population survey is involved. The measured data are usually graded into percentiles, and thereby are only suitable for a 'proportional fitting' or fitting in population. They are however not able to give a precise solution for a task which requires 3D shape information.

Drawbacks in traditional anthropometry are obvious with respect to data acquisition and processing. Firstly the data acquisition is a one-go process. The subjects have to be recalled if a new measurement is required or correction to data needs to be verified. This is

usually not feasible in most cases because of costs, availability of subjects and the variation of subjects with time lapse. Secondly the recording of measurement data is time-consuming work and could be error-prone. Without automation of data processing, the cost of a large scale measurement task, especially a population survey, could be high.

Taking photographs of a subject and making measurements from the photograph can overcome the first problem. This was practised as early as 1958 [Roebuck *et al.* 1975]. Based on the modern image acquisition and processing techniques, automatic anthropometric systems from a 2-D image of a subject have been developed, e.g. SYNCAD of Telmat [1991]. The most dimensional measurements of the human body in the SYNCAD system are obtained from two orthonormal views (front and side views). The key anthropometric landmarks are identified by some pattern recognition methods. The measurements are subsequently taken from these landmarks automatically. However, circumference can not be found directly from the silhouette of a body. An estimation has to be made, which could result in a significant error. Moreover, the identification of anthropometric landmarks in the SYNCAD mainly relies on the geometric feature of the silhouette, which has been proven to be unreliable. As it is not possible to reconstruct a 3-D surface accurately, this kind method may be called a 2-D or $2\frac{1}{2}$ dimensional method.

2.1.3 3D surface anthropometry

3D surface anthropometry is a new concept growing during the 1990s, although some practices can be traced back to the 1950s. 3D surface anthropometry starts from the success of 3D shape measurement of the human body and is drawing more attention from different areas [Vannier, Yates & Whitestone, 1992]. However, there is no a standardised definition for 3D surface anthropometry.

3D surface anthropometry has a much wider and more complicated technical content than traditional anthropometry. It is involved in 3D shape measurement, surface modelling, image and graphics processing, computational geometry and data interrogation. A definition of 3-D surface anthropometry could be drawn from a general point of view as follows: *3-D surface anthropometry is the art, science, and technology of acquiring, modelling and interrogating 3-D surface data of the human body.* This definition covers

the main activities in 3-D surface anthropometry, although it could be argued that the definition does not mention the usage and objectives of the measured data. The reason to give such a general definition is that 3-D surface anthropometry is motivated and developed from diverse areas.

3D surface anthropometry relies on contemporary electronic, optical and computing technology. For example, the acquisition of surface data of the human body needs advanced 3-D measurement technologies which are computer-dominated; and real-time visualisation and manipulation of 3D surface data of the human body need a new graphics platforms and faster computer hardware. In addition to these modern technologies, data interrogation from digitised body surface requires completely different computational methods from those used in traditional anthropometry. How to fully exploit the 3-D surface data to extend traditional anthropometric application, and what an application can do from acquired 3-D surface data are still in development. Review of 3-D surface anthropometry will be based on existing applications and systems, and concentrate on three main aspects: data acquisition, interrogation and surface modelling. The data acquisition section reviews important techniques to acquire the surface data of the human body, particularly by non-contact measurement methods. The data interrogation section reviews applications of 3-D surface anthropometry and summarises relevant data interrogation methods. The surface modelling of the human body section addresses the modelling method of surface data and its application in dealing with scanned data and anthropometric data interrogation. Furthermore anthropometry based human body modelling is viewed as a branch of human body modelling. 3-D surface anthropometric data will be beneficial to the existing human body modelling systems.

2.2 DATA ACQUISITION AND REDUCTION

Non-contact measurement of the human body surface is parallel with the development of non-contact engineering measurement. Three principal non-contact methods used in engineering measurement are: stereo photogrammetry, moiré fringe and structured light methods. Special considerations, when these methods are applied to measure the human body, must be taken. These include:

- avoidance of the movement of the human body, i.e., the effect from breathing and body sway;
- non-contact and non-invasive measurement;
- ability to place the subjects in a variety of positions and postures.

In addition to these factors, types of illumination and lighting condition should be considered as well because the human skin has special properties in the reflection and absorption of light, as indicated by Takasaki [1973] and Rioux [1992]. This section will focus on the principles and applications of the three methods, rather than technical details.

2.2.1 Stereophotogrammetry

This method was originally used in aerial or terrestrial photogrammetric surveying [Wolf 1983]. It requires two cameras with a defined relationship of relative position, i.e. known baseline equation. A 3-D point which projects in two camera image planes produces the disparity. The depth of the 3-D point can be solved from the disparity and known camera relative position. Therefore, the stereo vision process contains three main steps: 1) detection of features in each image, 2) matching of features between the images under certain geometric and other constraints, and 3) calculation of depth using the disparity values and geometric parameters of the camera configuration.

Since traditional photogrammetry works on film, mechanical and manual corresponding of two photographs, such as using a stereoscope to view a stereo photograph pair and a stereoscopic plotter to plot 3-D contours from stereo-photographs, is necessary to fulfil step 1) and 2). This takes considerable time and skill. Figure 2-1 illustrates three stages of a traditional stereo-photogrammetry approach to acquire 3D shape of the human face [Duncan and Mair, 1983]. Figure 2-1a shows two photographs taken by stereoscopic camera pair. Figure 2-1b is a contour diagram and Figure 2-1c a 3-D surface from the contour diagram. Stereo-photographs can be processed by computer with new digital camera/video technology and image processing methods [Burke, Banks, Beard, Tee & Hughes, 1983]. Even so, the automatic detection and corresponding of feature points is still difficult, especially for the human body which is a featureless shape from the point of view of stereo vision.

Hertzeburg was a pioneer in using the stereo-photogrammetry method for whole body anthropometry [Green *et al.*, 1995]. Weissman [1968] presented a method to acquire full size front and back shape of the human body simultaneously by two sets of stereoscopic cameras. He also gave a detail description of how to acquire anthropometric measurement (area, volume, circumference) from contour line produced by a stereoscopic plotter. Stereo-photogrammetry, although it is a classic non-contact measurement method, is not suitable measuring the human body for large scale survey because of the difficulty in the corresponding process of stereoscopic images. Nevertheless, it is useful if only a number of 3-D co-ordinates from the body surface are to be measured or the number of subjects is small.

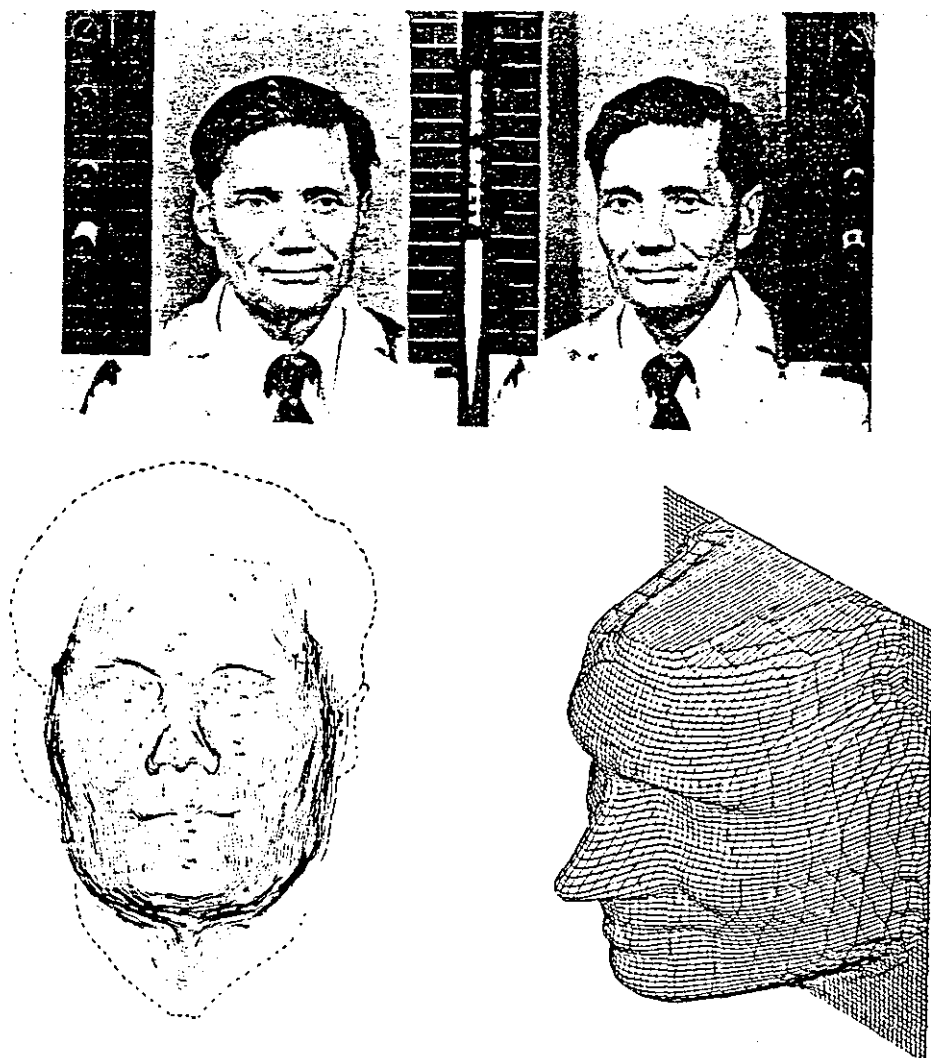


Figure 2- 1. Stereo vision to measure human face (Duncan & Mair 1983)

2.2.2 Moiré fringes

The moiré fringe is a result of interference of two plane waves. The so-called shadow- moiré, where moiré fringes are formed between a grating and its own shadow casting on a curved surface, is used to measure the surface of an object. The interference fringes are alternate bright and dark stripes. Each bright stripe represents those position with the same depth from a surface. By tracing a stripe, a contour line of the surface can be acquired. Typical application of moiré fringe method to measure the human body was described by Takasaki [1970, 1973]. Figure 2-2 shows an image of moiré fringe on a live body. Relevant difficulties and problems in applying moiré fringe to the human body were discussed by Takasaki [1973]. One major difficulty is that it requires certain knowledge or operator assistance to analyse the shape of the surface from the acquired pictures. Re-entrance shape of the body may cause discontinuity of fringes. Moreover, the moiré fringe method only produces one view image. To acquire full image of a cylinder-like object, multi-exposure is necessary. Merging of multi-view images is again difficult to implement.

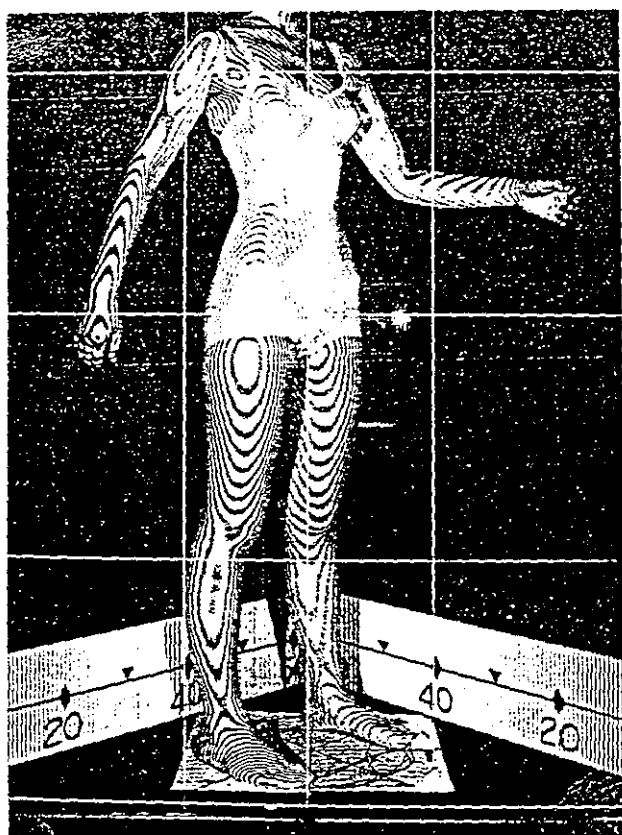


Figure 2- 2. Moiré fringe image of a live body, from Takasaki [1973]

2.2.3 Structured light method

The structured light method uses an active light pattern to illuminate the measured object. The distortion of the light pattern, caused by the curved shape of the object, is recorded by the camera. The 3-D shape of the object can be calculated by triangulation from the image of the object and known position relationship between the camera and the light projector. The structured light systems can be divided into two classes on the basis of their work modes: stationary and scanning systems.

2.2.3.1 Stationary systems

A stationary system usually projects a complex light pattern on the object. The light patterns cast 'feature points' on an object and are specially encoded so that they can be distinguished from each other in a single picture. Each light pattern has its fixed position relationship with the camera. The entire surface of the object can be measured by triangulation and interpolating the image from the distorted light pattern. *Rasterstereography*, as described by [Frobin and Hierholzer, 1983; Drerup and Hierholzer, 1994], is such a method. It projects a series of parallel horizontal light beams onto the object, a video camera is located at a fixed angle position with the projector to capture image. Ishida *et al.* [Ishida, Mori, Kishimoto, Nakazima & Tsubakimoto, 1987] reported a similar configuration.

Lewis & Sopwith [1986] presented a combination of structured light and stereo vision. They used two cameras to capture the image of a projected pattern of spots. The light spots cast feature points on the object surface to assist corresponding of stereoscopic image pairs. Precise calibration of the position relationship between the projector and cameras is unnecessary since calibration of the relative position of the two cameras is sufficient. Although the pattern of spots technique is simple for image analysis, ambiguity may be produced because the discrete spots overlap each other when they are projected around a curved surface, e.g. the chestwall. If the density of spots increases, it is more difficult to distinguish and correspond them in two different images. A similar system was reported by Aliverti, A., Ferrigno, G., & Pedotti [1993].

The grid light is another alternative of projection patterns [Wang, Mitiche & Aggarwal, 1987; Hu and Stockman, 1989]. It uses a continuous line to avoid the drawback

of spot patterns. However, a potential problem is the difficulty in generating a distortion-free grid pattern for a full size human body at a short distance.

In summary, the advantage of a stationary system is its short exposure time, simplicity and reliability. It usually takes only one picture by the camera system. The stationary systems avoid complex motion mechanisms and therefore have a high reliability. Short exposure time and a stationary subject platform can eliminate or reduce the body sway.

The disadvantage of the stationary system is its lower resolution because of the limitation in the density of light patterns. As one camera-projector unit can partially cover the surface of a cylinder-like object, the multi-cameras and multi-projectors configuration is required to overcome this problem [Vannier *et al.*, 1991]. Unavoidably, this increases the complexity of a system.

2.2.3.2 Scanning system

A scanning system basically consists of an imaging unit and a motion unit. The imaging unit contains a camera and a projector with known geometric relationships. By motion of either the imaging unit or the subject, a large scanning volume can be achieved. An advantage of the scanning system over the stationary system is that a simpler pattern of the projected light, usually a slit beam of light can be used to reduce the complexity in feature detection and image processing. Single light stripes avoid the ambiguity of pattern recognition. The scanning system can cope with a large or cylinder-like object with simpler camera-projector configuration. The implementation of the scanning system has been presented by Halioua *et al.* [Halioua, Krishnamurthy, Liu & Chiang, 1985], Jones *et al.* [1989], and Moss *et al.* [Moss, Linney, Grindrod & Mosse, 1989]. Representative commercial products (CYBERWARE 4020/PS, 3030/PS) are already available.

The data capture time of a scanning system is decided by three factors: the sampling interval between two continuous image frames, the total number of image frames (steps of scanning) and the maximum acceptable speed of scanning. The third factor depends on which part moves. If the imaging unit moves, the maximum speed is decided by projection and exposure time, sampling and storage speed of camera. If the platform on which a

subject stands rotates, then the maximum speed must take into account body sway, hazards of fast acceleration/deceleration, and comfort level acceptable to the subject.

Most developed scanning systems have adopted a TV format camera as the image sensor. The resolution of such a camera can not cover the height of the whole human body within acceptable accuracy of data and permissible space distance. Hence, the configurations with multi-cameras and multi-projectors have been invented to overcome this problem. The LASS [Jones *et al.* 1989] and the latest CYBERWARE whole body scanner [Cyberware 1996] are two such implementations. The LASS system uses seven cameras to cover 2.1 metres height with a spatial resolution of 1 mm. The imaging unit of CYBERWARE's whole body scanner (WBS) can translate along the height direction of the scanned body in a resolution of 2 mm. Because a single imaging unit can not cover a 360° body surface, two or four imaging units must be used in WBS.

There are other varieties of scanning systems, for example, encoded light pattern [Halioua *et al.*, 1985], translation of motion unit (CYBERWARE 's M series model), and synchronous scanning unit [Rioux 1992, Rioux & Bird, 1993, Uesugi, 1991]. It is worthwhile mentioning that synchronous scanning is an important type of scanning system. Its motion unit is a projection mirror. The rotation of the mirror changes the orientation and position of the projected light. The mirror is lightweight and, therefore, easy to control. Synchronous scanning avoids large motion mechanisms and probably cuts scanning time, although it does not overcome the multi-exposure problem if a cylinder-like object is measured.

In summary, most existing full body scanners adopt the scanning system to cope with the large dimension and cylinder-like shapes of the human body. However the longer exposure time in scanning mode is a major drawback when the human body is measured, and certain techniques are required to alleviate or correct the body sway.

2.3 Applications of 3D surface anthropometry and data interrogation

This section reviews applications of 3D surface anthropometry in medical, engineering design/ergonomics, clothing design and size surveys, etc. The development of 3-D surface anthropometry is stimulated by the requirements from these disciplines. A review of these applications will give a clear picture on data interrogation methods.

2.3.1 Medical application

The medical application of 3-D measurement and data interrogation of the human body and its parts is an important branch of 3-D surface anthropometry. The medical application of 3D surface anthropometry can be categorised into two classes: disease diagnosis [Drerup *et al.*, 1983 & 1994; Ishida *et al.*, 1987; Jones, Baker, Hardy & Mowat, 1994], plastic surgery and prosthetic fitting [Burke *et al.* 1983; Duncan & Mair 1983; Arridge *et al.* 1985; Vannier *et al.* 1993; Schreiner and Sanders 1995; Macleod 1986; Moss *et al.* 1989; Naftel 1989].

In disease diagnosis category, applications are oriented to those requiring surface measurement or surface feature, e.g. scoliosis and kyphosis. Drerup *et al.*, [1983, 1994] attempted to relate the deformity of the human spine with the shape of the back surface. In their study, the spine mid-line was derived from three essential types of shape data:

- 1) the line of the spinous processes;
- 2) surface rotation at the locus of the line of the spinous process;
- 3) anatomical landmarks.

To produce these data surface curvature analysis was employed. Clinical parameters for diagnosing scoliosis and kyphosis are derived on the basis of an estimated spinal midline.

Ishida *et al.* [1987] described a similar study to Drerup's by using 3-D surface measurement of the human back to evaluate scoliosis. Their method is to correlate three shape indices of a series of cross sections to Cobb angle which is an index to scoliosis. The shape indices used are rotation, shear and size asymmetry of a cross section.

A commercial system, ISIS, developed by Oxford Metrics Ltd [MacCleod, 1986] has been applied in the evaluation of spinal deformity, in which the curvature of the spine was estimated from the curvature of a surface.

Jones *et al.* [1994] applied 3-D scanned data of the whole body to calculate the surface areas of normal and liver-diseased children for estimation of drug dosage based on the body surface area. More accurate area/volume estimation is required in skin transplant [Naftel, 1989] and wound treatment [Jones and Plassmann, 1995].

3-D surface anthropometry has been applied in plastic surgery. 3-D surface measurement of the human face for orthognatic surgery was discussed by Burke *et al.*

[1983]. By providing the measurement of change in facial soft tissue morphology, the clinician can have a better knowledge in surgery planning and of the stability of soft tissue after surgery. Even patients can have a better understanding of their new appearance by observing the change of 3-D morphology as seen via a computer screen. The method of interrogating 3-D data in Burke's work was to calculate linear parameters connecting identifiable landmarks, and to construct horizontal, vertical and oblique profile outlines of the face measured.

Arridge *et al.* [1985] aimed to provide a computerised platform for orthodontic surgery. It incorporated an optical scan of the human face and skull and planned to model the 3-D data in such a way that a surgeon can interactively manipulate the data and observe the result on a graphic screen, such that a real three dimensional planning and evaluation of plastic surgery could be achieved. A prototype system for surgical planning, although the raw data was not from 3-D surface scanning, was reported by Yoshida *et al.* [Yoshida, Miyazawa, Doi & Otsuki, 1993].

A further application in facial plastic surgery was introduced by Vannier *et al.* [1991, 1993]. Several data interrogation methods were discussed in their papers, including:

- Anthropometric measurement manually taken from screen by mouse operation;
- Preoperative and postoperative assessments achieved by observing and superimposing images;
- Volume monitoring implemented by scanning before and after operation and calculating the differences from 3-D images;
- Potential applications in customisation of implant and interactive planning.

Other applications of 3-D surface measurement in medical modelling were described by Duncan & Mair [1983]. For example, the 3-D surface data of the limb stump can be used to optimise the socket design for an artificial limb. If one side needs repair or modification, the 3-D data of the symmetrical other side can be mirrored for a prosthetic model, presuming the symmetry of the human body. Similar studies were also reported by Schreier and Sander [1995].

2.3.2 Engineering design/ergonomics application

The suitability of an engineering design for human users is a major concern in human factor/ergonomics research. Traditional anthropometric data have been widely applied in the design of size, reachability and optimal workspace of engineering products. However, these data are insufficient. If the interface between the surface of the human body and a product must be optimised, a complete surface model of a body is required. Robinette and Whitestone [1994] described a method which has been adopted to develop a helmet for pilots. Their study demonstrated the advantage of 3D anthropometry and revealed the inappropriateness and inaccuracy of traditional anthropometry. In the study, the 3-D scanning of subjects with and without helmets were taken and the scanned data visualised. The distances from the head surface of subjects to internal surface of the helmet were displayed from different viewpoints. These visualisation methods provide a better understanding of the physical and spatial relationships between the helmet and pilots' heads.

Automotive industries have strong interests in seating comfort study. This has stimulated the need of using 3-D surface data of the human body for contact pressure analysis [Case, Xiao & Porter 1995]. The 3-D surface model could be useful in other computer aided engineering analyses, e.g., the analysis of thermal and electromagnetic fields.

Currently there is a plan to use 3-D scan data of the human body in stress analysis for heavy labour workers (Cyberware News: 3-D development No.8) in a project by the National Institute for Occupational Safety and Health (NIOSH) in USA. The 3-D scanned data can provide accurate information about size, volume/mass of the body in stress analysis.

2.3.3 Clothing design/size survey application

Clothing designers have worked on real human bodies or design stands for centuries. The use of 3-D surface data of the human body in clothing design is not new. In spite of this, to acquire and to produce a 3-D average body shape would be very difficult without 3-D measurement techniques. The massive production of clothes requires design stands with average human shapes for good fitting, correct sizing and grading of block patterns. It is

clear that the 3-D measurement and modelling of the human body is paramount in the clothing industry.

A pioneering study to acquire average 3-D bodies from a sample population has been conducted at Loughborough University, UK [Jones, West, & Brook-Wavell, 1993]. This study utilises the LASS system to scan more than 200 female subjects covering a range of clothing sizes and creates a procedure to develop a manikin with average shape from a database of scanned subjects. A software tool is developed to manipulate the 3-D scanned data, to extract measurements and to average 3-D surface data.

A large scale survey which involved 34,000 subjects between 1992 and 1994, assisted with a 3-D surface scanner, has been reported from the Research Institute of Human Engineering for Quality Life in Osaka, Japan [RIHEQL, 1995]. The subjects were measured by traditional anthropometric methods and by a NKK's 3-D whole body scanner Voxelan®. A 3-D shape database is to be constructed from this survey and will be used to produce CAD manikin with average shapes or with shape for special groups of people.

There are a number of research projects on the development of 3-D computer-aided design packages for clothing. The 3-D surface model of the human body is a basic element in design and evaluation of clothing in such software [McCartney and Hinds, 1992, Okabe Imaoka, Tomiha & Niwaya, 1992, Computer Design Inc., 1995]. The complete integration of the acquisition, conversion, and grading of the 3-D human body surface into a CAD package is still at the preliminary research stage.

2.3.4 Other application

Besides the above three categories, there are other application areas which could benefit from 3-D surface anthropometry. These include: 1) cross sectional and longitudinal human growth studies- 3-D shape data of the human body can be recorded at different ages to reveal the rheological process of humans [Erb, 1992]; 2) virtual reality and physically based modelling of the human body which deals with the soft and moveable aspects of the human body [Waters, 1992] or dynamic behaviour of the human body [Ko and Badler, 1996]. When the interaction of the human body and external forces occurs, the shape of the 3-D surface interface will change with the position, posture of the body and external conditions. Research on this topic is receiving increasing attention.

2.3.5 Data interrogation method

Data interrogation methods required in 3-D surface anthropometry are summarised from aforementioned application examples into five major categories:

- 1) identification of anatomical landmarks;
- 2) linear (one-dimensional) anthropometric measurements, including: width, length, circumference and surface distance;
- 3) higher dimensional anthropometric measurements of a surface, including: area and volume;
- 4) curve/surface shape analysis: including normal, tangent, and curvature analysis of a surface;
- 5) comparison and average of 3-D shape, and 3-D image superimposing, etc.

Category one is fundamental for other anthropometric measurements. It is difficult to identify anatomical landmarks from 3-D scanned data by software without the operator's interference. This could form a bottleneck in the applications of 3-D surface anthropometry. Category two reflects the area of traditional anthropometry. Traditional anthropometry is easier and more convenient than 3-D surface anthropometry unless an automatic extraction of linear measurement from 3-D surface data is achieved. Category three is an area in which 3-D anthropometry shows more promise than traditional anthropometry. The earlier practice of 3-D anthropometry has concentrated on this area [Weissman, 1968, Dunn, Keizer and Yu, 1989]. Categories four and five are two areas in which traditional anthropometry can not deal with at all. 3-D surface anthropometry opens the possibility of exploiting surface data of the human body by comparison, average and analytic analysis, although how to compare and analyse the data would depend on the application. Chapter eight will elaborate these requirements and relevant computational methods in data interrogation.

2.4 3-D surface modelling of the human body

3-D modelling of the human body is largely a computerised technique to visualise the human figure in the static or dynamic form. Simple applications require only a single body form to be presented, whilst complex applications may need the presentation of interaction between the human bodies and environment. The representative of a body model

varies from one application to another. Figure 2-3 shows four different representations of the human body model, namely: stick, boundary, contour and shaded surface.

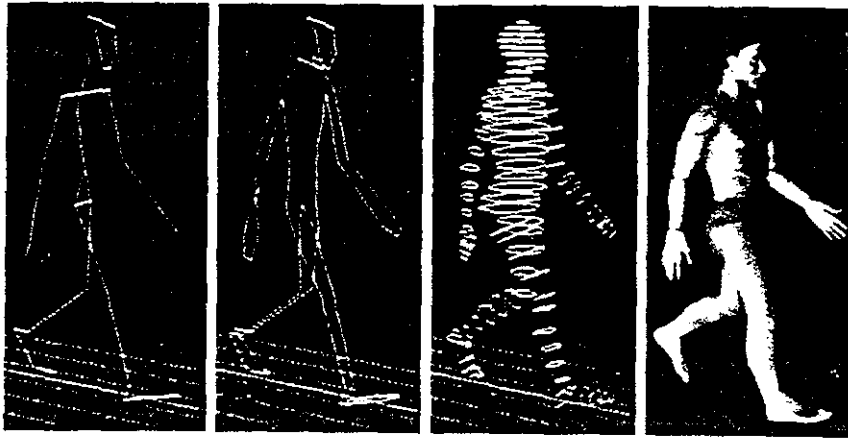


Figure 2- 3. Four representations of the human body, from Calvert et al.[1993]

3-D surface modelling represents an object in a realistic form, and therefore has wide applications in many areas. Three frequently used forms to represent a surface are polygon mesh, wireframe and parametric surface. Polygon mesh approximates a surface by connecting a great number of triangular or quadrilateral polygons. The accuracy of approximation can be increased by subdividing each polygon into several finer polygons. Figure 2-4 shows the polygon version of 'Fourth men'. The wireframe form of a surface usually represents a surface in regular sectional curves or merely connects surface points into regular curves. Contour line representation of the body in Figure 2-3 is such a example. The parametric surface represents a surface by a blended parametric function which requires much less data points than the other two models. Surface data can be generated from the parametric model to any density as required. Hence the parametric surface is a concise and compact model. Its disadvantage is that one parametric surface is not able to represent the whole human body. A limb, hand or foot must be represented by different parametric surfaces or wireframe forms.

Accuracy is an important criteria in evaluating a representative form. The representative accuracy of the human body with respect to a 3-D model could be differentiated at three levels: anthropometry accuracy, engineering design accuracy and

display accuracy. The model with anthropometry accuracy conforms with traditional anthropometric data of the population. Such a model has been used in several human body modelling software packages [Dooley, 1982, Das and Sengupta, 1995]. Models with engineering design accuracy must represent a surface at a high level of precision. 3D models for general visualisation and virtual reality should be of display accuracy. The display accuracy could vary from applications. It is hard to describe in a quantitative way and will not be further discussed.

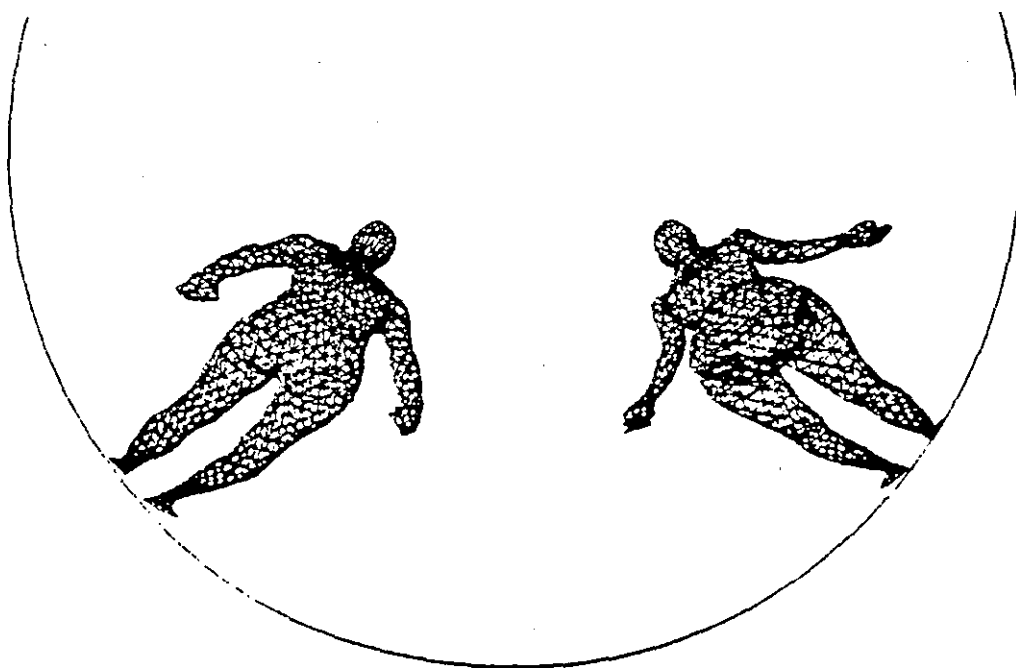


Figure 2- 4. Polygon form of the 'Fourth Men' [Fetter 1982]

2.4.1 Surface modelling of the human body with engineering design accuracy

Accurate surface models are usually expressed as a polygon mesh, wireframe or parametric surface form. The polygon mesh and wireframe forms joint discrete surface points into an organised net. They are simple in computation but difficult in data exchange and interrogation. The approach of parametric surface modelling includes surface interpolation and surface approximation. The computation of a parametric surface is complex but data storage, exchange and interrogation are simpler.

Surface interpolation based on cross-sectional curves is an established technology, which is called lofting or skinning [Faux and Pratt, 1978]. Surface interpolation can reduce the amount of data, and smooth the noise in raw scanned data. There are certain errors between the generated surface from a skinning method and the raw data because the interpolation only pass through given cross-sectional data. The errors are unavoidable but could be reduced providing that proper cross-sectional data are selected.

Compared with the interpolation, surface approximation is a global computation. It uses a surface function to approximate all raw data in some optimal measure, for example, the least square sum distance. Because all raw data, especially the scanned data, are involved in the computation, the approximation is more complicated and time-consuming. Moreover the approximation usually adopts an iterative method to select parametric values, number of control points to achieve an optimal solution. This costs longer computational time.

Mesh based approximation is another technique to approximate surface data, which has wide applications in modelling raw scanned data [Chen & Schmitt, 1994].

2.4.2 Anthropometry-based modelling of the human body

Anthropometry-based modelling is concerned with the representation of the human figure with consideration of anthropometric measurements. Because the traditional anthropometric measurement is 'linear'--i.e. only a distance relationship is obtained, the control of a body model is limited to these linear dimensions. The most simple model of the human body is based on a stick figure in which the movement and action of the human body can be simulated [Fetter, 1980]. The stick figure describes a simplified human skeleton which consists of linked segments. Joints of segments coincide with some important anatomical/anthropometric joints, such as ankle, knee, hip, and shoulder. The most famous workplace simulation packages use similar human skeleton model [Karwowski, Genaidy and Asfour, 1990] because they mainly deal with the reachable envelope and posture of the human body. When the volume of the human body must be counted or for visualisation purposes, simple polyhedron, wireframe entities are used as flesh of the skeleton models [Karwowski *et al.*, 1990, Badler, Phillips and Webber, 1993].

In an anthropometry-based modelling system, the modification of the models depends largely on the percentile of anthropometric measurements. The system must be backed with an anthropometry database. Some systems merely use an anthropometric data file as the control parameters of a model [Case *et al.*, 1990; Badler, *et al.*, 1993]. Other systems incorporate a complete anthropometric database for more flexible model control, for example, SAFEWORK [Fortin, Gilbert, Beuter, Laurent, Schiettekatte, Carrier & DeChamplain, 1990].

Surface modelling of the human body with anthropometry accuracy (shortened to *anthropometry based surface modelling*) has not been fully investigated yet. This is because:

- 1) The traditional anthropometric measurement does not provide much 3-D information. The link between the 3-D shape of the human body and anthropometric data is not sufficient.
- 2) Applications in workplace design and other ergonomics areas do not require accurate 3-D variation of a body model. They need a 3-D model mainly for visualisation.
- 3) Precise engineering analysis and design related to body shape is individual and expensive. An accurate 3-D model is only used in very special applications such as G-suit design [Roebuck *et al.*, 1975].
- 4) Anthropometry based surface modelling must be backed with a 3-D body database which was not available a few years ago.

It is clear that anthropometry based surface modelling is a new topic in the 3-D surface anthropometry era. It could be beneficial to design and manufacturing industries in a number of ways, such as: a) establishing a link between traditional anthropometric measurement and 3-D modeling of the human body, turning existing anthropometric survey data into 3-D model; b) classifying and grading a 3-D body surface on the basis of simple anthropometric measurements and creating better fitting criteria. With more and more 3-D scanned database available, anthropometry based surface modeling will become more representative.

2.5 Summary

This chapter has briefly reviewed the evolution and main features of 3-D surface anthropometry. The scope and function of 3-D surface anthropometry is introduced by reviewing its three components: data acquisition, data interrogation and body modelling from existing systems and applications.

The data acquisition is concerned with non-contact 3-D surface scanning methods of the human body. Three principal types of methods are described. The data interrogation of 3-D scanned data is extracted from a number of applications which belong, or are close, to the anthropometry domain. Five categories of data interrogation are recognised. The body modelling is confined in surface modelling task in conjunction with 3-D scanned data and anthropometry based modelling. These three components will be discussed further in following chapters.

CHAPTER THREE

THREE DIMENSIONAL SURFACE MODELLING OF THE HUMAN BODY

Surface modelling is an important approach to describe the raw 3-D scan data. This chapter focuses on surface interpolation and approximation of 3-D scanned data of the human body. Non-Uniform Rational B-Spline (NURBS) is chosen as the basic function for the modelling process. Surface interpolation is applied to model the human trunk from LASS curve-fitting data. Relevant parameterisation problem of surface interpolation is investigated. Curve and surface approximation are employed to trim arms from raw scanned data and to fill and smooth the data gap caused by trimming. This is a stage towards automatic curve fitting of raw data.

3.1 Tensor-product approach of parametric surface interpolation and its application in human body modelling

The tensor-product approach is an established method to generate a parametric surface from two blending functions. This section describes the basic principle and steps in applying the tensor-product of the NURBS functions for human body modelling.

3.1.1 The basic definition of non-uniform rational B-spline curve and surfaces

A parametric B-spline curve is a vector-valued polynomial function of the form [de Boor 1978; Piegl, 1991]

$$C(t) = \sum_{i=0}^n P_i \cdot N_{i,p}(t) \quad \text{where } 0 < t < 1 \quad (3.1)$$

where P_i are control points, and $N_{i,p}(t)$ are the normalised B-spline of degree p defined over the non uniform knot partition $T = \{t_0, t_1, \dots, t_m\}$, where $m = n + p + 1$. $N_{i,p}(t)$ is recursively defined as

$$N_{i,0}(t) = \begin{cases} 1 & \text{if } t_i < t < t_{i+1} \\ 0 & \text{otherwise} \end{cases}$$
$$N_{i,p}(t) = \frac{t - t_i}{t_{i+p} - t_i} N_{i,p-1}(t) + \frac{t_{i+p+1} - t}{t_{i+p+1} - t_{i+1}} N_{i+1,p-1}(t) \quad (3.2)$$

and satisfies: $\sum_{i=0}^n N_{i,p}(t) = 1$

For a Bezier-like curve on the interval $[0, 1]$, the knot vector T has the form:

$$T = \{ 0, 0, \dots, 0, t_{p+1}, \dots, t_{m-p-1}, 1, \dots, 1, 1 \} \quad (3.3)$$

Such a curve interpolates the endpoints and is tangential at the endpoints to the first and last legs of a control polygon.

The control points of a B-spline are associated with certain parameter values. These parameter values are called the nodes or Greville abscissas, defined as follows [Farin, 1988]:

$$p_i = (t_{i+1} + t_{i+2} + \dots + t_{i+p})/p \quad (3.4)$$

Therefore the shape of a parametric B-spline curve is decided by its control points and knot vector according to the form (3.1).

A NURBS is a generalised rational B-spline function defined [Piegl 1991] as:

$$C_w(t) = \frac{\sum_{i=0}^n w_i \cdot P_i \cdot N_{i,p}(t)}{\sum_{i=0}^n w_i \cdot N_{i,p}(t)} \quad \text{where the } w_i \text{ are the so-called weights, (3.5)}$$

When all weights, w_i are equal to 1, the curve becomes its non uniform non rational version.

According to the parametric surface theory, a surface, represented by two parameters u and v , can be defined as [Farin 1988] :

$$S(u, v) = \sum_{i=0}^m \sum_{j=0}^n P_{i,j} \cdot N_{i,p}(u) \cdot N_{j,q}(v) \quad \text{where } 0 < u, v < 1 \quad (3.6)$$

where $P_{i,j}$ form a control patch and $N_{i,p}(u)$ and $N_{j,q}(v)$ are the normalised B-spline basis functions with form (3.2), and defined respectively over the knot vectors:

$$U = \{ 0, 0, \dots, 0, u_{p+1}, \dots, u_{r-p-1}, 1, 1, \dots, 1 \} \quad (3.7a)$$

$$V = \{ 0, 0, \dots, 0, v_{q+1}, \dots, v_{s-q-1}, 1, 1, \dots, 1 \} \quad (3.7b)$$

Again, the knot vectors (3.7a) and (3.7b) assume a Bezier-like boundary condition for the surface. The equation (3.6) is often called the tensor product representation of a surface.

A NURBS surface is the rational generalisation of the tensor-product B-spline surface, which is defined as:

$$S_w(u, v) = \frac{\sum_{i=0}^m \sum_{j=0}^n w_{i,j} \cdot P_{i,j} \cdot N_{i,p}(u) \cdot N_{j,q}(v)}{\sum_{i=0}^m \sum_{j=0}^n w_{i,j} \cdot N_{i,p}(u) \cdot N_{j,q}(v)} \quad (3.8)$$

where $w_{i,j}$ are the weights. When all weights $w_{i,j}$ are equal to 1, the surface is a true tensor-product surface.

3.1.2 Curve interpolation

The curve interpolation problem is to find M control points P_i , ($i=0, \dots, M$) so that the B-spline curve can pass through the given data points C_k , ($k=0, \dots, n$). Figure 3-1 shows the data and control points of a curve. The interpolation procedures of a curve are derived from the B-spline representation (3.1) and knot vector form (3.3).

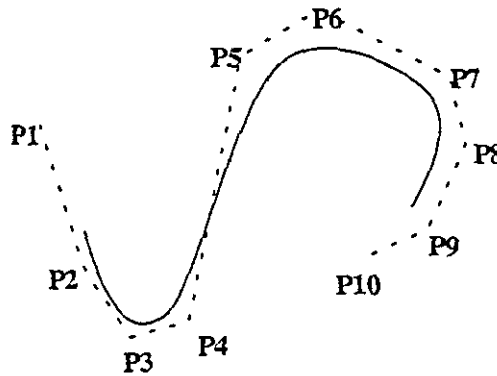


Figure 3-1. A B-spline curve and its control points.

a) Parameterisation

The parameterisation is to find a set of parameter values s_k , ($k=0, \dots, M$) so that

$$C_k = \sum_{i=0}^n P_i \cdot N_{i,p}(s_k) \quad (3.9)$$

when $M < n$ equation (3.9) is under-determined, and when $M > n$ it is over-determined. An interpolation problem requires $M = n$ so that a unique solution may be achieved.

The value of control points P_i is determined by data points C_k and parameters s_k , which are also related to data points C_k . A reasonable distribution of parameters s_k can guarantee the Crame matrix of equation 3.9 is full rank. Therefore, before solving equation 3.9, adequate parameters s_k must first be decided. The process of finding parameter s_k is called parameterisation. The most frequently used method of parameterisation is cumulative chord length parameterisation, i.e.

$$s_0=0, \quad s_i = s_{i-1} + \frac{|C_i - C_{i-1}|}{\sum_{j=1}^n |C_j - C_{j-1}|}, \quad s_n=1, \quad (3.10)$$

where $|C_i - C_{i-1}|$ is the Euclid distance of two vector data points.

b) Defining an adequate knot vector T

Given the parameter values, the knot vector should reflect the distribution of these parameters. An approximation of the knot vector from the parameter values is given by Greville abscissas (3.4). Therefore the knot vector (3.3) can be found by

$$t_p=0, \quad t_{p+j} = \frac{1}{p} \sum_{i=j}^{j+p-1} s_i, \quad j=1, \dots, n-p, \quad (3.11)$$

c) Solving control points

The solution of control point P_i is a linear equation system problem. With a proper knot vector and node distribution, the coefficient matrix in equation 3.9 will be totally positive and of bandwidth [de Boor, 1978]. Therefore, linear systems (3.9) can be solved by triangular decomposition [Stewart, 1973].

Algorithm 3.1: Curve interpolation

Input: Order of curve p ;
 Number of data points n ;
 Data vector C .

Output: Control vertex vector P of the B-spline curve;
 Knot vector T .

Step-1: Compute parametric vector t (Equation 3-10) and
 knot vector T (Equation 3-11);

- Step-2: Compute coefficient matrix $N(i, j)$ ($i=0, \dots, n$; $j=0, \dots, n$) according to Equation (3.2) from which $n_{i,j}$ equals $N_{j,p}(s_i)$;
- Step-3: Solve linear system $N^*P=C$ by triangular factorisation.

3.1.3 Tensor-product surface interpolation: skinning approach

In computer aided geometric design, the surface interpolation method, based on a family of given cross-sectional curves, is known as the skinning or lofting technique [Faux and Pratt, 1978; Piegl, 1991; Farin, 1988]. The surface generated by interpolation passes through the selected cross-sectional curves exactly. Middle slices of the surface between the feature positions are approximated by interpolating the cross-sectional curves.

From the viewpoint of computation, the surface interpolation is an inverse process of surface generation, that is, surface interpolation involves finding the control patch according to the known data points on the surface. There are $(n+1) \times (m+1)$ unknown variables P_{ij} for the surface interpolation problem in the form of equation 3.6. They can be acquired by solving a $(n+1)(m+1) \times (n+1)(m+1)$ order linear equation system. Nevertheless, when n and m are large, this approach is very time-consuming and usually unfeasible.

Based on the tensor-product equation 3.6, the surface interpolating can be simplified to a series of curve interpolating and the solving process produces a much lower order linear system if we rewrite equation 3.6 as:

$$S(u, v) = \sum_{i=0}^n \left[\sum_{j=0}^m P_{i,j} N_{j,q}(v) \right] N_{i,p}(u), \quad (3.12)$$

where the part in brackets is a curve expression and thereby the control patch is replaced by a family of control curves $C_i(v)$:

$$C_i(v) = \sum_{j=0}^m P_{i,j} N_{j,q}(v), \quad (3.13)$$

therefore:

$$S(u, v) = \left\{ \sum_{i=0}^n C_i(v) N_{i,p}(u), v \in [v_0, v_m] \right\}, \quad (3.14)$$

The surface $S(u,v)$ is represented as an infinite set of isoparametric curves corresponding to v parameter. For a fixed v value, equation 3.14 is a u curve and is called the cross-sectional curve of the interpolated surface. [Woodward, 1988, Piegl, 1991].

The calculation of control points can be divided into two steps: calculating the control points of every cross-sectional curve and calculating the control points of the surface.

1) *The calculation of the control points of curve*

Presuming that each cross-sectional curve is an isoparametric curve with a fixed v value, $(n+1)$ data on a cross-sectional curve are sampled and equation 3.15 is subsequently formed:

$$\left\{ \sum_{i=0}^n b_{i,j} N_{i,p}(u) = s_{k,j}, \quad k = 0, \dots, n \right\} \quad j = 0, \dots, m. \quad (3.15)$$

here $S_{k,j}$ is the point on the j th cross-sectional curve corresponding to parameter u_k (i.e. $S(u_k, v_j)$), and $b_{i,j}$ are unknown control points of the j th cross-sectional curve and can be solved from the linear equation system 3.15. In order to find all the $b_{i,j}$, $(m+1)$ equations of the order of $(n+1)$ must be solved.

2) *The calculation of the control points of surface*

The resulting $b_{i,j}$ from step one are substituted into equation 3.13, this time they act as known data of the equation, that is:

$$\left\{ \sum_{j=0}^m P_{i,j} N_{j,q}(v) = b_{i,l}, \quad l = 0, \dots, m \right\} \quad i = 0, \dots, n. \quad (3.16)$$

The control points, $P_{i,j}$, of the surface $S(u,v)$ can be solved from the linear equation system 3.16. There are $(n+1)$ equations of order $(m+1)$ to be solved in this step.

In total, $(m+1)$ linear equations of the order of $(n+1)$ and $(n+1)$ linear equations of the order of $(m+1)$ are needed to be solved in the calculation of $P_{i,j}$. Figure 3-2 illustrates two steps of the skinning method.

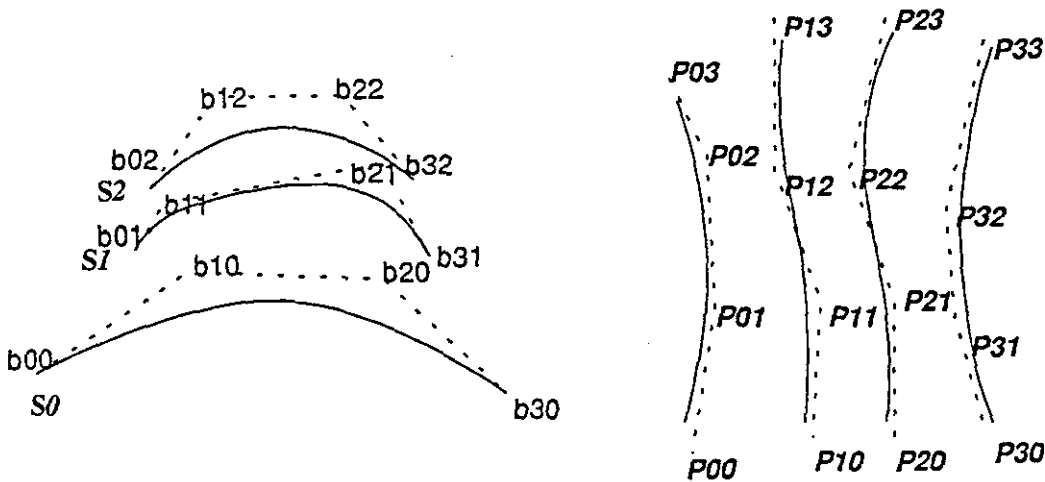


Figure 3-2. Two-steps of skinning method: surface control point and cross-sectional curves

Algorithm 3.2: Surface interpolation

- Input:** Orders of surface p and q ;
 Number of data points m and n ;
 Data matrix S .
- Output:** Control point matrix P of the B-spline surface;
 Knot vectors U and V .
- Step-1:** Compute parametric vectors u, v and knot vectors U, V ; (again Equation 3-10 & Equation 3-11)
- Step-2:** Compute coefficient matrix $N(i, j)$ ($i=0, \dots, n$; $j=0, \dots, n$) according to Equation(3.2) from which $n_{i,j}$ equals $N_{i,p}(u_i)$;
- Step-3:** Solve linear system $N \cdot B_k = S_k$ ($k=0, \dots, m$) by triangular factorisation.
- Step-4:** Compute coefficient matrix $N(i, j)$ ($i=0, \dots, m$; $j=0, \dots, m$) according to Equation(3.2) from which $n(i, j)$ equals $N_{j,q}(v_j)$;
- Step-5:** Solve linear system $N \cdot P_k = B_k$ ($k=0, \dots, n$) by triangular factorisation.

3.1.4 Surface interpolation of the human body

3.1.4.1 LASS shape matrix: a format for exchange of body data

It has been recognised that cross-sectional representation is one basic form for the human body [Thalmann *et al.*, 1991, McCartney *et al.*, 1992]. West [1994] put forward cross-sectional data as a standard exchange format for 3-D scanning data of the human torso. The data format is known as the LASS shape matrix.

The LASS shape matrix contains a number of data rows. Each row consists of 16 pairs (x, z) co-ordinate which define one half of a cross-section of the human body, as arranged in Figure 3-3.

n	S															
	$x_{1,1}$	$z_{1,1}$	$x_{1,2}$	$z_{1,2}$	$x_{1,16}$	$z_{1,16}$	y_1								
	$x_{2,1}$	$z_{2,1}$	$x_{2,2}$	$z_{2,2}$	$x_{2,16}$	$z_{2,16}$	y_2								
	.															
	.															
	.															
	$x_{n,1}$	$z_{n,1}$	$x_{n,2}$	$z_{n,2}$	$x_{n,16}$	$z_{n,16}$	y_n								

Figure 3- 3. Format of LASS shape matrix

These 16 points comprise the interpolated data points of a cardinal spline which fits to one cross-sectional slice of raw data. An interactive fitting procedure was developed so that a good distribution of data points is acquired [West 1994].

For representing a human torso eight levels are recognised as key cross-sectional curves, as shown in Figure 3-4. Some middle slices are inserted between them to improve the accuracy. These eight key slices correspond to key anatomical locations, namely: *crotch, hips, waist, under bust, maximum bust, underarm, bideltoid, and neck*. They represent the most common used anthropometric positions on the human torso, and thereby are significant for many applications. In addition these cross-sections present main shape features of the human torso. By interpolating these cross-sections, the shape of the human

torso could be well regenerated. Following sub-sections discuss how to apply skinning method to generate a surface of the human body from the LASS shape matrix.

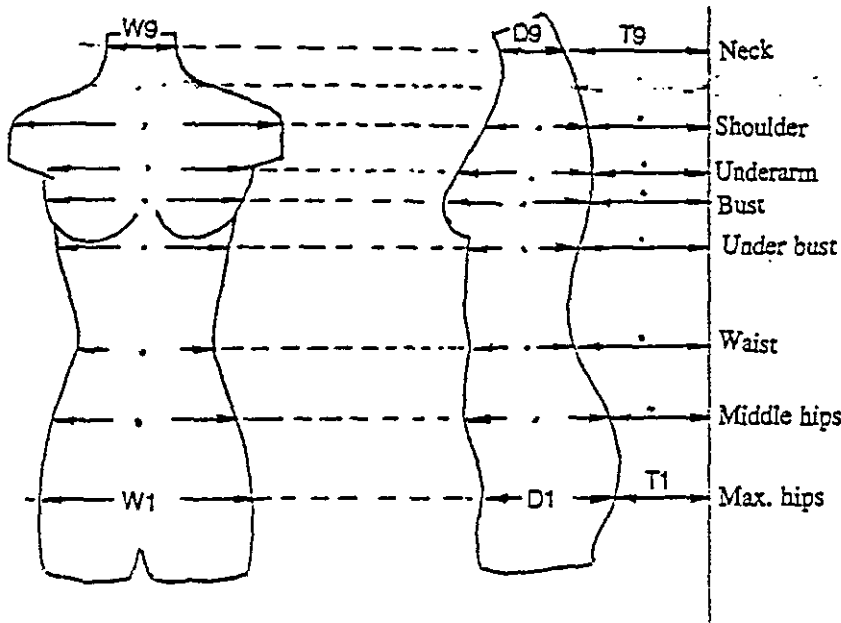


Figure 3- 4 Eight key levels of the human torso

3.1.4.2 The parameterisation problem in the skinning technique

The success of the skinning technique relies largely on the proper selection of the isoparametric curves. The isoparametric curves are easy to define from scanner data because the data are usually arranged on a rectangular area of a uniform space. The LASS shape matrix defines all data with the same height in the same data row, which makes it possible to define every row of the shape matrix having consistent parameter in v direction. From this definition, different data rows have different v values. That is, the v parameter varies in the vertical direction of the human body.

The problem to assign adequate parameter values to interpolated data is known as parameterisation [Farin 1988]. According to equation 3.16, each cross-sectional curve is a u parameter curve. The distribution of the u parameter, reflecting the distribution of cross-sectional data, varies from slice to slice since cross-sectional shape of the human body varies at different levels. Moreover, the LASS shape matrix is formed on the basis of a manual

fitting procedure. A good u parameter distribution for one slice could be a 'poor' distribution for other slices. Figures 3-5 (a) and (b) show adequate data distribution for chest and upper hip levels of a female body under constraint of 16 interpolated points. However, their parametric vectors from the chord length parameterisation are different:

$$U_{\text{upperhip}} = [0, 0.091, 0.157, 0.239, 0.324, 0.409, 0.486, 0.560, 0.644, \dots, 1.0];$$

$$U_{\text{chest}} = [0, 0.083, 0.139, 0.210, 0.292, 0.379, 0.471, 0.560, 0.663, \dots, 1.0].$$

This could cause serious distortion in the regeneration of a surface from interpolation.

A similar parameterisation problem exists in the v parameter direction. A 'good' distribution of data for all cross-sectional curves has no guarantee of 'good' data distribution in the v direction. Here is an example of two v parameter vectors taken from a body in Figure 3-6 (d) which is a surface with a uniform distribution of the u parameter across all cross-sections:

$$V_{0h} = [0.000, 0.094, 0.167, 0.239, 0.311, 0.384, 0.456, \dots, 1.000]$$

$$V_{15h} = [0.000, 0.063, 0.128, 0.191, 0.253, 0.315, 0.378, \dots, 1.000]$$

Distortion of a generated surface due to bad parameterisation can be observed from Figure 3-6 (a). In this example, 26 cross-sections are well curve-fitted. Each curve-fitted section contains 16 data points. Although the generated surface passes through all interpolated cross-sections, distortion occurs as a result of dramatic change of the u parameter distribution crossing the under bust level.

3.1.4.3 Suggested parameterisation method

Various parameterisation methods can be found [Hoschek, 1988; Farin, 1988; Lee 1989]. Most of them discussed how to calculate the 'good' parameter values from given data points for curve interpolation. Parameterisation for surface interpolation is much more complicated and needs an iterative optimisation process [Sarkar and Menq, 1991]. From engineering viewpoint, good parameter distribution comes from good raw data distribution. Well organised raw data can dramatically improve the quality of surface modelling.

In order to acquire good accuracy in surface interpolation, a two stage procedure is proposed to fulfil the u parameterisation process: The first stage is to interpolate or fit the raw cross-sectional data by a reasonable parameterisation method (the chord length method is used in this thesis). This produces a set of interpolated data points or control vertices for curve interpolation. The second stage is to re-sample the generated curves from the data points produced in the first step in such a way that new data distribution is more uniform than the old ones. This procedure could improve the parameterisation of surface interpolation. This proposed method is named as parameter-based relocation of cross-sectional data in the following description.

When the new relocation method of the cross-sectional data is applied to the LASS shape matrix, it consists of three steps: 1) interpolating 16 data points by a degree-3 cardinal spline and regenerating a cross-section in high accuracy (presuming that the existing 16 data points have been well located to represent the cross-section by the cardinal spline); 2) re-sampling the new cross-sectional curve in a higher resolution (say 30 ~ 40 points or more) and interpolating these new data points by a degree-3 non-uniform B-spline; and 3) generating new interpolated data at those positions which are determined by a given u parameter vector.

For the purpose of tensor-product interpolation, all cross-sectional curves must be normalised to have the same number of control points (or interpolated data points), even if these cross-sections are formed by different number of original data points. Usually this requires the number of data points in some cross-sectional curves to be raised to a number that the most complex shape of the cross-sectional curve requires. The above relocation procedure can meet this requirement. A predetermined u parameter vector used in the re-sampling process governs the number and distribution of new interpolated data in each cross-sectional curve. Algorithm 3.3 provides further details.

Algorithm 3.3: Relocation of cross-sectional data

Input: A predetermined parameter vector T
 Data vector D ;
 Number of input data k ; (i.e the dimension of D)

Order of B-spline curve p ;

Number of output data n ; (i.e. the dimension of C and T)

Output: New data vector C ;

Step-1: Curve interpolation of D by the cardinal spline;

Produce a temporary data vector LD with m elements;

Step-2: Apply algorithm 3.1 to interpolate LD by non-uniform B spline and output control point vector P and knot vector U ;

Step-3: compute $C(i)$ ($i=0..n$) by setting $T(i)$ in Equation(3.1), i.e.:

$$C(i) = \sum_{j=0}^m P(j) \cdot N_{j,p}(T(i))$$

In current practice, the vector T is assigned equidistant parameter values. It is also possible to assign T a special structure of parameter distribution to allow variable data density spanning a different range, so that the most complex shapes on all cross-sections can be well represented.

The v parameter vector must be defined properly after new cross-sectional data are generated from the relocation method. This consists of two steps: 1) the cumulative chord-length method is used to calculate v parameter vector for each vertical slice (i.e. data in the same column); 2) the final v parameter vector for surface interpolation is an average of all or some of v parameter vectors.

Photographs presented in Figures 3-6 (a), (b), (c) and (d) show four shaded surfaces generated from different parameterisation methods: Figure 3-6(a) is a result of direct surface interpolation to a LASS shape matrix without relocation of cross-sectional data. In this case, 16 data points are contained in a cross-sectional curve and the cardinal spline is used in the surface interpolation. Distortion in the generated surface is caused by the change of distribution of interpolated data, especially from under bust level to bust level, and around the upper bust level. Some minor distortions occur at hip level and upper chest level as well. Figure 3-6(b) comes from a surface interpolation to the same data set with the proposed parameter-based relocation procedure of cross-sectional data. In this case each cross-section

contains only 16 interpolated data points. It is clear from comparison of these two figures that the proposed parameterisation method removes the surface distortion effectively.

Figure 3-6(c) is a surface generated from an angle average method [West 1994] which is an attempt to acquire a uniform distribution of interpolated data for all cross-sections. In this method, the 16 interpolated data points produced from the curve-fitting procedure are relocated by uniform angular spacing. It is observed from Figure 3-6 (b) and (c) that the simple angle average causes severe distortion in the generated surface, although the distribution of interpolated data from this method is more uniform than the original data as illustrated in Figure 3-7. The reason that the angle average method failed is that the original interpolated data in each cross-section are generated by an 'optimal' fitting procedure under the constraint of 16 interpolated data points, improper relocation of these interpolated data destroys the fitting accuracy. Figure 3-8 (a) and (b) compare errors of surface interpolation of two methods at chest section. In these figures, the curve in blue is raw scanned data and the curve in red is from the surface model. It is clear that surface model from the angle average is not acceptable.

The parameter-based relocation method provides a uniform data distribution according to the parametric distance. Since the chord length parameterisation is employed in dealing with the cross-sectional data, the spatial distribution of new data points from the relocation method is uniform according to the chord length distance. Figures 3-7 (c) and (d) show the side view and the back view of the distribution of the new data set. Figures 3-7 (e) and (f) show the distributions of 16 and 32 data points at the bust section respectively.

Although, in general, increasing the number of interpolated data points of each cross-section in the original curve-fitting procedure can alleviate the distortion problem of surface interpolation, West [1994] has discussed the limitation of such an approach in conjunction with editing of raw scan data, in which the major compromise must be made between the number of interpolated data points and time for manual curve fitting. Moreover, taking fitting error as a single criterion in selection of the interpolated data will result in too many data points, and prevent the filtering of high frequency noise in raw data.

On the other hand, it can now be observed from figures 3-6(b) and 3-6(d) that increasing interpolated data from 16 points to 32 points does not considerably improve the

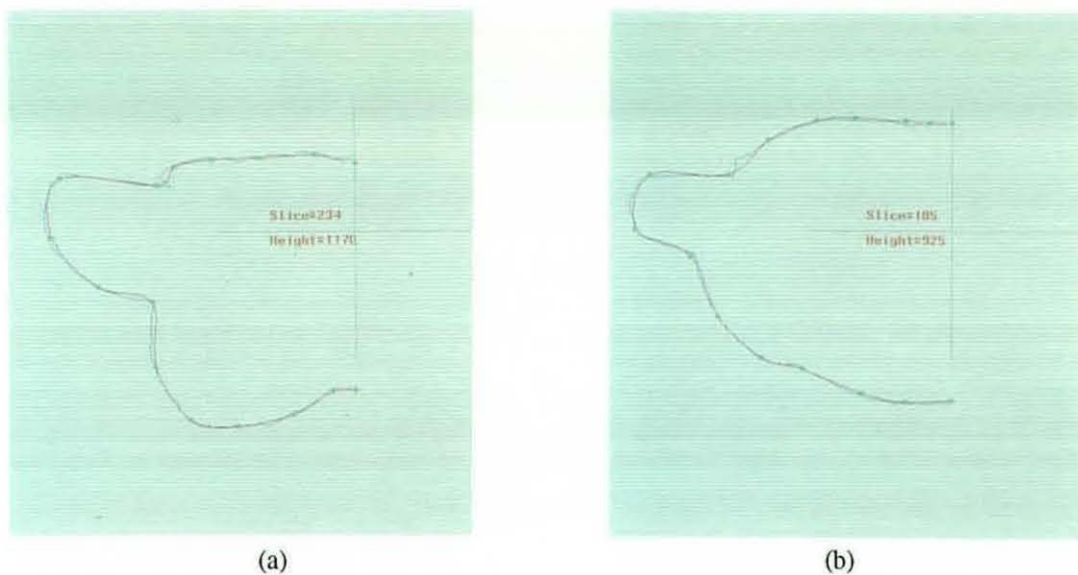


Figure 3- 5. *Distribution of interpolated data points at (a) chest section;(b) hip section*

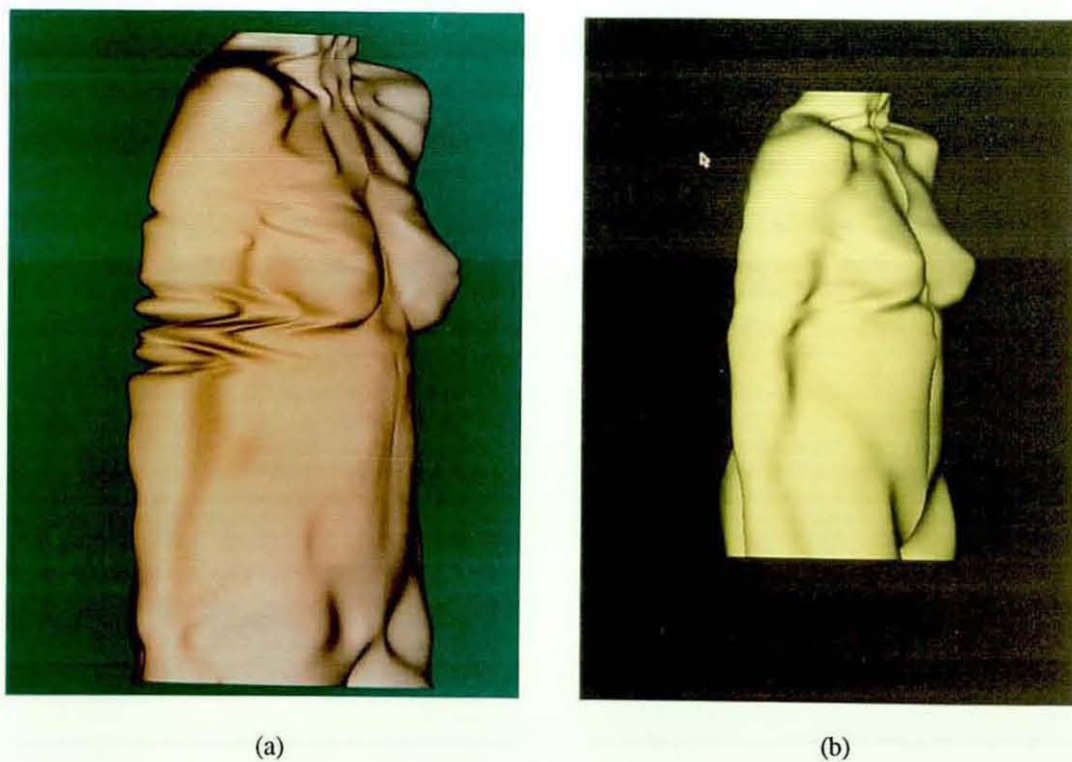


Figure 3-6. *Effect of parameterisation: (a) surface interpolation without relocation of cross-sectional data, 16 points case; (b)surface interpolation with the parameter-based relocation, 16 points case;*

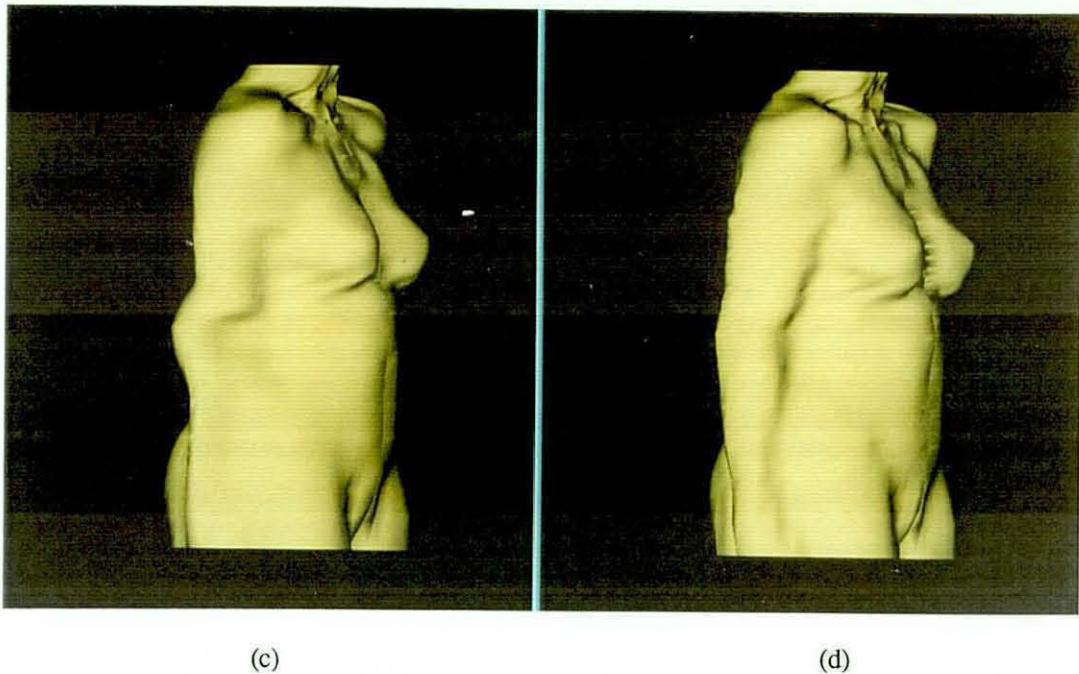


Figure 3- 6. Effect of parameterisation: (c) surface interpolation with relocation by the angle average, 32 points; (d) surface interpolation with the new relocation method, 32 points;

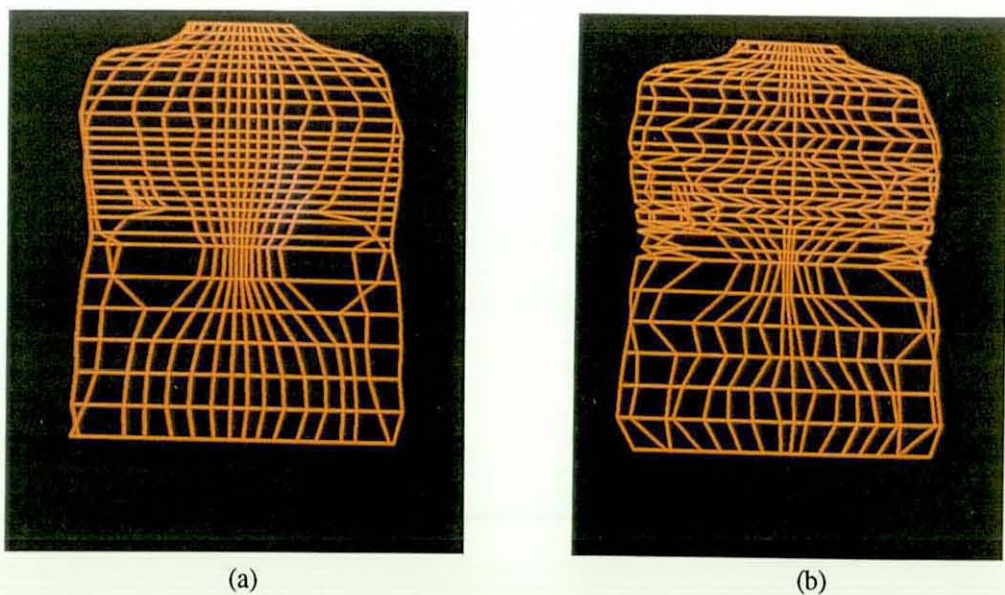
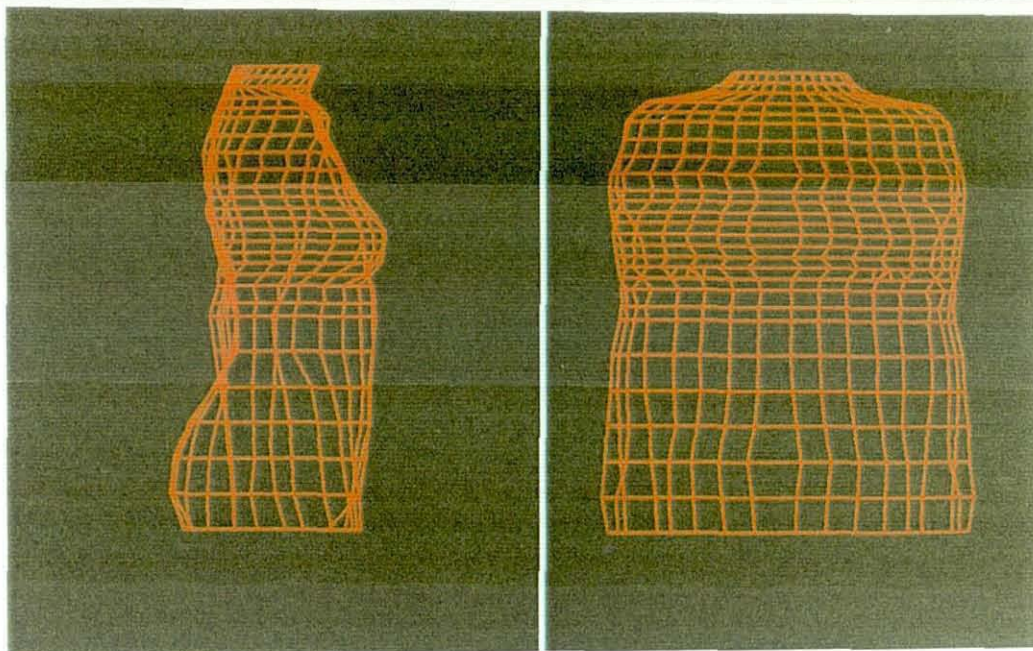
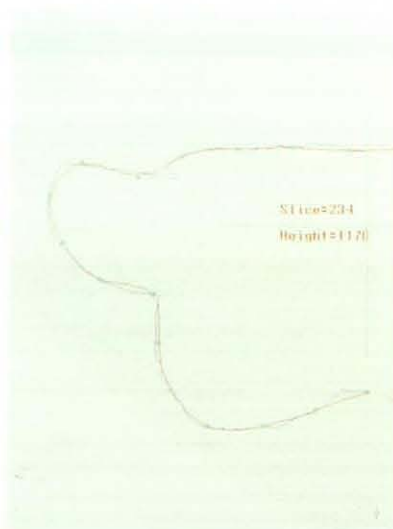


Figure 3- 7. Wireframe form of data distribution: (a) from the angle average method; (b) the original curve fitted data



(c)

(d)



(e)



(f)

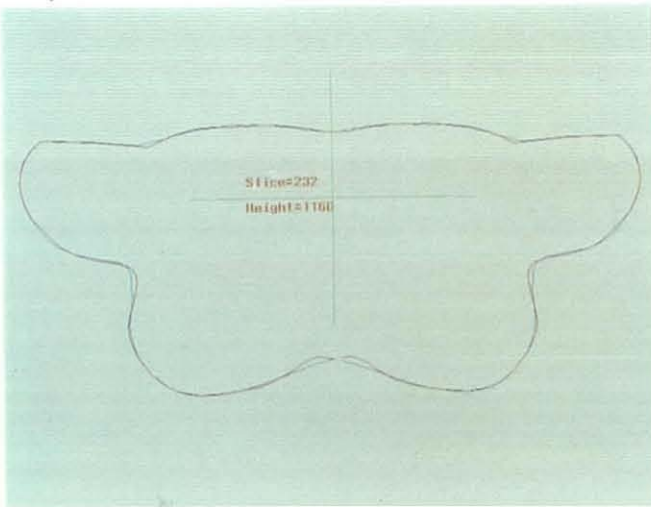
Figure 3- 7. Wireframe form of data distribution:
(c) the side view of data from the relocation method;
(d) the back view of data from the relocation method;
(e) the cross-sectional view of 16 point data from the relocation method;
(f) the cross-sectional view of 32 point data from the relocation method.



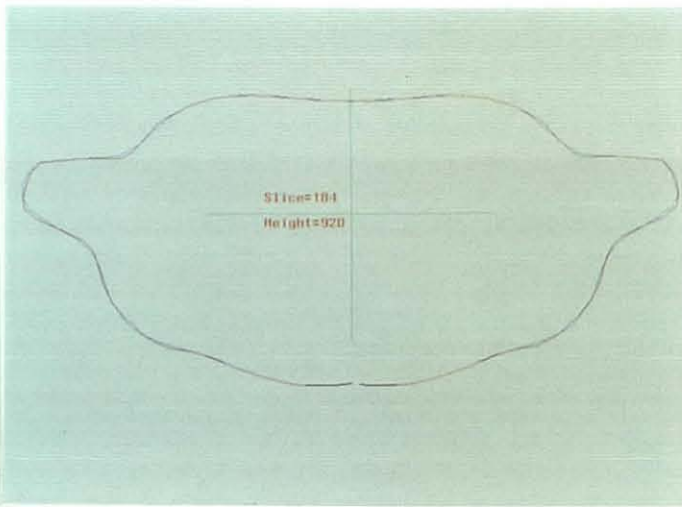
(a)



(b)



(c)



(d)

Figure 3- 8. (a) error of angle average method at chest section; (b) error of new parameterisation method at chest section; (c) error of 16 points and 32 points interpolation of new parameterisation method at chest section; (d) error of 16 points and 32 points interpolation of new parameterisation method at hip section

quality of the generated surface from the parameter-based relocation method in this case. In figure 3-6(d), the 16 interpolated data come from the original curve-fitting procedure are interpolated by a cardinal spline for recovery of raw data. A non-uniform B-spline is used to interpolate the recovered cross-sectional data, then the re-sampling procedure with equidistant u parameter, together with the average method of the v parameter, is applied to produce 32 new data points. Finally the surface interpolation is accomplished on the new 32 point form by non-uniform B-spline. Figure 3-8 (c) to (d) show further cross-sectional view of two surfaces with different number of interpolated points, in which the 16 point form surface is plotted in blue and the 32 point form surface in red. The difference between these two surfaces is very small. This indicates that the parameter-based relocation of cross-sectional data is effective and satisfactory, even only 16 data points are allowed. However, it can also be observed from figures 3-7 (e) and (f) how the 32 point form improve the accuracy of curve interpolation in the positions with sharp curvature change.

Finally, a numerical comparison of surface distance error between the above methods (total number of sample points on the surface is 8745) and raw data is listed in the following table (*Note: The absolute value of the surface distance is used in calculation*):

Comparison of methods	Sum of distance errors	Average distance error
Raw data surface : angle average method	39668.51 mm	4.54 mm
Raw data surface : parameter-based relocation	24858.05 mm	2.84 mm
Parameter-based relocation method, 16 : 32 points	9019.67 mm	1.03 mm

3.1.4.4 Steps to interpolate LASS shape matrix and surface generation

Based on the previous discussion, the interpolation scheme for the LASS shape matrix is drawn as follows:

- 1) acquire the LASS shape matrix by fitting raw data of cross-sections with 16 data points each slice;
- 2) apply curve interpolation to the original 16 data points to recover raw data of a cross-section; (*There is a shortcoming in LASS shape matrix format if only the interpolated data are stored. Accurate recovery of raw data requires the original curve-fitting method for curve interpolation, otherwise serious distortion may be caused. To avoid this, an alternative is to store control vertices of B-spline, like defined in IGES format.*)

- 3) apply the relocation procedure of the u parameter to acquire 32 new data points for each slice;
- 4) acquire the v parameter vector by a parameter average method;
- 5) apply tensor-product surface interpolation method to new data point set.

Step 2), 3) and 4) are called a normalisation. After the normalisation, skinning can be performed according to two steps of interpolation introduced in section 3.2.3. If a symmetrical body is required, the control data on the left side body will be mirrored to the right side. For interpolating an asymmetrical body, the data of the left half body and right half body are loaded and merged. In both situations a closed surface with C^0 continuity at the front joint point and C^2 continuity at the back joint point is interpolated.

The interpolation computation produces control points of a B-spline surface, the surface data can be generated via parameters u and v according to equation 3.6. However, the generating of data may be required to pass through given co-ordinate values instead of parametric values. For example, a cross-section with a given height is preferred. The corresponding v value for the given height can not be found from equation 3.6. In this case one-dimensional search is required. Algorithm 3.4 uses the golden section search (0.618) method [Gill, Murray & Wright, 1981] for this purpose. Similarly, given a spatial point (x, y, z) , its corresponding (u, v) parameter on the surface must be searched in two-dimension.

Algorithm 3.4: v parameter search by the golden-section method

Input: A predetermined height value h (y);
 Numbers of data m and n ;
 Orders of surface p and q ;
 Control points P ;
 Knot vector V .

Output: parameter value v ;

Step-1: Compute $N_{i,p}(u_p)$ by given u_p ;

Step-2: Initialise parameter interval $t_0=0$ and $t_1=1$;

Step-3: do { $v=0.618 \times (t_1-t_0)+t_0$;

Step-4: compute the surface point p by Equation(3.6);

Step-5: If $(t_1-t_0)<\epsilon$ or $(p.y-h)<\delta$ then Step-6;

Else If ($p.y > h$) then $t0 = v$;

Else $t1 = v$;

Step-6: } end of do.

It must be pointed out here that generating a surface by equation 3.6 is slow because of the repeated calculation of the recurrence representation 3.2 of B-spline. If equation 3.6 is used to generate a surface with $(M \times N)$ subdivision, i.e.

$$S(u_k, v_l) = \sum_{i=0}^m \sum_{j=0}^n P_{i,j} \cdot N_{i,p}(u_k) \cdot N_{j,q}(v_l) \quad k = 0 \dots M-1; \quad l = 0 \dots N-1.$$

the formula 3.2 will at least be calculated $(N \times M \times (n+1) \times (m+1))$ times. This needs considerable computer time. It is therefore worth to store all possible B-spline value before calculating equation 3.6. This is implemented by algorithm 3.5. In this implementation, a $(m+1) \times M$ array and a $(n+1) \times N$ array are required.

Algorithm 3.5: Calculation of B-spline surface based on equation 3.6

Input: Numbers of control points, m and n ;

Orders of surface, p and q ;

Control points P ;

Knot vectors U & V

Steps M and N of the surface in U and V direction

Output: Surface co-ordinates $(x, y, z) \{M \times N\}$;

Step-1: Calculate and store $N_{i,p}(u_k)$ ($i=0 \dots m$; $k=0 \dots M-1$);

Step-2: Calculate and store $N_{j,q}(v_l)$ ($j=0 \dots n$; $l=0 \dots N-1$);

Step-3: For $k=0$ to $M-1$

For $l=0$ to $N-1$

Calculate $x(u_k, v_l), y(u_k, v_l), z(u_k, v_l)$ by equation 3.6.

So far the rational form of B-spline has not been used in the interpolation, since equation 3.8 is not a tensor-product and its computation is complex. Moreover, the weights of NURBS are difficult to define in advance. In the interpolation all weights $w_{i,j}$ are treated as one, and only non uniform B-spline is used. Nevertheless, keeping NURBS as a representative form of the model makes it possible to adjust the shape of surface by changing the weights. Piegl discussed the use of the weights in shape control of NURBS

curves and surfaces [Piegl 1989a, 1989b]. The weights, under given control points and knot vectors, could be used to improve the accuracy of surface fitting. The complete procedure of defining all weight values will involve a non-linear optimisation process.

3.2 Approximation of raw scanned data

In the last section the data interpolation is used to acquire a surface model of the human body. This section will introduce an approximation method. Given a set of raw data, g_i , ($i=0, \dots, M$) and a parametric function, $f(t)$, the approximation problem is defined as: to find a set of control points, c_j , and parameter, t_j , to satisfy:

$$\min \sum_{i=0}^M (g_i - \sum_{j=0}^n c_j \cdot f(t_j))^2 \quad (3.17)$$

In an approximation problem, the number of raw data is larger than the number of unknown control points. The control points and their parameters are adjusted in such a way that the distance between the approximation function and the raw data is minimised. The control points c_j , however, are determined by their parameters t_j in a parametric function approximation problem. Simultaneously adjusting control points and their associated parameters is very difficult. The problem is usually broken into two independent sub-problems: calculating control points with given fixed parameters or calculating parameters with given control points. This suggests an iteration to refine the computational process [Hoschek, 1988; Sarkar and Menq, 1991]. However, a simple parameterisation method, like cumulative chord length distance, could deliver 'good' parametric values without the need to seek further optimisation, if the number of raw data is far bigger than the number of control points.

The selection of the function f and the distance measure are two important issues in parametric function approximation. This section focuses on the least square solution of parametric B-spline approximation.

3.2.1 Curve approximation of raw data by linear least-square method

3.2.1.1 Linear least square problem and its solution [Stewart 1973]

A linear least square (LS) problem is defined to determine a vector \mathbf{x} that minimises the function:

$$e^2(\mathbf{x}) = \|\mathbf{b} - \mathbf{A} \cdot \mathbf{x}\|^2. \quad (3.18)$$

where \mathbf{A} is a fixed $m \times n$ matrix and \mathbf{b} is an n -vector. The function $e(\mathbf{x})$ is called the residual sum of squares and $\mathbf{r} = \mathbf{b} - \mathbf{A} \cdot \mathbf{x}$ is called the *residual vector*.

If matrix \mathbf{A} has linearly independent columns, the problem 3.18 has a unique solution:

$$\mathbf{x} = (\mathbf{A}^T \mathbf{A})^{-1} \mathbf{A}^T \mathbf{b} \quad (3.19)$$

which minimises the residual sum of squares and makes $\mathbf{A}^T \mathbf{r} = 0$. Here the matrix $\mathbf{A}^p = (\mathbf{A}^T \mathbf{A})^{-1} \mathbf{A}^T$ is called the pseudo-inverse of \mathbf{A} .

For seeking a solution of the linear least square problem 3.18, a direct Gaussian elimination can be applied to equation 3.19, or the QR factorisation method (refer to Appendix A.1) can be applied to the *residual vector* representation $\mathbf{r} = \mathbf{b} - \mathbf{A} \cdot \mathbf{x}$.

3.2.1.2 Linear least square approximation using parametric B-spline

Let \mathbf{g} be a vector of the raw data and \mathbf{c} be a vector of the control vertices. A linear least square approximation to \mathbf{g} by B-spline can be expressed as:

$$\min \sum_{i=0}^M \{g_i - \sum_{j=0}^n c_j \cdot N_{j,p}(t_i)\}^2 = \min \|\mathbf{g} - \mathbf{A} \cdot \mathbf{c}\|^2$$

the matrix \mathbf{A} is a $(M+1) \times (n+1)$ matrix with elements

$$\begin{bmatrix} N_{0,p}(t_0) & N_{1,p}(t_0) & \dots & N_{n,p}(t_0) \\ N_{0,p}(t_1) & N_{1,p}(t_1) & \dots & N_{n,p}(t_1) \\ \vdots & \vdots & \ddots & \vdots \\ N_{0,p}(t_M) & N_{1,p}(t_M) & \dots & N_{n,p}(t_M) \end{bmatrix} \quad (3.20)$$

With a well-defined knot vector, as produced by equation 3.11, the matrix \mathbf{A} will be column full rank. This guarantees the existence of the solution of equation 3.19. \mathbf{A} is a limited band-width matrix, the LS solution of the approximation problem is implemented by the QR factorisation.

3.2.1.3 An application of curve approximation: refilling of data gap in raw scanned data after arm trimming

Data editing is required to deal with raw scanned data. For example, when subjects take a natural standing posture during the scanning process, the raw scanned data of a subject contain his/her arms which deform the partial profile of the torso, as shown in figure 3-9(a) for one cross-section. To recover a complete profile of the torso, it is necessary to trim those data points on the arms and refill the gap left. Figure 3-9(b) shows the gap after arm data are trimmed. The method to detect the arm will be discussed in Section 3.3.

Presuming the arms have been trimmed and data are voided. The refilling of the void data gap can be implemented by a curve approximation. However, the approximate function can take any value to fill the gap without losing accuracy at existing data points because of the big data gap. Figure 3- 10(a) shows an oscillatory fitting to the gap although C^2 continuity is kept at the two ends of the gap. In order to avoid oscillation of data approximation, some constraints must be applied to the approximate process. A solution is to generate some supporting data or bounds bridged at the gap so that the approximate function will not generate an oscillation bigger than the bounds.

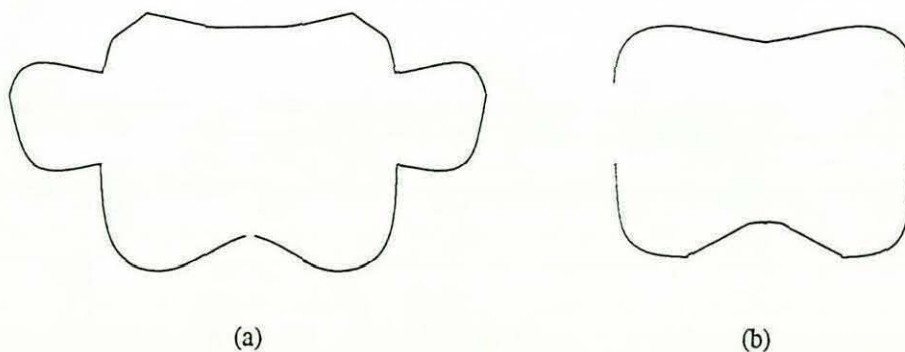


Figure 3- 9. (a) cross-sectional data with arm ; (b) cross-sectional data after deleting arm.

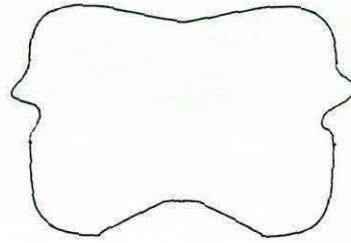


Figure 3- 10. *Incorrect fitting of arm gap*

Figure 3-11 shows a radial form or 'unwrapped' form of data at the bust section, i.e. the cross-sectional data are converted to a polar (or cylindrical) co-ordinate system in which a point at the section is represented by an angle and radius. This is admissible since the cross-sections of the human trunk are simple closed curves and have a centroid inside each sections. A set of supporting data to bridge the gap is constructed by inserting a number of middle points into the gap (cross marks in Figure 3-11). However, these data points should not be paid too much attention during the approximation process because they are estimated values. In mathematical terminology, they should be given a lower weighting. A weighted least square approximation method, therefore, is used to refill the gap. B-spline is employed as the approximate function because the data at two sides of the gap have a complicated shape. Figure 3-12 shows a cross-section after automatic arm trimming, in which the original raw scanned data are in yellow and refilling data in red.



Figure 3- 11. *Radial curve of a cross-section, the horizontal axis is angle space
and the vertical axis is length of radius*

The refilling process of the arm gap can be described as follows:

- 1) insert linearly some points between the gap;
- 2) calculate parametric vector from the revised data set;
- 3) calculate the knot vector from the parametric vector ;
- 4) calculate matrix A and multiple A by a weight vector;
- 5) apply the LS method to compute the control points of a B-spline;
- 6) generate the B-spline curve and fill the gap.

Figure 3- 13a shows a shaded body before arm trimming and Figure 3-13b after refilling the gap by curve approximation. The raw scanned data were acquired from a CYBERWARE 3030RGB/PS scanner.

3.2.2 Surface approximating by tensor-product representation

Similar to the curve approximation, a surface approximation problem can be defined as:

$$\min \sum_{i=0}^M \sum_{j=0}^N (g_{i,j} - S(u_i, v_j))^2 = \min \sum_{i=0}^M \sum_{j=0}^N (g_{i,j} - \sum_{l=0}^m \sum_{k=0}^n c_{l,k} \cdot N_{l,p}(u_i) \cdot N_{k,q}(v_j))^2 \quad (3.23)$$

The residual sum of squares is a function of control points c , parameters u and v

$$e^2(c, u, v) = \sum_{i=0}^M \sum_{j=0}^N (g_{i,j} - \sum_{l=0}^m \sum_{k=0}^n c_{l,k} \cdot N_{l,p}(u_i) \cdot N_{k,q}(v_j))^2 \quad (3.24)$$

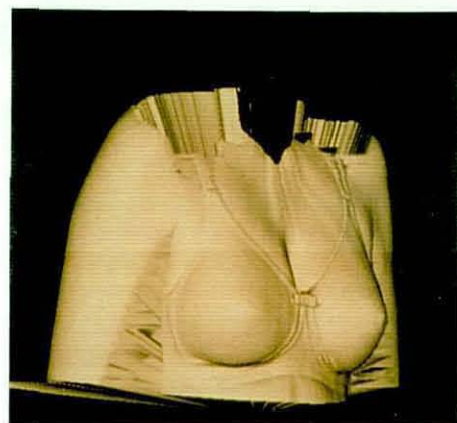
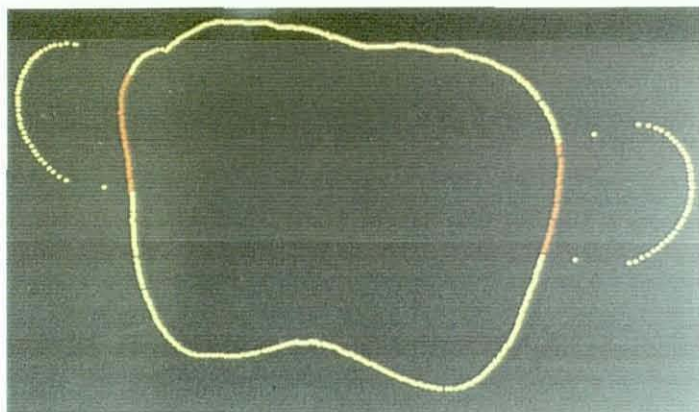
There are $(M+1) \times (N+1)$ raw data (known vector) and $(m+1) \times (n+1)$ unknown elements in the above surface approximation problem. The two B-spline matrices, U and V , are defined as:

$$\begin{aligned} U &= \{N_{l,p}(u_i)\} \quad i = 0 \dots M, \quad l = 0 \dots m \\ V &= \{N_{k,q}(v_j)\} \quad j = 0 \dots N, \quad k = 0 \dots n \end{aligned} \quad (3.25)$$

then U is a $(M+1) \times (m+1)$ matrix and V is a $(N+1) \times (n+1)$ matrix. The matrix A for the least square approximation is

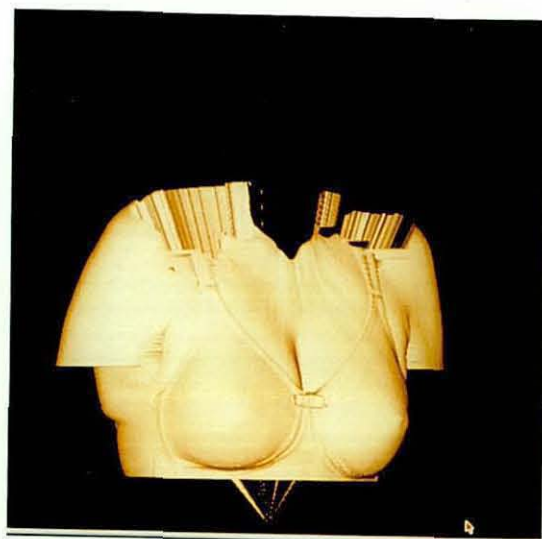
$$A = U \otimes V \quad \text{here } \otimes \text{ is the Kronecker product of two matrices}$$

and the dimension of matrix A is $(M+1) \times (m+1) \times (N+1) \times (n+1)$. It is clear that the solution is almost infeasible if equation 3.23 is directly applied to the raw data set of 3-D scanning



LEFT: **Figure 3- 12.** *Cross-sectional view of arm trimming with trimmed arm image superimposed on the raw data*

RIGHT: **Figure 3- 13.** *(a) raw scanned surface*



LEFT: **Figure 3- 13.** *(b) a surface with refilled data gap after arm editing*

RIGHT: **Figure 3- 14.** *Refill arm gap by tensor-product approximation*

(imagining $M = 300$, $N = 200$, $m=10$ and $n=10$ so that the matrix A contains 6,000,000 elements).

In order to overcome the problem of large matrix dimension, a two-step solving strategy is proposed here which is based on the structure of tensor-product of equation 3-23. In the first step, a series of curve approximations are performed on the raw data (provided such curves can be identified from the raw data). These curves are isoparametric curves with same parametric direction (say u direction). The resultant output of the approximation is an array of the control points of curves. If m control points are selected, then the amount of the data is reduced to m/M of the original raw data. If there are N slices of data to be approximated, the total number of control points is $N \times m$.

In the second step, the curve approximation is used to fit the control points produced from the first step. This time the approximation is performed in the v direction and n control points are used to approximate N data points (they are the control points for the u curves). There are m slices of data to be approximated in this step and the resultant control points comprise the control points of a surface. The number of final control points is $n \times m$.

At the second step, there are several possible alternatives: it is possible to use interpolation instead of approximation to fit the control points of u curves, or perform a surface interpolation to these data picked from u curves.

The introduced tensor-product approximation method has been used to refill the same data gap described in Section 3.2.1. Figure 3-14 shows the result from the two-step approximation. Clearly the surface approximation produces a smoother surface than curve approximation does, but there is a small oscillatory area which may be caused by parameterisation.

3.3 Pre-processing methods of raw scanned data

Raw data from the 3-D surface scanner inevitably contain some unwanted data due to the positioning, reflection, colour, and surface characteristics of a scanned object. These data are usually presented as missing data points (void data), large spike and unexpected jump of data, etc. It is, therefore, desirable to filter these unwanted data from the raw data

prior to further data processing. Two methods are adopted in the pre-processing of raw data.

1. Detection of invalid values: for example, according to the knowledge of the dimension (radius) of the scanned object an upper limit can be set to eliminate the large spike;

2. Low pass filter: the singular data and noise can be filtered by an average value of its 4-neighbour (a terminology from image processing [Pavlidis, 1982]);

The detecting of arm edges is an application of variation of data. Because the gap between arms and torso is deep, the scanned data usually have a big jump, as shown in Figure 3- 9a. This jump can be detected by the forward difference of the data and a threshold. Hence, the trimming of arm data is a process to detect the rising and falling edges in the 'unwrapped' cross-sectional data. Once a pair of rising and falling edges is detected, the data between two edges are set to the void value (which is zero in this example).

The forward difference of raw data can be defined as:

$$d_i = \frac{r_{i+1} - r_i}{a_{i+1} - a_i} \quad (3.26)$$

here r is the radius value of a point and a is the corresponding angle in a cylindrical co-ordinate system. Therefore, the threshold of edge detection can be derived from knowledge about the scanned object. For example, for the CYBERWARE 3030RGB/PS scanner, the increment of the rotation angle is 0.012 radian. Presuming the maximum variation in radius of two adjacent data points from a human trunk should be less than 15 mm. The threshold could be set as $1250 \approx 15/0.012$.

3.4 Summary

This chapter described the application of NURBS curve and surface in human body modelling. Three techniques in relation to human body modelling have been addressed: curve approximation to a cross-section, surface interpolation and tensor-product surface approximation to generate a surface model.

In the application of surface interpolation, the skinning method is employed to interpolate a number of cross-sectional curves of the human body. These cross-sectional curves may have different number of data points and different distribution of data. Re-parameterisation is required for surface interpolation. A uniform parameter-based relocation of data points in the u parameter direction and averaging v parameters method have been developed to improve the quality of generated surface. Use of non-uniform B-spline facilities the parameterisation computation. The modelling result shows that proposed method can deliver a more accurate and smoother surface.

Regarding automatic data editing and curve-fitting, the first-order forward difference has been chosen to automatically detect arms from a cross-sectional curve of the human trunk. Arm data are removed and the gap left is refilled by the least square approximation of non-uniform B-spline function. Both curve and surface approximations are implemented on this example. In the computation of surface approximation, the tensor-product approach is designed and tested. The quality of the generated surface from the tensor-product surface approximation is smoother than that from curve approximation.

CHAPTER FOUR

ANTHROPOMETRY-BASED SURFACE MODELLING

With the raw data from the 3D scanner, a parametric surface, discussed in the previous chapter, can represent the human body with a high degree of accuracy. However, 3D scanning/digitising devices are not widely available. Traditional anthropometric measurement, which mainly uses callipers and tape measures, is still an important data collection method used in many applications. Numerous anthropometric data banks have been built in different countries by traditional anthropometric methods. These data banks could be valuable resources for computer-aided engineering design and manufacturing if the 2-D measurement data can be exploited to provide 3-D shape information of the human body. This chapter develops an approach to create and modify a parametric surface model of the human body on the basis of certain traditional anthropometric measurements.

There is large variation in the shape of the human body. To improve the modelling ability of the anthropometry-based parametric surface model, it is necessary to classify the body shape according to anthropometric measurements. A classification method of the cross-sectional shape is proposed in this chapter. Details of its implementation are also discussed.

Exploring the relationship between anthropometry measurements is another direction to improve anthropometry-based surface modelling. A preliminary analysis of breadth, depth and circumference is briefly discussed.

4.1 *Anthropometry-based parametric surface model*

Traditional anthropometry, as described in chapter 2, takes only 'linear' measurements such as depth, width, length and circumference of the human body. Table 4-1 and Figure 4-1 show some typical measurements used in the clothing industry.

To achieve a 'linear' measurement controlled model, simple geometric primitives, e.g. a cylinder, have been used to represent the human figure. They are easy to change in length or circumference. However, these simple geometric primitives are merely a coarse approximation of real body shape and are not suitable for a more precise analysis related to the surface shape of the body, for example, pressure, comfort and thermal analysis.

A parametric surface can approximate complex geometric shapes, but its shape is usually controlled by global 3-D data. It is desirable to generate a free-form parametric surface model of the human body according to the anthropometric measurements listed in Table 4.1, so that a more useful human body model can be obtained. However, there is few publication addressing these issues. This section exploits a method to modify a parametric surface model by simple anthropometric measurements. The implementation of the method is described in Section 4.1.1. Resultant models are compared with anthropometric data in Section 4.1.2.

4.1.1 Selection of anthropometric data

The skinning technique, as discussed in Chapter 3, provides a feasible means to model a realistic shape of the human body surface by interpolating a family of cross-sectional curves. If the link between anthropometric measurements and the shape of a cross-section is built, the skinning technique can be used to produce an anthropometry-based 3-D model of the human body. To build such a link, adequate anthropometric measurements must be selected. The selection of these measurements have an important influence on the computational method and the accuracy of the resultant model.

The silhouettes from the side and front views are essential to describe the shape of the human body, although a more presentable 3-D model should be comprised of projections from multiple views. There have been some applications to obtain anthropometric data from two orthogonal projections of the human body [Gazzuolo Delong, Lohr, LaBat & Bye, 1992, Telmet, 1995]. These applications can not produce 3-D anthropometric measurements from their models. It is sometimes unsuccessful to automatically identify anthropometric landmarks only from the shape of silhouettes. Key feature positions must be given by some means to constrain the shape description.

Table 4-1 Example of some anthropometric measurements

Loughborough University of Technology
British Women's Size Survey
 (Primary & Secondary Measurements)

Area, Number

Date of Exam. (DD,MM)

Date of Birth (DD,MM,YY) Age

1. Body Weight, kg <input type="text"/>	27. Side Seam <input type="text"/>
2. Stature, cm <input type="text"/>	28. Ankle Girth <input type="text"/>
3. Cervicale - foot <input type="text"/>	29. Knee Girth <input type="text"/>
4. Inside Leg <input type="text"/>	30. Thigh Girth <input type="text"/>
5. Knee Height <input type="text"/>	31. Crotch Length <input type="text"/>
6. Head Girth <input type="text"/>	32. Across Back <input type="text"/>
7. Neck Base Girth <input type="text"/>	33. Cervicale to Back Waist <input type="text"/>
8. Shoulder Width <input type="text"/>	34. Neck Pt to Back Waist <input type="text"/>
9. Upper Arm Girth <input type="text"/>	35. Back Neck to Nck Pt <input type="text"/>
10. Elbow Length <input type="text"/>	36. Back Neck to Nipple <input type="text"/>
11. Arm Length <input type="text"/>	37. Back Neck to Waist <input type="text"/>
12. Wrist Girth <input type="text"/>	38. Neck Pt to Centre Front Waist <input type="text"/>
13. Across Chest Width <input type="text"/>	39. Shoulder to Nipple <input type="text"/>
14. Inter nipple distance <input type="text"/>	40. Shoulder to Waist <input type="text"/>
15. Chest Girth at Scye <input type="text"/>	41. Datum to Cervicale <input type="text"/>
16. Bust Girth <input type="text"/>	42. Datum to Waist <input type="text"/>
17. Under Bust Girth <input type="text"/>	
18. Waist Girth <input type="text"/>	Bust clothing <input type="checkbox"/>
19. Upper Hip Girth <input type="text"/>	1= No bra, 2=Light Bra, 3=Firm Bra
20. Mid Hip Girth <input type="text"/>	Girdle <input type="checkbox"/>
21. Max Hip Girth <input type="text"/>	
22. Inter acromion <input type="text"/>	Ethnic Appearance <input type="checkbox"/>
23. Inter deltoid <input type="text"/>	1=European, 2= African, 3=Indian
24. Waist Depth <input type="text"/>	4=Chinese, 5=Others
25. Body Depth at Max Hip <input type="text"/>	Recorder Number <input type="text"/>
26. Waist to Hip <input type="text"/>	Observer Number <input type="text"/>

HJH/FRM/12/86

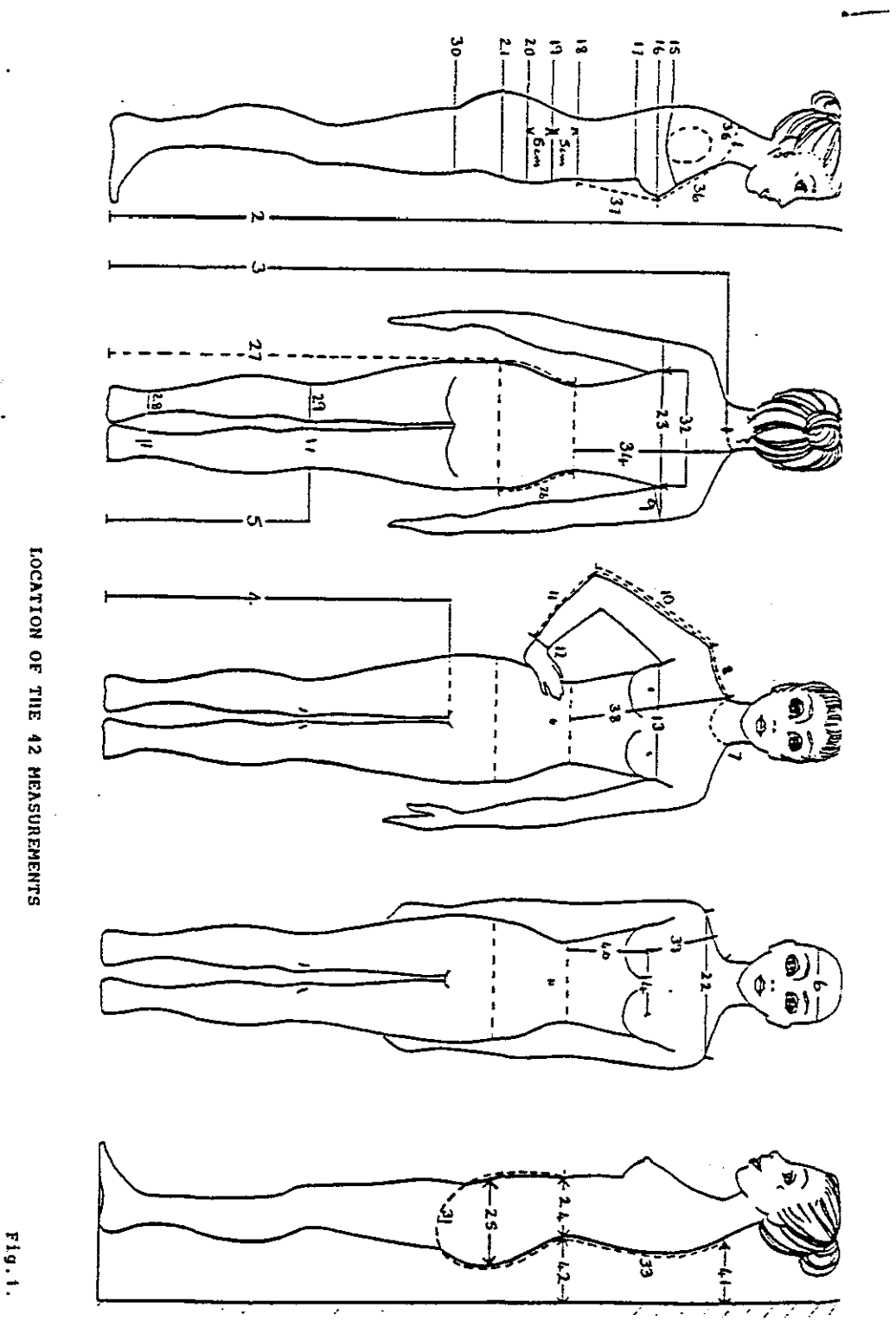
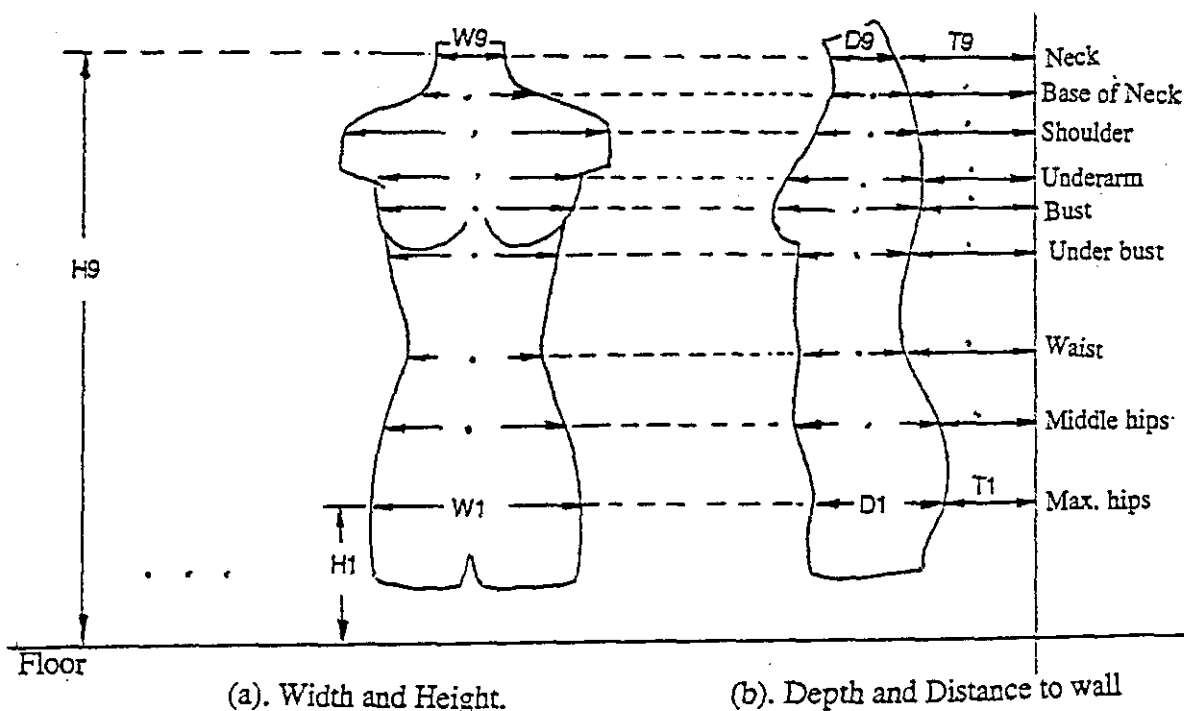


Figure 4- 1. Illustration of anthropometric measurement

To describe the shape of the front and side profile views of the human body, a number of feature positions were selected in this thesis. These are nine levels, at **Maximum Hips, Middle Hips, Waist, Under bust, Bust, Underarm, Shoulder, Base of Neck and Neck**. These levels generally conform to key measurements for clothing design. The width (or breadth, measured from left side to right side), depth (from front to back), distance from middle back to a wall, and height of each section are essential variables for the shape description, as shown in Figures 4.2 (a) and (b). The widths give a shape of the silhouette from the front view, and the depths, together with distances to a wall, describe the shape of a body from the side view. Clearly, these data can be measured by traditional anthropometry. In order to create a 3-D surface model from these measurements a method is needed to relate them to the shape of cross-sectional curves so that the shape of a cross-section can be modified accordingly.



H = Height, T = Distance to a wall
D = Depth, W = Width

Figure 4- 2. Key measurements from the front view and side view

4.1.2 Method of shape modification

The surface of the human body is free-form so that it can not be expressed as an analytical function of the width and depth of the cross-sections. A numerical approach is developed to cope with this problem with three steps:

- 1) a set of reference shape vectors of cross-sections are created and stored;
- 2) the size and shape of reference shape vectors are modified by using anthropometric data from a subject and subsequently, a set of new cross-sectional curves generated;
- 3) a 3-D surface model of a body is created by a surface interpolation technique based on the cross-sectional curves generated in step 2.

The technique related to step 3 was covered in Chapter 3. The following two subsections focus on steps 1 and 2, i.e. the creation and modification of the reference shape vectors.

4.1.2.1 Creation of a reference body

Definition of shape vector:

A cross-sectional curve of the human torso can be represented in polar co-ordinate form by its radius and angle (r_i , b_i) with the original point at the geometric centre of the curve. Considering the symmetry of the human torso model, only 16 pairs of co-ordinates on half of a cross-section are necessary to define a cross-section, as demonstrated in Figure 4-3(a). The co-ordinate system is selected so that r_0 is located at 0 degree and r_{15} at 180 degree. There is an equal angle spacing between two adjacent radii, i.e.

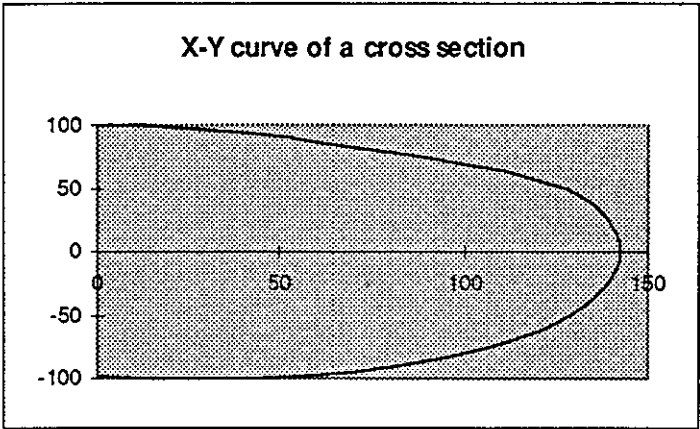
$$b_i = i \times (180/15) \text{ degree. and } i=0 \dots 15.$$

The **shape vector** of a cross-section of the human torso is defined as a vector with 16 elements in which the i th element is a ratio of the i th radius to the first radius corresponding to the polar co-ordinate form of the curve, i.e.

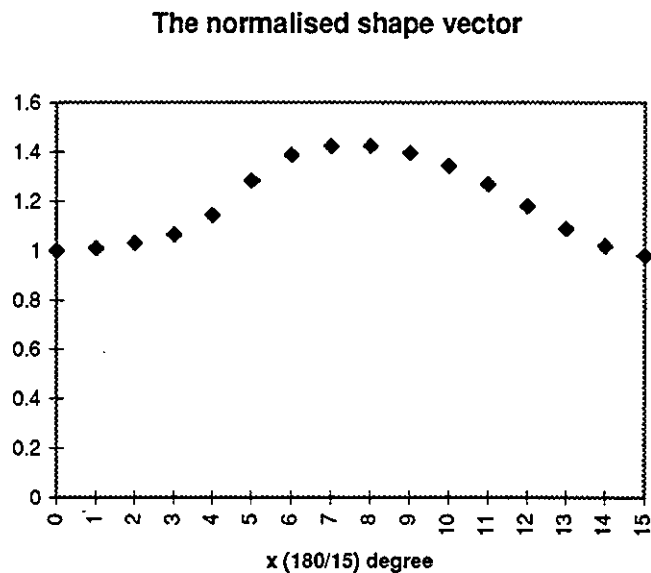
$$S = \{ s_0, s_2, \dots, s_{15} \} \quad \text{and} \quad s_i = r_i / r_1, \quad i = 0, \dots, 15. \quad (4.1)$$

The reason for taking a ratio as the element of the shape vector is to exclude the size factor of the curve. The computation shows that the shapes of cross-sections among

subjects with different sizes are highly correlative. Hence the shape vector could be extracted so that only the abstract shape information remains without reference to real co-ordinates.



(a) Right side of a cross-section



(b) Corresponding shape vector

Figure 4- 3. (a) A cross-section curve and(b) its shape vector

Extraction and representation of a shape vector:

The shape vectors are calculated from existing LASS shape matrices by three steps:

- 1) the cross-sectional data in a LASS shape matrix are interpolated by a B-spline curve;
- 2) the geometric centre of a cross-sectional curve is found and the curve re-sampled with uniform angle interval (180/15 degree); (*Note: for a torso model, uniform angle sampling is acceptable.*)
- 3) 16 sampled radii in a cross-section are calculated and normalised into a shape vector.

A **reference shape vector** of a cross-section is defined as an average vector over a group of people at the same anthropometric level. At present, data from 20 female and 10 male subjects are used to construct the reference shape vectors. A **reference body** is composed of nine reference shape vectors corresponding to the nine key cross-sectional levels of the human body defined in Section 4.1.

4.1.2.2 Anthropometry-based modification of the reference shape vector

Surface data of a body can be recreated from the reference body. The core of the recreation is to modify the reference shape vectors with anthropometric measurements taken from nine key levels of an individual. Because a normalised shape vector does not contain any dimensional information, it must be assigned dimension from measurement data of an individual. As defined in section 4.1.1, basic anthropometric measurements used are depth, D, width, W, height, H and distance to a wall T. The following is a derivation for a relationship of these variables with a reference shape vector. According to the polar co-ordinate representation of a cross-section, the depth, D, is approximately expressed by:

$$D = r_0 + r_b, \quad (4.2)$$

where r_b is the maximum projection of r_i ($i=12, 13, 14, 15$), as illustrated in Figure. 4-4., i.e.

$$r_b = \max\{r_i \cdot \cos b_i; i = 12, 13, 14, 15\}$$

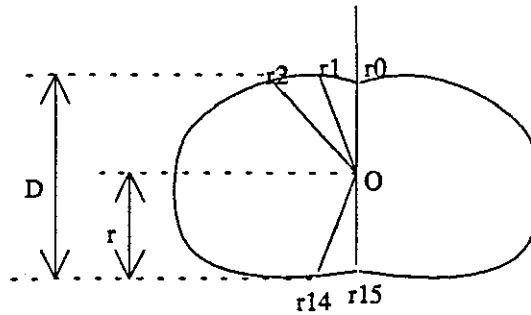


Figure 4- 4. Relationship between depth measurement and shape vector

If D is applied to the shape vector equation 4.1, the value of polar radii r_i of the cross-sectional curve can then be approximately regenerated by

$$r_0 \approx D/(s_0 + s_b) = D/(1 + s_b) \quad \text{and} \quad s_b = \max\{s_i \cdot \cos b_i; i = 12,13,14,15\} \quad (4.3)$$

and then $r_i = r_0 \times s_i$, $i = 1 \dots 15$.

The presented derivation assumes that the r_0 is maximum projection of r_i at 0 degree direction. If this is not true, as happens at the bust section of the female body, particular modification rules must be applied to the data set.

All Cartesian co-ordinate pairs (x_i, y_i) of the cross-sectional curve can be found by:

$$x_i = r_i \times \sin(b_i) = r_i \times \sin(ix180/15) \quad (i=0,1,\dots,15) \quad (4.4)$$

$$z_i = r_i \times \cos(b_i) = r_i \times \cos(ix180/15)$$

However, the above calculation does not yet consider the constraint of width W , some modifications are required. A modification method adopted is based on the ratio of width/depth of a cross-section which reflects, to a certain extent, the shape of the cross-section. If w_A is the ratio of width/depth from anthropometric measurements (i.e. W/D) and w_R is the ratio of width/depth of the reference shape vector, their difference, t , represents the shape difference between a cross-section of a subject and that of the reference body. The value t is therefore used to adjust the elements of shape vector.

Figure 4-5 illustrates two shape vectors with different ratios of width/depth. According to the definition of the shape vector, the ratio of width/depth w_R is equal to the maximum projection of its element at 90° direction (i.e. the direction in which width measurement takes place) divided by $(s_0 + s_p)$, as defined in equation 4.1 and equation 4.3. The new ratio w'_R , after adjusting, is

$$w'_R = w_R + t \quad (4.5)$$

For each element of the shape vector s_i , the following adjustment is applied:

$$s_i = s_i + t \cdot \cos(90 - i \cdot \frac{180}{15}) \quad (i=0....15) \quad (4.6)$$

Finally a complete 3-D cross-sectional curve is formed by three steps:

- 1) all 16 elements of a shape vector are modified
- 2) the new r_i and (x_i, z_i) of a cross-section are generated from the depth measurement D by equation 4.3 and 4.4.
- 3) the distance T is added to all z co-ordinates and the height, H , is assigned to the y co-ordinate.

Two shape vectors with different W/D ratio

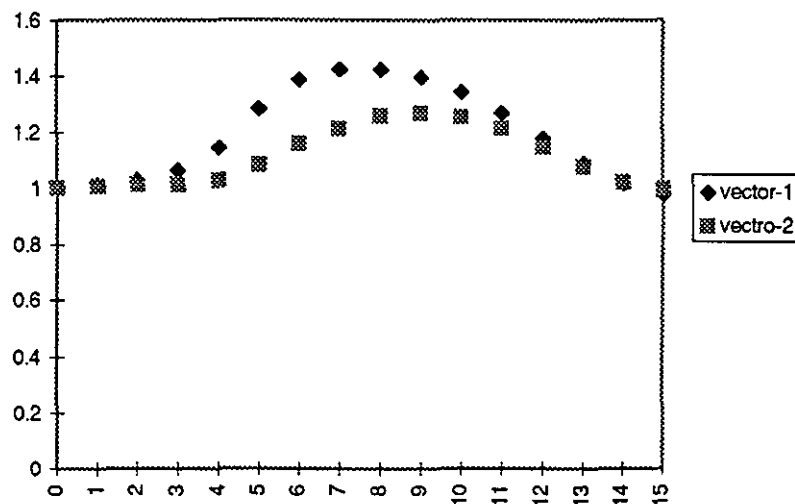


Figure 4- 5. Two shape vectors with different Width/Depth ratios

Following these procedures, nine shape vectors of a reference body are modified by their corresponding anthropometric measurements. The generated cross-sectional curves are ready for surface interpolation.

4.1.2.3 Experimental comparison

The procedures described in the last section have been implemented as a Microsoft Windows® based program. Figure 4-6 shows the input panel for anthropometric data and Figure 4-7 the re-generated body surface according to input data in Figure 4-6.

The method was tested on 10 males and 15 females who were scanned by LASS. The same anthropometric measurements were taken from 3-D scanned data of subjects and surface data of recreated bodies. The error distribution (mean and standard deviation of the differences between two measurements) of these measurements for female subjects is summarised in Table 4-2. Results for male subjects show smaller error than females.

In this experiment, all anthropometric measurements from raw scanned bodies are taken from curve-fitted scanned data by direct numerical computation instead of the observation of a human operator. Anthropometric measurements of a recreated body are produced by numerical computation as well. It rules out any inter and intra observer errors. Results in table 4-2 show that the under arm and shoulder levels of a recreated surface have the most serious errors. This is mainly caused by sharp changes of the cross-sectional shape from under arm to shoulder so that the surface interpolation delivers an oscillating result. Increasing interpolated points at these two sections could improve the accuracy.

The width errors at maximum hip and base of neck section levels are significant. The modification rules of shape vector might be inappropriate at these levels because of their widely differential anatomical shapes..

Generally, the girth is an important key variable in traditional anthropometry. The method presented can produce girth with good accuracy using only width and depth information, as shown in Table 4-2, although it does not use girth constraint directly. A method to modify the cross-sectional data with girth constraint was reported by West [1994]. In fact there exists some linear regression relationship in depth, width and girth of a

cross-section of the human torso. It is possible to calculate the third element from any two elements from width, depth and girth. This will be discussed in Section 4.4.

Female Data Entry				
	Width	Depth	Height	Dist To Wall
Max Hips	338.2	217.2	861.1	79.6
Mid Hips	320.8	219.1	953.0	92.9
Top Hips	281.0	198.5	1024.0	114.5
Waist	235.7	171.0	1095.1	140.4
Under Bust	268.3	173.7	1231.3	144.2
Bust	275.5	207.7	1286.1	136.8
Above Bust	309.1	181.9	1356.0	133.2
Shoulder	415.9	141.6	1404.5	125.7
Base Neck	135.2	89.4	1489.1	133.8
Neck	101.0	90.0	1520.4	142.8

Ok Cancel

Figure 4- 6. Anthropometry input panel of the software

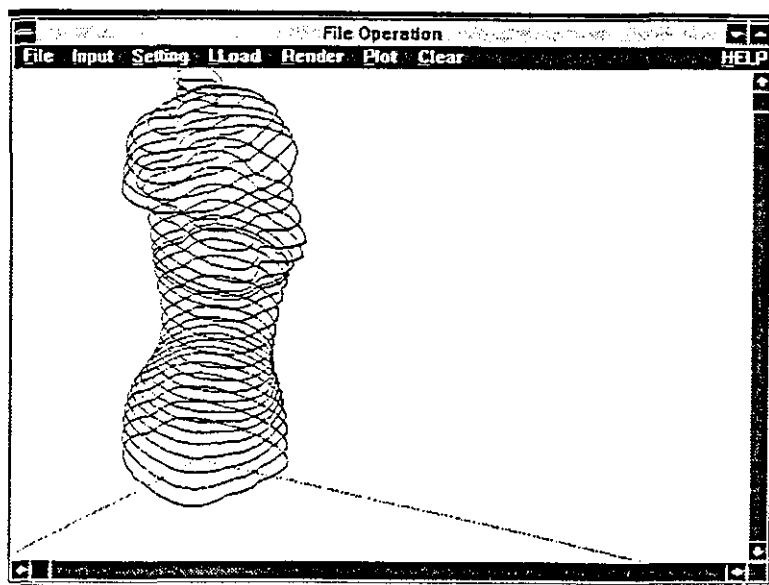


Figure 4- 7. A re-generated body surface

Table 4- 2: Comparison of differences (MEAN and SD) of anthropometric measurements between raw scans and recreated bodies of 15 female subjects (Unit: mm)

Position	Width (mm)		Depth (mm)		Girth (half) (mm)	
	Mean	SD	Mean	SD	Mean	SD
Neck	1.11	0.94	-0.11	0.17	-1.36	4.29
Base of Neck	-4.10	2.85	-0.49	0.38	2.44	2.42
Shoulder	-4.30	1.43	-1.61	4.25	2.61	5.60
Underarm	4.24	0.83	-4.37	4.60	-1.44	8.95
Bust*	0.09	0.18	0.04	1.49	n/a	n/a
Under Bust	-0.63	-0.50	-0.37	0.19	-4.51	4.38
Waist	-1.19	0.54	-0.11	0.32	-1.05	4.10
Middle Hips	-0.71	0.30	0.11	0.17	-0.77	4.13
Max. Hips	4.08	0.41	0.63	4.24	4.24	2.97

* No girth data available for subjects wearing lycra garment.

4.2 Shape classification of cross-section of the human body

The method of shape modification described in the last section assumes that a measured cross-section has a similar shape to the corresponding reference shape vector. If large differences between them exist, shape modification would lead to an unsatisfactory result. This is because the modification of the shape vector only takes place at 16 discrete positions. This does not guarantee smoothness of the generated cross-sectional curve. Investigation of different modification methods suggest that a data bank of reference shape vectors could provide a better solution. To sort the shape vectors, a shape index should be related to anthropometric measurements so that adequate shape vectors are selected for the 3-D modelling process. Therefore, a shape classification method is required to generate the shape index and associated shape vectors. This section will concentrate on this issue and build an experimental classification method.

4.2.1 Shape classification of silhouette of the human body

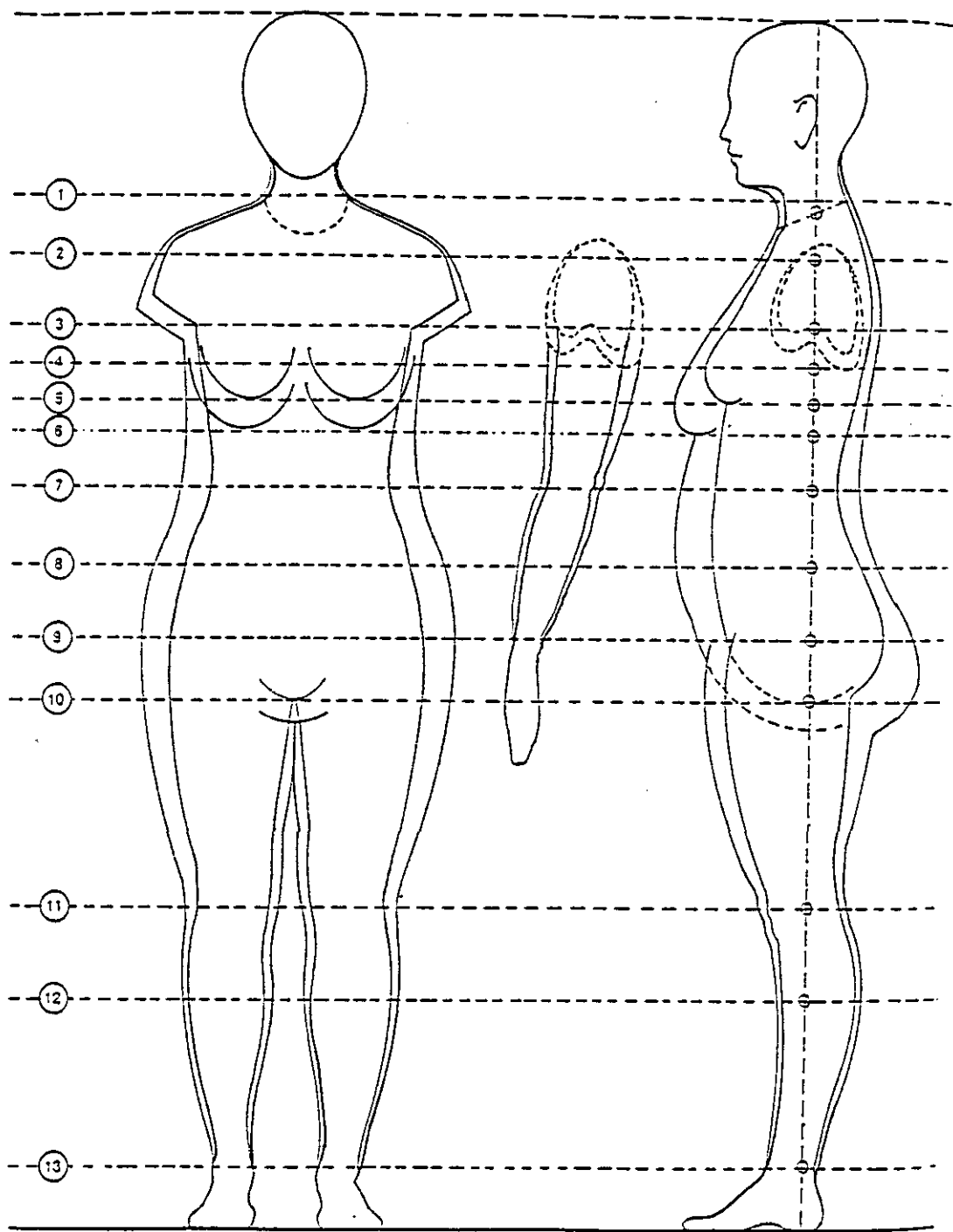
The shape analysis of the silhouette of the human torso has been investigated in fitting model of clothes [Ito, Kurokawa, Shinozaki & Nakano, 1982; Takabu, Matsuyama, Akizuki, Kuki, Uetake, Isoda and Yanagisawa, 1986; Takabu, Uetake, Uetake, Matsuyama, Isoda and Yanagisawa, 1990, Gazzuolo *et al.*, 1992], etc.

The method presented by Ito *et al.*[1982] attempted to classify the human body shape by extracting the human silhouette from both side and front views. A series of key points on the silhouette composed a body pattern vector. Principal component analysis and hierarchical cluster analysis were applied to the abdominal region for 170 female subjects. Takabu *et al.* [1986, 1989] presented the analysis of the side view of the human body shape by principal component analysis. The side view silhouette of the subject was acquired from a camera with a telescopic lens and 15 key measurements were taken from photographs. Their study extracted two principal components of human posture: the degree of erectness of the figure and the curvature around the waist. Furthermore, a classification of the static posture of the human body was conducted. These general classifications of silhouettes of the human body could be made use of in human body modelling.

Gazzuolo *et al.*[1992] compared and evaluated the role of traditional linear anthropometric measurement and photographic silhouette measurement in clothing pattern development. It showed the possibility of relating body silhouette to certain pattern dimensions. They also suggested an expanded concept of sizing categories based on body configuration.

4.2.2 The classification of cross-sections

The clothing industry has a strong interest in the cross-sectional growth of the human body, because the shape change of the cross-sections is an important factor in determining grading rules for clothing design [Taylor & Shoben, 1990]. Figure 4-8 shows the silhouette and section changes of bodies of two sizes. However, cross-sectional data are difficult to acquire without a 3-D whole body surface scanner. The classification of cross-sections is rarely reported. This issue will be addressed in this section.



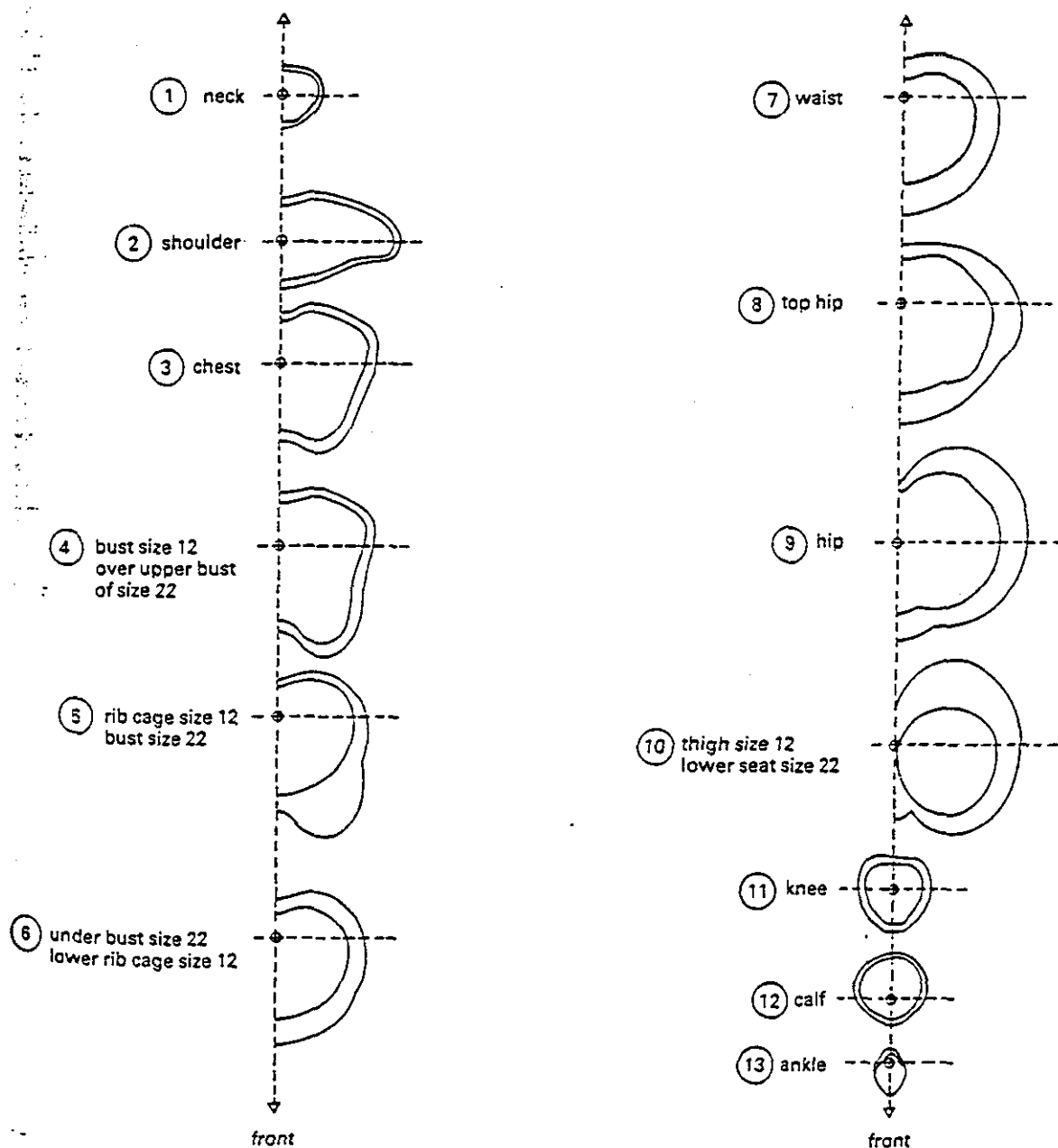
This drawing is to scale: scale = 162.0 cm divided by height of drawing

(a)Front and side view

Figure 4- 8. Body growth and sections change (size 12 with size 22 superimposed)

[Taylor & Shoben, 1990]

Major body sections of size 12 and 22 superimposed on each other. Taken from Figure 25 on opposite page. These sections are also exact scale reproductions.



(b) Cross-section view

Figure 4-9. Body growth and sections change (size 12 with size 22 superimposed)

[Taylor & Shoben, 1990]

The cross-sectional curve is a planar contour. The shape description of a planar contour has been widely studied in computer image processing and pattern recognition areas. The methods developed for contour analysis include the auto-regression model, the Fourier descriptor, and the chain code [Duda and Hart, 1973; Pavlidis, 1982]. These methods have been applied to object recognition, handwriting recognition, wave form classification, etc. The selection of a method greatly depends on the task and the data form. Correct selection of shape description methods is an important step towards the success of a classification problem. This section discusses the selection of the shape descriptor for cross-sectional curves and the classification method based on the selected description.

4.2.2.1 The selection of shape description for a cross-sectional curve

Before reaching a decision in the selection of shape description, an intuitive data analysis is conducted to identify major features in cross-sectional data. Figure 4-10 shows typical radial wave forms corresponding to some cross-sections in Figure 4-8. The definition of radial wave form follows the definition of the shape vector introduced in Section 4.1. It is noticeable that most of them contain only one maximum value and a few extreme points, therefore the shape of the radial curves is not complicated. Because of its simplicity, one-dimensional radial curve is chosen as a basis of classification instead of 2-dimensional (x-z) plane curve.

The effectiveness of classification and computation are usually the main criteria for method selection. Two particular points are considered in the present application: 1) Similarity of cross-sectional curves of different subjects of the same anatomical height are far greater than those discussed in pattern recognition and computer vision literature. Conventional methods, e.g. correlation analysis, and auto regression, could not show significant classification ability; 2) Feature variables in a classification algorithm should be related to anthropometric measurements of a cross-section. This requires an explicit geometric relationship between 'classes' and feature values of a cross-section. It is observed that, from a radial wave form of a cross-sectional curve, the sum of the radial values at the two end points of interval $[0, \pi]$ is approximately equal to the depth of

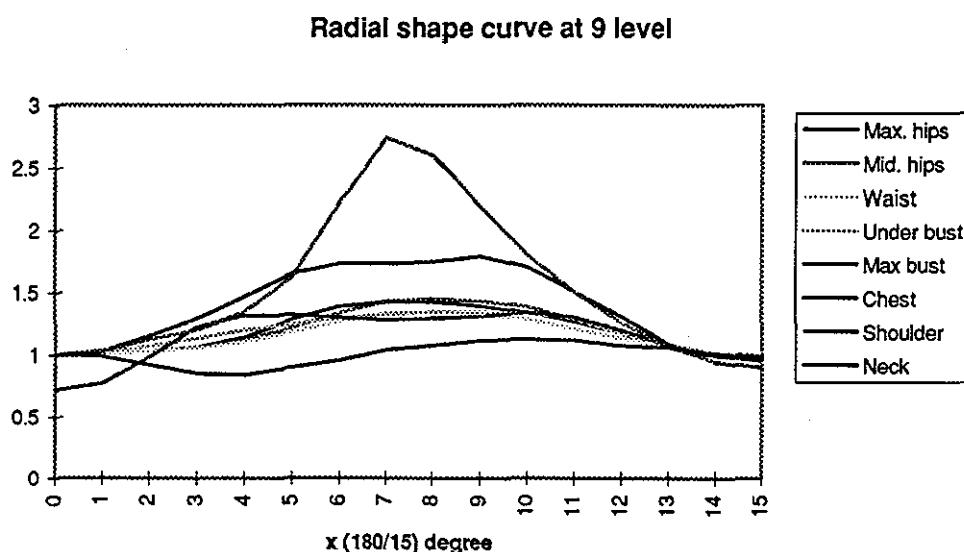


Figure 4- 10. *Typical radial shape curves*

the cross-section; the extreme of the radial wave form approximately represents 1/2 width of the cross-section; and the total length of the wave form corresponds to the 1/2 circumference of the cross-section. These values could be used in the shape analysis method.

It is accepted that shape is a concept independent of the magnitude of the data, i.e. certain normalisation should be used to eliminate the effect of magnitude. The shape vector discussed in Section 4.1 is an approach to eliminate the magnitude effect of a cross-sectional curve, therefore it is selected as a basic representation of a cross-section in the following discussion and the 'radial wave form' is interchangeable with the 'shape vector'.

Based on the above discussion, the principal feature variables selected to describe a shape vector are: the zero point (roots), the extremes and their positions, and the curvature at the extreme points of a shape vector. This implies that the analysis method will be based on the computation of zero, 1st and 2nd order derivatives of the curve.

4.2.2.2 Feature extraction

The feature extraction includes data preparation and computation of feature values. The data preparation deals with the data conversion and the construction of the shape

vectors. Two methods are used in the computation of feature values: the polynomial fitting method and the Fourier descriptor.

Data Preparation

A sample of 76 bodies covering a range of sizes are selected from the existing LASS data bank. The original curve-fitted data of a cross-section are first normalised according to their centroid. The normalised data are then fitted by B-spline and sampled into 32 points with uniform angular spaces. These 32 points, originally in x-z planes, are converted into a polar co-ordinate form. After applying the normalisation process (section 4.1.2.1.) to the 32 radii, a shape vector with 32 elements is formed (because they have equal angular spacing where their indices give sufficient information about the angle distribution). The shape vector is equivalent to a one dimensional wave form.

Computation of feature values

1) Polynomial fitting method

In order to calculate its zero points and derivatives, the shape vector is fitted by a 5th order polynomial. That is:

$$y = a_5 \cdot x^5 + a_4 \cdot x^4 + a_3 \cdot x^3 + a_2 \cdot x^2 + a_1 \cdot x + a_0 \quad (4.7)$$

The fitting is implemented by the least square method. Matrix representation of the least square fitting is:

$$\begin{bmatrix} 1 & x_1 & . & x_1^5 \\ 1 & x_2 & . & x_2^5 \\ . & . & . & . \\ 1 & x_{32} & . & x_{32}^5 \end{bmatrix} \cdot \begin{bmatrix} a_0 \\ a_1 \\ . \\ a_5 \end{bmatrix} = \begin{bmatrix} y_1 \\ y_2 \\ . \\ y_{32} \end{bmatrix} \quad \text{i.e., } \mathbf{X} \cdot \mathbf{a} = \mathbf{y} \quad (4.8)$$

Here \mathbf{y} is the normalised shape vector of a cross-section and \mathbf{X} is the normal matrix with elements

$$x_i = i \cdot \pi / (N - 1), \quad N = 32 \text{ and } i = 0, \dots, 31.$$

According to equation 4.7, the feature extraction problem is mainly to find the roots of the fitting polynomial and its 1st and 2nd order derivative. Five elements $\{r_1, r_2, e, a_e, c\}$ are selected as the feature values of a shape vector : r_1 and r_2 are the two roots of the fitting polynomial within an interval $[-1, 4]$ (a minor revision to the shape vector is that all elements of a shape vector is reduced by one, therefore the shape vector has at least one root), e is the maximum value of the fitting polynomial in interval $[0, \pi]$ and a_e is the co-ordinate value corresponding to e . The element c represents curvature at an extreme point.

For finding the numerical roots of a polynomial, the Newton-Raphson method [Radston, 1965] is used.

2) Fourier descriptor

An alternative feature extraction method is the Fourier descriptor which is believed to be a good method for 2D shape classification [Kauppinen, *et al.*, 1995]. The Fourier transformation of a finite-length discrete signal is described by [Oppenheim and Schafer, 1989]:

$$F_k = \sum_{n=0}^{N-1} x_n \cdot e^{-j(2\pi/N)kn} \quad (4.9)$$

The series $\{F_k\}$ is called the Fourier spectrum of the discrete signal. F_k is a complex coefficient, which represents the phase and magnitude of the k th sinusoid harmonic.

Since all cross-sectional data are sampled from the same starting position, they do not have any potential phase difference. The magnitude of the Fourier coefficients is sufficient to describe the shape vector. The Radius Fourier descriptor [Kauppinen *et al.*, 1994] of a shape vector is represented by

$$\mathbf{f} = \left[\frac{|F_1|}{|F_0|}, \dots, \frac{|F_n|}{|F_0|} \right] \quad (4.10)$$

where F_i denotes the i th component in the Fourier spectrum, N is 32 and n is set as 7. That is, seven elements of \mathbf{f} represent the feature of a shape vector.

4.2.2.3 Cluster analysis and classification of shape

The data acquired from the feature extraction are in a high dimensional form and therefore difficult to classify by intuitive judgement. If there is no knowledge about how many classes exist, the cluster analysis [Everitt, 1993] is a suitable tool to overcome this problem.

Cluster analysis is the generic name for a wide variety of procedures involved with identifying groups within data. By organising multivariate data into such subgroups, clustering may reveal the characteristics of any structure or pattern present. However, considerable care must be taken when applying cluster methods in practice. The result from clustering is often a guidance for further refinement of feature description and classification.

Agglomerative hierarchical clustering

Hierarchical cluster methods attempt to classify the data by a sequence of steps. An *agglomerative* (bottom-up) procedure starts with n singleton clusters and forms the sequence by successively merging clusters. Duda & Hart [1973] summarised the major steps contained in Agglomerative hierarchical clustering, as follows:

1. Let $c=N$ and $X_i=\{x_i\}$, $i=1, \dots, N$.
- Loop: 2. If c is less or equal to p , stop.
3. Find the nearest pair of distinct clusters, say X_i and X_j .
4. Merge X_i and X_j , delete X_j , and decrement c by one.
5. Go to Loop.

where p is a specified number of clusters.

Hierarchical classification can be represented by a two-dimensional diagram known as a dendrogram which illustrates the fusion made at each successive stage of the analysis. Figure 4-11 shows a dendrogram for an agglomerative hierarchical clustering. Vertical level 1 shows all samples as singleton cluster with a maximum scaled distance of 10. At level 2, with a smaller distance the samples are grouped into two clusters: sample 1 & 2; sample 3, 4 & 5. Finally at level 5, the distance between clusters is zero therefore all

samples are independent of each other. The horizontal rule shows a scale of the dissimilarity between clusters.

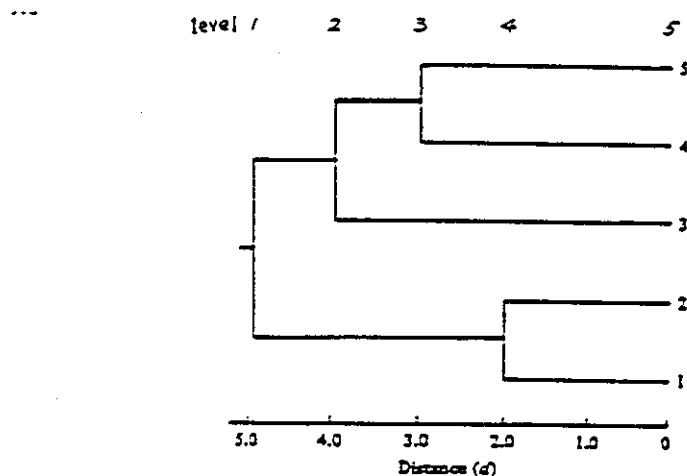


Figure 4- 11. Dendrogram of hierarchical clustering

Result of the clustering about maximum hips section

The agglomerative hierarchical cluster technique is applied to polynomial fitted data and the Fourier descriptor for the maximum hip section. From polynomial fitted data three variables were selected for cluster analysis. They were the extreme, the extreme point and the curvature at the extreme point of the fitted polynomial. The positions of roots of the polynomial were abandoned. From the Fourier description, seven coefficients of the Radius Fourier Descriptor were used. Seventy-six cases were contained in both data sets, which had the same numbering order. The data were imported by SPSS for Windows and average linkage distance between groups was employed in the cluster analysis. The dendrograms of the two kinds of descriptors are shown in Figures 4-12. (a) and (b), for polynomial fitting and Fourier description respectively. Figure 4-12(a) shows a clear classification which consists of five groups with scaled distance of approximately 1 (the first group which contains cases 33, 70, 1 and 2 is an invalid set because of bad data, thereafter four valid groups are analysed). At the scaled distance 5, all valid cases formed a singleton cluster. A statistical description of the feature vector of these four groups is summarised in Table 4-3. These four groups can be clearly discriminated by their extreme

values and curvatures with minor overlap. Classification from Fourier description is not as clear as polynomial fitting, although a certain overlap exists in the produced clusters from the two methods. At the scaled distance 1, the Fourier descriptor produced more than seven clusters. Even at the distance 5 there still exist three clusters. This may be caused by two reasons:

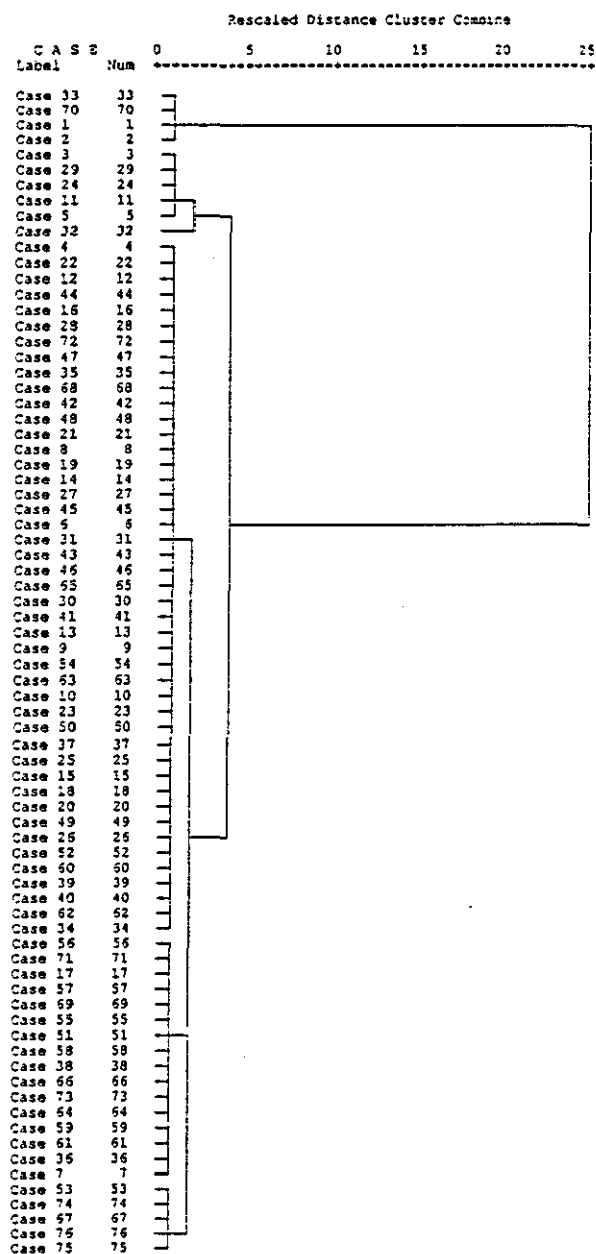
- 1) Fourier description contains more details of the shape vector (seven parameters are used) and this makes the distance of clusters bigger;
- 2) Principal features are not adequately extracted and presented. In addition, the coefficients of Fourier descriptor are difficult to interpret with anthropometric meaning.
- 3)

Table 4- 3. Descriptive statistics of the feature values from polynomial fitting

	Group 1			Group 2		
	<i>Extreme pt</i>	<i>Extreme</i>	<i>Curvature</i>	<i>Extreme pt</i>	<i>Extreme</i>	<i>Curvature</i>
Mean	1.92472	0.24896	-0.63512	1.528875	0.328231	-0.65777
SE	0.037702	0.03272	0.077665	0.027919	0.009337	0.021497
SD	0.084305	0.073163	0.173665	0.111676	0.037349	0.085987
Variance	0.007107	0.005353	0.030159	0.012472	0.001395	0.007394
Minimum	1.8393	0.1496	-0.8626	1.3238	0.2692	-0.805
Maximum	2.056	0.3259	-0.3902	1.7316	0.374	-0.4807
Count	5	5	5	16	16	16
	Group 3			Group 4		
	<i>Extreme pt</i>	<i>Extreme</i>	<i>Curvature</i>	<i>Extreme pt</i>	<i>Extreme</i>	<i>Curvature</i>
Mean	1.410204	0.482913	-1.1028	1.33438	0.69812	-1.62682
SE	0.011085	0.009122	0.024346	0.028482	0.066673	0.039277
SD	0.074361	0.061191	0.16332	0.063687	0.149086	0.087826
Variance	0.00553	0.003744	0.026674	0.004056	0.022226	0.007713
Minimum	1.2408	0.3601	-1.4558	1.2385	0.6046	-1.7699
Maximum	1.5376	0.6065	-0.8114	1.3939	0.9607	-1.5422
Count	45	45	45	5	5	5

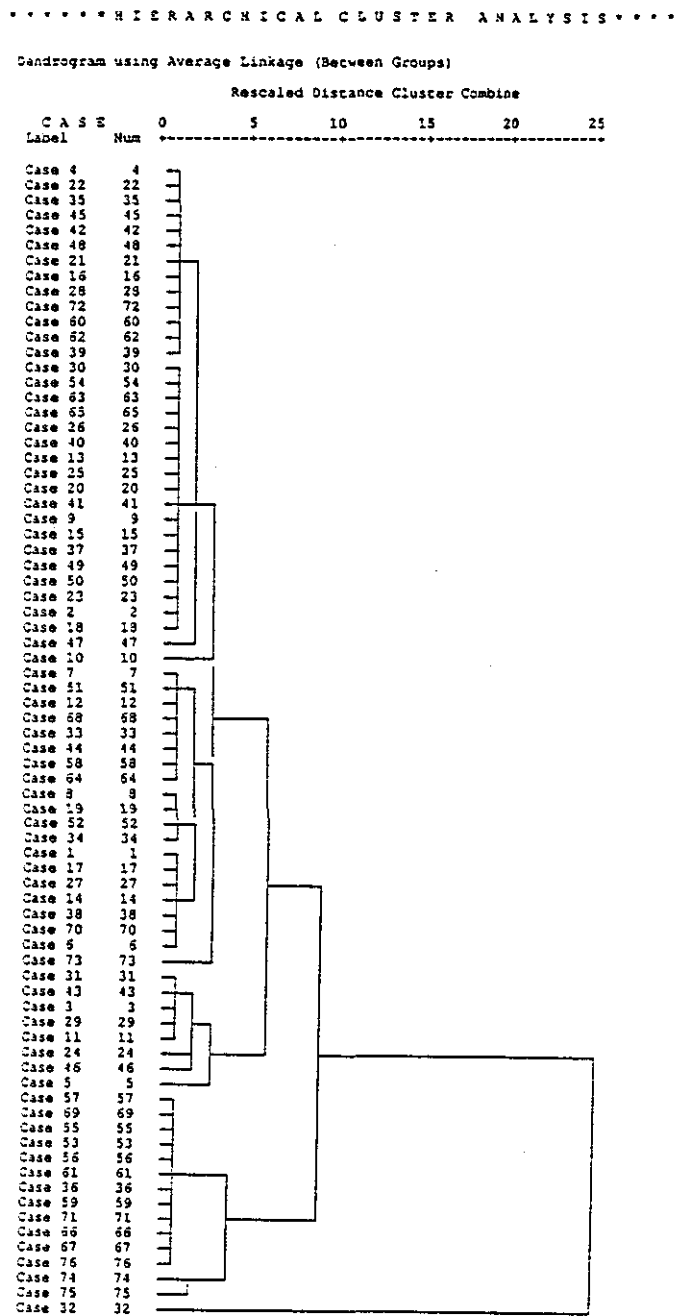
***** HIERARCHICAL CLUSTER ANALYSIS *****

Dendrogram using Average Linkage (Between Groups)



(a) polynomial fitting method

Figure 4-11. Dendrograms of the clustering about maximum hips section



(b) Fourier Descriptor method

Figure 4- 12. Dendrograms of the clustering about maximum hips section

4.2.2.4 Discussion of classification results

The extreme value of the shape vector in the classification of the hips section has geometric significance. It represents the approximate ratio of width to depth of a cross-sectional curve, i.e.

$$\text{Extreme} \equiv \text{Width/Depth} - 1 \quad (4.10)$$

This is because, from the definition of the shape vector in Section 4.1.2.2, the element s_1 represents approximately 1/2 depth of a cross-sectional curve and all s_i are radius ratio to s_1 . The projection of the extreme at $1.57079 \equiv \pi/2$ (rad) coincides with the width direction of the cross-section. It is important that the extremes of four groups in Table 4-3 remain separable after projected to 1.57 (rad). Conclusions can be drawn from the above discussion.

1) The ratio of width to depth of a cross-section can be an index value of the cross-sectional shape for the maximum hips level. Moreover, curvature values of these classes have a clear and consistent boundary corresponding to extreme values except for curvatures in groups 1 and 2. This feature provides support for the classification and indicates that there is a smooth and similar shape within class members.

2) The location of extremes could be a secondary index to the shape of a cross-section. Figure 4-13 shows the geometric meaning of the extreme position in cross-sectional curves and radial curves. The location of extremes reflect the shape difference of cross-sections, but is difficult to relate to a simple anthropometric measurement.

3) The shape classification based on equation 4.10 has a reasonable distribution: the majority of the shape is represented by groups 2 and 3 with the extreme index from 0.328 to 0.482913 at maximum hip level (61 out of 76 cases).

4.2.3 Representation of reference body

The results achieved from the hierarchical clustering provides a basis for representing the structure of the reference body. Instead of using one or more independent reference bodies, the new reference body is composed of a set of families of cross-sectional shape vectors. A family of shape vectors are sorted, at each cross-section, by the ratio of

width to depth. The modelling program automatically selects an adequate shape vector of a cross-section by this ratio. This implies that the width and depth measurements at key sections are compulsory. A complete classification of all key cross-sections should be carried out and all classes and their width/depth ratio should be compiled into the modelling program in order to build such a reference body.

In addition to the knowledge of width/depth ratio, the distribution of curvature is useful in the modification of the shape vector. The range of curvature for each class could be used to impose a constraint on the lower and upper limits of shape modification.

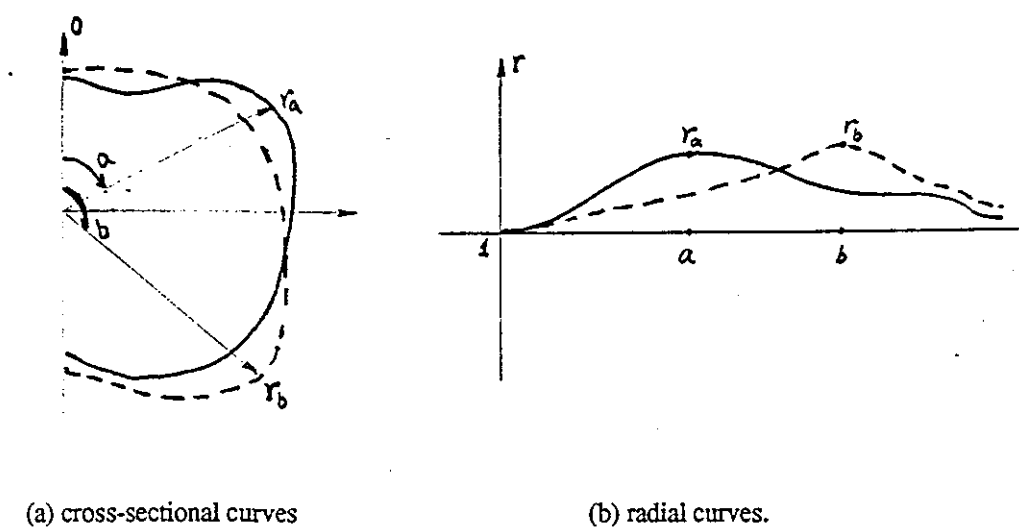


Figure 4- 13. Two locations of extreme and corresponding curve shapes

4.3 Relationship between width, depth and circumference of a cross-section

The previous two sections present a methodology to relate the shape of cross-sections of the human torso to finite anthropometric measurements. The methodology attempts to bridge the gap between traditional anthropometry and modern computer aided geometric modelling techniques. The effort is confined to modifying a reference cross-sectional curve by its depth and width. However, most of survey data do not contain complete depth and width measurements for all measured cross-sections of the human torso. These can be observed from Table 4-1 and Figure 4-1. An experiment is designed to

investigate method of predicting the third variable when two variables of depth, width and circumference are known..

Table 4-1 shows the measurement frame of British Women’s Size Survey 1987. Key cross-sections related to a torso are defined as **maximum hips, waist, under bust, chest and shoulder**. At these sections, there is no complete measurement available for all three variables of depth, width and circumference, but two of three variables are available or derivable at some place. To investigate the feasibility of predicting the third variable form the other two, 15 female subjects were scanned by LASS. Their depth, width and circumference at key cross-sections were measured and computed from scanning data. The linear regression method was employed to define the relationship between these three variables.

A regression equation is described by:

$$\text{Depth/Width}=\alpha(\text{Depth/Girth})+\beta \tag{4.11}$$

and results are shown in Table 4-4.

Table 4- 4. Regression Equations of Depth, Width and Girth for five cross-sections

	α	β	Residual
Max. hip	4.200529	-0.1021	0.03
Waist	4.88658	-0.5626	0.03
Under bust	4.305221	-0.38025	0.02
Chest (Max. Bust)*	-5.03974	2.419851	0.06
Shoulder	2.686539	-0.05632	0.008

* Regressive equation of chest is presented by: $\text{Depth/Width}=\alpha(\text{Width/Girth})+\beta$

From the regression equation, one of the variables width, depth or girth at a cross-section can be predicted from the other two. The prediction error (residual) is comparable with a manual measurement error, for example, at the under bust level a set of measured data for width, depth and girth are 31.2 cm, 30.6 cm and 97.5 cm, and the corresponding predicted value are: 31.5 cm, 31.4 cm and 96.7 cm. In this way, some survey data sets, which contain only two variables such as depth and girth, or width and girth, could be expanded to a complete data set (containing all three measurements).

4.4 Summary

This chapter describes the anthropometry-based modelling of the human body. It derives a method to modify a 3-D parametric surface model of the human torso according to certain anthropometric measurements. Concept of the reference body is introduced to provide a generic model which is comprised of nine key cross-sections. A shape vector corresponding to a key cross-section is modified with simple anthropometric measurements. It is the shape vectors to provide basic cross-sectional data for the modification of the surface model.

A single shape vector for one cross-section is not sufficient for accommodating the shape variations of the cross-section. In order to improve the modelling accuracy, a group of shape vectors for one cross-section is desirable. Selection and acquisition of multi-shape vectors rely on good classification of the cross-section. This chapter explored a shape classification scheme for cross-sectional curves of the human body. A number of shape features which have certain anthropometric meaning are selected and cluster analysis is used to group these features. A test on the hip section has shown promising classification results.

Finally the exploitation of anthropometric survey data for 3-D body modelling is discussed. Preliminary tests of the linear regression relationships between width, depth and circumference of five cross-sections were carried out. Results of the test are acceptable when compared to the traditional anthropometric methods..

CHAPTER FIVE

3D MEASUREMENT TASK-I: CALIBRATION OF DIGITAL CAMERA SYSTEMS

Calibration of a camera system is clearly of paramount importance in a vision-based measurement system. This chapter reviews calibration methods used for digital camera systems, particularly for close-range measurement tasks, and evaluates two types of calibration methods in a simulation environment. Practical calibration of a digital camera system is discussed and three analytical calibration methods are verified in the camera system.

5.1 *Modelling a digital camera system*

The measurement of 3-D co-ordinates based on camera imagery can be traced back through many decades. It was first applied in land surveys and civil engineering and later became a scientific discipline known as photogrammetry. Photogrammetry is concerned with object measurement and interpretation from photographs, often known as metric photogrammetry and interpretative photogrammetry respectively. Metric photogrammetry takes precise measurements from a photograph in order to determine the relative location of points. Interpretative photogrammetry principally deals with recognising and identifying objects and judging their significance [Wolf, 1983].

'Close-range' photogrammetry which takes photographs from a short distance (less than 300 metres) [Faig, 1975], has been introduced to the tasks of industrial measurement, metrology, machine vision for robot location and assembly, etc. In these applications there is a considerable use of the 'non-metric' cameras. Non-metric cameras use relatively cheap 'off-the-shelf' lenses, have flexibility of focal range, and are easy to acquire. However, disadvantages in the use of 'non-metric' camera are: no fiducial marks, poor lens quality, absence of level bubbles and orientation provisions, and lower resolution of image. These create great difficulties in calibration.

The advent of digital image techniques has driven photogrammetry into a digital era [DP, 1992]. The digital image technique brings together a greater range of image sources for photogrammetrists. The medium for recording and storing a picture is a computer file.

The image could come from a camera, a scanner or a photocopying machine rather than merely from film. Distortion caused by film development and processing is thus avoided. The digital form of image allows semi-automatic and automatic recognition and interpretation of the picture by computer hardware with the aids of software of image processing and pattern recognition. The digital form of an image also facilitates the pre and post-processing of output product, such as editing, plotting and database management.

The use of digital cameras draws greater attention to the calibration of the imagery process because more “non-metric” equipment is involved [Shortis, 1988]. For example, early digital photogrammetric systems consisted of a TV or solid-state camera, a frame grabber and a computer graphics/image workstation. Such a system has limitations in the application of vision-based industrial measurement because of the low resolution of the camera and poor performance of the frame grabber. The recent emergence of high resolution digital cameras, which can provide the image with 4000x4000 pixels and 100% filling factor of CCD sensor array, and high precise frame grabbers, has greatly enhanced the implementation of totally digital, high performance photogrammetric systems. However, they are very expensive.

In summary, digital close-range photogrammetry has become a basic feature of modern vision based measurement systems. This section will introduce the geometric and distortion model of a camera system used in digital close-range photogrammetry and machine vision.

5.1.1 Ideal geometric model of a camera system

An ideal camera model presents a collinearity relationship between an object point, its image and the exposure station. Three co-ordinate systems are used for completing camera geometry. They are a camera-centred co-ordinate system, an image co-ordinate system and a world co-ordinate system. The relationship between them is shown in Figure 5-1. In the camera-centred co-ordinate system, its origin coincides with the focus centre of the camera, and the z_c axis coincides with the optical axis of the camera. The image co-ordinate system is a 2-D plane which is assumed to be parallel to the (x_c, y_c) plane of the camera co-ordinate system and located at a distance of $-z_a$ from the origin of the camera co-ordinate system. The intersection of the optical axis of camera and the image plane is

termed the *principal point* which is (x_p, y_p) in the image co-ordinate system. If (X_c, Y_c, Z_c) and (X_A, Y_A, Z_A) represent the position of the camera and the object point in the world co-ordinate system respectively, (x_a, y_a) represents the position of the object point in the image plane. If the axes of the camera co-ordinate system are parallel to corresponding axes of the world co-ordinate system, the collinearity condition equations can be described as:

$$\frac{x_a - x_p}{X_A - X_c} = \frac{y_a - y_p}{Y_A - Y_c} = \frac{-z_a}{Z_A - Z_c} \quad (5.1)$$

From collinearity condition equation (5.1), if z_a , (X_c, Y_c, Z_c) and one of (X_A, Y_A, Z_A) are known, the other two co-ordinate elements of the object point can be easily decided from their image co-ordinate (x_a, y_a) .

In a digital camera system, the pixel plane is not the same as the image plane due to the digitised sample and conversion process. The pixel co-ordinates of the object are recorded as (u, v) which represents column and row values in the pixel plane. A linear relationship is usually assumed to be between the pixel plane co-ordinate and the image plane co-ordinate, that is:

$$\begin{aligned} u - u_0 &= k_x \cdot (x - x_p) \\ v - v_0 &= k_y \cdot (y - y_p) \end{aligned} \quad (5.2)$$

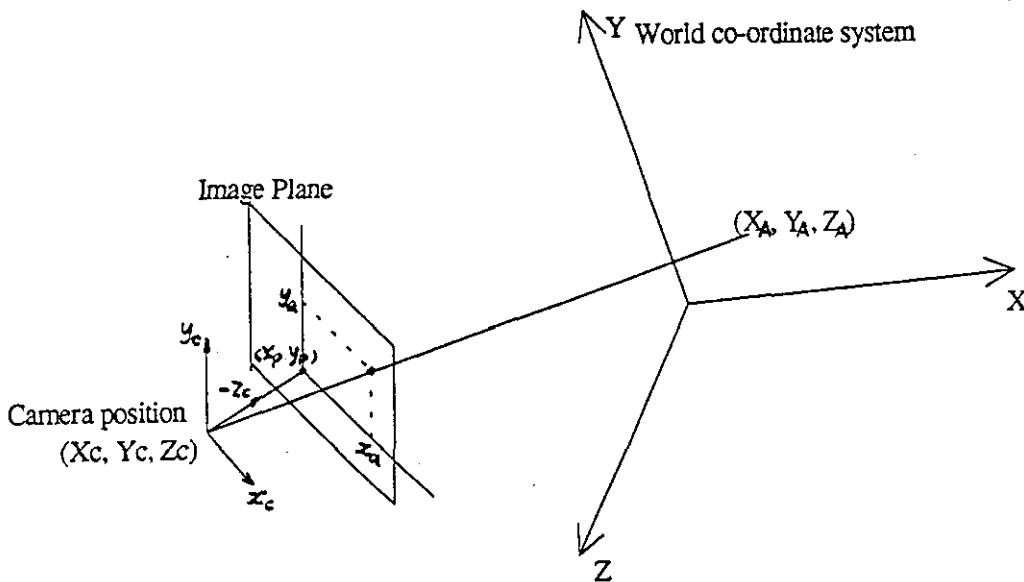


Figure 5-1 Three co-ordinate systems of a camera model

where (u_0, v_0) is the pixel co-ordinate corresponding to the camera optical centre and (k_x, k_y) are pixel/image ratios. k_x/k_y represents the aspect ratio of the pixel plane.

Equation 5.1 describes an ideal situation in which the camera co-ordinate system is parallel to the world co-ordinate system. This is not always true in practical situations. In fact, the image plane is usually tilted to the X-Y plane of the world co-ordinate system. The position of the exposure centre and the direction of the optical axis of a camera in a world co-ordinate is defined as the exterior orientation of a camera.

Figure 5-2 shows the co-ordinate relation of a camera exposure station in a world co-ordinate system. The position of the camera is defined at X_c, Y_c, Z_c and its orientation is defined by three rotation angles omega (ω), phi (ϕ) and kappa (κ) about the x', y' and z' axes respectively. The co-ordinate system $x'-y'-z'$ is parallel with the world co-ordinate system X-Y-Z. The tilted image point (x_a, y_a, z_a) may have its rotated co-ordinate (x'_a, y'_a, z'_a) in the $x'-y'-z'$ co-ordinate system. The rotation relationship can be described by matrix form:

$$x = M \cdot x' \quad (5.3a)$$

where

$$x = \begin{pmatrix} x_a \\ y_a \\ z_a \end{pmatrix}, \quad M = \begin{bmatrix} m_{11} & m_{12} & m_{13} \\ m_{21} & m_{22} & m_{23} \\ m_{31} & m_{32} & m_{33} \end{bmatrix} \equiv \begin{bmatrix} m_x \\ m_y \\ m_z \end{bmatrix}, \quad \bar{x} = \begin{pmatrix} x'_a \\ y'_a \\ z'_a \end{pmatrix} \quad (5.3b)$$

The elements m_{ij} of M are derived from the rotation equation of the co-ordinate system [Wolf, 1983] as follows:

$$\begin{aligned} m_{11} &= \cos \phi \cos \kappa \\ m_{12} &= \sin \omega \sin \phi \cos \kappa + \cos \omega \sin \kappa \\ m_{13} &= -\cos \omega \sin \phi \cos \kappa + \sin \omega \sin \kappa \\ m_{21} &= -\cos \phi \sin \kappa \\ m_{22} &= -\sin \omega \sin \phi \sin \kappa + \cos \omega \cos \kappa \\ m_{23} &= \cos \omega \sin \phi \sin \kappa + \sin \omega \cos \kappa \\ m_{31} &= \sin \phi \\ m_{32} &= -\sin \omega \cos \phi \\ m_{33} &= \cos \omega \cos \phi \end{aligned} \quad (5.4)$$

Substituting $(-f)$ for z_a , the image co-ordinate can be acquired by the collinearity condition from Equations 5.1, 5.3:

$$\begin{aligned} x_a - x_p &= -f \frac{m_{11}(X_A - X_c) + m_{12}(Y_A - Y_c) + m_{13}(Z_A - Z_c)}{m_{31}(X_A - X_c) + m_{32}(Y_A - Y_c) + m_{33}(Z_A - Z_c)} \\ y_a - y_p &= -f \frac{m_{21}(X_A - X_c) + m_{22}(Y_A - Y_c) + m_{23}(Z_A - Z_c)}{m_{31}(X_A - X_c) + m_{32}(Y_A - Y_c) + m_{33}(Z_A - Z_c)} \end{aligned} \quad (5.5a)$$

or denoted as

$$\begin{aligned} x_a - x_p &= -f \frac{R}{Q} \\ y_a - y_p &= -f \frac{S}{Q} \end{aligned} \quad (5.5b)$$

An equivalent expression of 5.3 is

$$x = M' \cdot X + T \quad (5.6)$$

where M' is M 's transpose and $T = (T_x, T_y, T_z)'$ is a position vector of the origin of world co-ordination in the camera co-ordination system.

The collinear relationship from the pixel plane to the world co-ordinate system can be acquired from Equations 5.2 and 5.5 as:

$$\begin{aligned} \frac{u - u_0}{k_x} &= -f \frac{R}{Q} \\ \frac{v - v_0}{k_y} &= -f \frac{S}{Q} \end{aligned} \quad (5.7a)$$

$$\begin{aligned} u - u_0 &= -f \cdot k_x \frac{R}{Q} = -f_x \frac{R}{Q} \\ v - v_0 &= -f \cdot k_y \frac{S}{Q} = -f_y \frac{S}{Q} \end{aligned} \quad (5.7b)$$

or

5.1.2 Distortion factors: Lens geometry and interior orientation of a camera

In pinhole geometry, an inverted image is theoretically in focus regardless of the distance from pinholes to the camera's image plane. However, the pinholes are so tiny that they only allow a little light to pass. This is often replaced by the glass lens. To describe the quality of lens, *aberration* and *distortion* are two criteria often used. The aberration describes the degradation of the sharpness of the image caused by imperfections in the lens.

The distortion describes the imperfections causing deterioration of the geometric quality (or position accuracy) of the image. Lens distortions are the main factors which affect the accuracy of a 3-D measurement.

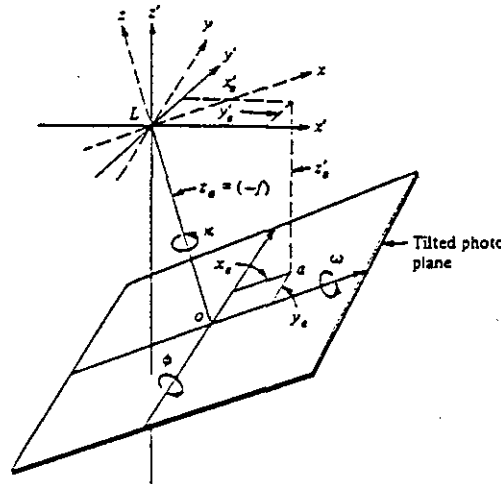


Figure 5- 2. Tilted photo plane in a world co-ordinate system

Lens distortions are further classified as radial and tangential distortions. Radial distortion causes points of an image to be distorted along radial lines from the optical axis. It is caused by faulty grinding of the lens elements. Tangential distortion occurs at right angles to radial lines from the optical axis. It is caused by faulty centring of the lens elements of a combination lens, therefore, it is also called decentering distortion. Figure 5-3 shows these two types of distortions. The magnitude of radial distortion is Δr and the magnitude of tangential distortion is Δt .

A non-linear equation is used to describe the relationship between the observed image co-ordinates and the true image co-ordinates:

$$\begin{aligned}\tilde{x} &= x + \delta_x(x, y) \\ \tilde{y} &= y + \delta_y(x, y)\end{aligned}\tag{5.8}$$

where \tilde{x}, \tilde{y} are observed image co-ordinates and x, y are true image co-ordinates, δ is a non-linear function and varies from different distortion sources. A general distortion model including radial and decentering distortion is described by Brown [1971]:

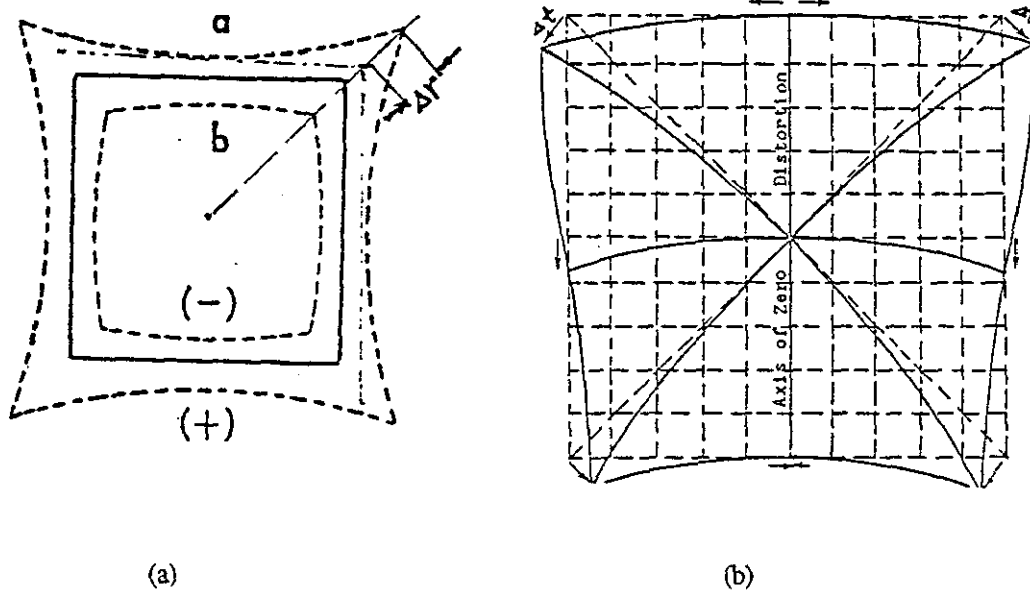


Figure 5-3. Lens distortions: a) pin-cushion shape of radial distortion; b) tangential distortion.

$$\begin{aligned}\delta_x &= \hat{x} \cdot (k_1 \cdot r^2 + k_2 r^4 + k_3 r^6 + \dots) + [p_1(r^2 + 2\hat{x}^2) + 2p_2\hat{x}\hat{y}][1 + p_3r^2 + \dots] \\ \delta_y &= \hat{y} \cdot (k_1 \cdot r^2 + k_2 r^4 + k_3 r^6 + \dots) + [2p_1\hat{x}\hat{y} + p_2(r^2 + 2\hat{y}^2)][1 + p_3r^2 + \dots]\end{aligned}\quad (5.9)$$

in which

$$\begin{aligned}\hat{x} &= x - x_p \\ \hat{y} &= y - y_p \\ r &= (\hat{x}^2 + \hat{y}^2)^{1/2}\end{aligned}$$

where r is the radial distance from the principal point of the image plane, k_1, k_2, k_3 are coefficients of radial distortion, and p_1, p_2, p_3 are coefficients of tangential distortion. A simplified version of Equation 5.9 is Equation 5.9a.

$$\begin{aligned}\delta_x &= \hat{x} \cdot k_1 \cdot r^2 + p_1(r^2 + 2\hat{x}^2) + 2p_2\hat{x}\hat{y} \\ \delta_y &= \hat{y} \cdot k_1 \cdot r^2 + 2p_1\hat{x}\hat{y} + p_2(r^2 + 2\hat{y}^2)\end{aligned}\quad (5.9a)$$

According to the 'Manual of Photogrammetry' [ASP 1980], the distortion coefficients of the lens, together with the focal length f and the co-ordinates of the principle point (x_p, y_p) , are described as the interior orientation of a camera.

Equation 5.2 introduces four parameters u_0, v_0, k_x and k_y for a digital camera system. Therefore the coefficients (u_0, v_0, k_x, k_y) or (u_0, v_0, f_x, f_y) should be included in the interior orientation of a digital camera.

The distortion model of a lens in pixel co-ordinate system is derived by substituting equation 5.2 into equation 5.8 and 5.9.

$$\begin{aligned}
 \delta_x &= \frac{\hat{u}}{k_x} \cdot k_1 \cdot \left(\frac{\hat{u}^2}{k_x^2} + \frac{\hat{v}^2}{k_y^2} \right) + p_1 \left(3 \cdot \frac{\hat{u}^2}{k_x^2} + \frac{\hat{v}^2}{k_y^2} \right) + 2p_2 \frac{\hat{u}\hat{v}}{k_x k_y} \\
 &\approx \hat{u} \cdot \hat{k}_1 \cdot (\hat{u}^2 + \hat{v}^2) + \hat{p}_1 \cdot (3\hat{u}^2 + \hat{v}^2) + 2\hat{p}_2 \hat{u}\hat{v} = \delta_u(\hat{u}, \hat{v}) \\
 \delta_y &= \frac{\hat{v}}{k_y} \cdot k_1 \cdot \left(\frac{\hat{u}^2}{k_x^2} + \frac{\hat{v}^2}{k_y^2} \right) + 2p_1 \frac{\hat{u}\hat{v}}{k_x k_y} + p_2 \left(\frac{\hat{u}^2}{k_x^2} + 3 \cdot \frac{\hat{v}^2}{k_y^2} \right) \\
 &\approx \hat{v} \cdot \hat{k}_1 \cdot (\hat{u}^2 + \hat{v}^2) + 2\hat{p}_1 \hat{u}\hat{v} + \hat{p}_2 \cdot (\hat{u}^2 + 3\hat{v}^2) = \delta_v(\hat{u}, \hat{v})
 \end{aligned} \tag{5.10}$$

where

$$\begin{aligned}
 \hat{k}_1 &= \frac{k_1}{k_x^3} \\
 \hat{p}_1 &= \frac{p_1}{k_x^2} \\
 \hat{p}_2 &= \frac{p_2}{k_x^2}
 \end{aligned} \tag{5.11}$$

Such approximation is reasonable because the k_x and k_y are much bigger than one and they are very close in a square pixel camera.

5.1.3 Other distortion factors

In addition to the radial and tangential distortions discussed in the last sub-section, there are many other factors which affect the accuracy of object measurement. In other words, the correction of the radial and tangential distortion cannot completely guarantee the accuracy of 3-D measurement (back-projection) since they reveal only 'geometric' factors which cause the distortion in camera lens.

Other factors also cause distortions in imagery process of a digital camera system including : 1) the uncertainty of the horizontal scale factor, which is the conversion factor

from the element unit in a computer image to the element unit of the sensor [Lenz & Tsai 1988]; 2) the uncertainty of the image centre and the camera centre [Wilson & Shaver, 1994]; 3) the illumination sensitivity of photo sensors and thermal stability of electronic circuit. All of these factors contribute to the distortion of an image. There is no complete explicit model available to describe all possible distortions, although many investigations have been carried out [Curry, Baumrind & Anderson 1986; Shortis 1988; Robson, Clarke & Chen 1993, Shortis and Snow 1993 and other papers in SPIE 1993].

As an alternative representation, additional compensation parameters are introduced into the distortion equation 5.10. A general distortion equation is formed accordingly:

$$\begin{aligned}\tilde{x} &= x + \delta_x(x, y) + \Delta x \\ \tilde{y} &= y + \delta_y(x, y) + \Delta y\end{aligned}\tag{5.12}$$

The additional terms Δx , Δy are called *additional parameters* (AP's) [ASP 1980; Fryer 1992]. There is a variety of AP models employed today. Although many of them are empirical because their exact physical meanings are unclear, they are considered to be effective way of dealing with the complexity of the entire distortion model of photogrammetric systems.

5.2 Calibration methods of the digital camera system: an overview

Camera calibration is a process to determine the geometric characteristics of an individual camera. The process is necessary to ascertain that the image obtained from the camera can be used to produce accurate results for a measurement task. The geometric characteristics of cameras include the interior and exterior parameters (orientations). Combining equation 5.5, 5.8 and 5.9, a complete calibration method must address nine interior parameters ($x_p, y_p, f, k_1, k_2, k_3, p_1, p_2, p_3$) and six exterior parameters ($\omega, \phi, \kappa, X_C, Y_C, Z_C$). For a digital camera system, the interior parameters must include the image/pixel ratio k_x, k_y as well. There are seventeen unknown parameters all together. However, a particular calibration method usually addresses partial geometric parameters of a camera for some practical purposes. A brief overview of calibration methods will be given in this section. The

discussion is divided into three sub-sections: calibration of interior parameters, calibration of exterior parameters, and hybrid calibration of interior/exterior parameters.

5.2.1 Calibration of the interior parameters

The elements of interior parameters to be calibrated may include: equivalent focal length, average radial measured distortion, tangential measured distortion, calibrated focal length, principle point of image, and radial and tangential distortion polynomial, as defined in '*Manual of Photogrammetry*' [ASP, 1980]. There are a number of approaches to calibrating the interior parameters of a camera in photogrammetry. Faig [1975] classified these approaches as: laboratory calibration, 'on the job' calibration, and self-calibration. The laboratory-based calibrations need complex and precise equipment to build control fields, to record and process the camera image, and to maintain the position and exterior orientation of the tested camera accurately. The control targets are usually produced by a high precision multicollimator. Such sophisticated equipment and methods are expensive and complex. They are mainly used for the calibration of high precision metric cameras in national-level laboratories [ASP 1980]. Non-metric cameras for ordinary machine vision and measurement tasks are rarely calibrated by this approach.

'On the job' calibration utilises photographs of the object and the object-space control simultaneously. It needs certain control objects, but mainly relies on computational approaches. These include the plumb line method, the cross-ratio method, and the modified DLT (Direct Linear Transformation) method. The plumb line method, developed by Brown [1971], is a well known analytical method in determining the radial and tangential distortion polynomials. The plumb line method is based on the projective principle that the image of any straight line in the world co-ordinate system is itself a straight line in the absence of lens distortions. Any systematic departure from strict linearity of the image of a straight line can be attributed to distortion. Wei and Ma [1994] presented a simpler but less powerful method to calibrate interior parameters of a camera. Their method is built on the basis of the invariant of the cross-ratio of four 3-D collinear points under projective transformation. The distortion centre of the image frame is firstly calculated from the cross-ratio equation of at least two collinear sets of calibration points by the iterative linearisation

method. The scale factor of the image frame and the radial distortion coefficient k_1 is then calculated, again by the linearised cross-ratio equation. This method assumes that the 2-D projection of 3-D collinear points is collinear so that the calibrated image points hold the same cross-ratio as their 3-D counterpart. The method could be sensitive to an observation error of image points, since only four points are sampled from a line equation.

The self-calibration approach does not require object-space control as much as other methods. In this approach, multiple *convergent* photographs are taken of the object. The convergent photographs mean that they are taken from different viewpoints over the same object. Each photograph is taken with the same interior orientation of a camera. The coplanarity condition is derived from the fact that the object point, P, and the two exposure station positions, U_1 , U_2 , are coplanar if the object P is seen from both exposure stations. Utilising the coplanarity condition and well identified object points, the basic parameters of interior orientation are computed [Faig, 1975].

5.2.2 Calibration of the exterior parameters

The calibration of the exterior parameters of a camera requires control of a known object because the exterior orientation must refer to some world co-ordinate system. Calibration based on equation 5.5 requires that the control points (X_i, Y_i, Z_i) and their image co-ordinates (x_i, y_i) are known. If focal length, f , and principle point co-ordinates (x_p, y_p) are given, equation 5.5 contains six unknown variables $(\omega, \phi, \kappa, X_C, Y_C, Z_C)$. The equation is non-linear as it involves the trigonometric functions of (ω, ϕ, κ) . The solution of calibration may be basically classified into two types: linear and non-linear approaches.

In order to avoid to solve a non-linear problem, the equation 5.5 is usually treated as a linear transformation between world co-ordinates and their image co-ordinates in which each element of the rotation matrix is treated as an independent variable. This leads to a linear calibration approach.

The non-linear calibration approach performs first-order linearisation and an iterative solution. It the setting of initial estimate values for the unknown variables. If the equation 5.5 is expanded further to include unknown interior parameters of a camera, the calibration problem becomes more complex. The coupled non-linear relationship between interior and exterior parameters increases the difficulty of computation. This usually

requires a hybrid computational approach which will be discussed in Section 5.3.3. The typical linear and non-linear methods are discussed in Section 5.3.2.1 and 5.3.2.2. respectively.

5.2.2.1 Linear calibration methods

The Direct Linear Transformation (DLT) method [Abdel-Aziz & Karara, 1971] is a typical example of the linear calibration method. As its name implies, the solution of the DLT method is based on the concept of direct transformation from image co-ordinates (could be pixel frame) into object-space co-ordinates. The basic transformation equations are expressed as:

$$\begin{aligned} x &= \frac{L_1 X + L_2 Y + L_3 Z + L_4}{L_9 X + L_{10} Y + L_{11} Z + 1} \\ y &= \frac{L_5 X + L_6 Y + L_7 Z + L_8}{L_9 X + L_{10} Y + L_{11} Z + 1} \end{aligned} \quad (5.13)$$

and the element L_i of the transformation matrix are considered as independent from each other. The solution of 5.13 can be derived from the following linear form of (5.14)

$$\begin{aligned} L_1 X + L_2 Y + L_3 Z + L_4 - x L_9 X - x L_{10} Y - x L_{11} Z - x &= r_x \\ L_5 X + L_6 Y + L_7 Z + L_8 - y L_9 X - y L_{10} Y - y L_{11} Z - y &= r_y \end{aligned} \quad (5.14)$$

where r_x, r_y are the residual errors.

Because each object-space co-ordinates (X, Y, Z) provide two equations 5.14, a minimum of six control points are required for a solution to the eleven unknown variables. Six control points can produce twelve equations, therefore the least squares solution is preferred. However, the elements of the transformation matrix are in fact coupled (this is due to the fact that the rotation matrix M in equation 5.5 is a unit orthogonal matrix.). Bopp and Krauss [Bopp and Krauss, 1977, refer to ASP 1980] developed an exact solution to the DLT basic equations by applying two constraints, which are:

$$\begin{aligned} (L_1^2 + L_2^2 + L_3^2) - (L_5^2 + L_6^2 + L_7^2) \\ + [(L_5 L_9 + L_6 L_{10} + L_7 L_{11}) - (L_1 L_9 + L_2 L_{10} + L_3 L_{11})] (L_9^2 + L_{10}^2 + L_{11}^2)^{-1} &= 0 \\ (L_1 L_5 + L_2 L_6 + L_3 L_7) - (L_9^2 + L_{10}^2 + L_{11}^2)^{-1} (L_1 L_9 + L_2 L_{10} + L_3 L_{11}) \\ (L_5 L_9 + L_6 L_{10} + L_7 L_{11}) &= 0 \end{aligned} \quad (5.15)$$

This leads to a least squares computation with linear observation equations and non-linear constraints, where an iterative procedure is needed.

The DLT method was also expanded to encompass interior parameters of cameras, which means that there are more than eleven parameters to be solved from the basic equation system [Abdel-Aziz & Karara, 1974; Karara & Abdel-Aziz, 1974, both refer to ASP 1980]. Fan & Yuan [1993] combined lens distortions and AP parameters in the DLT scheme. A multiple steps and non-linear optimisation computation is required.

A variation of the DLT method is to solve the combined parameters from equation 5.6 with eleven exterior parameters (T_x, T_y, T_z), ($m_{11} - m_{33}$) and some interior parameters. Ito and Ishi [1994] and Shih, Hung & Lin [1993, 1995] presented two such examples.

The vanishing point methods [Wang & Tsai, 1991; Chen & Jian, 1991] solve the exterior parameters of a camera, without taking lens distortion into account, by the perspective vanishing point of a group of parallel lines in 3-D object space. The method is based on the fact that the parallel straight lines in 3-D object space converge at a point in an image plane after a perspective transformation. At least two vanishing points are needed to decide the rotation matrix, and more vanishing points as well as vanishing lines are needed to calculate the location of a camera.

5.2.2.2 Non-linear calibration methods

The classic non-linear method is based on the linearisation of the collinearity condition equation 5.5 [Wolf, 1983]. Equation 5.5 can be rewritten as follows:

$$F_i = 0 = Q_i x_i + R_i f \quad (5.16a)$$

$$G_i = 0 = Q_i y_i + S_i f \quad (5.16b)$$

where

$$\begin{aligned} Q_i &= m_{31}(X_i - X_C) + m_{32}(Y_i - Y_C) + m_{33}(Z_i - Z_C) \\ R_i &= m_{11}(X_i - X_C) + m_{12}(Y_i - Y_C) + m_{13}(Z_i - Z_C) \\ S_i &= m_{21}(X_i - X_C) + m_{22}(Y_i - Y_C) + m_{23}(Z_i - Z_C) \end{aligned} \quad (5.16c)$$

and (X_C, Y_C, Z_C) are the co-ordinates of the camera centre. (X_i, Y_i, Z_i) are observed values of control points. According to Taylor's theorem, equation 5.16 may be expressed in first-order linearised form at its equilibrium point F_0, G_0 as:

$$0 = F_0 + \left(\frac{\partial F}{\partial x}\right)\Delta x + \left(\frac{\partial F}{\partial \omega}\right)\Delta \omega + \left(\frac{\partial F}{\partial \phi}\right)\Delta \phi + \left(\frac{\partial F}{\partial \kappa}\right)\Delta \kappa + \left(\frac{\partial F}{\partial X_L}\right)\Delta X_L + \left(\frac{\partial F}{\partial Y_L}\right)\Delta Y_L + \left(\frac{\partial F}{\partial Z_L}\right)\Delta Z_L \\ + \left(\frac{\partial F}{\partial X_i}\right)\Delta X_i + \left(\frac{\partial F}{\partial Y_i}\right)\Delta Y_i + \left(\frac{\partial F}{\partial Z_i}\right)\Delta Z_i \quad (5.17a)$$

$$0 = G_0 + \left(\frac{\partial G}{\partial y}\right)\Delta y + \left(\frac{\partial G}{\partial \omega}\right)\Delta \omega + \left(\frac{\partial G}{\partial \phi}\right)\Delta \phi + \left(\frac{\partial G}{\partial \kappa}\right)\Delta \kappa + \left(\frac{\partial G}{\partial X_L}\right)\Delta X_L + \left(\frac{\partial G}{\partial Y_L}\right)\Delta Y_L + \left(\frac{\partial G}{\partial Z_L}\right)\Delta Z_L \\ + \left(\frac{\partial G}{\partial X_i}\right)\Delta X_i + \left(\frac{\partial G}{\partial Y_i}\right)\Delta Y_i + \left(\frac{\partial G}{\partial Z_i}\right)\Delta Z_i \quad (5.17b)$$

In equation 5.17, the function F and G are evaluated at the initial approximations of nine variables $(\omega, \phi, \kappa, X_C, Y_C, Z_C, X_i, Y_i, Z_i)$ and image co-ordinates (x_i, y_i) .

Let

$$\begin{aligned} x_i &= x_i^0 + v_x^i, \\ y_i &= y_i^0 + v_y^i, \\ \omega &= \omega^0 + \Delta \omega, \\ \phi &= \phi^0 + \Delta \phi, \\ \kappa &= \kappa^0 + \Delta \kappa, \\ X_C &= X_C^0 + \Delta X, \\ Y_C &= Y_C^0 + \Delta Y, \\ Z_C &= Z_C^0 + \Delta Z, \\ X_i &= X_i^0 + \Delta X_i, \\ Y_i &= Y_i^0 + \Delta Y_i, \\ Z &= Z_i^0 + \Delta Z_i \end{aligned} \quad (5.18)$$

be increment corrections of all variables. Since v_x and v_y are corrections to measured image co-ordinates x_i and y_i , they may be interpreted as residual errors in the measurements. The simplified form of equation 5.17 can be obtained:

$$\mathbf{V}_i = \mathbf{B}_i \mathbf{D}_i + \mathbf{e}_i \quad (5.19)$$

where

$$\mathbf{V}_i = \begin{pmatrix} v_x^i \\ v_y^i \end{pmatrix}, \text{ is the residual vector.}$$

$$\mathbf{B}_i = \begin{bmatrix} b_{11}^i & b_{12}^i & b_{13}^i & -b_{14}^i & -b_{15}^i & -b_{16}^i & b_{14}^i & b_{15}^i & b_{16}^i \\ b_{21}^i & b_{22}^i & b_{23}^i & -b_{24}^i & -b_{25}^i & -b_{26}^i & b_{24}^i & b_{25}^i & b_{26}^i \end{bmatrix}, \text{ is the partial derivation matrix}$$

(Jacobian matrix) of Equation (5.16)

$$\mathbf{D}_i = \begin{bmatrix} \Delta\omega \\ \Delta\phi \\ \Delta\kappa \\ \Delta X_c \\ \Delta Y_c \\ \Delta Z_c \\ \Delta X_i \\ \Delta Y_i \\ \Delta Z_i \end{bmatrix}, \quad \mathbf{e}_i = \begin{pmatrix} J \\ K \end{pmatrix}.$$

According to equation (5.19), if m ($m > 5$) observation points are given, a least squares solution of \mathbf{D}_i can be obtained by minimising the squared residual vector \mathbf{V}_i of these measurements. An iterative scheme is needed, since the solution starts from the initial estimate of the unknowns. After each iteration the calculated increments are added to the unknowns, as shown in 5.18 and new values of the unknown variable are used for next iterative calculation of \mathbf{B} and \mathbf{e} in equation 5.19.

A similar iterative scheme is used by Liu, Huang & Faugeras [1990], but the basic equations are derived from a different viewpoint.

5.2.3 Hybrid calibration methods

This section reviews the methods to calibrate both the interior and the exterior parameter. The methods may be classified into two classes, namely: the single step method and the multiple-step method.

5.2.3.1 Single-step methods

The single step methods, which include non-linear optimisation and the modified DLT method, calculate and adjust exterior and interior parameters simultaneously. A close-form solution, e.g. the DLT method, is preferred in single-step methods as it calculates unknowns without iteration. However the close-form solution could conflict with the non-linear constraint condition inherited in the simultaneous calibration of interior and exterior parameters. Karara and Abdel-Aziz [1974] modified the DLT method to take radial lens distortion into account. The modified DLT method can be solved by one step, but an iterative approach must be adopted if constraints of the rotation matrix are imposed. Shih's method [Shih *et al.*, 1993, 1995] may be classified as a single-step method as well.

5.2.3.2 Multiple-step methods

The multiple step methods are developed to overcome the shortcomings of single-step methods in need of the initial estimate value of unknowns. Multiple step methods adopt different strategies to calculate different parameters in separated steps.

Faig's [1975] non-linear optimisation to solve collinearity or coplanarity condition equations adopted two-step iterations to solve the coplanarity condition equations: the first step calculates only the coarse exterior parameters which are involved in the observation equations; the second iteration step calculates the refined exterior and interior parameters based on the results of the first step. The results of the second step are in turn employed as the initial values of the first step. An iterative chain is formed. This continues until differences between subsequent results are less than the tolerance limit.

Other multiple-step methods typically use a close-form solution to calculate partial parameters (for example, intermediate parameters) and an iterative solution to calculate the rest of the parameters. This could avoid the difficulty of setting initial values of unknown variables in the single-step methods. It is extremely useful in machine vision application where the initial settings are difficult to obtain due to the dynamic environment encountered. Two of the typical multiple-step methods are: Tsai's method [Tsai, 1987] and Weng's method [Weng, Cohen & Herniou, 1992].

Tsai's method:

Tsai proposed a two-stage method to accomplish camera calibration of exterior and interior parameters based on a lens model which considers radial distortion only. At the first

stage a close form solution is derived for some intermediate parameters. Let projective transformation from world co-ordinates of object points to camera co-ordinates be defined as:

$$\begin{pmatrix} x \\ y \\ z \end{pmatrix} = \begin{bmatrix} r_{11} & r_{12} & r_{13} \\ r_{21} & r_{22} & r_{23} \\ r_{31} & r_{32} & r_{33} \end{bmatrix} \begin{pmatrix} X \\ Y \\ Z \end{pmatrix} + \begin{pmatrix} T_x \\ T_y \\ T_z \end{pmatrix} = \mathbf{R} \begin{pmatrix} X \\ Y \\ Z \end{pmatrix} + \mathbf{T} \quad (5.20)$$

and transformation from camera co-ordinates to distorted image co-ordinates as:

$$\begin{aligned} X_d + D_x &= X_u = f \frac{x}{z} \\ Y_d + D_y &= Y_u = f \frac{y}{z} \end{aligned} \quad (5.21)$$

Radial Alignment Constraint (RAC), proposed by Tsai, states that the vector from the origin of the image plane to the image point (X_d, Y_d) is parallel to a vector from object point (x, y, z) to the optical axis whose z co-ordinate is equal to the z value of the object point, assuming that distortion is radial. Therefore the two vector outer product is zero, i.e.

$$(X_d, Y_d) \times (x, y) = 0$$

or

$$X_d \cdot y - Y_d \cdot x = 0 \quad (5.22)$$

Substitute (5.20), (5.21) into (5.22), then

$$X_d \cdot (R_y + T_y) - Y_d \cdot (R_x + T_x) = 0 \quad (5.23)$$

where

$$R_x = r_{11}X + r_{12}Y + r_{13}Z, \quad R_y = r_{21}X + r_{22}Y + r_{23}Z, \quad R_z = r_{31}X + r_{32}Y + r_{33}Z.$$

From (5.23), by re-arranging unknown variables, the following linear equation is acquired:

$$\begin{bmatrix} Y_d X_i & Y_d Y_i & Y_d Z_i & Y_d & -X_d X_i & -X_d Y_i & -X_d Z_i \end{bmatrix} \begin{bmatrix} T_y^{-1} r_{11} \\ T_y^{-1} r_{12} \\ T_y^{-1} r_{13} \\ T_y^{-1} T_x \\ T_y^{-1} r_{21} \\ T_y^{-1} r_{22} \\ T_y^{-1} r_{23} \end{bmatrix} = X_d$$

$$(i=0, \dots, n) \quad (5.24)$$

Equation 5.24 contains seven unknown variables. In the other words, at least seven observation points are needed to solve the equation. The solution of 5.24 is close-form to the intermediate variables $(T_y^{-1}r_{11}, T_y^{-1}r_{12}, T_y^{-1}r_{13}, T_y^{-1}T_x, T_y^{-1}r_{21}, T_y^{-1}r_{22}, T_y^{-1}r_{23})$ and the original variables can be solved from orthogonal constraints of the rotation matrix \mathbf{R} .

At the second stage an iterative solution is used to calculate the effective focal length f , T_z and distortion coefficient k_l . The initial values of f and T_z are approximated by ignoring lens distortion. The initial value of k_l is set to zero. A non-linear minimisation procedure is then employed in iteration. During these processes, the scale factors and image centre of the camera system are presumed to be known or derivable from the manufacturer's specification. A physical method to calibrate the scale factor of a camera has been developed by Lenz and Tsai [1988].

Weng's method:

Weng *et al.* [1992] presented an entire distortion model which included radial, tangential and prism distortions. The distortion model, after neglecting its higher order items, contains five unknown coefficients $(k_l, g_1, g_2, g_3, g_4)$. The distortion-free part of the camera model contains six exterior parameters $(\omega, \phi, \kappa, T_x, T_y, T_z)$ and four interior parameters (u_0, v_0, f_x, f_y) .

The coefficients of the distortion model are denoted as \mathbf{d} and the coefficients of the distortion-free model as \mathbf{m} , i.e.:

$$\mathbf{d} = (k_l, g_1, g_2, g_3, g_4)$$

$$\text{and } \mathbf{m} = (u_0, v_0, f_x, f_y, \omega, \phi, \kappa, T_x, T_y, T_z)$$

The complete solution of the calibration problem is accomplished in two steps. At the first step, \mathbf{d} is considered as fixed and the solution of the coefficients of the distortion-free model \mathbf{m} is computed. At the second step, with \mathbf{m} fixed as the current estimation, \mathbf{d} is computed by a close-form method. The current estimation of \mathbf{d} is applied to the next iteration of \mathbf{m} .

When computing \mathbf{m} for the first time, a close-form solution, followed by a non-linear optimisation, is used. The close-form solution is based on a DLT-like linear homogeneous equation. The solution of the linear system is used as the initial value of \mathbf{m} in a non-linear optimisation refining procedure.

5.4 Evaluation of calibration methods

Previous sections reviewed methods used for calibration of interior and exterior parameters of a digital camera system. This section will focus on hybrid methods to calibrate interior and exterior parameters of a camera system. Two types of calibration methods are to be evaluated. They are: non-linear optimisation method and Tsai's method.

5.4.1 Non-linear optimisation method

Section 5.2.2.2. discussed a non-linear optimisation approach to estimating exterior parameters of a camera using equations 5.16a and 5.16b. This section develops the complete non-linear optimisation equations to estimate thirteen camera parameters (exterior and interior).

5.4.1.1 Unconstrained non-linear least-squares theory

According to the theory of non-linear optimisation [Gill *et al.*, 1981], the non-linear optimisation problem of sums of squares

$$\text{minimise } \{F(x) = \frac{1}{2} \sum_{i=1}^m f_i(x)^2 = \frac{1}{2} \|f(x)\|_2^2\} \quad (5.25)$$

is equivalent to the solution of a linear least-squares problem:

$$\text{minimise } \left\{ \frac{1}{2} \|J_k p + f_k\|_2^2 \right\} \text{ where } J_k \text{ is the Jacobian matrix of } f(x) \quad (5.26)$$

The above problems are also equivalent to a solution problem of non-linear equations based on the first order Taylor-series expansion, i.e. to solve non-linear equation

$$f(x^*) = 0 \quad (5.27)$$

A linear approximation to f :

$$f(x^*) \approx f(x_k) + J(x_k)(x^* - x_k) \quad (5.28)$$

where $J(x)$ is the Jacobian matrix of function f . Let p_N be the Newton step to approximate $x^* - x_k$, then p_N satisfies:

$$J(x_k)p_N = -f(x_k) \quad (5.29)$$

and equation 5.29 can be solved by the least-square method if $J(x)$ is non-singular.

5.4.1.2 Implementation of non-linear optimisation

The estimation of camera interior and exterior parameters (Section 5.2.3.1) is a non-linear problem and can be well fitted into the above theory either from the minimisation of projection error of the collinearity equation:

$$C = \frac{1}{2} \sum_{i=1}^m \left\{ \left\| x_i + \delta_x - f \frac{R_i}{Q_i} \right\|_2^2 + \left\| y_i + \delta_y - f \frac{S_i}{Q_i} \right\|_2^2 \right\} \quad (5.30)$$

or from solving non-linear equations:

$$\begin{aligned} F_i &= 0 = (x_i + \delta_x) \cdot Q_i + f \cdot R_i \\ G_i &= 0 = (y_i + \delta_y) \cdot Q_i + f \cdot S_i \end{aligned} \quad (5.31)$$

where Q_i, R_i, S_i, F_i, G_i as defined in 5.16a, 5.16b and 5.16c.

A complete camera model taking radial and tangential lens distortion into account can be acquired by combining equation 5.5, 5.8 and 5.9 and re-written as:

$$\begin{aligned} u_i - u_0 + \delta_x &= -f_x \frac{m_{11}(X_i - X_C) + m_{12}(Y_i - Y_C) + m_{13}(Z_i - Z_C)}{m_{31}(X_i - X_C) + m_{32}(Y_i - Y_C) + m_{33}(Z_i - Z_C)} \\ v_i - v_0 + \delta_y &= -f_y \frac{m_{21}(X_i - X_C) + m_{22}(Y_i - Y_C) + m_{23}(Z_i - Z_C)}{m_{31}(X_i - X_C) + m_{32}(Y_i - Y_C) + m_{33}(Z_i - Z_C)} \end{aligned} \quad (5.32)$$

where

$$\begin{aligned} \delta_x &= \hat{u} \cdot \hat{k}_1 \cdot r^2 + \hat{p}_1(r^2 + 2\hat{u}^2) + 2\hat{p}_2\hat{u}\hat{v} \\ \delta_y &= \hat{v} \cdot \hat{k}_1 \cdot r^2 + 2\hat{p}_1\hat{u}\hat{v} + \hat{p}_2(r^2 + 2\hat{v}^2) \\ \hat{u} &= u_i - u_0 \\ \hat{v} &= v_i - v_0 \\ r^2 &= \hat{u}^2 + \hat{v}^2 \end{aligned} \quad (5.33)$$

Here the higher order items of radial and tangential distortions of the lens have been neglected.

Equation 5.32 relates 3-D control points and their image co-ordinates in the pixel plane. It is therefore more general. Equation 5.33 describes the lens distortion in the pixel plane, which is an approximation of equation 5.10. In equations 5.32 and 5.33 the interior parameters of the camera model are $(u_0, v_0, f_x, f_y, k_1, p_1, p_2)$, and the exterior parameters of the camera system are $(\omega, \phi, \kappa, X_C, Y_C, Z_C)$. In total there are thirteen unknowns to be estimated. The Jacobian matrix of functions F and G at the i th control point is:

$$\begin{aligned}
\mathbf{J}_i &= \begin{bmatrix} J_F \\ J_G \end{bmatrix}_i \\
&= \begin{bmatrix} \frac{\partial F_i}{\partial u_0} & \frac{\partial F_i}{\partial v_0} & \frac{\partial F_i}{\partial f_x} & \frac{\partial F_i}{\partial f_y} & \frac{\partial F_i}{\partial \hat{k}_1} & \frac{\partial F_i}{\partial \hat{p}_1} & \frac{\partial F_i}{\partial \hat{p}_2} & \frac{\partial F_i}{\partial \omega} & \frac{\partial F_i}{\partial \phi} & \frac{\partial F_i}{\partial \kappa} & \frac{\partial F_i}{\partial X_c} & \frac{\partial F_i}{\partial Y_c} & \frac{\partial F_i}{\partial Z_c} \\ \frac{\partial G_i}{\partial u_0} & \frac{\partial G_i}{\partial v_0} & \frac{\partial G_i}{\partial f_x} & \frac{\partial G_i}{\partial f_y} & \frac{\partial G_i}{\partial \hat{k}_1} & \frac{\partial G_i}{\partial \hat{p}_1} & \frac{\partial G_i}{\partial \hat{p}_2} & \frac{\partial G_i}{\partial \omega} & \frac{\partial G_i}{\partial \phi} & \frac{\partial G_i}{\partial \kappa} & \frac{\partial G_i}{\partial X_c} & \frac{\partial G_i}{\partial Y_c} & \frac{\partial G_i}{\partial Z_c} \end{bmatrix} \\
&= \begin{bmatrix} a_1^i & a_2^i & a_3^i & a_4^i & a_5^i & a_6^i & a_7^i & a_8^i & a_9^i & a_{10}^i & a_{11}^i & a_{12}^i & a_{13}^i \\ b_1^i & b_2^i & b_3^i & b_4^i & b_5^i & b_6^i & b_7^i & b_8^i & b_9^i & b_{10}^i & b_{11}^i & b_{12}^i & b_{13}^i \end{bmatrix}
\end{aligned} \tag{5.34}$$

The detailed expression of \mathbf{J} 's elements is given in Appendix A.2

Hence, the camera calibration is to solve the linear least-squares problem:

$$\text{minimise } \frac{1}{2} \left\| \begin{bmatrix} J_F \\ J_G \end{bmatrix}_k \cdot \mathbf{p} + \begin{bmatrix} F \\ G \end{bmatrix}_k \right\|_2^2 \tag{5.35}$$

where

$$\mathbf{p} = [\Delta u_0 \quad \Delta v_0 \quad \Delta f_x \quad \Delta f_y \quad \Delta \hat{k}_1 \quad \Delta \hat{p}_1 \quad \Delta \hat{p}_2 \quad \Delta \omega \quad \Delta \phi \quad \Delta \kappa \quad \Delta X_c \quad \Delta Y_c \quad \Delta Z_c].$$

Let

$$\begin{aligned}
\mathbf{m} &= [u_0 \quad v_0 \quad f_x \quad f_y \quad \hat{k}_1 \quad \hat{p}_1 \quad \hat{p}_2 \quad \omega \quad \phi \quad \kappa \quad X_c \quad Y_c \quad Z_c] \text{ and} \\
\mathbf{m}_{k+1} &= \mathbf{m}_k + \mathbf{p}
\end{aligned}$$

Because of the non-linearity of equation 5.31 an iterative scheme is required to approximate the solution. The subscript k in equations 5.29 and 5.35 denotes the k th iteration. The Jacobian matrix \mathbf{J} and function F and G are first evaluated at the initial value \mathbf{m}_0 , and the least-squares method is used to produce increment vector \mathbf{p} of \mathbf{m} . The new \mathbf{m} is used as the initial value for the next iteration. The iteration is terminated when the magnitude of \mathbf{p} is smaller than a pre-defined value. The steps of the iteration are illustrated in Figure 5-4.

The method to solve the linear least-squares equation 5-35 is based on the QR factorisation, which is described in Appendix A.1.

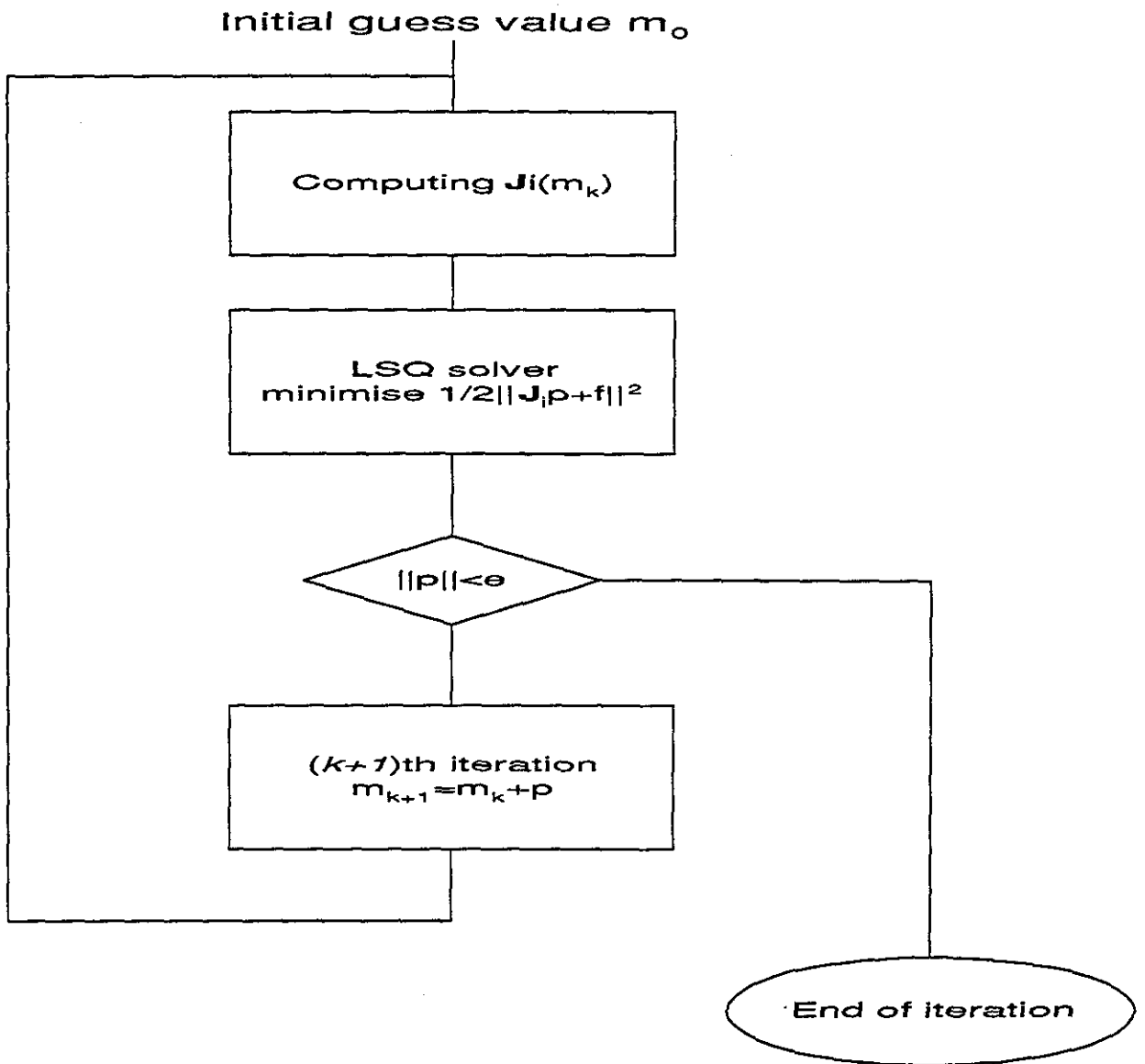


Figure 5-4. Flowchart of the non-linear optimisation method

5.4.2 Improvements of Tsai's method

The Tsai method [Tsai, 1987], reviewed in Section 5.3.3, is based on the radial alignment constraint (RAC). A coplanar condition of the object vector and the vector of its image can be maintained if the tangential distortion of lens are neglected. For non-coplanar control points, equation 5.24 is derived and the combined camera parameters $\{s_x T_y^{-1} r_{11}, s_x T_y^{-1} r_{12}, s_x T_y^{-1} r_{13}, T_y^{-1} T_x, T_y^{-1} r_{21}, T_y^{-1} r_{22}, T_y^{-1} r_{23}\}$ can be solved at the first stage. At the second stage the camera parameters $\{k_l, T_z, f\}$ are calculated by a non-linear

optimisation method. However, methods to calculate the rotation matrix, R , and parameters $\{k_I, T_z, f\}$ were not elaborated in Tsai's papers. They will be addressed in this section. Furthermore, a complete computational procedure, together with suggestions for improvement are also presented.

5.4.2.1 Calculation of rotation matrix elements

If parameters $\{s_x T_y^{-1} r_{11}, s_x T_y^{-1} r_{12}, s_x T_y^{-1} r_{13}, T_y^{-1} T_x, T_y^{-1} r_{21}, T_y^{-1} r_{22}, T_y^{-1} r_{23}\}$ are denoted as $\{a, b, c, d, e, f, g\}$ in Tsai's method, then elements $r_{11}, r_{12}, r_{13}, r_{21}, r_{22}, r_{33}$ of a rotation matrix can be calculated by solving

$$\begin{aligned} T_y^{-1} &= \sqrt{e^2 + f^2 + g^2} \\ s_x &= T_y \sqrt{a^2 + b^2 + c^2} \end{aligned} \quad (5.36)$$

and

$$\begin{aligned} r_{21} &= T_y \cdot e; \quad r_{22} = T_y \cdot f; \quad r_{23} = T_y \cdot g \\ r_{11} &= s_x^{-1} T_y \cdot a; \quad r_{12} = s_x^{-1} T_y \cdot b; \quad r_{13} = s_x^{-1} T_y \cdot c \end{aligned} \quad (5.37)$$

Elements r_{31}, r_{32}, r_{33} of the rotation matrix are calculated by the orthonormal condition:

$$\begin{vmatrix} r_{11} & r_{12} & r_{13} \\ r_{21} & r_{22} & r_{23} \\ r_{31} & r_{32} & r_{33} \end{vmatrix} = 1 \quad (5.38)$$

where $\{r_{11}, r_{12}, r_{13}\}$ and $\{r_{21}, r_{22}, r_{23}\}$ have been normalised as unit vectors according to equations 5.36 and 5.37. Therefore $\{r_{31}, r_{32}, r_{33}\}$ should satisfy:

$$\begin{aligned} r_{11} \cdot r_{31} + r_{12} \cdot r_{32} + r_{13} \cdot r_{33} &= 0 \\ r_{21} \cdot r_{31} + r_{22} \cdot r_{32} + r_{23} \cdot r_{33} &= 0 \\ A \cdot r_{31} - B \cdot r_{32} + C \cdot r_{33} &= 1 \end{aligned} \quad (5.39)$$

$$\text{where } A = \begin{vmatrix} r_{12} & r_{13} \\ r_{22} & r_{23} \end{vmatrix}, \quad B = \begin{vmatrix} r_{11} & r_{13} \\ r_{21} & r_{23} \end{vmatrix}, \quad C = \begin{vmatrix} r_{11} & r_{12} \\ r_{21} & r_{22} \end{vmatrix}.$$

Although the above linear equation is usually solvable, the orthogonal relationship of $\{r_{11}, r_{12}, r_{13}\}$ and $\{r_{21}, r_{22}, r_{23}\}$ is not guaranteed from the combined parameters $\{s_x T_y^{-1} r_{11}, s_x T_y^{-1} r_{12}, s_x T_y^{-1} r_{13}, T_y^{-1} T_x, T_y^{-1} r_{21}, T_y^{-1} r_{22}, T_y^{-1} r_{23}\}$ due to raw data or numerical computational error. The computed R is only a near orthogonal matrix, which can be further orthonormalised by [Horn, Hilden & Negahdaripour, 1988]:

$$\mathbf{R} = \mathbf{R}(\mathbf{R}^T \mathbf{R})^{-1/2} \quad (5.40)$$

5.4.2.2 Iterative solution of $\{k_l, T_z, f\}$

To estimate parameters $\{k_l, T_z, f\}$, Tsai proposed using the minimised collinearity equation (5.41) in his earlier paper:

$$y(1+k_l r^2) = f \frac{r_{21}X + r_{22}Y + r_{23}Z + T_y}{r_{31}X + r_{32}Y + r_{33}Z + T_z} \quad (5.41)$$

The iterative non-linear least-squares method can be used to tackle this equation. However, the estimated $\{k_l, T_z, f\}$ will be biased if only y projection equations are utilised in the computation. This is because: 1) there may exist different scale factors for x and y coordinate, due to the characteristics of digital cameras and frame grabbers; 2) asymmetrical noise may be distributed in x and y directions.

An improvement to this problem is to exploit both x and y collinearity equations in the optimisation process. The computation of $\{k_l, T_z, f\}$ is divided into two steps: the square sum of the y (or x) projection error is minimised; and the resultant $\{k_l, T_z, f\}$ is used as initial values for the next step. The square sum of the x (or y) projection error is then minimised. Experiments show that the improvement of the estimation value of $\{k_l, T_z, f\}$ is significant. Table 5-1 gives a computational result of $\{k_l, T_z, f\}$ from simulation data. If the projection equations are related to the pixel plane, then equivalent focal lengths f_x and f_y should be computed, and all x and y projection equations must be exploited. The computational results of f_x and f_y can be found from Table 5-1. Figure 5-5 illustrates the flowchart which shows the improvement to Tsai method.

Table 5- 1. Simulation result of iteration improvement of Tsai's method

Variables	True value	Estimated value (after the 1st iteration)	Estimated value (after the 2nd iteration)
k_l	0.000000000	0.000000001	0.000000000
T_z	1100.000	869.980	1037.558
f	-53.000	-42.348	-50.033

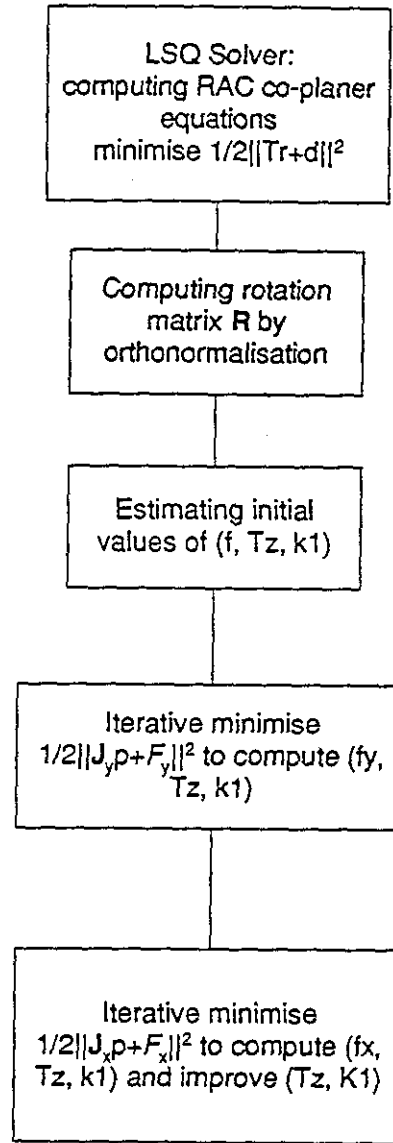


Figure 5- 5 The flowchart of the improved Tsai's method

5.4.3 Simulation tests of three calibration methods

This section presents test results of the non-linear optimisation method and Tsai's method. In order to compare two methods in the same parameter condition, the non-linear optimisation method is revised to consider the radial distortion only (RDO) camera equations, i.e. only eleven unknowns parameters (without p_1 and p_2) are estimated. For convenience, three tested methods are denoted as: 1) *the non-linear method* which deals

with thirteen camera parameters using non-linear optimisation technique; 2) *the RDO method* which deals with eleven camera parameters using the non-linear optimisation technique and 3) *Tsai's method*.

The control field to be simulated has the following geometric dimensions:

$Z = 1100 \sim 1000$ mm,

$Y = -55 \sim 55$ mm, span in vertical direction;

$X = -80 \sim 80$ mm, span in horizontal direction.

The control points are randomly generated in this control field. The relative position of the camera system and control field is illustrated in Figure 5-6. The image co-ordinates of control points are generated from the collinearity equation 5.32. The range of image co-ordinates is designed to conform to a real camera-frame grabber system which has a 768(H)x512(V) pixel sensory area.

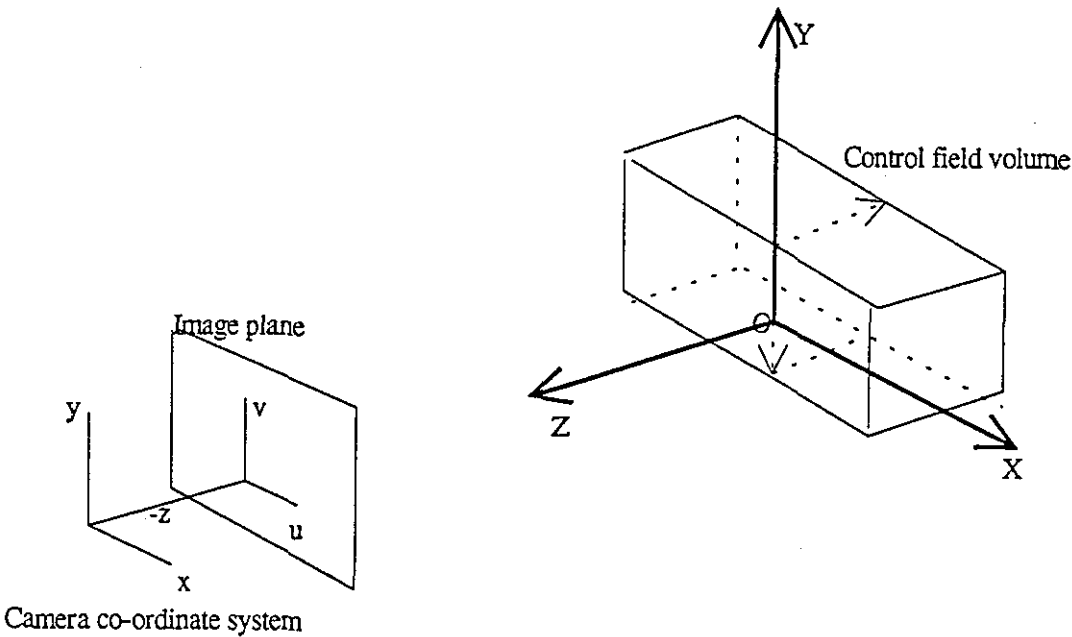


Figure 5- 6. Camera and world co-ordinate systems

Calibration methods are tested under different conditions to provide a quantitative analysis of their performance. Test results are compared on the consideration of the discrepancy of the estimated values and the true values of the unknown parameters, and the Root Mean Squares (RMS) value of the 3-D to 2-D projection error sum at the pixel plane (abbreviated as *prjerr* in below), that is

$$prjerr = \sqrt{\frac{\sum_{i=1}^N [(\hat{x}_i - x_i)^2 + (\hat{y}_i - y_i)^2]}{N}}$$

where \hat{x} and \hat{y} are the 3D-2D re-projected image co-ordinates, and x and y are the real image co-ordinates.

Three methods are evaluated as to the: 1) effect of lens distortion; 2) effect of initial value condition; 3) effect of noise level; 4) effect of noise distribution; 5) effect of control point distribution; 6) effect of camera orientation; 7) effect of object distance. In test 1) different amounts of lens distortion are simulated and their effect on the calibration methods observed. Test 2) is designed to observe the convergence of a calibration method under different initial conditions. Test 3) shows the effect of noise in image co-ordinates on a calibration method. Test 4) and 5) are designed to check random characteristics of added noise and selection of control points. In test 6) the effect of camera orientation is examined to see whether it causes ill-conditioning computational equations. Finally the effect of the thin lens formula is examined in test 7). Detailed test results and conclusions are presented in Appendix C. This section focuses on Tests 1 and 3 and discusses their significance.

5.4.3.1 Effect of lens distortion

Lens distortion induces a highly non-linear relationship into the calibration problem. This test is designed to investigate how the lens distortion affects the calculation process, in particular the parameter estimation.

The radial distortion plays a principal role in lens distortion [ASP, 1980, Tsai, 1987, Fryer, 1992]. The coefficient k_1 of the radial distortion is therefore taken as a variable in the tests. The numerical range of k_1 for the default camera model, varies from $0.1 \cdot 10^{-7}$ to $5 \cdot 10^{-7}$. When $k_1 = 2.4 \cdot 10^{-7}$ it can cause about 20 pixels distortion offset at the outer edge of

an image plane, which is severe. The tangential distortion coefficients $p1$ and $p2$, causing similar pixel offset, are about

$$p1=0.00004; p2=0.0001 \text{ (for } \delta x \text{ only)}$$

Table 5-2 shows the performance of the non-linear method under different lens distortion.

Table 5-2. Two tests of the non-linear method under different $p1, p2$

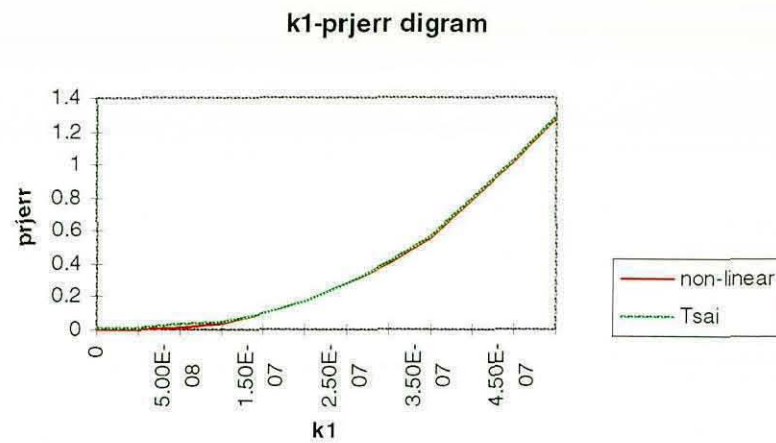
Test 1: $p1=0.00001, p2=0.00002$.

Interior parameters								
k1	prjerr	fx	fy	u0	v0	k1(est.)	p1(est.)	p2(est.)
5.00E-08	0.06289	-4239.50	-4134.52	380.021	256.510	5.3E-08	1E-05	2.03E-05
1.00E-07	0.09504	-4239.84	-4135.62	381.231	254.880	1.05E-07	1.01E-05	2.06E-05
2.00E-07	0.22462	-4243.70	-4139.20	381.754	255.560	2.17E-07	1.04E-05	2.14E-05
3.00E-07	0.44983	-4252.82	-4149.64	384.659	252.640	3.38E-07	1.16E-05	2.12E-05
Exterior parameters								
k1		omega	phi	kappa	Xc	Yc	Zc	
5.00E-08		0.000139	0.000924	-1.9E-05	-0.018	-0.021	1099.627	
1.00E-07		-0.00025	0.000655	-4E-06	-0.001	-0.025	1099.673	
2.00E-07		-0.0001	0.000589	0.000004	0.062	-0.012	1100.452	
3.00E-07		-0.00082	-2.2E-05	0.000027	0.141	0.000	1102.410	

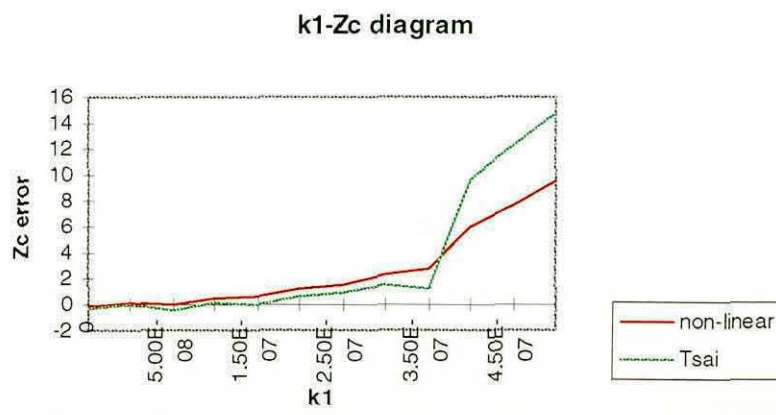
Test 2: $p1=0.00002, p2=0.00001$

Interior parameters								
k1	prjerr	fx	fy	u0	v0	k1(est.)	p1(est.)	p2(est.)
5.00E-08	0.1054	-4245.20	-4140.48	377.888	255.064	5.6E-08	2.02E-05	1.01E-05
1.00E-07	0.1616	-4249.36	-4143.89	376.944	255.779	1.09E-07	2.03E-05	1.03E-05
2.00E-07	0.3407	-4257.07	-4153.24	381.037	255.226	2.22E-07	2.15E-05	1.04E-05
3.00E-07	0.5790	-4263.05	-4164.46	393.027	251.715	3.44E-07	2.62E-05	9.51E-06
Exterior parameters								
k1		omega	phi	kappa	Xc	Yc	Zc	
5.00E-08		-0.0002	0.0015	0.0000	0.032	0.023	1100.648	
1.00E-07		-0.0001	0.0017	0.0000	0.077	0.024	1101.504	
2.00E-07		-0.0002	0.0009	0.0000	0.188	0.024	1103.838	
3.00E-07		-0.0011	-0.0018	0.0000	0.327	0.025	1106.724	

The prjerr and discrepancies of parameter Zc , ω and $k1$ for the RDO method and Tsai's method are shown in Figure 5-7.

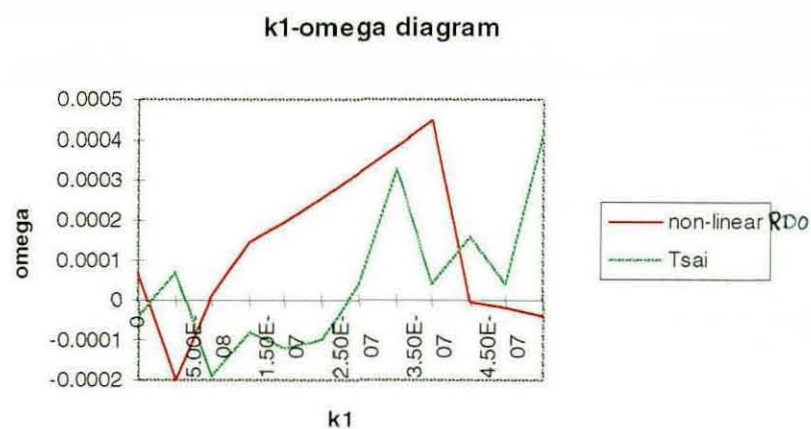


(a)

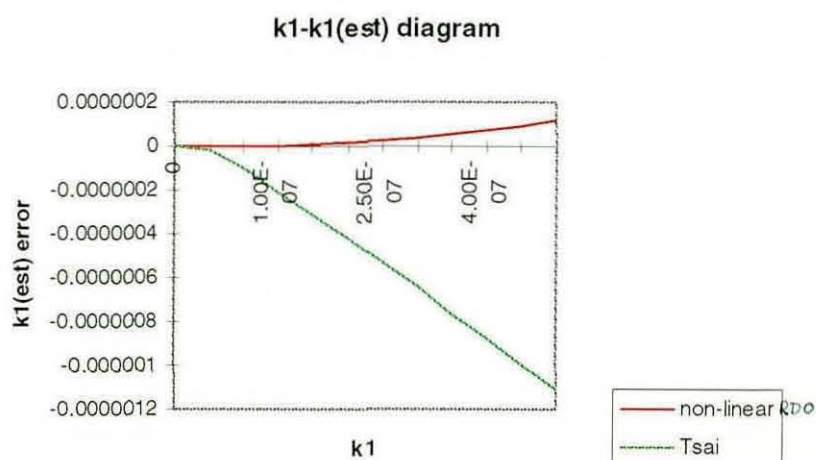


(b)

Figure 5-7. Projection error and estimated parameter error in the RDO method and Tsai's method with different lens distortion coefficients k_1 : a) $prjerr$ curve; b) Z_c error;



(c)



(d)

Figure 5-7. Projection error and estimated parameter error in the RDO method and Tsai's method with different lens distortion coefficients k_1 : c) ω error; d) k_1 error

These tests show that:

- 1) these three methods demonstrate similar performance with noise-free test data, according to the RMS residuals and estimated parameter values;
- 2) increasing k_1 always causes an over-estimated k_1 and object distance Z_c ;
- 3) increasing k_1 always causes a greater projection error because of greater parameter discrepancies.

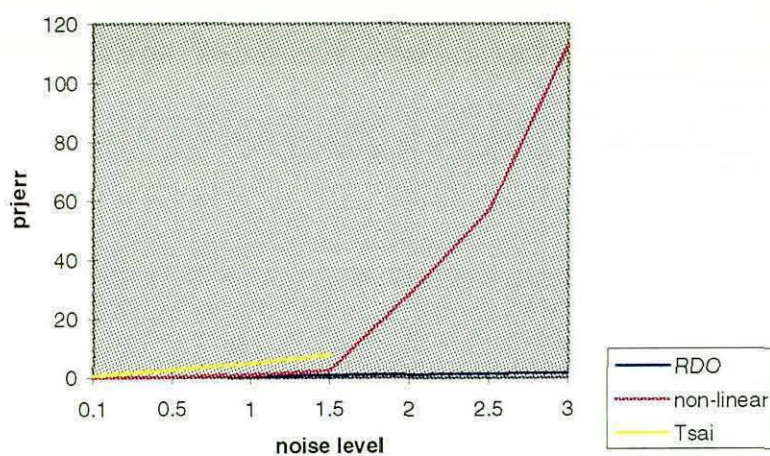
5.4.3.2 Effect of noise level

Camera systems usually suffer from forms of noise which are difficult to model, such as thermal, electronic fluctuation in the camera-frame grabber systems, and image processing error. The net effect of these error sources could be equivalent to observation error of image co-ordinates. In this test, a $[0, 1]$ uniform distribution random noise is added to image co-ordinates, the magnitude of noise is pre-multiplied by a noise level which varies from 0.1 to 3 pixels. Three methods are tested under these noise conditions. The results are shown into Figure 5-8.

It can be concluded from these test results:

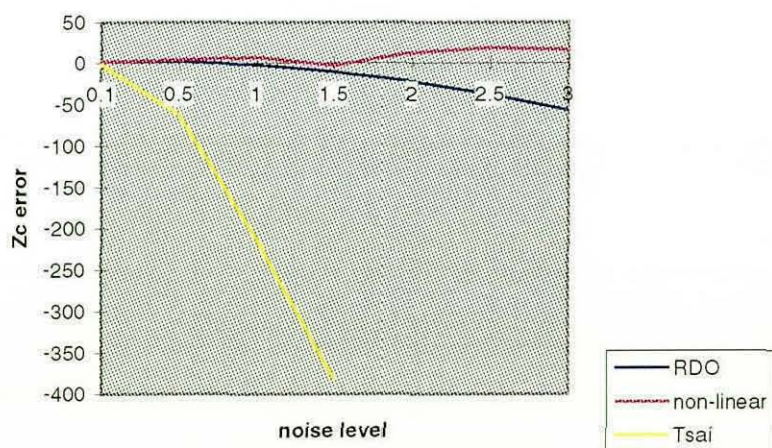
- 1) Noise causes deterioration of parameter estimation in all three methods. The most significantly affected parameters in the non-linear optimisation method are the principal point position (u_0, v_0) and Z_c (Note: the variations of f_x, f_y are associated with Z_c 's variation). For Tsai's method, the most affected parameter is Z_c because the principal point position is fixed.
- 2) The non-linear method is obviously superior to Tsai's method with respect to the RMS error and discrepancy of estimated parameters. When the noise level is bigger than 1.5 pixels, Tsai's method is not applicable.
- 3) The RDO method is the best of the three methods. It provides a robust estimation and small projection error in a large noise range.

noise-prjerr curves



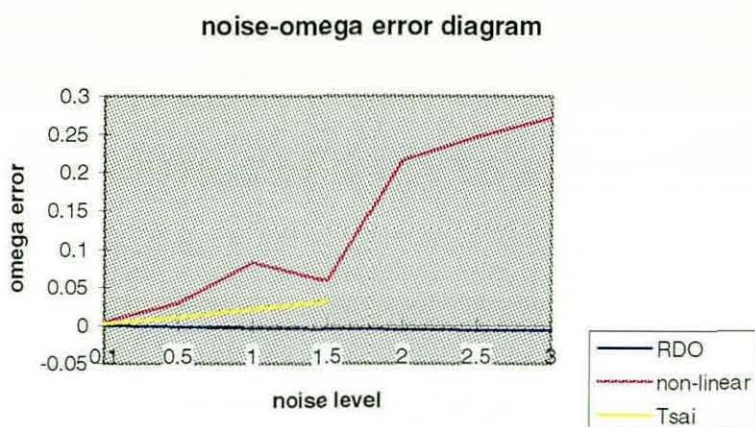
(a)

noise-Zc error diagram

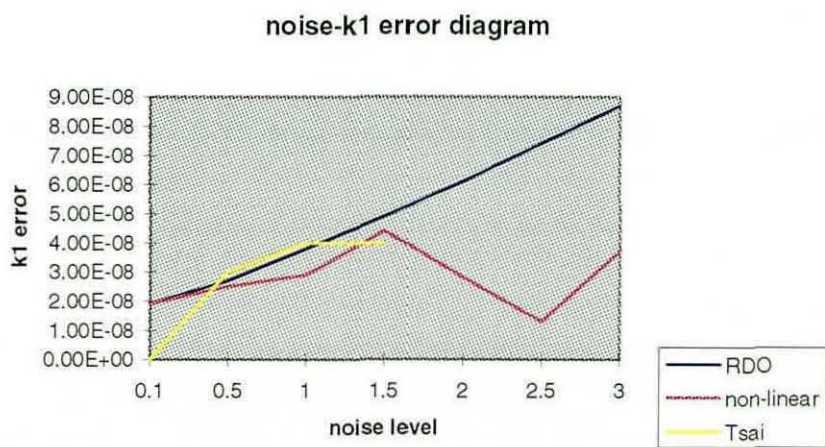


(b)

Figure 5-8. Effect of noise level for three methods: a) prjerr curve; b) Zc error;



(c)



(d)

Figure 5-8. Effect of noise level for three methods: c) ω error; d) k_1 error

5.4.4 Discussions

Extensive simulations of camera calibration show that all three methods have satisfactory performance in a noise-free environment. However, the situation becomes complicated if noise exists. Noise in observation data causes deterioration in the performance of the three methods. The non-linear method is sensitive to noise because it contains more non-linear links between the unknowns. Tsai's method does not work if a large amount of noise exists. This may be caused from the separation of interior and exterior parameter estimations. Because the camera orientation (the rotation matrix) is estimated independently, estimate errors of these parameters are propagated to the second stage of interior parameter estimation without optimisation. The RDO method is the most robust method in a noise environment due to its compromise strategy.

Three methods will be examined in a practical camera set-up in the next section. Their error effect for a 3-D measurement task will be analysed in the next chapter.

5.5 *Practical calibration of a digital camera system*

The literature review and simulation tests revealed that certain non-linear links exist between the camera interior and exterior parameters. These links could lead to incorrect estimation for camera parameters. Some noise conditions could cause the estimated value of a camera parameter to drift significantly from its true value. Moreover, many factors of distortion in a real system have not been included in the calibration equation. Laboratory-based calibration methods are usually used to acquire *a priori* knowledge of some camera parameters, in order to achieve a highly accurate calibration result. This section introduces some physical methods to calibrate the digital cameras and the application of analytical methods to two digital camera systems.

5.5.1 Camera system

The digital camera system to be calibrated in this section consists of a digital camera and Data Translation®'s Vision-EZ™ frame grabber. The camera is equipped with a Fujinon f50mm 1:1.4 lens. Two types of camera are tested in this configuration: a Panasonic's WV-

1550 Newvicon® camera and a PULNiX TM500 CCD camera. The WV-1550 Newvicon® camera employs a 2/3" (8.8 mm x 6.6 mm) static focus Newvicon® pick-up tube as the image sensor. The output signal of the Newvicon® camera is in CCIR format with 625 lines/25 frames scanning frequency. The horizontal central resolution is 650 lines. The TM500 employs a 1/2" (6.4 mm x 4.8 mm) CCD array as the image sensor. Its density of pixel array is 580(H)x500(V) and its central resolution is 450 lines. The frame grabber digitises the video signal and stores it into a 768x512x8bit frame buffer. An image from the frame grabber is displayed using square-pixels with a 1:1 pixel aspect ratio. Because of these system features, only the combination of focal length of the lens and scale factors of frame-grabber can be calibrated. The interior parameters of the camera system are defined as: a) image centre (u_0, v_0); b) effective focal length f_x and f_y which are products of focal length and x, y scale factors respectively; c) coefficients of lens distortion (k_1, p_1, p_2).

Mounted with the same Fujinon lens, the TM500 CCD camera has a smaller field of view than the WV-1550 TV camera because of its smaller sensor area. Even so the spatial resolution of TM500 is not much greater than the WV-1550. This can be verified as follows. Assuming an object distance at 1 metre and fixed f-stop, fields of view of the two camera systems in X direction are:

$$FOV_{CCD} = \frac{6.4mm \times 1000mm}{50mm} = 128mm$$

and

$$FOV_{TV} = \frac{8.8mm \times 1000mm}{50mm} = 176mm$$

Their resultant spatial resolutions are:

$$Res_{CCD} = \frac{128mm}{450pixel} = 0.284mm / pixel$$

$$Res_{TV} = \frac{176mm}{650pixel} = 0.271mm / pixel$$

Although both cameras claim low lux performance (WV-1550 requires minimum illumination 0.3 lux, and TM500 0.2 lux), the TM500 shows greater versatility on the illumination characteristics. This was tested under specific illumination conditions in which the WV-1550 only allowed three stops of aperture to acquire a clear image, but, in comparison, the TM500 allowed a seven stop range to acquire the same quality of image.

This was further tested in a very weakly illuminated environment in which the image captured in the WV-1550 was nearly dark at f1.4 stop, however the TM500 got visible details of the object using even f2 stop.

The TM500 camera has a wider adaptability of illumination condition, but the sharpness and resolution of its image are not as good as of the WV-1550. The TM500 also has serious line 'alias' effects, which may be caused by CCD sensory array.

5.5.2 Stability test of frame grabber, Newvicon® and CCD cameras

The pixel stability is essential to ensure measurement accuracy. A digital camera system with electronic circuits suffers from the influence of thermal and electrical fluctuations. These fluctuations may result in the acquired pixel co-ordination of a point being unstable. Shortis[1988] reported that the warm-up stage of a CCD camera took about one hour or more. The test reported in this section aims to evaluate the pixel drift caused in the frame grabber and digital camera system.

The field of control object and image capturing:

The control object consisted of an array of Light Emitting Diode (LED) spots. The LEDs were mounted on the back of synthetic resin banded fabric board (TUFNEL) with the front painted matt black. Each LED position was a 0.8 mm diameter drilled hole. Figure 5-9 shows the LED array. The control field has about three metres away from the camera.

The LED array image was captured by the camera and digitised into the frame grabber. The pixels representing a LED spot were separated by an aggregation and discrimination method and the image co-ordinates of each LED spot were acquired by centroid at sub-pixel accuracy. The pixel drift was investigated by observing the drift of each spot centre. In such a process the stability of the camera and frame grabber was not distinguishable, because the pixel drift in a captured image was always caused by combination of the camera and frame grabber fluctuations. Fortunately, the warm-up effects were the main source of errors in the CCD camera and the frame grabber. They could be separated by turning on one device prior to the other.

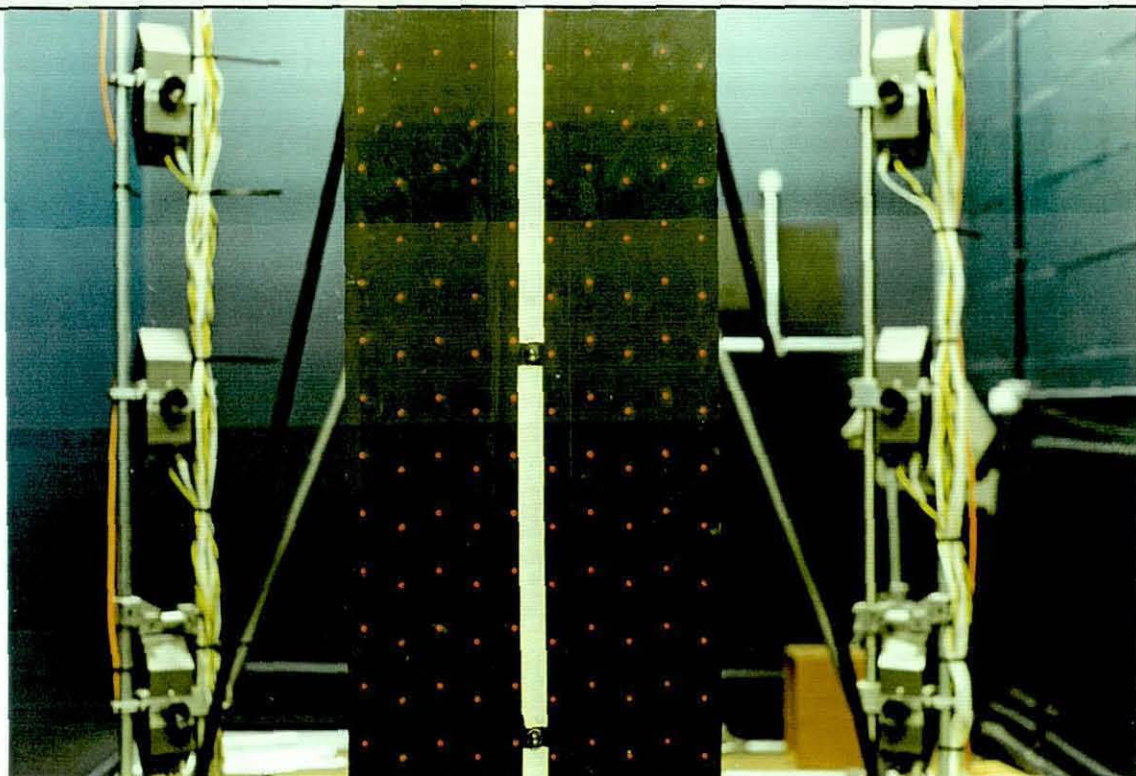


Figure 5-9. Photograph of LED calibrator

Stability test of the frame grabber:

To test the stability of the frame grabber, the TM500 CCD camera was employed because it was relatively more stable than a Newvicon® camera. The TM500 was switched on two hours prior to turning on the frame grabber. After turning on the frame grabber, images of the LED array were taken at the 5th, 10th, 15th, 20th, 25th, 30th, 45th 60th, 90th minute, and the fluctuation of LED spot co-ordinates analysed. Table 5-3a shows the results of pixel fluctuation which contain x-mean, y-mean, x-variance, y-variance, x-standard deviation, y-standard deviation, maximum error in x and maximum error in y of nine object points. Figure 5-10a shows the fluctuation of co-ordinates from the mean with time.

Similarly, the stability of cameras was tested by turning on the frame grabber two hours prior to turning on the camera. Images of the LED array were then taken over a one and a half hour time span. Tables 5-3b and 5-3c list the results of pixel drift for the CCD camera and the Newvicon® camera respectively. Figures 5-10b and 5-10c show the corresponding pixel fluctuations.

The test result shows that the Newvicon® camera had an x pixel drift ten times greater than that of the CCD camera. Moreover, the x pixel drift of the Newvicon®

camera was not alleviated after the warm-up stage. While the frame grabber and the CCD camera showed a small pixel drift after the warm-up period. The y pixel drift had a similar pattern and magnitude for both cameras.

Table 5-3. Pixel Stability statistics

a) Pixel stability of Frame-grabber

x-mean	y-mean	x-var	y-var	x-std	y-std	x-max	y--max
112.702	172.841	0.001	0.004	0.031	0.063	0.058	0.111
19.504	261.276	0	0.002	0.013	0.044	0.036	0.126
238.5	171.5	0	0	0	0	0	0
145.15	259.46	0	0	0	0	0	0
364.651	169.567	0.005	0.006	0.071	0.076	0.151	0.143
270.701	257.636	0.006	0.003	0.079	0.057	0.119	0.114
490.4	167.6	0	0	0	0	0	0
397.08	255.728	0.032	0.011	0.18	0.106	0.42	0.228
116.5	346.29	0	0	0	0	0	0

b). Pixel stability of CCD camera

x-mean	y-mean	x-var	y-var	x-std	y-std	x-max	y--max
112.63	172.961	0.008	0.042	0.09	0.206	0.13	0.539
19.492	261.284	0.001	0.005	0.036	0.068	0.092	0.154
238.39	171.591	0.015	0.089	0.123	0.298	0.18	0.769
144.968	259.473	0.026	0.002	0.162	0.04	0.258	0.097
364.432	169.702	0.005	0.054	0.073	0.231	0.142	0.588
270.509	257.806	0	0.037	0.018	0.192	0.031	0.484
490.213	167.81	0.02	0.013	0.142	0.113	0.213	0.26
396.604	255.693	0.002	0.072	0.04	0.268	0.104	0.707
116.482	346.226	0.001	0.03	0.033	0.173	0.082	0.274
23.35	434.238	0.008	0.034	0.09	0.183	0.15	0.382

c) Pixel Stability of Newvicon® camera

x-mean	y-mean	x-var	y-var	x-std	y-std	x-max	y--max
154.502	231.951	0.187	0.126	0.433	0.355	0.788	1.141
177.951	295.939	0.135	0.029	0.368	0.17	0.881	0.539
249.973	233.445	0.496	0.097	0.704	0.312	1.093	1.025
273.305	297.179	0.802	0.071	0.895	0.267	1.305	0.449
345.575	234.567	2.118	0.165	1.455	0.406	2.435	1.337
368.897	298.587	2.862	0.054	1.692	0.232	2.847	0.587
440.989	235.594	5.172	0.136	2.274	0.369	3.749	0.974
464.138	299.291	6.331	0.107	2.516	0.326	4.088	0.549
155.291	359.409	0.133	0.036	0.364	0.191	0.791	0.409
179.33	424.095	0.125	0.142	0.353	0.377	0.73	0.635

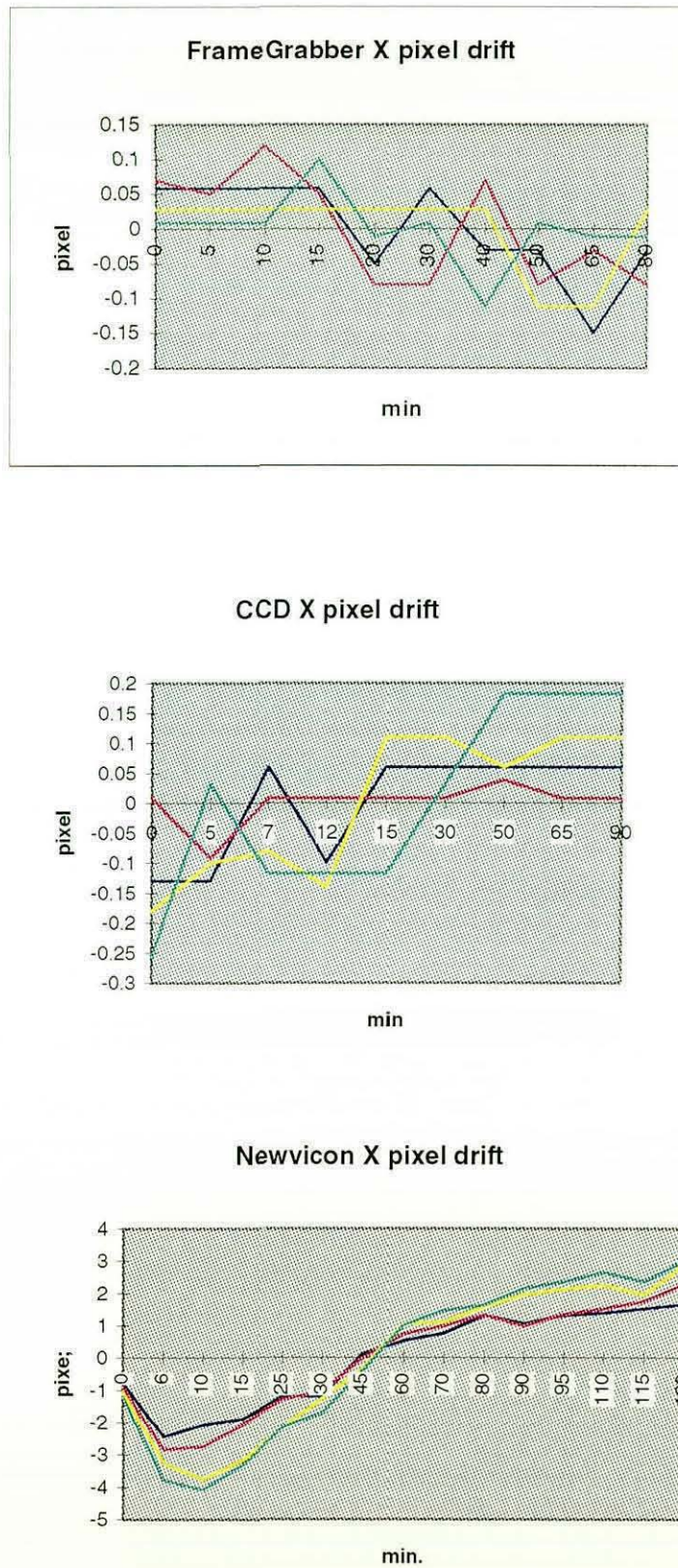


Figure 5- 10. a). *Frame Grabber pixel fluctuation curve*; b) *CCD camera X pixel fluctuation curve*;
c) *Newvicon® camera X pixel fluctuation curve*

5.5.3 Physical calibration of image centre

a) Design of a test bench and control field

A test bench was designed to provide accurate control of the object field for camera calibration. The bench consisted of two parallel steel bars which formed a base unit, a camera base which contained two micrometer drives to adjust the elevation and pan angles of the camera, a 2-D linear translation stage with a 25 mm translating range in the x and y directions, and a z direction translation platform which supported the 2-D translation stage. The Z translation platform had four wheels which provided linear tracking along a steel slide rail and a translation range of 200 mm over 1000 mm distance. A stop pin on the steel rail was used for a reference point in the z direction.

The control field could comprise a 2-D planar graphic such as lines, a grid or circles. The 2-D plane graphic is mounted on the translation stage and its depth can be changed by translation of the platform. Accurate z positioning is achieved by moving the translation platform a fixed distance from the stop pin using length gauges.

b) Auto-collimating method

The Auto-collimating method [Curry *et al.*, 1986; Tsai, 1987] is employed to find the image centre (principal point). A laser beam generator is installed on the translation stage of the test bench. By adjusting the translation stage, the laser beam is roughly aligned to the camera centre (*Notes: a) using the smallest iris stop, $f/22$, to allow the laser beam to pass through the centre of the aperture; b) avoiding the laser beam directly hitting the Newvicon® tube by placing a blind paper between the tube and the camera lens. For a CCD array there is no harm from the laser beam.*). The complete alignment of the laser beam and the camera optical axis is achieved by adjusting the rotation angles (pan and elevation) together with the laser beam positions (X and Y), until the reflective laser beam from the camera lens glass is returned along the path of the incident beam. The alignment precision is estimated at 0.5 degrees which is decided by two factors: the diameter of a laser beam and the observable reflective beam. The diameter of the laser beam is about 1~2 mm and the reflective beam is observed at a distance of 40 ~ 60 mm from the camera lens. This provides a precision of at least $1/60$ radian. A higher precision can be achieved with assistance from micrometers. After alignment, the image of the laser beam is captured by

placing a black paper, which has a very tiny pinhole, over the laser beam generator. The image centre is measured from the pixel position of the laser beam. Measured image centres are:

the CCD camera at (351, 252);

the Newvicon® camera at (353, 246).

It is necessary to point out that the measured image centre contains some errors:

- 1) the pinhole may not be located exactly at the central axis of the incident ray due to the focus method of the laser beam;
- 2) sticking the paper to the laser could cause a slight offset of the laser beam from its original position.

Resultant image centre from these error sources may vary by up to 10~20 pixels.

5.5.4 Analytical calibration of the digital camera system

The non-linear method, the RDO method and Tsai's method are applied to calibrate the CCD camera-Frame Grabber system and the Newvicon® camera-Frame Grabber system respectively. The exterior orientation of the camera system is known: the CCD camera at (140 ± 5 mm, 5 ± 3 mm, 1200-50 mm), and the Newvicon® camera at (4 ± 2 mm, 0 ± 1 mm, 1150-50 mm). Calibration results are listed in Table 5-4. Table 5-4a shows that all three methods work very well on the CCD camera. They produced small RMS errors and consistent estimated values of the camera parameters. The calibration results of the Newvicon camera presented in Table 5-4b show that the estimated exterior parameters are acceptable according to the practical set-up, and the estimated distortion coefficient k_1 is consistent with the observation to distortion characteristics of the camera. Results of interior parameters from the non-linear method are not compatible with the RDO method and Tsai's method for the Newvicon® camera.

Table 5-4. Practical calibration of camera systems

a) CCD camera - Frame Grabber system (the camera is at the right side of z-axis)

Parameters of camera-frame grabber system	Complete non-linear method	Radial distortion only (RDO) non-linear method	Tsai's method
u0	429.433	324.369	351*
v0	206.086	313.516	252*
fx	6513.310	6521.473	6514.463
fy	6268.892	6276.941	6177.539
k1	0.000000014	0.000000019	0.000000011
p1	0.00000106	n/a	n/a
p2	-0.00000134	n/a	n/a
ω	0.00995	-0.00734	0.000374
ϕ	0.1567	0.14057	0.14762
κ	0.00216	0.00475	0.00319
Xc	-146.643	-146.740	-147.554
Yc	-3.560	-3.599	-2.957
Zc	-1170.395	-1170.722	-1153.307
prjerr	0.32139	0.33534	4.5068

* assigned image centre

b) Newvicon® camera - Frame Grabber system

Parameters of camera-frame grabber system	Complete non-linear method	Radial distortion only (RDO) non-linear method	Tsai's method
u0	-674.325	335.689	353*
v0	285.037	281.638	246*
fx	-3475.465	-4467.045	-4186.044
fy	-4173.002	-4445.145	-4271.444
k1	0.000000058	0.0000001	0.000000087
p1	-0.0000547	n/a	n/a
p2	0.00000726	n/a	n/a
ω	0.00356	0.00614	-0.00068
ϕ	0.2636	0.01401	0.00957
κ	0.01329	0.01476	0.00695
Xc	3.378	5.060	4.555
Yc	-0.396	-1.135	-2.566
Zc	-1079.476	-1046.121	-1005.186
prjerr	31.25	1.421	5.32687

* assigned image centre

Conclusions are drawn from the analysis reasoned in this section:

1) The non-linear method may produce poor estimation results despite the small residual error as shown in Table 5-6a. The method is unstable for the Newvicon® camera, because of its severe distortion. This method should not be used in a complete unknown environment in the first instance. Instead the RDO method is preferred for its robust characteristics.

2) Tsai's method shows consistency with the RDO method, even with the Newvicon® camera data.

3) The RDO method is the most reliable because its estimated results are close to the actual camera system, and the RMS errors are reasonably small.

4) The Newvicon® camera has more severe distortion than the CCD camera according to the estimated distortion coefficient, k_1 , and the projection error.

5) The estimate of exterior parameters is relatively stable. The estimate of interior parameters shows significant differences, even for the same CCD camera. The major reasons could be three non-linear linked relationships between parameter pairs ($u_0 \sim \kappa$), ($v_0 \sim \omega$) and ($f_x, f_y \sim Z_c$).

5.5.5 Discussions

Physical and analytical calibration shows that the Newvicon® TV camera suffers from serious electronic fluctuation and image distortion, and therefore is not suitable for high precision machine vision tasks, particularly if individual pixel co-ordinates are required. It could be used in a controlled environment such as the 3D scanner in which the absolute orientation of the camera station is not critical to the calibration process, and the necessary warm-up time could be taken into account. The Newvicon® camera has an obvious fluctuation effect which cannot be overcome with a warm-up stage. Whenever it is possible, repeatedly taking an image several times and averaging them is an effective method for reducing the instability of the image pixels.

The CCD camera is superior to the Newvicon® TV camera in stability and low level illumination range, but not good in sharpness. Its alias problem could cause difficulty in the feature extraction process.

The RDO method and Tsai's method show general suitability to the CCD camera - Frame Grabber system. But for Tsai's method it is necessary to acquire an *a priori* image centre.

5.6 Summary

This chapter has discussed calibration methods for digital camera systems. A camera model which contains lens distortion was introduced. The calibration methods for digital camera systems have been reviewed in three categories, namely calibration for interior parameters, calibration for exterior parameters, and hybrid calibration methods for interior and exterior parameters. The methods in the last category are frequently used in close range measurement applications. Therefore an extensive evaluation is given to two types of hybrid calibration methods, namely: the non-linear optimisation method and Tsai's method. The non-linear optimisation method for thirteen unknown parameter of a digital camera system was derived. Tsai's method is improved in computation of orthonormal matrix and optimal search of parameters. These methods were evaluated from different parameter conditions and noise conditions. The experimentation showed that the non-linear optimisation method to consider radial lens distortion only (RDO method) delivers the best results overall, although in noise-free situations all methods give very good estimation results. Finally the practical and analytical calibration of two digital camera - frame grabber systems were presented.

CHAPTER SIX

3-D MEASUREMENT TASK-II: LOCATING FEATURE POINTS IN 3-D SCANNED SURFACE DATA

Acquiring co-ordinates of anthropometric feature points from the human body surface is an essential function in 3D surface anthropometry, as discussed in Chapter 2. This chapter discusses the requirements and methods for locating feature points from 3-D scanned data, and describes the implementation of a method for the LASS system. The error of the location algorithm is analysed. Surface trimming of the raw scanned data, which is a direct application of the method, is introduced.

6.1 *Location of feature points in 3D surface anthropometry*

Chapter 2 identified two types of methods to locate anthropometric feature points. They are the geometric reasoning method, based on surface analysis (curvature, normal or continuity, etc.), and the artificial marking method. The geometric reasoning method, although it is an automatic method, has limited application in dealing with the human body surface, because many anatomical feature points cannot be identified from the surface geometry of a body. Artificial marking or the operator's observation are normally required to locate the anatomical landmarks. Ferrario *et al.* [1995] discussed a method in which a number of reflective marks were stuck on 16 landmarks of the subject's face and those marks were measured by infrared photogrammetry. An alternative method used by Vannier *et al.* [1991, 1993] relied on interactive mouse operation to pick feature points from 3-D scanned data.

The existing measurement methods of artificial marks can be roughly grouped into two types: direct co-ordinate measurement without relation to 3-D surface scanned data; and co-ordinate measurement from 3-D surface scanned data. Examples of the first group of methods are: stereophotogrammetry, and 3-D co-ordinate measurement machine. Because these methods are not related to 3-D scanned data, they are less valuable for a 3-D surface anthropometric task.

The second group of methods can be further divided into texture-based or density-based. The texture-based methods identify the artificial marks from an image (RGB or grey-scale) of an object surface and acquire their 3-D co-ordinates by mapping the image onto

corresponding 3-D scanned data. This has been a practical method with some colour scanners (for example, Cyberware 3030RGB/PS). The density-based methods exploit the high resolution of a scanner and identify the feature marks according to their geometric feature. These two kinds of methods require a fairly high resolution (say: 2 mm X 2 mm) of the scanner, which is difficult to achieve for a whole body scanner. For example, the LASS system has the worst data resolution, 5 mm X 10 mm at its maximum object radius 300 mm. Cyberware's whole body scanner has a resolution 2 mm X 5 mm (VxH) [Cyberware, 1996].

A texture-based method was explored by Bhatia *et al.* [1992] which automatically identifies cross marks on a scanned body surface. Their method combined digital image processing and optimal estimation to deal with multisensor scanning data. 3-D co-ordinates of a fiducial point were acquired from a spatial intersection of multiple rays. Ko *et al.* [1994] applied both a texture-based method and a surface analysis method to recognise the feature points from a scanned face. In this work, image data were used to extract feature points of small size, for example, the eyes, and surface analysis was used to identify outstanding feature area, e.g. the nose.

According to this discussion, general approaches to enhancing a surface scanning system to capture and locate anthropometric or artificial marks include:

- 1) making the scanner head capable of capturing colour/grey-scale image;
- 2) making the scanner achieve a higher resolution;
- 3) making the scanner head (camera unit) have stereo vision capability;

A practical implementation must take the available hardware condition into account, particularly when an established scanner is to be modified. The following section will explore the feasible methods of modification to the LASS system.

6.2 Modifying LASS system to capture grey-scale image

6.2.1 Structure and principle of the LASS system

The LASS system, as a whole body surface scanner, has four major technical features, namely

- 1) it adopts multi-cameras to cover the whole human body to 2.1 metres high, a total of 14 cameras are used on two camera columns;
- 2) it projects four vertical stripes of light onto a body surface;

- 3) it uses a threshold comparator to detect (digitise) the edge of projected light strips, instead of capturing the grey-level image; and
- 4) it scans a subject by rotating the turntable 360 degrees to produce 150 vertical profiles of the subject.

The block diagram of the LASS system is shown in Figure 6-1.

Using seven TV cameras (CCIR non-interlaced format, 312.5 lines/per field) in a column, LASS can cover 2.1 metres in height with 1 mm resolution. When a projected light stripe is shed on a body, the body image is split into a bright side and a shaded side. The threshold comparator and digital counter return a digitised distance from the shadow edge to the central axis of the turntable. The data resolution in a radial direction is about 1.3 mm according to the current angle set-up of the projectors. However, the data acquisition software reduced the resolution of the vertical data to 5 mm. The data resolution in a tangential direction of a horizontal slice (cross-section) is a variable of the radius. In the worst situation (maximum object radius 300 mm), the data resolution is $300 \text{ (mm)} \times 0.042 \text{ (radian)} \approx 12.6 \text{ (mm)}$ because the minimum rotation step is 0.04187 radian.

LASS has 150 rotation steps for a complete 360° scan. For each step, the data collection time is 14/25 second (14 cameras in serial operation, 25 frame/per second for each camera). This results in the minimum scanning time being about 1.5 minute for 150 steps without taking rotation and acceleration/deceleration time of the turntable into account.

6.2.2 Comparison and selection of modification methods

It is clear that the original LASS system structure is not able to measure the coordinates of individual feature points because these points are not identifiable from 3-D scanned data. Some modification is necessary. The LASS system may be modified in three ways considering its structure feature:

- 1) an auxiliary camera may be added for stereo vision;
- 2) grey-scale image may be captured with existing cameras or an additional camera;
- or
- 3) data density may be increased in height and angle dimensions.

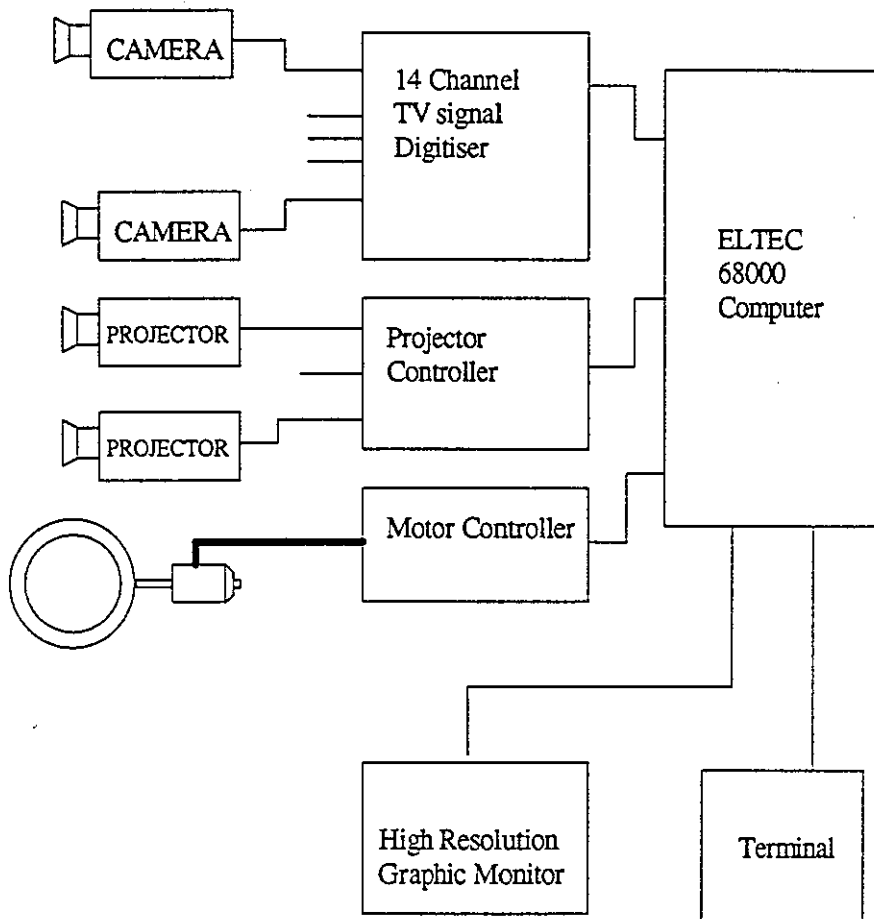


Figure 6- 1. Block diagram of the LASS system.

Requirements, advantages, and disadvantages of these options are discussed as follows:

Option I: Stereo vision method

To implement a stereo vision ability in the LASS, it requires

- one or two additional cameras to constitute a stereoscopic camera pair;
- (minimum) a frame grabber system plus a multi-channel adapter to allow two cameras to capture a grey-scale image.

- a precise camera calibration procedure to obtain the positions and orientations of stereoscopic cameras;
- a program to correspond the feature points in two (left and right camera) images;
- a program to match the co-ordinates of a feature point with 3-D scanned data.

Advantages:

- it provides an independent stereo vision system to the scanning operation.
- it necessitates no radial change to the original system.

Disadvantages:

- separate image capturing and scanning operation results in mismatch error between feature points and surface data due to body sway;
- longer measurement time (taking images and scanning sequentially) makes the measurement result less reliable;
- it is limited to existing mechanical structure, a short distance (baseline) between two cameras could produce insufficient measurement accuracy.

Option II: Grey-scale image capture -I

If the existing camera of the LASS is used to capture a grey-scale image by additional image input hardware, it requires:

- a frame grabber system for image input;
- a relevant camera calibration procedure
- a program to map grey-scale image to 3D scanned surface.

Advantages:

- it provides a simpler image capture system compared with stereo vision method.
- it requires no change to the original system.

Disadvantages:

- Separate image capture and scanning operation results in mismatch error between feature points and surface data due to body sway;
- longer measurement time (taking image and scanning sequentially) makes the measurement result less reliable;

Option III: Grey-scale image capture -II

If an additional or existing camera is used to capture a grey-scale image of the scanned object synchronous to the scanning process, it requires:

- a special frame grabber to acquire grey-scale image aligned with the edge of projected light or a modification of the existing hardware to register grey-scale and edge information simultaneously;
- special mechanical structure for alignment and calibration of the additional camera;
- new software for control and data processing of the new hardware function.

Advantages:

- simultaneous grey-scale image and surface range capture can deliver a consistent surface data and avoid data mismatch caused by body sway;
- it simplifies data correspondence calculation for end-user.

Disadvantages:

- redesign of partial hardware and software of the LASS system.
- the new structure does not improve the resolution of the data capture, therefore it does not guarantee that every feature point is captured during the scanning.

Option IV: Increasing the resolution of the system

Increasing the system resolution is another option to improve the recognition ability of feature points, but it relies on physical marks and is not able to identify print marks. For the LASS system this requires

- output data at 1 mm space in height dimension in order to fully exploit camera resolution.
- more scanning steps (for example, if the rotation step are increased to 450 steps then a 2.7 mm by 2 mm physical mark at 200 mm radius of an object could be detectable).
- precise system calibration and a camera performance test to eliminate camera and system error.

Advantages:

- it provides a unified and unambiguous data output.

Disadvantages:

- longer scanning time is needed because of more rotation steps, this could not be permissible due to body sway.
- modifications to original hardware and software are needed to capture data, control rotation motor and reduce scanning time.
- a huge amount of the scanned data will cause problem for the existing computer system.
- it is necessary to adopt cameras with high precision and high stability to replace existing cameras.

Although the best modification is a combination of option III and IV, a feasible modification based on the above discussion is option II because it is simple and economic. Option II requires minimum modification to the existing hardware and software of the LASS system. Additional hardware and software can stand alone, therefore is of the least risk. It can meet project time and budget constraint.

To implement this modification, an auxiliary frame grabber (Data Translation's Vision-EZ board) has been selected for image capture, and a 486-Personal Computer (Dell Optiplex 466/MX) is used to interface with the frame grabber and store grey-scale images. The frame grabber is connected with one of the existing cameras in the LASS system. Image capture is operated before or after surface scanning. Using the existing camera has the advantage of avoidance of extra camera calibration work. The system block diagram is shown in Figure 6-2.

6.3 Ray-tracing method to map 2D points to 3D surface

This section discusses a *direct mapping* method to relate the 2-D image of an object to its 3-D scanned data. The mapping method is based on the principle of projective geometry. It needs to know:

- the location and orientation of a view point from which the 2D image is taken;
- the equation of the 3D surface (analytical or numerical).

This section focuses on the geometric relationship of the mapping method, i.e. 2-D image co-ordinates of a point and its 3-D co-ordinates.

6.3.1 Basic ray-projection equation and ray-tracing method

The direct mapping method contains two tasks: labelling feature points in the 2-D image plane and computing their 3-D co-ordinates. This section will concentrate on the

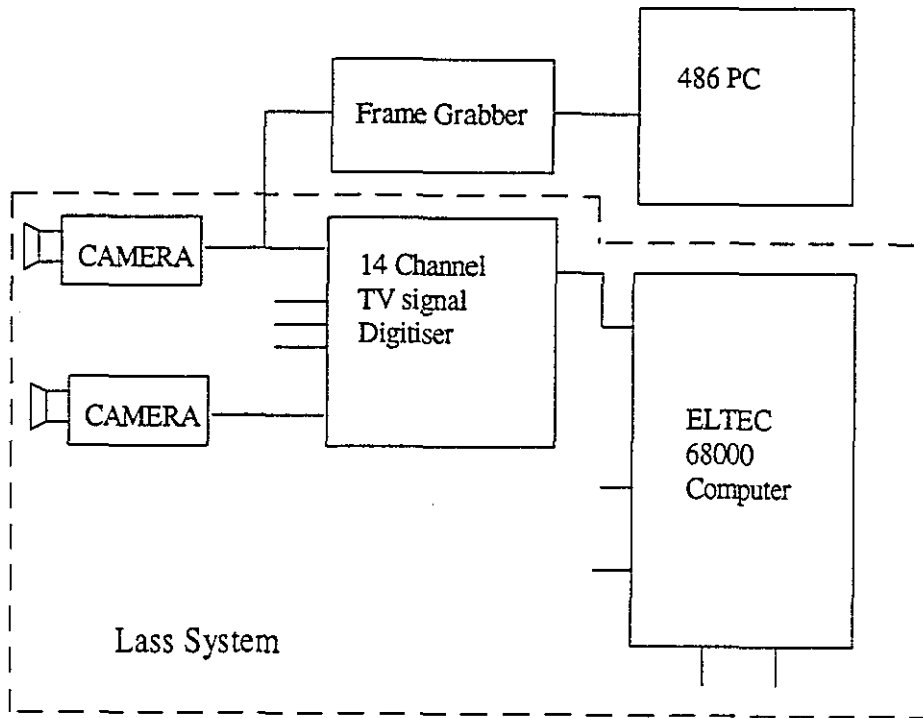


Figure 6- 2. An additional imaging system to the LASS.

latter since the former is performed by a manual operation on an interactive graphics interface.

6.3.1.1 Introduction of ray/surface intersection problem

Problem description:

From a known 3-D surface and its 2-D visual image, the 2-D to 3-D mapping problem is defined as: given a point in the image plane, its corresponding point in the 3-D surface must be found. The problem can be geometrically described as: finding an intersection of a straight line ray with the 3-D surface. The ray starts from a viewpoint (the exposure station of camera) and passes through an imagery point in the image plane. Hence this is a ray/surface intersection problem as shown in Figure 6-3.

The Method:

As illustrated in Figure 6-3, let the viewpoint be located at z_0 plane and its coordinates are (x_0, y_0, z_0) . The ray passes through the image plane z_p of the camera at point (x_p, y_p, z_p) . Let the intersection of the ray and the surface be (X_i, Y_i, Z_i) . According to projective geometry, three points (x_0, y_0, z_0) , (x_p, y_p, z_p) and (X_i, Y_i, Z_i) are collinear, namely:

$$\begin{aligned} \frac{Y_i - y_0}{Z_i - z_0} &= \frac{y_p - y_0}{z_p - z_0} \\ \frac{X_i - x_0}{Z_i - z_0} &= \frac{x_p - x_0}{z_p - z_0} \end{aligned} \quad (6.1)$$

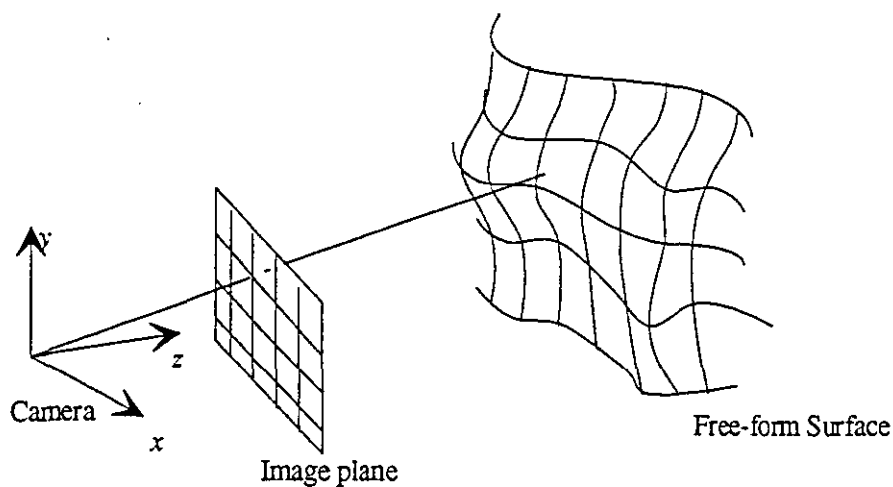


Figure 6- 3. Ray/surface intersection

As an alternative, the image plane co-ordinates (x_p, y_p, z_p) can be replaced by the co-ordinates of any 3-D point which is lying on the ray. Therefore the equation (6.1) is a general collinearity form of three spatial points. From two known points (x_0, y_0, z_0) and (x_p, y_p, z_p) the ray equation can be found, but the solution to three unknown values (X_i, Y_i, Z_i)

is impossible. If a 3D surface equation is provided, a solution could be found by a ray/surface intersection method.

A 3-D ray equation can be defined by the origin and direction vector of the ray as follows:

Let

$$\begin{aligned} R_{origin} &= R_o = [x_o, y_o, z_o] \\ R_{direction} &= R_d = [x_d, y_d, z_d] \end{aligned} \quad (6.2)$$

where $x_d^2 + y_d^2 + z_d^2 = 1$ and

$$\begin{aligned} x_d &= \frac{x_p - x_o}{\sqrt{(x_p - x_o)^2 + (y_p - y_o)^2 + (z_p - z_o)^2}} \\ y_d &= \frac{y_p - y_o}{\sqrt{(x_p - x_o)^2 + (y_p - y_o)^2 + (z_p - z_o)^2}} \\ z_d &= \frac{z_p - z_o}{\sqrt{(x_p - x_o)^2 + (y_p - y_o)^2 + (z_p - z_o)^2}} \end{aligned} \quad (6.3)$$

and a ray is represented by a parametric equation:

$$R(t) = R_o + R_d \cdot t, \text{ where } t > 0 \quad (6.4a)$$

$$\begin{aligned} x(t) &= x_o + x_d \cdot t \\ \text{or } y(t) &= y_o + y_d \cdot t \\ z(t) &= z_o + z_d \cdot t \end{aligned} \quad (6.4b)$$

There are three types of surface representations: implicit surface equation, parametric surface equation and discrete surface meshes. Accordingly, different solving methods are required. The implicit 3-D surface equation is expressed by $f(x,y,z)=0$. Substituted by 6.4, the intersection problem is to solve the equation

$$f(x_o + x_d \cdot t, y_o + y_d \cdot t, z_o + z_d \cdot t) = F^*(t) = 0 \quad (6.5)$$

Except for some simple cases, $F^*(t)=0$ is a higher order non-linear equation. Its roots (zero points) must be solved by a numerical method. The intersection is non-unique since multiple roots may exist, and additional criteria may be required to find the real solution.

When a surface is represented by a parametric equation, for example, bicubic form [Foley *et al.*, 1990]:

$$\begin{aligned}x &= u^T \cdot M^T \cdot G_x \cdot M \cdot u \\y &= u^T \cdot M^T \cdot G_y \cdot M \cdot u \\z &= u^T \cdot M^T \cdot G_z \cdot M \cdot u\end{aligned}\tag{6.6}$$

the intersection equation is complicated, especially if equation 6.6 is turned into a implicit surface form [Hanrahan, 1993]. The numerical method, instead of an analytical method, is often used to solve the problem of ray/parametric surface intersection.

When a surface is represented by discrete polygon meshes, each mesh can be finally decomposed into several triangular meshes. A triangular mesh represents a 3-D plane. The ray/surface intersection can be, therefore, solved by computation of ray/plane intersections with the aid of a searching process.

6.3.1.2 Solution for ray/plane intersection

A normalised plane equation is expressed by

$$A \cdot x + B \cdot y + C \cdot z + D = 0, \text{ where } A^2 + B^2 + C^2 = 1\tag{6.7}$$

Given three non-collinear points $p_1 = (x_1, y_1, z_1)$, $p_2 = (x_2, y_2, z_2)$ and $p_3 = (x_3, y_3, z_3)$, A, B, C in equation 6.7 can be computed from:

$$A \cdot i + B \cdot j + C \cdot k = \begin{vmatrix} i & x_2 - x_1 & x_3 - x_1 \\ j & y_2 - y_1 & y_3 - y_1 \\ k & z_2 - z_1 & z_3 - z_1 \end{vmatrix}\tag{6.8}$$

$$\text{and } D = -(A \cdot x_1 + B \cdot y_1 + C \cdot z_1)$$

Substitute the parametric expression 6.4 of a ray into equation 6.7, the ray/plane intersection equation is

$$A \cdot (x_0 + x_d t) + B \cdot (y_0 + y_d t) + C \cdot (z_0 + z_d t) + D = 0\tag{6.9}$$

This is a single parameter equation and t can be obtained from

$$t = \frac{-(A \cdot x_0 + B \cdot y_0 + C \cdot z_0 + D)}{A \cdot x_d + B \cdot y_d + C \cdot z_d} \quad (6.10)$$

By substituting t into equation 6.4, an intersection point which is on the ray can be acquired.

6.3.1.3 Containment test for ray/triangular mesh intersection

A containment test of the intersection point must be carried out to verify whether the intersection is out of the triangular area of the plane, because the solution from the ray/plane intersection may not lie within the triangular mesh. There are several methods available to test if a point is contained in a planar triangle:

- 1) The Jordon curve theorem: if a point is in the interior of a triangle (more general, a simple polygon), then all lines passing through the point have an even number of intersections with the edges of the triangle, as shown in Figure 6-4(a).
- 2) The area theorem: if a point is within the interior of a triangle, then the area sum of the three internal triangles which are comprised by the point and any two vertices of the triangle is equal to the area of the original triangle. Otherwise the sum of the areas is larger than the area of the original triangle, as shown in Figure 6-4(b).
- 3) The angle theorem: To connect a point with three vertices of a triangle produces three new triangles. If the point is on the interior of a triangle, then the angles of the new triangles which have a common side with the original triangle are always smaller than their corresponding angles in the original triangle (that is $\text{angle} \langle qab \rangle \leq \text{angle} \langle cab \rangle$, $\text{angle} \langle bcq \rangle \leq \text{angle} \langle bca \rangle$, and so on), as shown in Figure 6-4(c).
- 4) The right hand theorem: if a point is on the interior of a triangle (more generally, a convex polygon), then the point must be on the right side of each edge provided all edges are counted clockwise, as shown in Figure 6-4(d).

Theorems 1) and 4) can deal with general polygon shapes, but they are difficult to apply in 3D space. Theorems 2) and 3) can be generalised to 3D space. However, theorem 2) may be sensitive to numerical error because the calculated ray/plane intersection point may be slightly out of the plane and result in a larger sum of three triangle areas. Theorem

3) can deliver more reliable results and also needs less computation than theorem 2). Therefore theorem 3) is chosen for the containment test. Computational details are shown as follows:

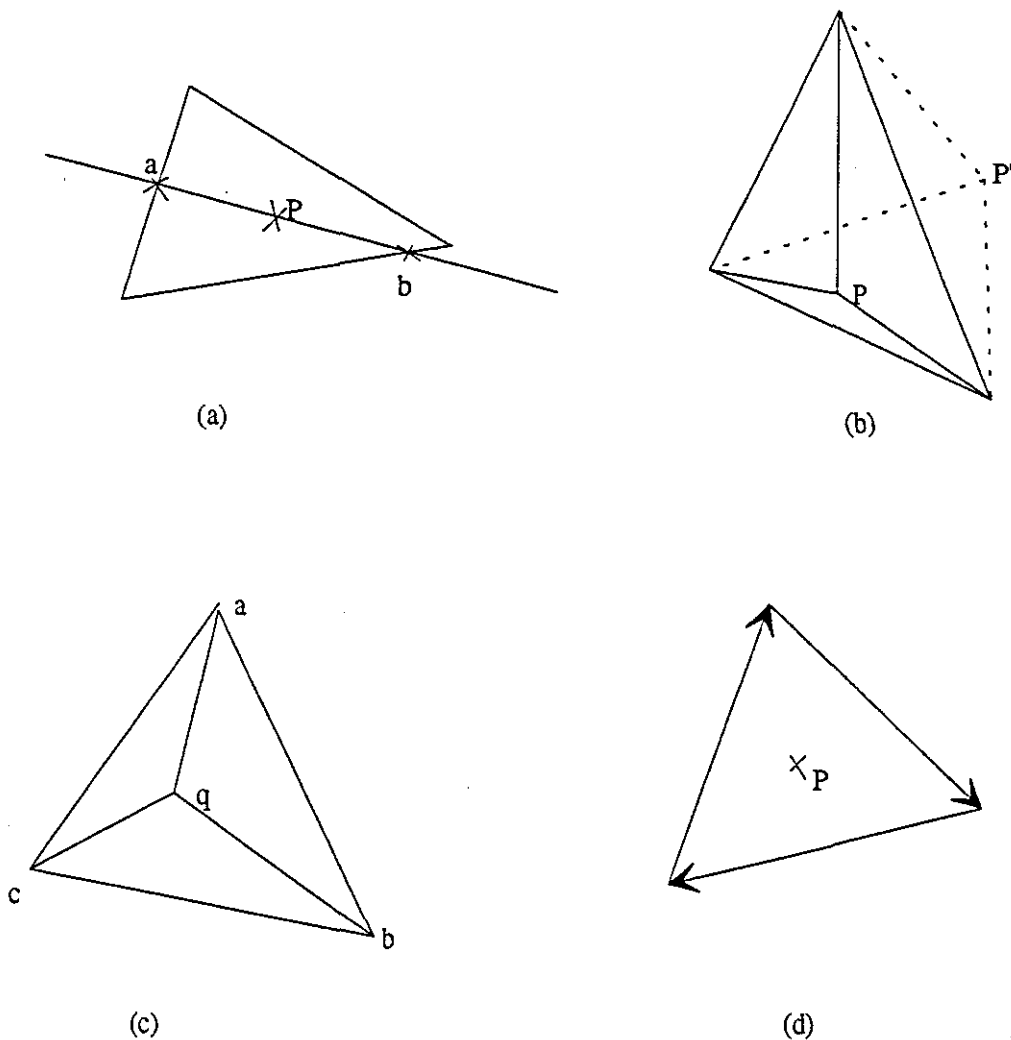


Figure 6- 4. Containment relationship of a point in a triangular area

To test if a point q is lying in the triangle (a, b, c) , the angles $\angle qab$, $\angle qbc$ and $\angle qca$ are calculated. If angle qab is smaller than angle cab , qbc is smaller than abc , and qca is smaller than bca , then the point q lies in the triangle (a, b, c) . An angle between three vector points can be calculated by vector dot product:

$$\theta_{qab} = \cos^{-1} \left(\frac{(qa, ab)}{\|qa\| \cdot \|ab\|} \right), \quad (6.11)$$

where (\bullet, \bullet) denotes a dot product and $\|\bullet\|$ is the two-norm.

6.3.1.4 Complete ray/triangular mesh intersection algorithm

Combining with the containment test, the ray/triangular mesh intersection is implemented by algorithm 6-1:

Algorithm 6-1. Ray/triangular mesh intersection

```
BOOL IntersectionRayTMesh(pstart, pend, pmid, Tmesh)
```

```
point3D_t pstart, pend, *pmid, Tmesh[3];
```

```
/* here:
```

```
-- pstart and pend are two ends of a ray
-- *pmid is a intersection returned
-- Tmesh[3] contains 3 vertex of a triangular mesh;
return TRUE if an intersection is found, otherwise
FALSE is returned.
```

```
*/
```

Step-1: Calculate the normal R_d of the ray;

Step-2: Use $Tmesh[0]$, $Tmesh[1]$ and $Tmesh[2]$ as three points of a sub-plane. Calculate the normal (A, B, C) of the sub-plane and D;

Step-3: Calculate t according to Equation (6.11);

Step-4: Calculate the intersection point $pmid$ according to Equation (6.4);

Step-5: Test if the intersection is within the triangle
if YES return TRUE, else return FALSE

The quadrilateral mesh is a frequently used representation form for a scanned surface and a parametric surface. The scanned data of the LASS are represented by a quadrilateral mesh form which is a two-dimensional array of heights and rotation angle (steps). The elements of the array are radii of surface points. Four vertices of the i th mesh are $\{ (h_i, \theta_i),$

$(h_{i+1}, \theta_j), (h_{i+1}, \theta_{j+1}), (h_i, \theta_{j+1})$ }. Similarly, a parametric B-spline surface form is a discrete quadrilateral (u, v) net. Four vertices of a (u, v) mesh are $\{ (u_i, v_j), (u_{i+1}, v_j), (u_{i+1}, v_{j+1}), (u_i, v_{j+1}) \}$. The calculation of ray/quadrilateral mesh intersection is a more sensible approach for a discrete ray/surface intersection problem.

However, four vertices of a quadrilateral mesh are not always co-planar. They must be decomposed into a triangular mesh for the calculation of ray/plane intersection. Let $(p_{i1}, p_{i2}, p_{i3}, p_{i4})$ denote four vertices of a quadrilateral mesh P_i . The mesh P_i can be split into two triangular meshes which consist of (p_{i1}, p_{i2}, p_{i3}) and (p_{i1}, p_{i3}, p_{i4}) respectively, as shown in Figure 6-5. The ray/quadrilateral mesh intersection can be accomplished by calling Algorithm 6-1 twice. If an intersection is found in the first call of Algorithm 6-1, the second call is unnecessary.

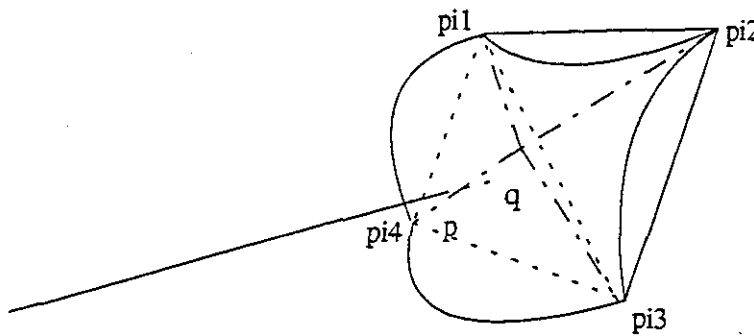


Figure 6- 5. Ray/quadrilateral mesh intersection

6.3.2 Searching a solution from a large surface

The algorithm discussed in the last section computes the intersection for one triangular/quadrilateral mesh each time. A searching process is required to deal with a large surface which consists of hundreds and thousands of quadrilateral meshes. The complete solving process for a surface is a two-dimensional traversing problem. When the number of meshes is large, it may take a considerable time to search for a solution in spite of the simplicity of the ray/plane intersection algorithm.

Moreover, due to the complex shape of a surface (for example, non-convex surface) multiple intersections may be found during the traversing process and thereby criteria are required to eliminate those inadmissible solutions. Two additional techniques are used to constrain the solving process and to delete inadmissible solutions. One is to constrain the searched space by normal direction of a sub-plane. Only those sub-planes facing the ray need to be searched, namely, the angle between the normal vector of a sub-plane and the direction vector of the ray should be greater than 90 degrees. This condition can be described by vector dot product:

$$\mathbf{n} \bullet \mathbf{R}_d < 0 \quad (6.12)$$

where \mathbf{n} is the normal vector of a plane. This is called a *visibility test*. The visibility test has been inserted into Algorithm 6-1 in the practical implementation to prevent non-visible intersection from calculation. Figure 6-6 shows the examples of visible and non-visible intersection.

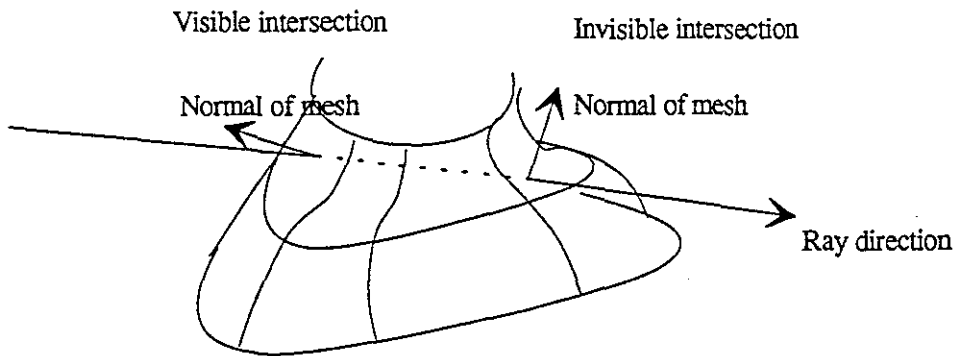


Figure 6- 6. Visible and non-visible intersection

The second technique adopted to constrain searched space is heuristic. It depends on the knowledge about the relationship between viewpoint position and the surface. A simple pre-estimation of the co-ordinate range to be searched can eliminate much unnecessary effort. Two estimated ranges have been utilised in relation to the LASS set-up:

1. *Constraint of searching range in height dimension:*

The scanned body is located in a central position on the turntable in the LASS system. The maximal radial length of the body surface should be less than 400 mm. Denote h as height and Z as distance from the centre of turntable. Let h_0 be the intersections of the ray and Z_0 ($Z = 0$) plane, and h_{400} be the intersection of the ray and Z_{400} ($Z = 400$) plane. Then the intersection of ray and body surface must be within h_0 and h_{400} , as illustrated in Figure 6-7a.

2. Constraint of searching range in angle dimension:

The LASS scanned data are organised by height (h) and angle (θ). The optical axis of the camera is assumed to align with the centre of rotation. The angle range of the scanned data can be divided into the left side and the right side by the position of a feature mark in an image plane, i.e. angle searching can only happen in a $(0 \sim 180)$ degree or a $(180 \sim 360)$ degree range. The searching angle may be further constrained by the intersections of the ray and a 400 mm radius circle which is assumed to be the maximum object radius, and the resultant angles are θ_a and θ_b , as illustrated in Figure 6-7b.

Finally the algorithm to search the whole body surface for intersections is described in Algorithm 6-2.

Algorithm 6-2. Search an intersection for scanned data

```

BOOL IntersectionRaySurfPatch(pstart, pend, pmid, Body)
point3D_t pstart, pend, *pmid, Body[MAXANGLE][MAXHEIGHT];
/* here:

```

```

    -- pstart and pend are two ends of a ray
    -- *pmid is an intersection returned
    -- Body[MAXANGLE][MAXHEIGHT] contains vertex of all
    quadrilateral meshes;
    return TRUE if an intersection is found, otherwise
    FALSE is returned. */

```

Step-1: Calculate the normal R_d of the ray;

Step-2: Calculate h_0 and h_{400}

Step-3: Calculate angle range θ_a , θ_b ;

Step-4: Loop I from h_0 to h_{400}

Step-5: Loop J from θ_a to θ_b

Step-6: Create *Qpatch* from four points of raw data matrix

Body[*J*][*I*], *Body*[*J*][*I*+1], *Body*[*J*+1][*I*], *Body*[*J*+1][*I*+1];

Step-6: Spilt *Qpatch* into *Tmesh1* and *Tmesh2*;

Step-7: if(**IntersectionRayTMesh**(*pstart*, *pend*, &*pmid*, *Tmesh1*)=TRUE)

then return TRUE, else

if(**IntersectionRayTMesh**(*pstart*, *pend*, &*pmid*, *Tmesh2*)=TRUE)

then return TRUE

Step-8: End of **Loops**, return FALSE.

6.3.3 Case study

A case study is carried out for applying the method derived in the two previous sections to locate artificial marks from a grey-scale image together with LASS scanned data of the human body. The grey-scale image is taken by one of the cameras in the LASS system. As mentioned before, the camera position (x_0, y_0, z_0) and projective co-ordinates (x_p, y_p, z_p) of the object point at a reference plane must be known to accomplish a ray-tracing algorithm. These are acquired by the camera/scanner calibration process. In this application case, the camera position was physically measured using a Leica WILD-T1610 digital theodolite. A calibration program similar to that in West [1994] produces a set of linear mapping parameters to convert the image (pixel) co-ordinates (u, v) of a point to its projective co-ordinates (x_p, y_p, z_p) on the Z_0 plane, where Z_0 is located at the centre of the turntable. A complete procedure for locating the feature points is:

Step 1: load in raw scanned data of a body surface;

Step 2: load in the grey-scale image of the body and display it in an image window;

Step 3: label the feature marks in the image window;

Step 4: execute calibration calculation to convert (u, v) co-ordinates of a feature mark to (x_p, y_p, z_p);

Step 5: execute ray-tracing computation to find the intersection of ray/surface;

Step 6: repeat step 3 to step 5 to process all feature marks.

Figure 6-8a shows the image window and labelled feature marks in the image plane. The 3-D co-ordinates of these feature marks are displayed on the raw scanned data (wireframe surface) in Figure 6-8b after ray-tracing computation.

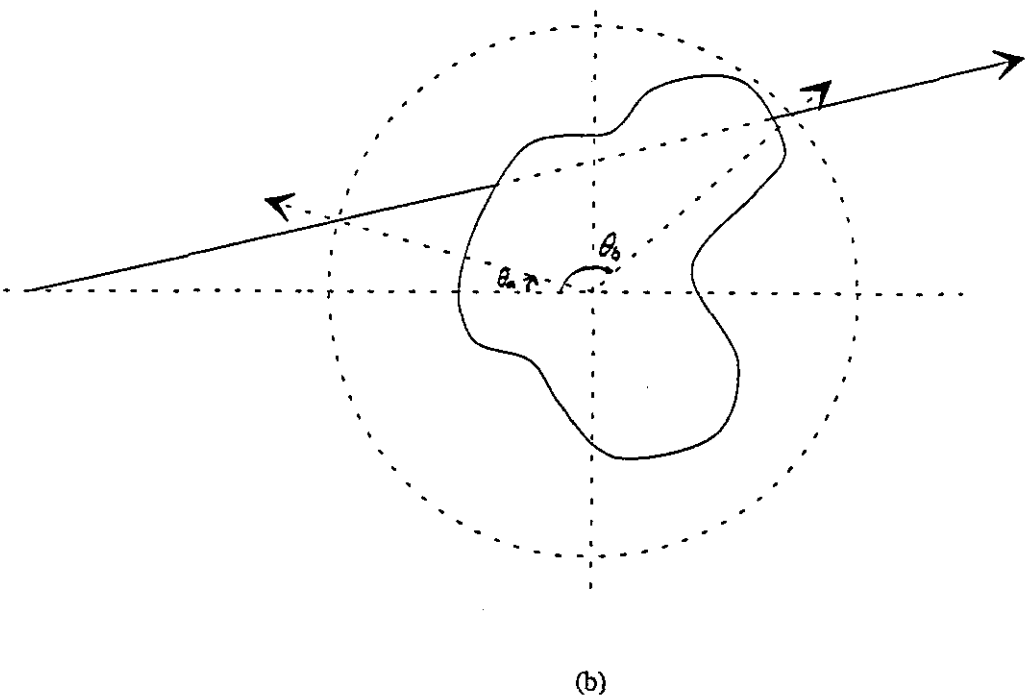
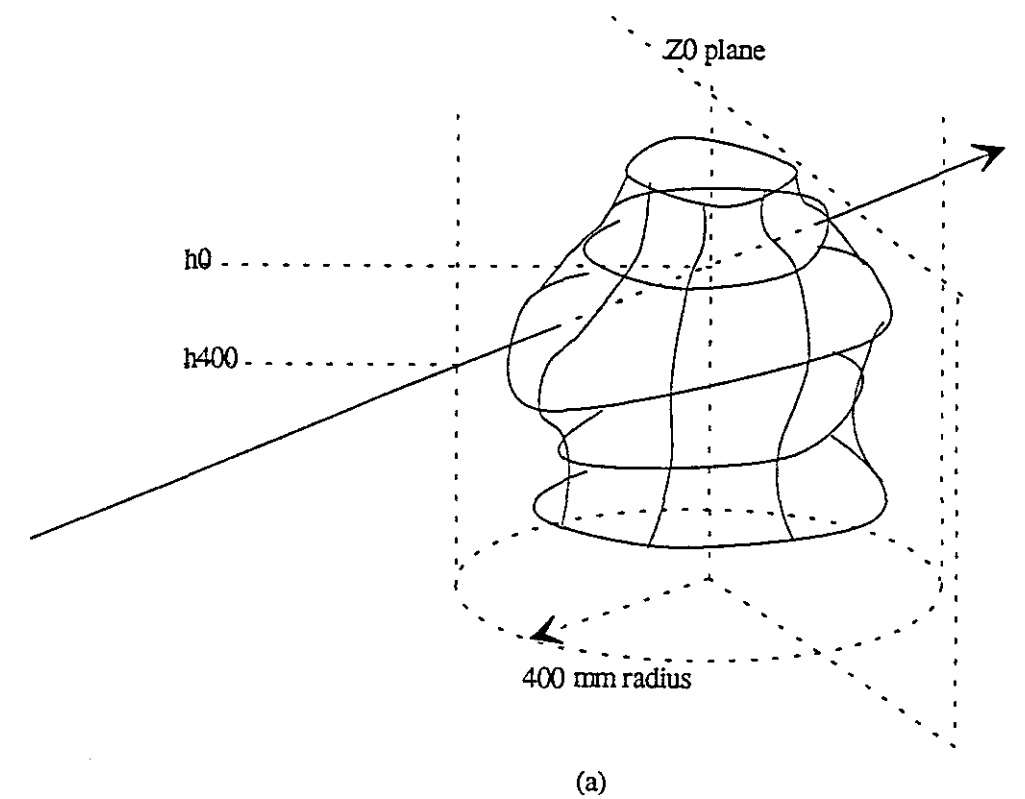
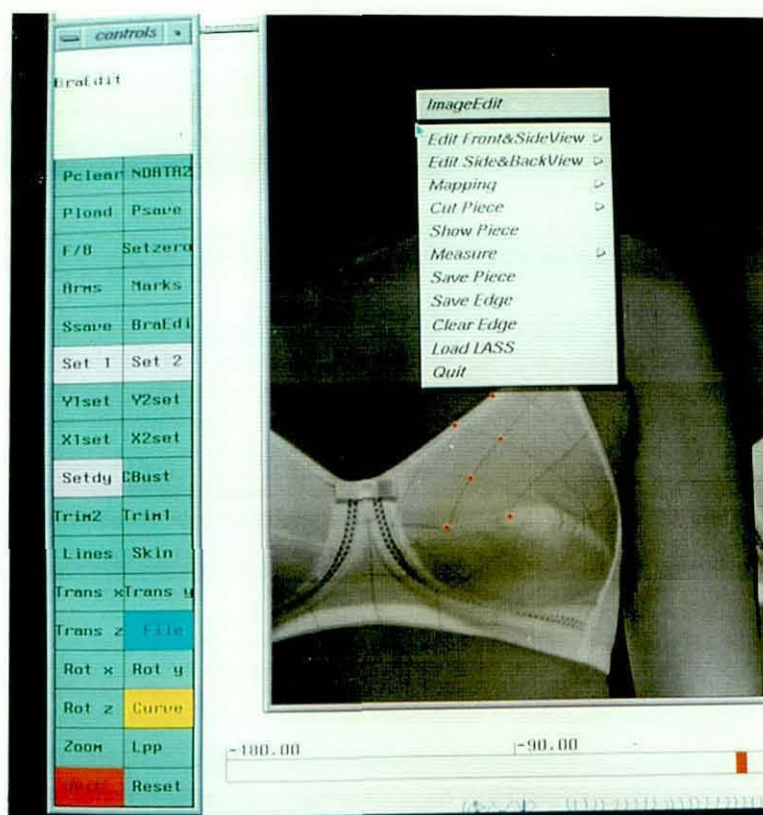
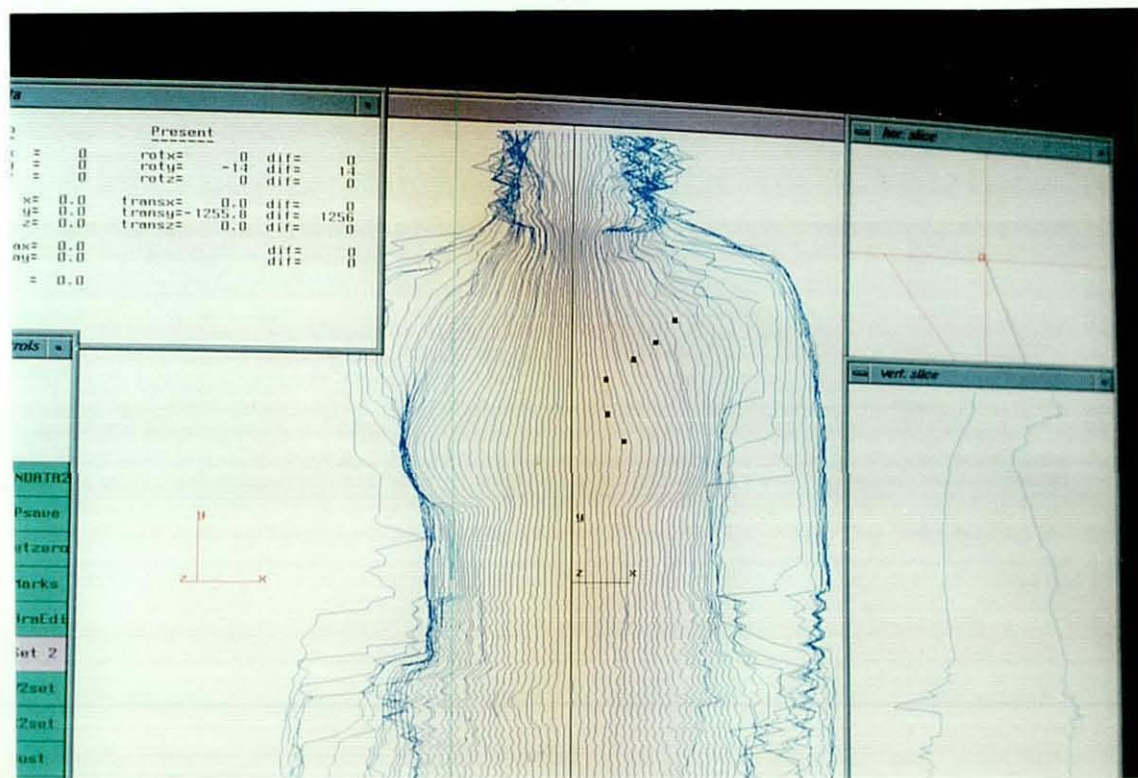


Figure 6- 7. Search space of a body surface a) height constraint; b) angle constraint.



(a)



(b)

Figure 6- 8. Case of feature point location: (a) labelling of feature marks in the image window; (b) mapped 3-D co-ordinates of the feature marks in the raw scanned surface.

6.4 Error analysis of the direct mapping method for feature point location

According to equation 6.3, 6.4 and 6.10, the co-ordinates of the ray/plane intersection are:

$$\begin{aligned} X_i &= x_0 - \frac{(x_p - x_0) \cdot (Ax_0 + By_0 + Cz_0 + D)}{A(x_p - x_0) + B(y_p - y_0) + C(z_p - z_0)} \\ Y_i &= y_0 - \frac{(y_p - y_0) \cdot (Ax_0 + By_0 + Cz_0 + D)}{A(x_p - x_0) + B(y_p - y_0) + C(z_p - z_0)} \\ Z_i &= z_0 - \frac{(z_p - z_0) \cdot (Ax_0 + By_0 + Cz_0 + D)}{A(x_p - x_0) + B(y_p - y_0) + C(z_p - z_0)} \end{aligned} \quad (6.13)$$

where A, B and C are the normal direction of the plane.

Equation 6.13 implies that there are three sources of error, namely: camera position error; projected co-ordinate error and plane direction error. The direction of the plane has a complex effect on the error analysis of ray/plane intersection. If the normal of the plane is perpendicular to the ray, the minor perturbation of the ray direction could result in a large error at the intersection (from infinity to finite error or vice versa). In contrast, the error of the ray direction has a minimum effect on the computation of (X_i, Y_i, Z_i) , if the normal of the plane is parallel to the ray direction. That is, the computational error of (X_i, Y_i, Z_i) is a function of the plane direction. To simplify the following error analysis, it is presumed that the plane direction is coincident with the Z plane, i.e. $A=0, B=0, C=1$ and $D = -Cz_p$. This will show clearly the effect of the first two sources of error.

The ray/plane intersection is, in fact, an approximation to the ray/surface intersection. The approximate process of triangular mesh to a curved surface will result in some error. This type of error will be analysed in Section 6.4.3.

6.4.1 Camera position error

Camera position error is the error of viewpoint (x_0, y_0, z_0) . It is caused by a calibration method of the camera system. This section estimates the error magnitude of (X_i, Y_i, Z_i) due to (x_0, y_0, z_0) error. Using the simplified Z plane equation $A=0, B=0, C=1$ and $D = -Cz_p$, the co-ordinates of the ray/plane intersection are:

$$\begin{aligned}
 X_i &= x_0 - (x_p - x_0) \frac{z_0 - Z_i}{z_p - z_0} \\
 Y_i &= y_0 - (y_p - y_0) \frac{z_0 - Z_i}{z_p - z_0} \\
 Z_i &= z_0 - (z_p - z_0) \frac{z_0 - Z_i}{z_p - z_0} = Z_i
 \end{aligned}
 \tag{6.14}$$

Taking the first order Taylor expansion of 6.14, we have:

$$\begin{aligned}
 \Delta X &= \frac{\partial X}{\partial x_0} \Delta x_0 + \frac{\partial X}{\partial y_0} \Delta y_0 + \frac{\partial X}{\partial z_0} \Delta z_0 \\
 \Delta Y &= \frac{\partial Y}{\partial x_0} \Delta x_0 + \frac{\partial Y}{\partial y_0} \Delta y_0 + \frac{\partial Y}{\partial z_0} \Delta z_0 \\
 \Delta Z &= 0
 \end{aligned}
 \tag{6.15}$$

where

$$\begin{aligned}
 \frac{\partial X}{\partial x_0} &= \frac{z_p - Z_i}{z_p - z_0}; & \frac{\partial X}{\partial y_0} &= 0; & \frac{\partial X}{\partial z_0} &= -(x_p - x_0) \frac{z_p - Z_i}{(z_p - z_0)^2} \\
 \frac{\partial Y}{\partial x_0} &= 0; & \frac{\partial Y}{\partial y_0} &= \frac{z_p - Z_i}{z_p - z_0}; & \frac{\partial Y}{\partial z_0} &= -(y_p - y_0) \frac{z_p - Z_i}{(z_p - z_0)^2}
 \end{aligned}
 \tag{6.16}$$

Three conclusions can be obtained from (6.16):

- 1) The X and Y errors are proportional to the x_0 and y_0 error respectively if the surface plane is perpendicular to the Z axis;
- 2) Errors of X and Y from x_0 and y_0 are independent of each other;
- 3) X and Y errors caused by z_0 are inversely proportional to the distance from the camera to projective plane.

Table 6-1. X error of ray/plane intersection from two calibration methods

	Physical calibration by digital theodolite (the estimated worst case)	Analytical calibration from the RDO method (at 2 pixels noise level)	Maximum X error of physical calibration	Maximum X error of analytical calibration
Δx_0	2 mm	0.5 mm	0.2 mm	0.05 mm
Δy_0	2 mm	0.3 mm	0	0
Δz_0	20 mm*	23 mm	1.18 mm	1.3 mm

* the error of distance from a camera centre to the reference plane is caused by the uncertainty of the camera centre. It is difficult from outside of a camera to identify where the camera centre is.

Taking the set-up of the LASS system as an example, in which $(z_p - z_0) = 3000$ mm and the maximum $(z_p - Z_i) = 300$ mm, the X error is 1/10 of x_0 error and 1/17 of z_0 error when $x_p - x_0 = 200$ mm. Table 6-1 shows the typical errors from physical and analytical camera calibrations.

6.4.2 Projected co-ordinate error

The projected co-ordinates (x_p, y_p, z_p) of an image point are obtained from a projective transformation. The projective transformation relies on the calibrated camera parameters. The projection plane could be an arbitrary reference plane in the world co-ordinate system or the image plane of a camera. Many 3-D surface scanners were calibrated by projected co-ordinates in one or several reference planes as reviewed in Chapter 5. If the projection plane is the image plane of the camera, the projection error is independent of the camera position, but related to the interior parameters of the camera. If the reference plane is a world plane, the exterior parameters of a camera play a crucial role in the error analysis. This suggests that different analysis methods are required for these two cases.

6.4.2.1 Error analysis related to projected plane method

For simplifying the analysis, the projection plane is presumed to be a world plane and parallel to the image plane of the camera system. Based on the computational formula 6.14, the error expression is

$$\begin{aligned}\Delta X &= \frac{\partial X}{\partial x_p} \Delta x_p + \frac{\partial X}{\partial y_p} \Delta y_p + \frac{\partial X}{\partial z_p} \Delta z_p \\ \Delta Y &= \frac{\partial Y}{\partial x_p} \Delta x_p + \frac{\partial Y}{\partial y_p} \Delta y_p + \frac{\partial Y}{\partial z_p} \Delta z_p \\ \Delta Z &= 0\end{aligned}\tag{6.17}$$

and

$$\begin{aligned}\frac{\partial X}{\partial x_p} &= -\frac{z_0 - Z_i}{z_p - z_0}; & \frac{\partial X}{\partial y_p} &= 0; & \frac{\partial X}{\partial z_p} &= (x_p - x_0) \frac{z_0 - Z_i}{(z_p - z_0)^2} \\ \frac{\partial Y}{\partial x_p} &= 0; & \frac{\partial Y}{\partial y_p} &= -\frac{z_0 - Z_i}{z_p - z_0}; & \frac{\partial Y}{\partial z_p} &= (y_p - y_0) \frac{z_0 - Z_i}{(z_p - z_0)^2}\end{aligned}\tag{6.18}$$

Three conclusions, which are similar to the camera position error analysis in the previous section can be obtained from equation 6.18:

- 1) The X and Y errors are proportional to the projected co-ordinate errors x_p and y_p respectively;
- 2) The X and Y errors are independent;
- 3) The X and Y errors caused by z_p are inversely proportional to the distance from the camera to the projective plane;

Again, taking the set-up of the LASS system as an example, the X error will be 0.9 times the x_p error and 1/17 of the z_p error at $x_p - x_0 = 200$ mm. This requires high accuracy co-ordinate mapping between the image (pixel) plane and the reference plane from a calibration method. However, it is difficult to evaluate the co-ordinate mapping accuracy of a calibration method which calculates projected co-ordinates directly. Such a calibration method is usually tested on dimensional measurements of a standard object. If the object plane is close to the reference plane of calibration, the measurement accuracy could be a criterion of the accuracy of the projected co-ordinate. Therefore, according to West [1994], the measurement error of an object dimension (horizontal direction) of the LASS system is about 2~5 mm in the X,Y and Z directions. The distance error from the camera centre to the reference plane, which relies on physical measurement, is less than 20 mm. In the worst case the resultant X errors subjected to x_p and z_p errors are about 4.5 mm and 1.18 mm respectively.

6.4.2.2 Error analysis related to analytical calibration methods

The analytical calibration methods, as described in Chapter 6, produce interior and exterior parameters of a camera system. The reference plane is a plane parallel to the camera image plane which may be at a slope to the Z plane of the world co-ordinate system. From the exterior orientation parameters of a camera, the projected co-ordinate of a point at the reference plane can be transformed to a Z plane of the world co-ordinate system. Error analysis of the ray/plane intersection can follow the method in the previous sub-section. However the analysis of the transformation error of two co-ordinate systems is difficult, especially if lens distortion is involved. In most situations, the camera image plane is almost parallel to the Z plane of the world co-ordinate system. The error of the co-ordinate transformation is negligible. Another difficulty is that the calibration methods described in Chapter seek minimisation of the projection error in the pixel plane rather than the

reference plane. The evaluation result of a calibration method can not be used in the error analysis of the ray/plane intersection directly. Only a rough estimation can be made. For example, for the RDO method under a 2 pixel noise level, the RMS residual of projection error is 1.079 pixels (Table 6-9). In the camera-frame grabber system attached to the LASS, it is approximately equivalent to 0.6 mm error in the Y direction and 0.8 mm error in the X direction at the reference plane ($Z=0$).

6.4.3 Error analysis related to surface approximation

The intersection algorithm of the ray/plane is an approximation of the ray/surface intersection problem. There is a certain error between a surface and its triangular mesh approximation. Figure 6-9 illustrated the intersection error if a curved surface is approximated by triangular meshes. In the figure the ray/surface intersection is p , but ray/mesh intersection is q . However, the error evaluation requires a more precise surface representation. As far as raw scanned data are concerned, there is no more data suitable for an error analysis of the ray/surface intersection.

Generally speaking, the error analysis related to surface approximation must be based on a parametric surface in which more surface data can be generated within a mesh area. For this purpose, an extension to the two-dimensional array form of surface mesh data is needed. The (u,v) parameters of each node of the surface meshes should be registered in a separate two-dimensional array in addition to the co-ordinate data stored. When error evaluation is required, middle data between the vertices of a mesh can be generated by the parametric surface equation.

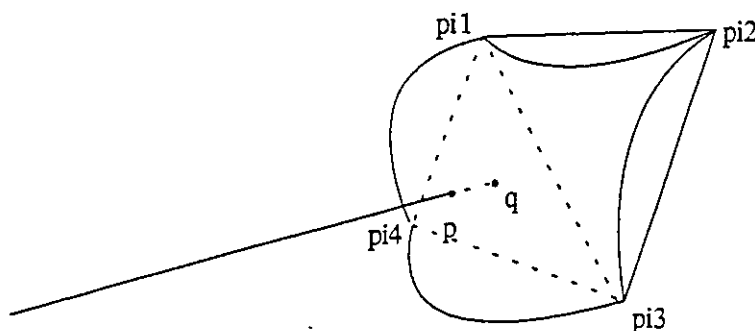


Figure 6- 9. Error of ray/surface intersection

6.4.4 Verification of mapping accuracy

The accuracy of the mapping method is verified by comparing co-ordinates measured from the mapping method and from a Co-ordinate Measuring Machine (CMM). A smooth sphere-like object was scanned by LASS and grey-scale image of the object taken. Seven points in the image were labelled and their co-ordinates calculated from the mapping method. These points were measured using a CMM as well. Table 7-2 shows the measurement result from two systems, in which the Y value is in the height direction, and the Z value is in the depth direction.

Table 6- 2. Co-ordinate values of seven points from two measurement methods

Point No.	Measurement from the mapping method			Measurement from CMM		
	X (mm)	Y (mm)	Z (mm)	X (mm)	Y (mm)	Z (mm)
1	38.7	1416.4	-115.3	37.5	1417.9	-113.7
2	-84.5	1415.0	-93.5	-83.6	1417.7	-86.0
3	1.2	1397.4	-137.2	-1.0	1395.8	-135.0
4	-25.6	1396.2	-135.8	-27.0	1395.9	-132.1
5	-27.9	1373.8	-147.8	-29.4	1373.7	-142.3
6	-46.0	1371.4	-144.3	-47.5	1373.8	-137.3
7	-48.3	1351.6	-150.7	-50.1	1352.1	-143.3

It can be observed from Table 6-2 that errors in the X and Y directions are reasonably small (all less than 3 mm). However, errors in the Z direction are significant. There are two factors which contribute to the error in Z direction: 1) alignment of the object in the Z direction, and 2) inherent LASS system error. Misalignment can be observed from the differences of Z values between two measurement methods. All values are positive except point 2. (Point 2 is the point farthest from the object axis, therefore the tangential error of the direction of the plane may be large.) There was an offset of about six millimetres in the Z direction. This is detected from the image of raw scanned data by the LASS edit program. Misalignment in the Z direction is not the only factor to affect depth measurement. Depth error in raw surface data and in the calibration equation are other likely factors. Nevertheless, these errors may not affect the accuracy of feature point location because they are inherent errors in raw data.

6.5 An application of located feature points: surface trimming

6.5.1 Introduction to surface trimming

Trimming of a surface is a process to define the boundary of a 3-D region and find all its interior points. Trimmed surfaces have a fundamental role in various application areas. They can be applied in area calculation for 3D surface anthropometry, pattern design for 3D computer-aided clothing design, etc. The boundary definition of a special region of a surface could be accomplished in different ways. In a CAD system, the boundary of a region can be formed by the intersection of multiple surfaces/objects or by interactive drawing from an operator. However, for a reverse engineering application or a 3-D surface anthropometry task, a particular region can be defined from a number of feature points of a surface. These feature points must be precisely identified and labelled on the surface. It is necessary to use the mapping method discussed in this chapter to assist the labelling procedure of feature points.

The boundary of a trimmed surface is called the trimming curve. There are different descriptions of trimming curves depending on the representations of the surface equation. In general, they can be distinguished as parametric space descriptions and co-ordinate space descriptions. Boundaries in parametric space description have been discussed in literature [Sheng and Hirsch, 1992, Piegl and Richard, 1995]. This kind of description gives a boundary of parametric values instead of surface co-ordinates for the trimming curve. The trimming curve in parametric space is often a result of a surface/surface intersection [Barhill & Kersey 1990]. McCartney & Hinds[1992] defined the boundary of a 3-D pattern for clothing design by directly mapping (i, j) values of a parametric surface onto a 2D tablet. When the cursor moves over the tablet plane, a pair of (i, j) co-ordinates are located and its corresponding 3-D co-ordinates on a parametric surface can then be decided.

The surface/surface or plane/surface intersection is also described in co-ordinate space [Hanna, Abel and Greenberg, 1983]. If a surface is represented by discrete polygon meshes in co-ordinate space, the trimming curve can be described by a piecewise linear function in co-ordinate space. It could be fitted by a smooth parametric function such as a parametric B-spline.

A trimmed surface consists of all interior points within the region that the trimming curves surround. Two principal methods to generate the trimmed surface, according to the types of trimming curves, are based on parametric space representation and co-ordinate space representation respectively. The parametric space representation generates the trimmed surface by a scanning process of the parametric space. The scanning steps in one parametric direction and calculates the bound of the other parameter from the trimming curves [Luken, 1995]. For example, only those surface points which have parametric values bounded in v values of the trimming curves are generated if the u parameter is fixed at a particular step of scanning.

The co-ordinate space representation generates the trimmed surface by a series of 3-D plane/plane intersection computations [Hanna *et al.*, 1983]. As a result, the trimming process in a 3-D co-ordinate space is much more difficult than in a parametric space. Therefore the trimming curves defined in a 3-D co-ordinate space are preferred to be converted into the parametric space in which the surface is represented.

6.5.2 Surface trimming of raw scanned data

This section describes the application of feature point location in the trimming of a raw scanned body surface. Since the co-ordinates of feature points are in (x,y,z) form, the trimming operation may have to be implemented in 3-D co-ordinate space, which proves difficult. To avoid a 3-D co-ordinate space trimming, the characteristics of raw scanned data must be utilised. As the raw scanned data are represented by a cylindrical co-ordinate system, they can be viewed as being in two dimensional parametric space in which the angle, θ , and the height, h , are two parametric dimensions. The identified feature points can be converted into cylindrical co-ordinates. The trimming process is implemented in the cylindrical co-ordinate space representation. Such an arrangement has similar advantages to parametric space representation, i.e. scanning and searching of trimming boundary are accomplished in 2-D space and surface data can be traced by iso-angles or iso-height curves. The implemented trimming process consists of three steps:

- 1) acquiring vertices of the trimming boundary by the ray/surface intersection method discussed in section 6.3;

- 2) converting the trimming curve into a cylindrical co-ordinate form and building a boundary expression by an edge list;
- 3) trimming the raw surface data in (θ, h) space.

Following are the detailed descriptions of Step 2) and 3).

6.5.2.1 Boundary expression by an edge list

The boundary of a region is defined by a *simple closed polygon* [Preparata & Shamos, 1985] which does not have any hole in its interior. Each vertex of boundary polygon is stored in a node of a double-link list called the *EdgeList*. 3D Cartesian co-ordinates (x, y, z) of the trimming curves can be converted into equivalent cylinder co-ordinates (r, θ, h) which represent radius, angle theta and height respectively. The order of boundary vertices can be arranged in a clockwise or an anti-clockwise direction. Following is the data structure of the *EdgeList* in the C programming language format:

```
struct EdgeList {
    point3D_t      p;
    float          r, h,  $\theta$ ;
    struct EdgeList *leftLink, *rightLink;
}
```

The *EdgeList* can be traversed either in a clockwise or in an anti-clockwise because it is a double link list. It is also a closed list which has no constraint on its head or rear.

6.5.2.2 Trimming surface

The trimming operation in a cylindrical co-ordinate space consists of three steps:

- 1) finding the maximum and minimum values of the trimming range in one parametric direction (for example the angle direction);
- 2) stepping from the minimum to the maximum value of the searching parametric direction and searching the intersections of each slice of raw data with trimming polygons; and
- 3) cutting interior data into a new data structure.

An implementation of these steps is a scanning line method used in polygon filling [Foley, 1990]. Taking the angle as the searching parameter, the scan starts from the minimum angle which can be find from the EdgeList, and each vertical slice of the raw data constitutes a scanning line. To constrain the search range in the height direction, the minimum and maximum heights of the trimming polygon are useful. When one slice of raw data is traversed from minimum height to maximum height, its intersections with the trimming polygon are counted: if an even number of intersections are found, the data between adjacent odd and even intersections belong on the trimmed surface, as shown in Figure 6-10.

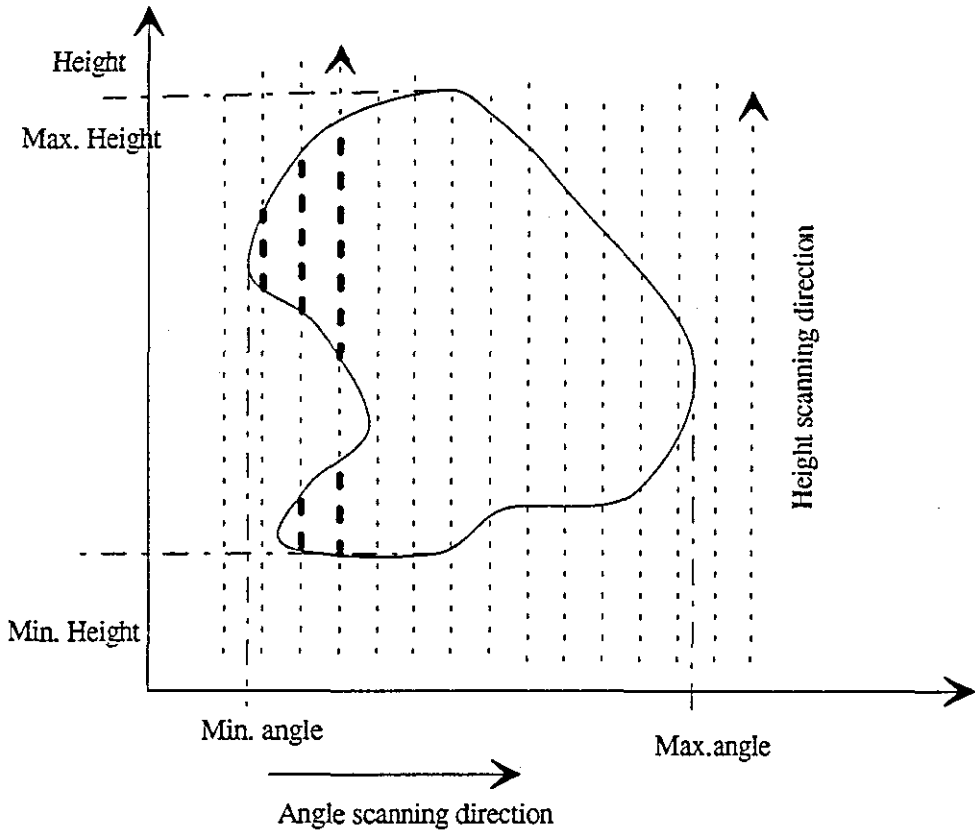


Figure 6- 10 Scanning line trimming of a surface

The above approach deals with an ideal situation in which the trimming curve and the raw data are smooth. In fact, the trimming polygon is a piecewise line function. Each side of the polygon may intersect with raw data of an iso-angle at a non-integral position,

namely the intersection is between two adjacent height co-ordinates. Or the vertices of the trimming polygon are located at a non-integral position of parametric space. Figure 6-11 shows these two cases.

These problems are caused by the non-continuous raw data format. Since the output data of the LASS are quantised in a 2.4 degree in the angle direction and in 5 mm in the height direction, the vertices of the trimming polygons, which are solved from the intersection of the ray/surface, do not necessarily coincide with a vertex of the raw data meshes. Moreover, it could be true that no intersection is found between a side of the trimming polygon and a vertical slice of the raw data because the trimming polygon does not contact with the raw data surface (although the vertices of the polygon do). Two techniques are adopted to prevent the loss of accuracy of the trimmed surface: 1) the intersection of a side of the trimming polygon with a vertical slice is defined as a point on the vertical slice with the least distance from the polygon side; 2) the precise intersection is stored, whether or not it is located at an integral or non-integral position.

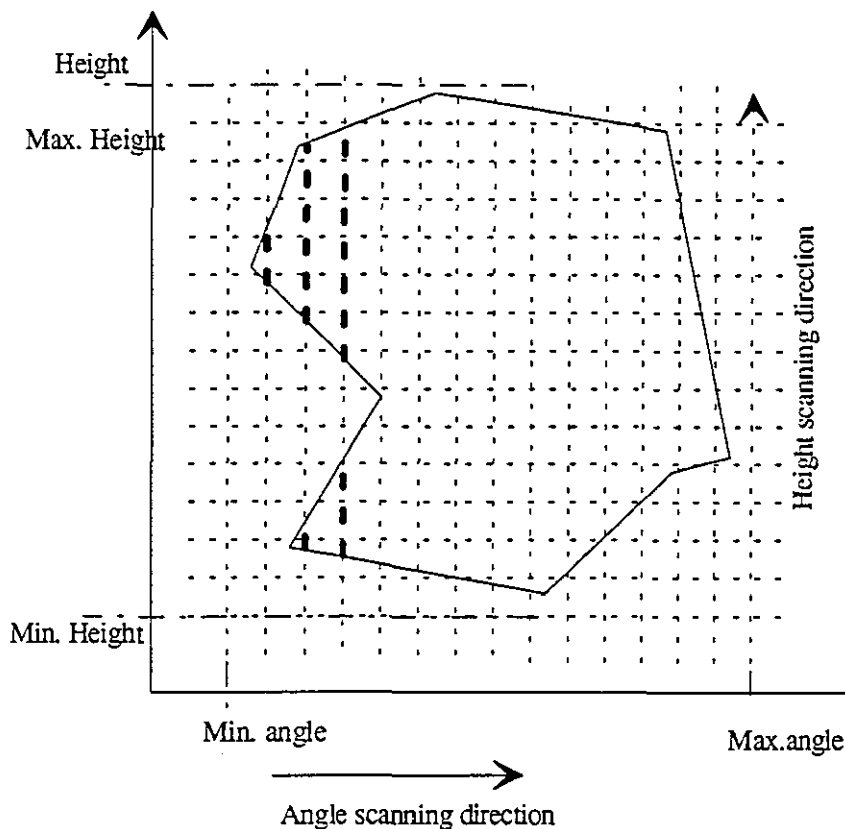


Figure 6- 11. Non-integral co-ordinate relationship between a trimming polygon and underlying surface

To implement a trimming algorithm, a data structure is needed to store the intersections of an edge with a vertical slice of the surface data. The data structure is defined as a *trimming vector* in which its element contains a parameter value (angle) and a pointer to a *IntersectionsList*. The *IntersectionsList* is defined as:

```
struct IntersectionsList {  
    float h,  $\theta$ ;  
    struct IntersectionsList *next;  
}
```

The complete trimming algorithm has the following steps:

- 1) the edge list is traversed and the minimum and maximum angles are found for scanning;
- 2) the *trimming vector* is created which has M elements, where the M is the number of vertical slices between scanning angle intervals;
- 3) the edge list is traversed once more. Two angles at two ends of an edge are obtained from the data structure of the edge list, therefore intersections of the edge with those vertical slices within the two angle range can be calculated. Each intersection (its angle, height and radius co-ordinates) is inserted into the corresponding *IntersectionsList* according to the angle value. Figure 6-12 illustrates the resultant *trimming vector* after the scanning process;
- 4) each intersection list is sorted by the height values of intersections after all edges are tested,.
- 5) the trimmed region is outputted by tracing the sorted *IntersectionsList* of each vertical slice. The Jordon curve theorem is applied to differentiate the *interior* and *exterior* data of the region (a simple polygon), i.e. the intersection height is counted as odd and even, and the data between an odd intersection and next even intersection are treated as the *interior* of the region.

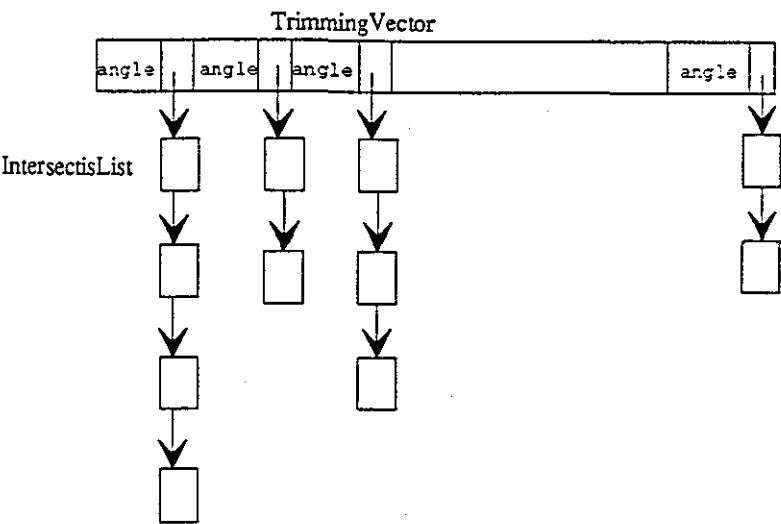


Figure 6- 12. *Trimming vector and its IntersectionsLists*

6.6 Summary

This chapter described a fundamental measurement task in 3-D surface anthropometry, i.e. the identification and measurement of feature points in 3-D scanned data of the human body. The definition and techniques related to this task, as well as its application in the LASS system were discussed. A digital image system has been built and relevant software has been developed to perform the acquisition, labelling and mapping of feature points. The ray-tracing method was used to map the 2-D image of an object to its corresponding 3-D scanned data. The location of feature points from a 2-D image to 3-D scanned data is solved by the ray/surface intersection. Surface trimming of raw scanned data, which is an application of the feature point location, has also been implemented and presented.

CHAPTER SEVEN

THE MATHEMATICS AND SOFTWARE STRUCTURE OF IN 3-D SURFACE ANTHROPOMETRY

An essential objective in 3-D surface anthropometry is to take measurement from the surface data of the human body. This consists of measurements and calculations at various *dimensions* and *orders*. The extraction and marking of feature points is considered as a zero-dimensional measurement, which has been discussed in Chapter 7. As a natural classification, the measurement of length is one-dimensional, including distance between points, arc length and circumference. The measurement of area is two-dimensional and could include the area of horizontal, vertical and even arbitrary oblique sections, and the area of a 3-D surface. Three dimensional measurement includes volume between sections, and volume between surfaces.

The measurement and calculation at various orders deals with direction (normal), tangential (first-order) and curvature (second-order) of a surface. These calculations are known as 'interrogation' in computer-aided geometric design. For a unified use, 'interrogation' is denoted for all higher-dimensional and higher-order measurements and calculation with respect to a 3-D surface in this thesis.

Analysis of the mathematics and algorithms for data interrogation is essential to a software implementation of 3-D surface anthropometry. This chapter discusses the basic scope of mathematical and computational problems confronted in 3-D surface anthropometry, but complete details of computational algorithms are beyond the scope of this chapter.

Software structure for 3-D surface anthropometry tackles more than the mathematics of data interrogation. Function decomposition of such a software is discussed in this chapter.

7.1 One-dimensional measurement

7.1.1 The measurement of length

Distance between two points:

This is a basic one-dimensional measurement. It requires only the locations of two feature points, which could be acquired by the method discussed in Chapter 6. Let $p_1=(x_1, y_1, z_1)$ and $p_2=(x_2, y_2, z_2)$, then the distance between them is

$$d(p_1, p_2) = \sqrt{(x_2 - x_1)^2 + (y_2 - y_1)^2 + (z_2 - z_1)^2} \quad (7.1)$$

Surface distance or arc length

A surface distance means the distance between two surface points along a surface path. If a series of points on this path are known, the distance can be approximated by a sum of accumulative chord length (i.e. the distance between two adjacent points). It is obvious that manually defining a series of points on a surface is uneconomic. A preferred method is to define the surface path by an intersection of the surface and a plane which contains the feature points. Because a plane must be defined by three points, the normal direction of the plane should be given in addition to two known feature points. The selection of the plane direction depends on the application. In 3-D surface anthropometry, an orthogonal view is acceptable since the measurement is usually taken from either the front view or the side view.

The calculation of the intersection of a plane and a surface is not simple. Assuming that the equation of the plane is known and can be expressed as:

$$\pi: Ax + By + Cz + D = 0 \quad (7.2)$$

and if the surface is represented by triangular meshes, the intersection of surface-plane is a search process of plane-plane intersection in which each triangular mesh represents a small plane. This process can be divided into five algorithm steps:

- S1. construct a strip expression for the surface, each strip is defined at one parametric direction. (for a parametric surface or for a 3D surface patches.)
- S2. starting from the first strip, find the feasible meshes which are intersecting with the plane.

S3. calculate the intersection of mesh-plane and register the co-ordinates of the intersection into a stack (or list).

S4. repeat S2 and S3 until all strips are processed.

S5. connect the ends of intersections by some distance criterion.

The efficiency of this method relies largely on the feasibility criterion of mesh-plane intersection which is used to constrain the search space. To calculate the position relationship of three vertices of a mesh to the plane occupies the majority of the computational time. An alternative solution is to transform all surface points from the original co-ordinate system to a new world co-ordinate system in which its x-y plane coincides with the plane equation and its z-axis coincides with the normal of the plane. As a result, the feasibility of a triangular mesh merely relies on the z values: if all the z-values of three vertices of the mesh are positive or negative, the mesh is excluded from the further computation. This could cut the computational time.

The intersection problem of a plane and a parametric surface was presented by Lee [1984].

7.1.2 The measurement of circumference

The measurement of circumference of a section is a basic element in anthropometry. The section to be measured could be a cross-section, vertical section or an oblique section. Some sections may have a concave shape. The measurement of circumference under consideration will mimic a tape measurement in which only a convex hull of the section is measured. For a planer simple closed polygon, if its vertex co-ordinates are normalised with an internal point, for example, its gravity point or centroid point, the criterion of a concave shape is that if the internal angle formed by three adjacent vertices $p_{i-1}p_i p_{i+1}$ is reflex (that is $\geq \pi$), then point p_i is a concave point and should be deleted. While the angle $p_{i-1}p_i p_{i+1}$ is reflex, then $p_{i-1}p_i p_{i+1}$ is said to be a "right turn", or a "left turn". To find the convex-hull of a planer polygon, the following algorithm is considered:

Convex hull algorithm--Graham method [Preparate & Shamos 1985]:

1. Let p_1, \dots, p_n be vertices of a planer polygon P and q be an internal point of P . Let the co-ordinate of q be the origin and all co-ordinates of p_i ($i=0 \dots n$) be normalised according to q . Sort the

points of P lexicographically by polar angle and distance from q and arrange them into a circular doubly-linked list, with $START$ pointing to the initial vertex. (Refer to Figure 7-1 a) and b)).

2. (Scan)

begin $v := START$;

while ($RLINK[v] \neq START$) **do**

if (the three points v , $RLINK[v]$, $RLINK[RLINK[v]]$ form a left turn)

then $v := RLINK[v]$

else begin DELETE $RLINK[v]$;

$v := LLINK[v]$

end;

end.

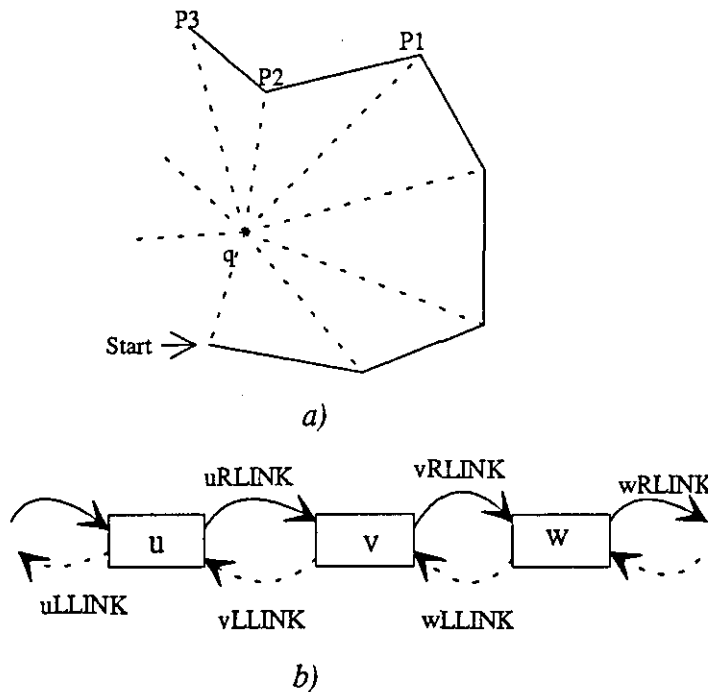


Figure 7- 1. Diagram of Graham scan: a) polygon P and its internal point q
b) doubly-link list of Graham scan

An implementation of the “left turn” check for $p_{i-1}p_ip_{i+1}$ is to test if point p_i is at the left of line $p_{i-1}p_{i+1}$. This is calculated by

$$c = x_i(y_{i-1} - y_{i+1}) + y_i(x_{i+1} - x_{i-1}) + (x_{i-1}y_{i+1} - x_{i+1}y_{i-1}) \quad (7.3)$$

if $c > 0$ then the point p_i is at the left of the line [Pavilidis 1982].

Circumference of arbitrary direction section:

The convex hull algorithm deals with planar curves only. Original co-ordinates are three dimensional for an arbitrary direction section. A geometric transformation is needed to convert them into two dimensional form. The required geometric transformation contains the following steps:

S1. compute the normalised equation of the section plane as

$$\pi: Ax + By + Cz + D = \frac{Ax + By + Cz + D}{\pm\sqrt{A^2 + B^2 + C^2}} = x \cos\alpha + y \cos\beta + z \cos\gamma - p = 0$$

S2. construct a new 3D co-ordinate system from the plane equation in which the z' -axis is at the direction of the plane normal $(\cos\alpha, \cos\beta, \cos\gamma)$, and x', y' axes are located on the plane.

S3. compute the rotation matrix between two co-ordinate systems.

S4. transform all vertices of the section into new co-ordinate system so that a planer curve is obtained.

It is clear that these steps need little interaction with an operator and are easy to be implemented by computer automatically.

7.2 Two-dimensional measurement**7.2.1 The area of a planar closed curve**

A planar closed curve can be approximated by a piecewise linear function which is a polygon. Let vertices of the polygon be $\{(x_0, y_0), (x_1, y_1), \dots, (x_n, y_n)\}$ and $(x_0, y_0) = (x_n, y_n)$, then the area that the polygon surrounds is calculated by

$$A = \frac{1}{2} \sum_{i=0}^{n-1} (y_i + y_{i+1})(x_i - x_{i+1}) \quad (7.4)$$

The area of any section of a surface can be calculated by transforming the section into a 2-D co-ordinate system as discussed in Section 7.1.2.

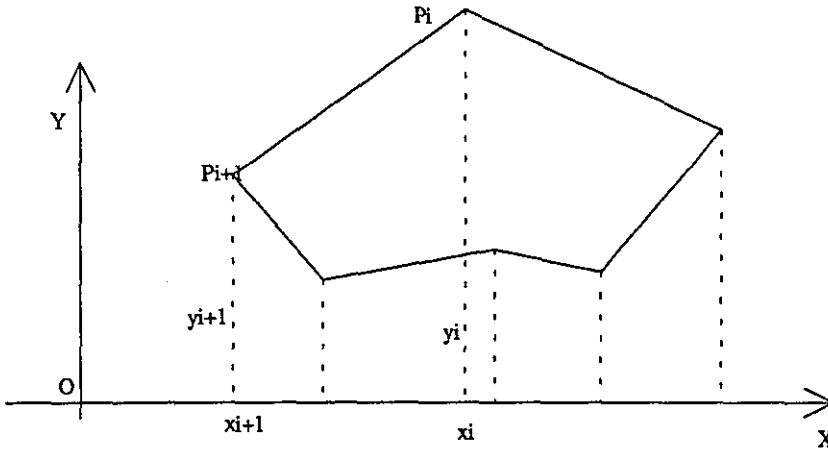


Figure 7-2. Area of any polygon.

7.2.2 The area of a surface

Assuming that a surface is represented by triangular meshes, the area of a surface is a sum of all mesh areas. The area of a 3D triangle can be computed by

$$A = \sqrt{p(p-a)(p-b)(p-c)}, \quad p = \frac{1}{2}(a+b+c) \quad (7.5)$$

where a , b and c are the lengths of the three sides of the triangle respectively.

The main difficulty in the calculation of surface area is how to identify and represent the boundary of the surface. The basic approximation to an irregular boundary surface is to use a number of strips. Each strip is defined in such a way that the top and bottom edges of the strip are increased along a parametric or co-ordinate direction. This could make the computation more efficient. Top and bottom edges of a surface segment may contain different number of co-ordinate points, therefore a triangular mesh representation is essential to connect them.

7.3 Three-dimensional geometric measurement

7.3.1 Volume between two planar sections

The volume between two parallel planar sections can be calculated by second-order Newton-Coats (Simpson) integral formula[Radston. 1965]:

$$V \approx \frac{h}{6}(A' + A'' + 4A_0) \quad (7.6)$$

Here the A' and A'' are the areas of top and bottom slice respectively and A_0 is the area of middle slice, h is height from bottom slice to top slice, as illustrated in Figure 7-3.

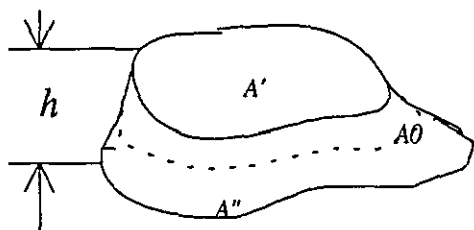


Figure 7-3. Volume between two cross-sections

The accuracy of calculated volume from the above formula depends on the step length h . A number of middle slices may be needed to improve the calculation accuracy if the value of h is too great. Two cases are considered when middle slices are inserted: two planes coincide with a direction of raw data or parameter (in a parametric surface case), or two planes are oblique to the data direction. In the first case, direct picking of a middle slice from the raw data or surface interpolation (in parametric surface situation) is possible. In the latter case, the middle slices must be generated by a series of plane-surface intersections with h as an increment of plane distance.

If two planar sections are not parallel, the volume can be divided into two parts: one part is composed of two parallel sections and the other is composed of two non-parallel sections. The described computational scheme is still applicable. For those generated middle slices between two non-parallel sections, the intersection method may contain two steps, one is plane-surface intersection and other is plane-plane intersection.

7.3.2 Volume between two surfaces

There are many types of relative relationship between two surfaces. The containment relationship is the most useful in 3-D surface anthropometry, if surface A completely contains surface B as its internal object, then the volume between surface A and B can be calculated as a difference of their internal volumes. In some situations a reference plane or surface must be provided for the volume calculation. An example of this will be given in the next section.

7.4 Application examples of the higher dimensional geometric measurement

Two examples are presented in this section to illustrate the application of high dimensional measurement. The major concerns are how to automatically define the data boundary, and how to carry out a batch processing of the data interrogator on a bulk of scanned data.

7.4.1 Surface area measurement of breast tissue

As discussed in the previous sections, the measurement of surface area requires an explicit definition of the boundary of the surface. However, it is quite often that the body model is not associated with an anthropometric data file or feature points set. For example, the scanned data from a LASS whole body scanner, after curve-fitting and editing, is represented by the LASS shape matrix. The breast boundary can not be identified from this data format. For a batch processing of the scanned data of a number of subjects, an automatic method to define breast boundary is desirable.

A method is developed to define breast boundary from the LASS shape matrix. The breast segment is defined as cross-sections from **under-bust** to **chest** level. For each cross-section of the breast, the boundary of data is defined to start from the central point C of the front body to a point S at the side body as illustrated in Figure 7-4. In fact the point S is decided by the intersection of line q and the cross-section. The equation of the straight line q is described by its starting point C and angle β . The angle β is experimentally measured from the plotting of cross-section curves of breast segment.

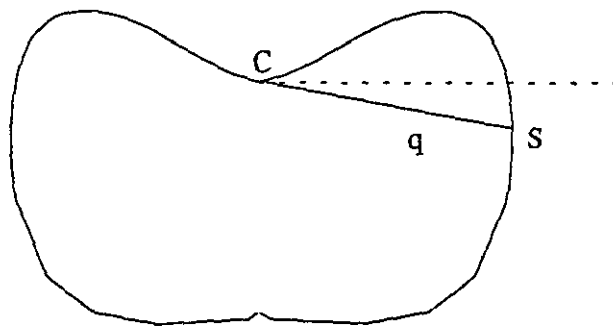


Figure 7- 4. Breast boundary definition from cross-sectional data

In this way, the breast region has its one vertical boundary at central front points, an other vertical boundary at the intersection points S, its lower boundary at the under bust section, and its upper boundary at the chest (under arm) section. To produce a high accuracy calculation, the surface data between under-bust level and chest level are generated by surface interpolation of the LASS shape matrix so that the density of data is at an order of 5 mm x 5mm. The number of data points in two adjacent slices may be unequal. The triangular mesh is used to connect two adjacent slices and the total surface area of breast is a sum of all the triangular mesh areas.

7.4.2 Volume calculation of breast tissue

The boundary of surface for volume calculation of breast is defined in a way discussed in the previous section. The volume of breast is approximated by a volume which is composed of an internal surface S, body surface and two parallel cross sections (under bust and chest section). The internal surface S is formed by the line q defined in the last section. The process is treated as volume calculation between two planar sections. The area of each middle section is a numerical integration of a closed curve, i.e. equation 7.4. Its accuracy depends on the number of points on a cross-sectional curve and the distance between two adjacent sections.

7.4.3 Conclusion

The application examples given in this section shows the importance of a standardised data format. Batch processing of survey data, especially comparison and average of data, requires an explicit definition of the reference information. Anthropometry is heavily based on the anatomical landmarks which should be properly described in the data format.

The LASS shape matrix provides a way to deal with anthropometric landmarks to some extent. As an alternative, a data structure of anthropometric landmarks could be included in a surface data file. This allows a greater flexibility in the data form of the body surface.

7.5 Software structure of 3-D surface anthropometry

There is an increasing need for software of 3-D surface anthropometry as more surface scanners become available. From the point of view of software design, the structure of such a software is of moderate complexity. It has similar functions to CAD software but has less geometric entities to be manipulated. The software structure for 3D surface anthropometry may be decomposed into five function groups based on various applications and the discussion in the last section. These contain: data import/export, data editing and modelling, anthropometric measurement, data interrogation and special modelling functions. Individual groups may contain a number of sub-functions which have been identified from several application areas such as the clothing industry, computer-aided ergonomics, and medical research. Figure 7-5 lists the main functions of these groups:

Function decomposition of the software for 3D surface anthropometry

Data Import/Export

Import Format:
LASS
Cyberware (movie.byu)
Cyberware (RGB colour)
Other data formats (e.g. 3DSCAN)
Open Inventor
IGES
Special format for anthropometry
....
Export Format:
IGES
DXF
LASS shape matrix
Anthropometric report
Special format for anthropometry
....

Data Editing and Modelling

Noise remove
Curve-fitting
Surface modelling
Multi-view fusion
Data split and merge
....

Anthropometric measurement (Data Interrogation)

RGB or grey-scale image mapping to the scanned data
Anthropometric landmarks display
Defining landmarks
Distance measurement
Arc length and circumference measurement
Defining section
Surface trimming

- Area measurement
- Surface definition and intersection
- Volume measurement
- Surface normal
- Tangential and curvature
- Offset surface

....

Special modelling functions

- Anthropometry-based modelling
 - Interface to anthropometric data file
 - Simple proportional polyline modelling from anthropometric data
 - Complex surface modelling from anthropometric data
- Articulation modelling
- Deformable modelling

.....

Figure 7- 5. Software functions of 3D surface anthropometry

7.5.1 Data import and export

This function group is to deal with geometric data of the human body imported from the scanning/digitisation process and exportation to other application packages. A wider range of data formats has been considered in this function because a variety of data input devices exist, and different application areas may be involved. Data formats consist of four major types: scanner-oriented format such as LASS, and Cyberware; more general mainstream 3-D graphics format -- Open Inventor which can include texture data of a surface; CAD-oriented format, such as IGES, DXF; and anthropometry-oriented format.

The scanner-oriented data formats, although there is no unified definition, should be standardised into two or three co-ordinate system oriented formats (for example, cylindrical co-ordinate system, Cartesian co-ordinate system) and stored as ASCII code for platform-independent transfer (ESPRIT 3DSCAN project). Inclusion of texture information into a data format can facilitate the feature extraction of anatomical landmarks. This is a reason to employ the Open Inventor format, which still remains in the development stage. The separate geometric and texture file (such as Cyberware's existing data format) is a temporary solution.

CAD-oriented formats are less efficient in describing the raw scanned data. However its popularity in CAD applications is an important factor in the selection of data format, particularly for an export format. IGES and AutoCAD's DXF are the two most common file formats, they should be selected for data exchange with CAD software.

None of the existing formats give room for anthropometric landmarks. Research is necessary to identify what landmarks are needed and how to record them. The anthropometric measurement related to the landmarks will rely on the texture (image) data of a surface for the time being. It is expected that anthropometric landmark data can first be incorporated into the export data format. An anthropometric report is the most important output from the software. A standardised report format should therefore be defined.

7.5.2 Data editing and modelling

This function manipulates the raw surface data and transforms them into an operable entity for further applications. Basic operations include noise removal, curve-fitting, surface modelling, multiview fusion, and data merge and split. Most surface scanners operate on the basis of structured light triangulation. Singular reflective light cause large sparkles which corrupt the raw data. Noise removal is necessary to acquire a clean and smooth surface. Curve-fitting and surface modelling can help to reduce data and to maintain the integrity of the data.

Multiple view fusion is a function to integrate data from multiple scanning or multiple view scanning when a complete body surface is needed. Alignment of raw scanned data and reconstruction of an entire surface are two key functions.

Data split and merge is useful if the parts of a body need to be modelled. For instance to acquire arm or leg from a whole body data requires a data split operation. A naming mechanism might be necessary to manage and group the modified data. At an early stage of development a unified data structure for entity definition is important. The data output from this function could be in a polygon mesh or wireframe form.

7.5.3 Anthropometric measurements and data interrogation

The mathematics for anthropometric measurements have been discussed in the previous part of this chapter. This section focuses on the data representation required for data interrogation. An essential problem in taking anthropometry-measurement from scanned data is how to relate landmarks to the surface data. The methods for the labelling and mapping of landmarks have certain influences on the data structure and software implementation. As discussed in chapter 6, there are three possibilities to identify

feature points in 3D scanned data: combining image and scanned data; using auxiliary camera systems or image sources; geometric analysis of scanned data. If the second method is used, the software must load relevant camera calibration parameters for data mapping, which is usually not practical since data sources vary from one system to another. An alternative method is to register landmark information into the raw scanned data file. This should be accomplished in a scanning software and require an extended data format for raw scanned data.

The first method requires a one-to-one mapping between image data and scanned data. Therefore image data and mapping function are required. The third method needs a surface analysis process to identify landmarks.

The data interrogation function mainly includes the computation of surface normal, tangential and curvature, and offset surface. It is not clear at present how to relate these measurements to anthropometry applications. However, the evaluation of human-device interface (for example, helmet, oxygen mask, etc.) will lead to a revised design of the original device and this may need higher order geometric information about the interface surface. Complex surface characteristics related to stress, or pressure analysis need higher-order geometric information as well.

7.5.4 Special modelling functions

This group creates new human body models from existing anthropometric data and scanned data. Three kinds of models may be defined: anthropometry-based surface model; skeletal model and deformable model. These models need anthropometric data in modelling process, i.e. the shape and proportion change of the model must conform with some anthropometric measurements. For this, further consolidated research is required. For example, the anthropometry-based modelling aims to interface an existing anthropometric database (survey data) and to generate a body model which satisfies the specified anthropometric measurement. A key problem is how to bring different anthropometric data sources (for example, different countries) into the modelling process. The deformable surface modelling is a challenge task.

7.6 Summary

This chapter discussed background mathematics and useful computational methods necessary for a 3D surface anthropometry environment. Further refinement of these methods depends on the particular implementation of software. Discussion in this chapter aimed to facilitate the identification of the requirements for 3D surface anthropometry.

There are a few software tools for anthropometry applications. However, these tools do not completely meet the discussed requirements of 3D surface anthropometry. There is, in fact, no formal requirements specification produced for 3-D surface anthropometry software yet. This chapter described a top-level function of 3-D surface anthropometry software. Functional modules were discussed from the point of view of requirements analysis. They were data import/export, data editing and modelling, anthropometric measurement, data interrogation, and special modelling. These needs to be further decomposed and specified for implementation.

CHAPTER EIGHT

CONCLUSIONS AND FUTURE WORK

This thesis has concentrated on 3-D surface modelling of the human body and 3-D surface anthropometry.

3-D surface anthropometry is a new interdisciplinary subject. There is no general accepted definition of its functions and boundaries. This thesis has identified and focused on three essential components of 3-D surface anthropometry, namely: data collection, data modelling and interrogation of surface data of the human body. Technologies employed in these three aspects are developed from multiple disciplines, such as computer-aided geometric design, photogrammetry, computational geometry and image processing. These technologies are explored in this thesis by two particular applications of 3-D surface anthropometry: 3-D surface modelling of the human body and data interrogation of the scanned data of the human body surface.

3-D surface modelling of the human body (i.e. 3-D body modelling) was developed independently prior to 3-D surface anthropometry. However their development is currently interlaced and 3-D body modelling can be viewed as a data modelling component of 3-D surface anthropometry. Methods and techniques developed in 3-D body modelling aim to assist transferring the raw scanned data to data interrogation applications. On the other hand, 3-D body modelling requires anthropometric data to enhance its applicability. Building a 3-D surface model with anthropometric controllability is important and useful. However, no report on this topic has been found to-date. This thesis has developed an innovative method to create a 3-D surface model of the human torso utilising 'linear' anthropometric measurements.

The ultimate objective of 3-D surface anthropometry is to measure the human body surface in an electronic manner and to transfer anthropometric measurement data to other applications. This thesis develops a method for locating anthropometric/feature landmarks during the data collection and data interrogation stages, and demonstrates the application of these feature data. A wider analysis of mathematics for data interrogation and software structure for 3-D surface anthropometry has also been presented.

The following section summarises the results achieved and the limitations which exist in the current research. Future work is discussed in the last section.

8.1 Results and Limitations

8.1.1 3-D surface modelling of the human body

8.1.1.1 Surface interpolation

This thesis has demonstrated the suitability of the NURBS function and the skinning interpolation in parametric surface modelling of the human body. Non-uniform parametric B-spline gives greater flexibility in dealing with parameterisation problems. The parameter-based relocation of cross-sectional data proposed in this research improves the quality of an interpolated surface. It makes a uniform distribution of interpolated data complying with parameter values, instead of spatial co-ordinates. This is particularly useful in coping with unequal number of data points or different distribution of interpolated data in cross-sectional curves, which often occurs due to uneven cross-sectional shapes. The parameter-based relocation method also makes better use of limited interpolated data points.

The selection of interpolated cross-sections reflects the essential requirement for an application of the skinning method. Key cross-sections for the human torso have been defined from anthropometric conventions so that the generated torso surface can pass precisely through these key slices.

A rational form of NURBS has been considered in the geometric algorithms implemented in this thesis. The interpolation of weighting values are not carried out in current skinning processes because there is no *a priori* knowledge about the distribution of assigning weighting. However, the surface generation can be adjusted by assigning different weightings when necessary.

One limitation of the surface interpolation is that it requires a family of well defined cross-sectional curves. At present, these cross-sectional curves are manually generated by an interactive curve-fitting procedure which is time-consuming. It would be desirable that the key cross-sectional slices could be automatically selected from the shape features of the body surface.

8.1.1.2 Surface approximation

Surface approximation is a suitable method for data reduction since the raw scanned data usually contain a huge amount of co-ordinates. This thesis explored a new application of surface approximation, i.e. to refill void data caused by an automatic arm trimming process. Although curve approximation can be used to refill the void data slice by slice, the resultant surface is not smooth. Complete surface approximation could produce a smooth surface but it is not feasible because the data dimensions are too large. Therefore, a tensor-product approximation is proposed, which employs a similar scheme to the skinning method. It not only reduces the dimension of computation from $(N \times M)^2$ to $(N \times M)$ but also provides greater flexibility. For example, the interpolation and approximation can be combined together. The selection of the number of control points for longitude and latitude direction could be two independent procedures.

8.1.2 Anthropometry based surface modelling

This thesis has explored a way to create an anthropometry based surface model of the human body. A reference body approach is developed on the basis of available cross-sectional data. The approach aims to create a 3-D surface model to meet width and depth measurements at nine key cross-sections. Therefore, the core of the method is to generate each cross-sectional data individually according to its width and depth. This has been achieved by modifying a reference shape vector for the cross-section. The skinning technique is employed to interpolate nine generated cross-sections.

Simple anthropometric measurements are insufficient to define a proper 3-D shape for a body. For this purpose, a shape classification of cross-sections and anthropometry based shape indices was explored. The shape classification of the hip level was accomplished from scanned data on 76 subjects by hierarchical cluster analysis. Three classes were categorised and they can be indexed by simple anthropometry. A reference shape vector database could be built up accordingly.

It is desirable to have a more general method to modify the reference shape vector by any combination of width, depth and girth constraints. An experimental analysis of the relationship between these three variables was presented in Chapter 4. The generation of a cross-sectional curve with constraint to its width or depth or girth has an infinite solution.

Obtaining an approximate, but reasonable, solution relies on the knowledge about the shape of the human body. To build up the relationship between width, depth and girth is a step towards more general anthropometry based modelling.

The shape classification presented in this thesis needs verification from other cross-sections. Therefore it could produce a family of reference bodies which could be selected by shape indices from nine key levels.

8.1.3 3-D surface anthropometry

8.1.3.1 Camera calibration

Camera calibration plays an essential role in a 3-D measurement task. It is concerned with the calibration of a digital camera system with the context of accurate surface scanning and location of feature points by image mapping.

Although the camera calibration has been widely investigated (refer to Chapter 5), detailed evaluation of various calibration methods, especially related to 2-D image noise, is not well documented. This thesis has thoroughly derived the non-linear optimisation method for thirteen and eleven parameters camera models and discussed an extensive simulation experiment which compares two types of calibration methods, namely: the non-linear optimisation method and Tsai's method. The experimental results show that image noise has a severe influence on parameter estimation of the camera. It also shows that the non-linear optimisation method, when applied to a camera model with radial distortion only (eleven parameters), gives the best performance in terms of stability of noise environment, RMS residual error and precision of estimated parameters.

Calibration to two kinds of digital cameras, and a frame grabber system has been studied. This includes stability testing of the sensing process, acquiring camera centre, analytical calibration of the camera parameters by applying the non-linear optimisation and Tsai's methods. It was found that image distortion and pixel fluctuation in a vidicon camera are more severe than those in a CCD camera. The pixel drift in a vidicon camera exceeds the noise threshold for a stable estimation of camera parameters by the tested calibration methods.

8.1.3.2 Locating anthropometric landmarks

Acquisition of anthropometric landmark positions is necessary for a surface anthropometric measurement task. This thesis focuses on methods to locate artificial marks from LASS scanned data. An artificial mark is a reliable source for defining feature points of the human body surface providing that the texture of body surface can be captured. Approaches for relating the image of artificial marks to their 3-D co-ordinates have been briefly reviewed and analysed. A new approach to incorporate a separate imaging system to the LASS system was developed in order to acquire the grey-scale picture of a body surface. A ray-tracing method was innovated to fulfil mapping of 2-D grey-scale image to 3-D scanned data. This approach can be applied to acquire the co-ordinates of artificial/natural anthropometric marks in association with 3-D scanned data. An example is presented to acquire the boundary of a region for surface trimming of raw scanned data. The accuracy of the mapping method was evaluated by measuring 3-D co-ordinates of seven points from a sphere-like object and comparing them with a CMM measurements.

Surface trimming is a specific application of data interrogation. The trimming boundary identified from a series of feature points forms a polygon in 3-D co-ordinate space. The surface trimming in Cartesian co-ordinate space is difficult. A strategy to convert the surface data and trimming boundary into a cylindrical co-ordinate system was implemented for simplifying the trimming process. This was employed to trim a region of the LASS raw data.

Mapping the 2-D image of feature points to 3-D surface modelling was implemented in 3-D Cartesian space, but not in parametric space. Mapping feature points to 3-D parametric space would be useful if the surface is represented as a parametric surface. As a result higher dimensional and higher order data interrogation tasks can be implemented in the parametric space. Many well-established methods in computer aided geometric design can then be directly integrated into 3-D surface anthropometry.

8.1.3.3 Data interrogation

Principal data interrogation tasks in 3-D surface anthropometry were specified according to the dimension of a measurement and the order of surface characteristics (derivatives).

Zero-dimensional measurement locates anatomical landmarks or feature points from scanned surface data. It forms the foundation for higher-order measurement but partially belongs to the data collection stage. High-dimensional measures were analysed and relevant mathematics and algorithms were discussed. The thesis also gives a high level structure analysis of functions in 3-D surface anthropometry in order to show the prospect of a general purpose tool kit for 3-D surface anthropometry.

8.2 Future work

3-D surface anthropometry is a new research area. This thesis explores major aspects in 3-D surface anthropometry to a rational extent. However, there remains many further developments and it is recommended that the future work should embark upon the following three topics:

- 1) Development of a complete surface model for the whole human body: the model should be in a hierarchical structure which allows the decomposition and integration of sub-models. Each sub-model could be a model of a part of the human body or a sub-surface from one particular perspective. The integrated whole body model could support different applications, such as clothing design, anthropometric measurement, workplace evaluation, ergonomic engineering, animation and virtual reality applications.
- 2) Anthropometry based surface modelling: further research is required to create 3-D surface models which conform with existing and future anthropometric survey data. The models could be generated from these 'linear' anthropometric survey data with support from accumulated 3-D surface shape information. It is also necessary to produce a complete classification to all key cross-sections used in the surface modelling.
- 3) A 3-D surface anthropometry software toolkit: since major components of 3-D surface anthropometry have been identified from various applications and a number of in-house software have been developed, we are now at a stage to produce a software toolkit for more general use. Such a software toolkit could promote a standardised data exchange format for human body modelling across different domains.

REFERENCES

- Abdel-Aziz, Y.I., [1973] 'Lens distortion and close range', *Photogrammetric Engineering*, pp. 611-615,
- Abdel-Aziz, Y.I., and Karara, H.M., [1974] 'Direct linear transformation from comparator co-ordinates in close-range photogrammetry', *Proceedings of ASP Symposium on Close-Range Photogrammetry*, Urbana, Ill.
- Aliverti, A., Ferrigno, G., & Pedotti, [1993] 'Surface analysis by laser beam scanning and stereophotogrammetry', *Videometrics II, Proceedings of SPIE*, Vol. 2267, pp. 209-219
- American Society of Photogrammetry (ASP), [1980] *Manual of Photogrammetry*, Fourth Edition
- Arridge, S., Moss, J., Linney, A., James, D., [1985] 'Three dimensional digitization of the face and skull', *Journal of Max.-Facial Surgery*, Vol. 13, pp 136-143
- Badler, N.I., Phillips, C.B., and Webber, B.L., [1993] *Simulating Humans*, Oxford University Press
- Barnhill, R.E., and Kersey, S.N., [1990] 'A marching method for parametric surface/surface intersection', *Computer Aided Geometric Design*, Vol. 7, pp. 257-280
- Bhatia, G., Godhwani, A., and Vannier, M., [1992] 'Fiducial point localization in multisensor 3D surface scanning', *Biomedical Image Processing and Three-dimensional Microscopy, Proceedings of SPIE* Vol. 1660, pp 375-386
- Blostein, Steven D. and Huang, Thomas S. [1987] 'Error analysis in stereo determination of 3-D point positions', *IEEE Transactions on Pattern Analysis and Machine Intelligence* Vol. 9, No. 6
- Boissonnat, J-D., [1988] 'Shape reconstruction from planer cross sections' *Computer Vision, Graphics and Image Processing*
- Brown, D.C., [1971] 'Close-range camera calibration', *Photogrammetric Engineering*, pp. 855-866
- Burke, P. H., Banks, P., Beard, L. F., Tee, J. and Hughes, C., [1983] 'Stereophotographic measurement of change in facial soft tissue morphology following surgery', *British Journal of Oral Surgery*, Vol. 21, pp. 237-245

References

- Calvert, T., Bruderlin, A., Dill, J., Schiphorst, T. & Welman, C., [1993] 'Desktop animation of multiple human figures', *IEEE Computer Graphics & Applications*, pp. 18-26, May
- Case, K., Porter, J.M., & Bonney, M.C., 1990] 'SAMMIE: a man and workplace modelling system', in Karwowski, W., Genaidy, A.M. and Asfour, S.S., (Ed) *Computer-Aided Ergonomics*, Taylor & Francis
- Case, K., Xiao, D-C., Porter, M.,[1995] 'Car seat and occupant modelling using CAD', in *Advances in Manufacturing Technology IX*, Edited by David Stockton and Charles Wainwright, Taylors & Francis, London
- Chang, M. and Tai, W-C. [1995] '360-degree profile noncontact measurement using neural network', *Optical Engineering*, Vol. 34, No. 12, pp. 3572-3576
- Chen, X. & Schmitt, F., [1994] 'Surface modelling of range data by constrained triangulation', *Computer-Aided Design*, Vol. 26, pp. 632-645, No. 8
- Computer Design Inc. [1995] *Manual of DesignConcept3D* Version 5.0 1995. Grand Rapids, Michigan, USA
- Curry, S., Baumrind, S. and Anderson, J.M. [1986] 'Calibration of an array camera', *Photogrammetric Engineering and Remote Sensing*, Vol. 52, No. 5, pp. 627-636, May
- Cyberware 1996. http://www.cyberware.com/product/wholebody_datasheet.html
- Das, B. and Sengupta, A., [1995] 'Computer-aided human modelling programs for workstation design', *Ergonomics*, Vol. 38, No. 9, pp. 1958-1972
- de Boor, [1978] *A Practical Guide to Spline*, Springer-Verlag, New York
- Dooly, M., [1992] 'Anthropometric modeling programs-a survey', *IEEE Computer Graphics & Applications*, Vol. 2, No.9, pp. 17-26
- DP 1992, Institut für Photogrammetrie Universität Bonn, [1992] *First Course in Digital Photogrammetry*
- Drerup, B., Frobin, W., Hieholzer, E., [1983] 'Computerized evaluation of surface measurement of kyphosis and scoliosis', *Moiré Fringe Topography*, pp. 155-162, Gustav Fischer, Stuttgart

References

- Drerup, B., Hierholzer, E., [1987] 'Automatic localization of anatomical landmarks on the back surface and construction of a body-fixed coordinate system', *Journal of Biomechanics*, Vol. 20, No. 10, pp. 961-970
- Drerup, B., Hierholzer, E., [1994] 'Back shape measurement using video rasterstereography and three-dimensional reconstruction of spinal shape', *Clinical Biomechanics*, Vol. 9, No.1 pp. 28-36
- Duda, R.O., Hart, P. E., [1973] *Pattern Classification and Scene Analysis*, John Wiley & Sons, Inc. New York
- Duncan, J. and Mair, S., [1983] *Sculptured Surface in Engineering and Medicine*
- Dunn, S.M., Keizer, R.L., and Yu, J., [1989] 'Measuring the area and volume of the human body with structured light', *IEEE Transactions on Systems, Man, and Cybernetics*, Vol. 19, No. 6, pp 1350-1364
- El-Hakim, S.F., [1989] 'A hierarchical approach to stereo vision', *Photogrammetric Engineering and Remote Sensing*, Vol. 55, No. 4, pp. 443-448, April 1989
- Erb, R.A., [1992] 'A plea for data useful in the fourth dimension', *Proceeding of Electronic Imaging of the Human Body*, Dayton, Ohio, pp. 151-160, 1992
- ESPRIT Project 6911, 3DSCAN, Draft Range Image Standard (RIS), 1993
- Everitt, B. S., [1993] *Cluster Analysis*, Third Edition, Edward Arnold, London
- Faig, W. [1975] 'Calibration of close-range photogrammetric systems: mathematical formulation', *Photogrammetric Engineering and Remote Sensing*, Vol. 41, No. 10, pp. 1479-1486
- Fan, H. and Yuan, B. [1993] 'High-performance camera calibration algorithm', *Videometrics II, Proceedings of SPIE*, Vol. 2267, pp. 2-11, Boston,
- Farin, G.,[1988] *Curves and Surfaces for Computer Aided Geometric Design*, Academic Press, Inc.
- Faugeras, O., [1993] *Three-Dimensional Computer Vision: A Geometric Viewpoint*, The MIT Press
- Faux, T & Pratt, M. [1979] *Computational Geometry for Design and Manufacture*. Ellis Horwood

References

- Ferrario, V. F., Sforza, C., Miani Jr, A. and Serrao, G., [1995] 'A three-dimensional evaluation of human facial asymmetry', *Journal of Anatomy*, Vol. 186, pp. 103-110
- Foley, J.D., Van Dam, A., [1990] *Computer Graphics: Principles and Practice*, (2nd Edition), Addison-Wesley
- Fortin, C., Gilbert, R., Beuter, A., Laurent, F., Schiettekatte, J., Carrier, R. and DeChamplain, B., [1990] 'SAFEWORK: a microcomputer-aided workstation design and analysis. New advances and future developments', in Karwowski, W., Genaidy, A.M. and Asfour, S.S., (Ed) *Computer-Aided Ergonomics*, Taylor & Francis
- Frobin, W., Hierholzer, E., [1982] 'Analysis of human back shape using surface curvature', *Journal of Biomechanics*, Vol. 15, No. 5, pp. 379-390.
- Frobin, W., Hieholzer, E., [1983] 'Automatic measurement of body surface using rasterstereography', *Photogrammetric Engineering and Remote Sensing*, Vol. 49, No. 3, pp 377-382
- Frobin, W., Hieholzer, E., Drerup, B., [1983] Shape analysis of surfaces: Extraction of shape from coordinate data, *Moire Fringe Topography*, Gustav Fischer, Stuttgart, 1983.
- Fryer, J., [1992] 'Recent developments in camera calibration for close-range applications', *International Archive of Photogrammetry & Remote Sensing*, pp. 594-599, 1992,
- Fryer, J., Clarke, T.A., and Chen, J., [1994] 'Lens distortion for simple C-mount lenses', *International Archive of Photogrammetry & Remote Sensing*, pp. 97-101, 1994
- Fryer, J. G., and Mason, S. O., [1989] 'Rapid lens calibration of a video camera', *Photogrammetric Engineering and Remote Sensing*, Vol. 55, No. 4, pp. 437-442
- Gazzuolo, E., Delong, M., Lohr, S., LaBat, K., Bye, E., [1992] Predicting garment pattern dimensions from photographic and anthropometric data, *Applied Ergonomics*, Vol. 23, No. 3
- Gill, P.E., Murray, W., and Wright, M.H., [1981] *Practical Optimization*, Academic Press, Inc
- Glassner, A.S. [1993] (ed) *An Introduction to Ray-Tracing*, Academic Press
- Golub, G.H., Van Loan, C.F., [1983] *Matrix Computations*, The Johns Hopkins University Press

References

- Godhwani, A Bhatia, G. and Vannier, M. W. [1994] 'Calibration of a multisensors structured light range scanner', *Optical Engineering*, Vol. 33, No. 4, pp. 1159-1167
- Green, R.J., Self, H.C., and Ellifritt, T.S., [1995] (Ed) *50 Years of Human Engineering: History and Cumulative Bibliography of the Fitts Human Engineering Division 1945-1995*, Crew systems directorate, Armstrong Laboratory, Air Force Materiel Command, Wright-Patterson Air Force Base, Ohio, 1995
- Grosky, W. I., Tamburino, L. A., [1990] 'A unified approach to the linear camera calibration problem', *IEEE Transactions on Pattern Analysis and Machine Intelligence* Vol. 10, No. 7, pp. 663-671
- Gruen, Armin W. [1989] 'Digital photogrammetric processing system: current status and prospects', *Photogrammetric Engineering and Remote Sensing*, Vol. 55, No. 5, pp. 581-586
- Halim Munjy, R. A. [1986] 'Self-calibration using the finite element approach', *Photogrammetric Engineering and Remote Sensing*, Vol. 52, No. 3, pp. 411-418
- Halioua, M., Krishnamurthy, R., Liu, H. and Chiang, F., [1985] 'Automated 360° profilometry of 3-D diffuse objects', *Applied Optics*, Vol. 24, No. 14, pp. 2193-2196
- Hanna, S.L., Abel, J.F., and Greenberg, D. P., [1983] 'Intersection of parametric surface by means of look-up tables', *IEEE Computer Graphics & Application*, pp. 39-48, October 1983
- Hanrahan, P. [1993] 'A survey of ray-surface intersection algorithms', in Glassner (ed) *An Introduction to Ray-Tracing*, Academic Press
- Holt, R. J., Netravali, A. N. [1991] 'Camera calibration problem: some new results', *CVGIP: Image Understanding*, Vol. 54, No. 3, pp. 368-383
- Hoschek, J., [1988] 'Intrinsic parametrization for approximation', *Computer Aided Geometric Design*, Vol. 5, pp. 27-31
- Hu, G. and Stockman, G., [1989] '3-D surface solution using structured light and constraint propagation', *IEEE Transactions on Pattern Analysis and Machine Intelligence*, Vol. 11, No. 4, pp. 390-402

References

- Ishida, A., Mori, Y., Kishimoto, H., Nakazima, T., Tsubakimoto, H., [1987] 'Body shape measurement for scoliosis evaluation', *Medical & Biological Engineering & Computing*, September 1987
- Ito, M., and Ishida, A., [1994] 'A non-iterative procedure for rapid and precise camera calibration', *Pattern Recognition*, Vol. 27, No. 2, pp. 301-310
- Ito, N., Kurokawa, T., Shinozaki, A., Nakano, H., [1982] 'Measurement of human body form using pattern processing techniques', *Anthropometry & Clothing*, IEA'82, pp. 220-221
- Jansa, J., Huang, Y., and Trinder, J.C., [1993] 'Problems of precise target location and camera orientation in digital close-range photogrammetry'. *Videometrics II, Proceedings of SPIE*, Vol. 2267, pp. 151-161
- Jones, B., and Plassmann, P., [1995] 'An instrument to measure the dimensions of skin wounds', *IEEE Transactions on Biomedical Engineering*, Vol. 42, No. 5, pp 464-470
- Jones, P. R. M, West, G, Harris, D. H., Read, J. B., [1989] 'The Loughborough anthropometric Shadow Scanner (LASS)', *Endeavour*, Vol.13, no 4, pp.162-168
- Jones, P. R. M., West, G. and Brook-Wavell, K., [1994] 'Interrogation of 3D body data for applications in manufacturing industries', in Directorate of the Science and Engineering Research Council, *Application of Computers to Manufacturing*
- Jones, P. R. M., Baker, A., Hardy, C. and Mowat, A., [1994] 'Measurement of body surface area in children with liver disease by a novel 3-D body scanning device', *European Journal of Applied Physiology*, Vol. 68, No. 6, pp. 514-518
- Jones, P.R.M, Li, P., Brook-Wavell, K., West, G, [1995] 'Format for human body modelling from 3-D body scanning', *International Journal of Clothing Sciences and Technology*, Vol. 7, No. 1, pp. 7-16
- Karwowski, W., Genaidy, A.M. and Asfour, S.S., [1990] (Ed) *Computer-Aided Ergonomics*, Taylor & Francis, 1990
- Kauppinen, H., Tapio Seppänen and Matti Pietikäinen, [1995] 'An Experimental Comparison of Autoregressive and Fourier-Based Descriptors in 2D Shape Classification', *IEEE Transactions on Pattern Analysis and Machine Intelligence*, Vol.17, No.2.

References

- Kayis, B, Iskander, PA, [1994] 'Three-dimensional human model for IBM/CATIA system', *Applied Ergonomics*, Vol. 25, No. 6, pp 395-397
- Ko, H., and Badler, N.I., [1996] 'Animating human locomotion with inverse dynamics', *IEEE Computer Graphics & Applications*, pp 50-59, March 1996
- Ko, H., Kim, M-S., Park, H-G., and Kim, S-W., [1994] 'Face sculpturing robot with recognition capability', *Computer-Aided Design*, Vol. 26, No. 11, pp 814-821
- Lee, E.T.Y., [1989] 'Choosing nodes in parametric curve interpolation', *Computer Aided Design*, Vol. 21, No. 6, pp. 363-370
- Lee, R.B., and Fredricks, D.A., [1984] 'Intersection of parametric surface and a plane', *IEEE Computer Graphics and Application*, pp. 48-51, August 1984.
- Lenz, R. K. and Tsai, R. Y., [1988] 'Techniques for calibration of the scale factor and image center for high accuracy 3-D machine vision metrology', *IEEE Transactions on Pattern Analysis and Machine Intelligence* Vol. 10, No. 5, pp. 711-722
- Lewis, J.R.T, & Sopwith, T., [1996] 'Three-dimensional surface measurement by microcomputer', *Image and Vision Computing*, Vol. 4, No. 3, pp. 159-166
- Liu, Y-C., Huang, T.S. and Faugeras, O.D. [1990] 'Determination of camera location from 2-D to 3-D line and point correspondences', *IEEE Transactions on Pattern Analysis and Machine Intelligence* Vol. 10, No. 1, pp. 28-37
- MaCleod, A., [1986] 'Medical application of close range photogrammetry', *Photogrammetry Record*, Vol. 12, No. 68, pp 155-165
- Manthey, D.W., Knapp II, K.N. and Lee, D. [1994] 'Calibration of a laser range-finding co-ordinate measuring machine', *Optical Engineering*, Vol. 33, No. 10, pp. 3372-3380
- Masmoudi, L., Coronado, J. L. *et al*, [1993] 'Stereo camera calibration with distortion model and using forgetting factor', *Videometrics II, Proceedings of SPIE*, Vol. 2267, pp. 14-22
- McCartney, J. and Hinds, B.K., [1992] 'Computer aided design of garments using digitized three-dimensional surfaces', *Proc. of Institute of Mechanical Engineers Part B: Journal of Engineering Manufacture*, Vol. 206, pp.199-206

References

- Moss, J., Linney, A., Grindrod, S., Mosse, C., [1989] 'A laser scanning system for the measurement of facial surface morphology', *Optical and Laser in Engineering*, Vol. 10, pp 179-190
- Naftel, A.J., [1989] 'Three-dimensional techniques for the geometric study of expanded skin surfaces', Ph.D. Thesis, Bradford University, England
- Nalwa, V.S. and Binford, T. O., [1986] 'On detecting edges', *IEEE Transactions on Pattern Analysis and Machine Intelligence* Vol. 8, No. 6, pp. 699-714
- Nurre, J. H., Whitestone, J. J., Hoffmeister, J. W. and Burnsides, D. B., [1995] 'Removing impulse noise from human head scan data' Technical Report of Armstrong Laboratory, Wright-Patterson Air Force Base, AL/CF-TR-1995-0054, March 1995
- Okabe, H., Imaoka, H., Tomiha, T., and Niwaya, H., [1992] 'Three dimensional apparel CAD system', *SIGGRAPH'92 Computer graphics* Vol. 26, No. 2, pp. 105-110
- Oppenheim, A. V., Schafer, R. W., [1989] *Discrete-time Signal Processing*, Prentice-Hall International, Inc.
- Pavlidis, T., [1982] *Algorithm for Graphics and Image Processing*, Computer Science Press
- Penn, M.A., [1991] 'Camera calibration: a quick and easy way to determine the scale factor', *IEEE Transaction on Pattern Analysis and Machine Intelligence*, Vol. 13, No. 12, pp. 1240-1245
- Piegl, L. [1989a] 'Modifying the Shape of Rational B-spline. Part 1: Curves' *Computer-Aided Design* Vol. 21, No. 8, pp509-518
- Piegl, L. [1989b] 'Modifying the Shape of Rational B-spline. Part 2: Surfaces' *Computer-Aided Design* Vol. 21, No. 9, pp539-546
- Piegl, L [1991] 'On NURBS: A Survey' *IEEE Computer Graphics & Application*. Vol. 11, pp 55-71
- Piegl, L. A., and Richard, A. M.,[1995] 'Tessellating trimmed NURBS surface', *Computer-Aided Design*, Vol. 27, No. 1, pp. 16-26
- Preparata, F.P., and Shamos, M. I., [1985] *Computational Geometry: An introduction*, Springer-Verlap, New York
- Radston, A., [1965] *A First Course in Numerical Analysis*, McGraw-Hill

References

- Research Institute of Human Engineering for Quality Life (RIHEQL), [1995] Technical Report, Osaka, Japan
- Rioux, M., [1992] '3D digital imaging of the human body using laser scanners', *Proceeding of Electronic Imaging of the Human Body*, Dayton, Ohio, pp. 49-66, 1992
- Robinette, K. and Whitestone, J., [1994] 'The need for improved anthropometric methods for the development of helmet systems', *Aviation, Space, and Environment Medicine*, pp. A95-A99, May 1994
- Robson, S., Clarke, T. A. and Chen, J. [1993] 'Suitability of the Pulnix TM6CN CCD camera for photogrammetric measurement', *Videometrics II, Proceedings of SPIE*, Vol. 2267, pp. 66-77
- Roebuck, J.A., Kroemer, K.H.E., and Thomson, W.G., [1975] *Engineering Anthropometry Method*, John Wiley & Sons
- Rosenfeld, A. and Kak, A. C., [1982] *Digital Picture Processing*, 2nd edition, Academic Press
- Sarker, B. and Menq, C.-H., [1991] 'Parameter optimization in approximating curves and surfaces to measurement data', *Computer Aided Geometric Design*, Vol. 8, No. 4, pp. 267-290
- Schreiner, R.E., and Sanders, J.E., [1995] 'A silhouetting shape sensor for the residual limb of a below-knee amputee', *IEEE Transactions on Rehabilitation Engineering*, Vol. 3, No. 3, pp 242-253
- Sheng, X., and Hirsch, B.E., [1992] 'Triangulation of trimmed surface in parametric space', *Computer-Aided Design*, Vol. 24, No. 8, pp. 437-443
- Shih, S-W., Hung, Y-P. & Lin, W-S., [1993] 'Accurate linear technique for camera calibration considering lens distortion by solving an eigenvalue problem', *Optical Engineering*, Vol. 32, No. 1, pp. 138-149
- Shih, S-W., Hung, Y-P. & Lin, W-S., [1995] 'When should we consider lens distortion in camera calibration', *Pattern Recognition*, Vol. 28, No. 3, pp. 447-461
- Shortis, M. R. [1988] 'Precision evaluations of digital imagery for close-range photogrammetric applications', *Photogrammetric Engineering and Remote Sensing*, Vol. 54, No. 10, pp. 1195-1401

References

- Shortis, M. R., Snow, W. L. *et al.* [1993] 'Influence of storage media on the accuracy and repeatability of photogrammetric measurement using CCD camera', *Videometrics II, Proceedings of SPIE*, Vol. 2267, pp. 80-92
- SPIE, *Videometrics II, Proceedings of SPIE*, Vol. 2267, 1993
- Stewart, G.W., [1973] *Introduction to Matrix Computations*, Academic Press, Inc.
- Tabatabai, A. J. and Mitchell, O. R. [1984] 'Edge location to subpixel values in digital imagery', *IEEE Transactions on Pattern Analysis and Machine Intelligence* Vol. 6, No. 2, pp. 188-219
- Takabu, H., Matsuyama, Y., Akizuki, M., Kuki, T., Uetake, M., Isoda, H., Yanagisawa, S., [1986] 'Analysis of side view of human body shape', *Japanese Journal of Domestic Sciences*, Vol. 38, No. 11, pp. 33-41
- Takabu, H., Uetake, T., Uetake, M., Matsuyama, Y., Isoda, H., Yanagisawa, S., [1990] 'Analysis of side view of human body shape (Part 2) Reproducibility on principal component of human posture', *Japanese Journal of Domestic Sciences*, Vol. 41, No. 1
- Takasaki, H., [1970] 'Moiré Topography', *Applied Optics*, Vol. 9, No. 6, pp. 1467-1472
- Takasaki, H., [1973] 'Moiré Topography', *Applied Optics*, Vol. 12, No. 4, pp. 845-850
- Taylor, P. J., & Shoben, M., [1990] *Grading for the fashion industry: the theory and practice*. Cheltenham: Thornes
- Telmat Informatique, MIDA general information, 1994
- Thalmann, N.M., and Thalmann, D., [1991] *Computer Animation*, Springer-Verlag
- Tsai, R. Y., [1987] 'A versatile camera calibration technique for high-accuracy 3D machine vision metrology using off-the-shelf TV camera and lenses', *IEEE Journal of Robotics and Automation*, Vol. 3, No. 4, pp. 319-344
- Uesugi, M., [1991] 'Three-dimensional curved shape measuring system using image encoder', *Journal of Robotics and Mechatronics*, Vol. 3, No. 3, pp. 190-195
- Vannier, M., Pilgram, T., Bhatia, G., Brunnsden, B., Commean, P., [1991] 'Facial surface scanner', *IEEE Computer Graphics and Application*, pp 72-80, November 1991.,

References

- Vannier, M., Pilgram, T., Bhatia, G., Brunnsden, B., Nemecek, J., Young, V., [1993] 'Quantitative three-dimensional assessment of face-lift with an optical facial surface scanner', *Annals of Plastic Surgery*, Vol. 30, No. 3, March 1993
- Vannier, M., Yates, R.E., and Whitestone, J.J., [1992] (Ed.), *Proceedings of Electronic Imaging of the Human Body*, Dayton, Ohio, 1992
- Wan, X., and Xu, G-Y., [1996] 'Camera parameters estimation and evaluation in active vision system', *Pattern Recognition*, Vol. 29, No. 3, pp. 439-447
- Wang, Y., Mitiche, A. and Aggarwal, J., [1987] 'Computation of surface orientation and structure of objects using grid coding', *IEEE Transactions on Pattern Analysis and Machine Intelligence*, Vol. 19, No. 1, pp. 129-137.
- Waters, K., [1992] 'Physically based modelling for facial synthesis', *Proceeding of Electronic Imaging of the Human Body*, Dayton, Ohio, pp. 49-66, 1992
- Wei, G-Q., Ma, S-D. [1994] 'Implicit and explicit camera calibration: theory and experiments', *IEEE Transactions on Pattern Analysis and Machine Intelligence* Vol. 16, No. 5, pp. 469-480
- Weissman, S.,[1968] 'Anthropometric photogrammetry', *Photogrammetric Engineering*, pp 1134-1140, 1968
- Weng, J., Cohen, P. and Herniou, M. [1992] 'Camera calibration with distortion models and accuracy evaluation', *IEEE Transactions on Pattern Analysis and Machine Intelligence* Vol.14, No. 10, pp. 965-992
- West, G., [1994] Ph.D. Thesis, *Automated Shape Anthropometry*, University of Loughborough, 1994, UK
- Wolf, P. R. [1983] *Elements of Photogrammetry*, International Edition, McGraw-Hill Book Company
- Wong, K-W. and Ho, W-H., [1986] 'Close-range mapping with a solid state camera', *Photogrammetric Engineering and Remote Sensing*, Vol. 55, No. 1, pp. 67-74
- Woodward, C. D., [1988] 'Skinning techniques for interactive B-spline surface interpolation', *Computer Aided Design* Vol. 20, pp 441-451
- Yee, S.R. and Griffin, P.M. [1994] 'Three-dimensional imaging system', *Optical Engineering*, Vol. 33, No. 6, pp. 2070-2075

References

- Yoshida, R., Miyazawa, T., Doi, A. and Otsuki, T.,** [1993] 'Clinical planning support system-ClipSS', *IEEE Computer Graphics and Application*, Vol. 33, No. 6, pp. 76-84

Appendix A. Some mathematic methods in this thesis

A-1. Q-R factorisation for solving the least square problem [Golub & Van Loan 1983, Stewart 1973]

The least square (LS) problem is described as:

$$\min \|Ax - b\|_2 \quad A \in \mathbb{R}^{m \times n}, b \in \mathbb{R}^m \quad (\text{A-1.1})$$

It is equivalent to the problem

$$\min \|(Q^T A)x - (Q^T b)\|_2 \quad Q^T Q = I_m \quad (\text{A-1.2})$$

Suppose that the orthogonal matrix Q has been computed such that

$$Q^T A = R = \begin{bmatrix} R_1 \\ 0 \end{bmatrix} \begin{matrix} n \\ m-n \end{matrix} \quad (\text{A-1.3})$$

is upper triangular. If

$$Q^T b = \begin{bmatrix} c \\ d \end{bmatrix} \begin{matrix} n \\ m-n \end{matrix} \quad (\text{A-1.4})$$

then

$$\|Ax - b\|_2^2 = \|Q^T Ax - Q^T b\|_2^2 = \|R_1 x - c\|_2^2 + \|d\|_2^2 \quad \text{for any } x \in \mathbb{R}^n \quad (\text{A-1.5})$$

If $\text{rank}(A) = \text{rank}(R_1) = n$, then x_{LS} is defined by the upper triangular system $R_1 x_{LS} = c$. And the square sum of residual is $\rho_{LS}^2 = \|d\|_2^2$. Thus the full rank LS problem can be solved by computing (A-1.3), which is referred to as the Q-R factorisation. In following algorithms, the elements of a vector are expressed by Greek letters with subscript, for example,

$$A = \{ \alpha_{ij} \}, b = \{ \beta_i \}.$$

Algorithm A-1.1. (QR factorisation) Let $A \in \mathbb{R}^{m \times n}$ and $r = \min \{ m-1, n \}$. This algorithm returns elementary reflectors U_1, U_2, \dots, U_r such that $A_{r+1} = U_r U_{r-1} \dots U_1 A$ is upper trapezoidal. The reflector U_k are in the form $U_k = I - \pi_k^{-1} u_k u_k^T$, where $u_k = (0, \dots, 0, v_{kk}, v_{k+1,k}, \dots, v_{mk})$. The nonzero elements v_{ik} overwrite α_{ik} . The scalars π_k overwrite $\alpha_{m+1,k}$. The nonzero element of A_{r+1} , that is the element R_{r+1} , overwrite the corresponding elements of A , except for the diagonal element ρ_{kk} which are store in $\alpha_{m+2,k}$.

1) For $k = 1, 2, \dots, r$ Do

$$1) \eta = \max \{ |\alpha_{ik}| : i = k, k+1, \dots, m \}$$

$$2) \text{ If } \eta = 0$$

$$1) \alpha_{m+1,k} = 0$$

$$2) k = k+1$$

$$3) \alpha_{ik} \leftarrow v_{ik} = \alpha_{ik}/\eta \quad (i = k, k+1, \dots, m)$$

$$4) \sigma = \text{sign}(v_{kk}) \sqrt{v_{kk}^2 + \dots + v_{mk}^2}$$

$$5) v_{kk} = v_{kk} + \sigma$$

$$6) \alpha_{m+1,k} \leftarrow \pi_k = \sigma v_{kk}$$

$$7) \alpha_{m+2,k} \leftarrow \rho_{kk} = -\eta \sigma$$

$$8) \text{ For } j = k+1, k+2, \dots, n \text{ Do}$$

$$1) \tau = \pi_k^{-1} \sum_{i=k}^m v_{ik} \alpha_{ij}$$

$$2) \alpha_{ij} \leftarrow \alpha_{ij} - \tau v_{ik} \quad (i = k, k+1, \dots, m)$$

$$2) \text{ If } m \leq n, \alpha_{m+2,m} \leftarrow \rho_{mm} = \alpha_{mm}$$

End of the algorithm.

Algorithm A-1.2. (Solution of the linear least square problem) Let the matrix A have linearly independent columns, let the array A contain the output of Algorithm A-1.1, and let $b \in \mathbb{R}^n$. This algorithm solves the linear least square problem of minimising the 2-norm of $r = b - Ax$. The residual vector r at the minimum overwrite b .

$$1) \text{ For } i = 1, 2, \dots, n \text{ Do}$$

$$b \leftarrow U_i b$$

$$2) \gamma_i = \beta_i \quad (i = 1, 2, \dots, n)$$

$$3) \text{ Solve the system } Rx = c$$

$$4) \beta_i = 0 \quad (i = 1, 2, \dots, n)$$

$$5) \text{ For } i = n, n-1, \dots, 1 \text{ Do}$$

$$b \leftarrow U_i b$$

A-2. Jacobian matrix of the non-linear optimisation method for 13 parameters camera model

Collinearity condition equations for a complete camera model containing radial and tangential lens distortion are:

$$\begin{aligned} u_i - u_0 + \delta_x &= -f_x \frac{m_{11}(X_i - X_c) + m_{12}(Y_i - Y_c) + m_{13}(Z_i - Z_c)}{m_{31}(X_i - X_c) + m_{32}(Y_i - Y_c) + m_{33}(Z_i - Z_c)} = -f_x \frac{R}{Q} \\ v_i - v_0 + \delta_y &= -f_y \frac{m_{21}(X_i - X_c) + m_{22}(Y_i - Y_c) + m_{23}(Z_i - Z_c)}{m_{31}(X_i - X_c) + m_{32}(Y_i - Y_c) + m_{33}(Z_i - Z_c)} = -f_y \frac{S}{Q} \end{aligned} \quad (\text{A-2.1})$$

where

$$\begin{aligned} \delta_x &= \hat{u} \cdot \hat{k}_1 \cdot r^2 + \hat{p}_1(r^2 + 2\hat{u}^2) + 2\hat{p}_2\hat{u}\hat{v} \\ \delta_y &= \hat{v} \cdot \hat{k}_1 \cdot r^2 + 2\hat{p}_1\hat{u}\hat{v} + \hat{p}_2(r^2 + 2\hat{v}^2) \\ \hat{u} &= u_i - u_0 \\ \hat{v} &= v_i - v_0 \\ r^2 &= \hat{u}^2 + \hat{v}^2 \end{aligned} \quad (\text{A-2.2})$$

Here the higher order items of radial and tangential distortions of the lens have been neglected.

Equ. (A-2.1) relates 3-D control points and their image co-ordinates in pixel plane. Equ. (A-2.2) describes the lens distortion in pixel plane. The interior parameters of the camera model are $(u_0, v_0, f_x, f_y, k_1, p_1, p_2)$, and the exterior parameters of the camera system are $(\omega, \phi, \kappa, X_c, Y_c, Z_c)$. In total there are 13 unknowns to be estimated.

The elements of the transformation matrix M are:

$$\begin{aligned} m_{11} &= \cos \phi \cos \kappa \\ m_{12} &= \sin \omega \sin \phi \cos \kappa + \cos \omega \sin \kappa \\ m_{13} &= -\cos \omega \sin \phi \cos \kappa + \sin \omega \sin \kappa \\ m_{21} &= -\cos \phi \sin \kappa \\ m_{22} &= -\sin \omega \sin \phi \sin \kappa + \cos \omega \cos \kappa \\ m_{23} &= \cos \omega \sin \phi \sin \kappa + \sin \omega \cos \kappa \\ m_{31} &= \sin \phi \\ m_{32} &= -\sin \omega \cos \phi \\ m_{33} &= \cos \omega \cos \phi \end{aligned} \quad (\text{A-2.3})$$

Let

$$\begin{aligned} F_i &= (u_i - u_0 + \delta_x(\hat{u}, \hat{v})) \cdot Q + f_x R \\ G_i &= (v_i - v_0 + \delta_y(\hat{u}, \hat{v})) \cdot Q + f_y R \end{aligned} \quad (\text{A-2.4})$$

The non-linear least square optimisation seeks

$$\min \frac{1}{2} \sum_{i=1}^m (F_i^2 + G_i^2) \quad (\text{A-2.5})$$

The linearisation of Equ. (A-2.5) is

$$\min \frac{1}{2} \left\| \begin{bmatrix} J_F \\ J_G \end{bmatrix}_i \cdot \mathbf{p} + \begin{bmatrix} F \\ G \end{bmatrix}_i \right\|_2^2 \quad (\text{A-2.6})$$

The Jacobian matrix of functions F and G at the i th control point is

$$\begin{aligned} \mathbf{J}_i &= \begin{bmatrix} J_F \\ J_G \end{bmatrix}_i \\ &= \begin{bmatrix} \frac{\partial F_i}{\partial u_0} & \frac{\partial F_i}{\partial v_0} & \frac{\partial F_i}{\partial f_x} & \frac{\partial F_i}{\partial f_y} & \frac{\partial F_i}{\partial \hat{k}_1} & \frac{\partial F_i}{\partial \hat{p}_1} & \frac{\partial F_i}{\partial \hat{p}_2} & \frac{\partial F_i}{\partial \omega} & \frac{\partial F_i}{\partial \phi} & \frac{\partial F_i}{\partial \kappa} & \frac{\partial F_i}{\partial X_c} & \frac{\partial F_i}{\partial Y_c} & \frac{\partial F_i}{\partial Z_c} \\ \frac{\partial G_i}{\partial u_0} & \frac{\partial G_i}{\partial v_0} & \frac{\partial G_i}{\partial f_x} & \frac{\partial G_i}{\partial f_y} & \frac{\partial G_i}{\partial \hat{k}_1} & \frac{\partial G_i}{\partial \hat{p}_1} & \frac{\partial G_i}{\partial \hat{p}_2} & \frac{\partial G_i}{\partial \omega} & \frac{\partial G_i}{\partial \phi} & \frac{\partial G_i}{\partial \kappa} & \frac{\partial G_i}{\partial X_c} & \frac{\partial G_i}{\partial Y_c} & \frac{\partial G_i}{\partial Z_c} \end{bmatrix} \\ &= \begin{bmatrix} a_1^i & a_2^i & a_3^i & a_4^i & a_5^i & a_6^i & a_7^i & a_8^i & a_9^i & a_{10}^i & a_{11}^i & a_{12}^i & a_{13}^i \\ b_1^i & b_2^i & b_3^i & b_4^i & b_5^i & b_6^i & b_7^i & b_8^i & b_9^i & b_{10}^i & b_{11}^i & b_{12}^i & b_{13}^i \end{bmatrix} \end{aligned} \quad (\text{A-2.6})$$

The detailed expression of \mathbf{J} 's elements are:

$$\begin{aligned} a_1 &= -[(3\hat{u}^2 + \hat{v}^2) \cdot k_1 + 6\hat{u}p_1 + 2\hat{v}p_2 + 1] \\ a_2 &= -2(\hat{u}\hat{v}k_1 + \hat{v}p_1 + \hat{u}p_2) \\ a_3 &= R/Q \\ a_4 &= 0 \\ a_5 &= \hat{u} \cdot r^2 \\ a_6 &= r^2 + 2\hat{u}^2 \\ a_7 &= 2\hat{u}\hat{v} \end{aligned}$$

$$\begin{aligned}
 a_8 &= [(\hat{u} + \delta_x) \cdot (-m_{33} \cdot \Delta Y + m_{32} \cdot \Delta Z) + f_x (-m_{13} \cdot \Delta Y + m_{12} \cdot \Delta Z)] / Q \\
 a_9 &= [(\hat{u} + \delta_x) \cdot (\cos \phi \cdot \Delta X + \sin \omega \cdot \Delta Y - \sin \phi \cos \omega \cdot \Delta Z) + \\
 &\quad f_x \cdot (-\sin \phi \cos \kappa \cdot \Delta X + \sin \omega \cos \phi \cos \kappa \cdot \Delta Y - \cos \omega \cos \phi \cos \kappa \cdot \Delta Z)] / Q \\
 a_{10} &= f_x \cdot (m_{21} \Delta X + m_{22} \Delta Y + m_{23} \Delta Z) / Q \\
 a_{11} &= -[(\hat{u} + \delta_x) \cdot m_{31} + f_x \cdot m_{11}] / Q \\
 a_{12} &= -[(\hat{u} + \delta_x) \cdot m_{32} + f_x \cdot m_{12}] / Q \\
 a_{13} &= -[(\hat{u} + \delta_x) \cdot m_{33} + f_x \cdot m_{13}] / Q
 \end{aligned}$$

$$\begin{aligned}
 b_1 &= -2(\hat{u} \hat{v} k_1 + \hat{v} p_1 + \hat{u} p_2) \\
 b_2 &= -[(\hat{u}^2 + 3\hat{v}^2) \cdot k_1 + 2\hat{u} p_1 + 6\hat{v} p_2 + 1] \\
 b_3 &= 0 \\
 b_4 &= S / Q \\
 b_5 &= \hat{v} \cdot r^2 \\
 b_6 &= 2\hat{u} \hat{v} \\
 b_7 &= r^2 + 2\hat{v}^2 \\
 b_8 &= [(\hat{v} + \delta_y) \cdot (-m_{33} \cdot \Delta Y + m_{32} \cdot \Delta Z) + f_y (-m_{23} \cdot \Delta Y + m_{22} \cdot \Delta Z)] / Q \\
 b_9 &= [(\hat{v} + \delta_y) \cdot (\cos \phi \cdot \Delta X + \sin \omega \cdot \Delta Y - \sin \phi \cos \omega \cdot \Delta Z) + \\
 &\quad f_y \cdot (\sin \phi \sin \kappa \cdot \Delta X - \sin \omega \cos \phi \sin \kappa \cdot \Delta Y + \cos \omega \cos \phi \sin \kappa \cdot \Delta Z)] / Q \\
 b_{10} &= -f_x \cdot (m_{11} \Delta X + m_{12} \Delta Y + m_{13} \Delta Z) / Q \\
 b_{11} &= -[(\hat{v} + \delta_y) \cdot m_{31} + f_y \cdot m_{11}] / Q \\
 b_{12} &= -[(\hat{v} + \delta_y) \cdot m_{32} + f_y \cdot m_{12}] / Q \\
 b_{13} &= -[(\hat{v} + \delta_y) \cdot m_{33} + f_y \cdot m_{13}] / Q
 \end{aligned}$$

where $\Delta X = (X_A - X_C)$, $\Delta Y = (Y_A - Y_C)$, and $\Delta Z = (Z_A - Z_C)$

Appendix B. Publications

- Li, P. and Jones, P. R. M. 'Anthropometry-based surface modelling of the human torso', Proceedings of the 1994 ASME international Computer in Engineering conference, pp. 469-474, Minneapolis, Minnesota, USA, 1994
- Jones, P. R. M., Li, P., Brook-Wavell, K., and West, G. 'Format for human body modelling from 3D scanning', *International Journal of Clothing Science and Technology*, Vol. 7, No. 1, pp. 7-16, 1995
- Li, P. and Jones, P. R. M., 'Mapping grey-scale image to 3D surface scanning data by ray-tracing', IS&T/SPIE Symposium on Electronic Imaging: Science and Technology (3D Image Capture), San Jose, California, USA, February 1997
- Li, P. and Jones, P. R. M., 'Automatic editing and curve-fitting of 3-D surface scan data of the human body', International Conference on Recent Advances in 3D Imaging and Modelling, Ottawa, Canada, May 1997

ANTHROPOMETRY-BASED SURFACE MODELING OF THE HUMAN TORSO

Peng Li and Peter R. M. Jones
HUMAG Research Group
Department of Human Sciences
Loughborough University of Technology
Leicestershire LE11 3TU
United Kingdom

ABSTRACT:

There is an increasing need for computerized surface model of the human body in human growth, garment design and ergonomics. However, there is a shortage of three-dimensional (3-D) models of the human body in practical applications. This paper presents a new approach for constructing a 3-D surface model of the human torso using anthropometry. The torso is created from a reference body of average shape which is represented by a family of cross-sectional curves. The shape and size of the reference body can be modified according to anthropometric data. This approach has been implemented on a personal computer. The resulting 3-D model is a parametric surface based on non-uniform B-splines and can easily be exported to other computer aided design applications.

Key words: Anthropometry, 3-D surface modeling, human body

INTRODUCTION

Computerized models of the human figure have been developed over some considerable time. Requirements on the representative form and accuracy of body models vary with applications. Simple models describe the human form as stick figures using lines or wire frame surface models and have been widely used in ergonomic design, evaluation and simulation of workstations (Fetter 1980, 1982, Nilsson 1994). Complex models, based on parametric surfaces or polygon patches can better represent surface shape of the human body and, therefore

have their merit in human growth (Jones *et al.* 1993), computer aided clothing design (McCartney and Hinds 1992) and ergonomic applications.

In contrast with other computer aided geometric modeling tasks, human body modeling usually requires that the geometric model of the body can be modified or controlled according to anthropometry which consists of length, width and circumference measurements (Dooley, 1982). If a human body is modeled by simple geometric entities like line segments, polygons or cylinders, it is relatively easy to modify the dimensions and shapes of these entities according to the anthropometry. However these entities can not give further shape information about a body.

We believe that a parametric surface model is a better approximation of its human counterpart than other geometric entities especially if the shape, volume and surface area of a body are required. However there are some difficulties when relating such a model to simple anthropometric measurements. This paper presents a feasible approach of dealing with these difficulties by representing the human body using a skinning surface. This surface is created by interpolating a family of cross-sectional data called a reference body. The reference body, originally acquired from the output of the Loughborough Anthropometric Shadow Scanner (LASS) (Jones *et al.* 1989), can be modified according to anthropometric data in its dimension and shape.

Such an approach is valuable because it could bridge some gaps between existing 3-D human body scanners and computer-aided design (CAD) applications. Three-dimensional scanners can provide a great deal of raw data

taken from a body surface, and thereby make it possible to build a body model to high precision. However, some difficulties have been recognized. Firstly, 3-D scanners, which can scan the whole human body, are too expensive and too big to be set-up in every design workplace. As a result traditional anthropometric devices and manual measuring methods are still widely used. Unfortunately these traditional methods of measurement cannot give sufficient information about the surface of a body. Secondly, size surveys which have been conducted in many countries should be utilized in modern CAD packages (clothing design, workspace design etc.) so that these packages can have detailed information about the size and shapes of sample populations. It is, therefore, highly desirable to relate anthropometry from cross-sectional or longitudinal size surveys with 3-D surface modeling of the human body.

LASS AND ITS DATA FORMAT

The Loughborough Anthropometric Shadow Scanner (LASS) is a computerized television measurement system based on triangulation principle. It has been successfully used in scanning the whole human body since 1989. The LASS measures radii of a body surface by projecting light strips on a body and turning the body through 360 degrees. LASS digitizes the body surface and produces around 30,000 data points for an average height person which are stored as cylindrical co-ordinates. The LASS output data can precisely represent the human body surface but the amount of data is too big to be manipulated in many CAD systems. Our research group have developed software to edit and reduce output data into a simpler form called the LASS shape matrix (West, 1993).

The LASS shape matrix contains 32 rows of horizontal cross-sectional data of a body. Each data row consists of 16 (x, y) co-ordinates and an additional z value to indicate the height of the cross-section. The sixteen co-ordinates only represent half of a cross-section, although if needed the data row can be expanded to contain 32 co-ordinates of cross-section which allows an asymmetry cross-section to be represented. Figure 1 shows the structure of the LASS shape matrix. The shape matrix represents a human torso surface from the crotch to the neck. In the shape matrix, 8 out of the 32 rows of cross-sectional data are key cross-sectional curves, between which middle slices can be inserted in order to improve the accuracy. These 8 key slices corresponds to particular anatomical positions: crotch, hips, waist, under bust, maximum bust, underarm, bideltoid, and neck. These key slices represent common anthropometric landmark on human torso, and are thereby significant to most applications.

SURFACE MODELLING TECHNIQUES OF HUMAN TORSO

Skinning technique of cross-sectional curves

According to the parametric surface theory, a surface, represented by two parameters u and v , can be defined as:

(1)

where $0 < u, v < 1$.

Equation (1) is often called the tensor product representation of a surface. $N_{i,p}(u)$ and $N_{j,q}(v)$ are basic blending functions of degree p and q in the u and v directions respectively. The control points, $P_{i,j}$, are arranged in a rectangular array and form a control patch. With a set of known control points, a complete surface can be generated as parameters u and v vary from 0 to 1.

In practical applications, however, often only a part of the data points of a surface are known and the surface must be approximated by surface interpolation. For equation (1) the surface interpolation is a process to find out the control points $P_{i,j}$ according to known data points. $P_{i,j}$ can be calculated by solving a $(n+1)(m+1) \times (n+1)(m+1)$ order linear equation system if enough known data points are provided. However, when n and m are large, this approach is very time-consuming and usually not feasible (Farin, 1988).

Another surface interpolation method, called skinning or lofting (Faux and Pratt 1979, Tiller 1983, Woodward 1988 and Piegl 1991), can significantly simplify computation of equation (1) into the computation of $(m+1)$ linear equations with order $(n+1)$ and $(n+1)$ linear equations with order $(m+1)$. The skinning method interpolates the surface over a family of cross-sectional data. These cross-section data vary at the same parametric direction of equation (1), and therefore are often known as isoparametric curves. Moreover, all isoparametric curves should be normalized so that they have the same number of data points and same parameter distribution. More details about the skinning technique has been described by Woodward (1988).

The interpolation of the human torso

As shown in the previous section, the success of the skinning technique relies on the proper selection of the isoparametric curves. It may be a natural selection to take horizontal cross-sections of a human torso as isoparametric curves (say, a family of u parameter curves). As a result the v parameter which varies in the surface's longitudinal direction should coincide with the vertical direction of the human body.

The second important pre-processing work for skinning is to decide on the distribution of parameters u and v . It is desirable to find a uniform distribution of the u parameters by averaging all of the u parameters for cross-sections. Then a curve interpolation can be used to rearrange data points so that they are located at desired parametric values. The averaging could be also used to acquire the distribution of v parameters. An averaged v parameter can provide good compatibility for the longitudinal curves across the front, especially the chest and bust, and the back of a body.

After the normalization procedure, skinning can be performed over known cross sectional curves. Degree 2 or 3 non-uniform B-spline have been used in calculation of u and v direction.

Having found the control points, the cross-sectional data of a body, at any height, can then be calculated by giving a v value in Equation (1). When 32 cross-sectional slices are used in the skinning calculation, a surface with high precision can be acquired. It is found that the number of cross-sections used in the skinning calculation can be further reduced to 10 or 8 slices with permissible loss of accuracy, if these cross-sections are reasonably located at some key geometric positions on the human torso, for example, at shoulder, maximum bust, waist or maximum hips. Figure 2 shows the wire frame of a human torso after skinning.

HUMAN TORSO MODELING WITHIN ANTHROPOMETRIC CONSTRAINT

The selection of anthropometric data

The skinning technique provides a feasible approach for modeling the surface of the human torso by interpolating the LASS cross-sectional data. However, it is difficult to get these cross-sectional data in many application areas where only anthropometric measurements can be taken. For example, in clothing design, tape measurement is still a major means to acquire the surface information about a human body. In order to relate the simple anthropometric measurement to 3-D surface model, an intuitive idea is to modify a family of cross-sections based on available anthropometric data such that the skinning technique can be applied to create a required body shape. Therefore, the selection of anthropometric data, has an important influence on the computational method and the accuracy of resultant model.

A selection has now been made from the user's requirement. It defines 9 levels to be measured on a body. They are: **Maximum Hips, Middle Hips, Waist, Under bust, Bust, Underarm, Shoulder, Base of Neck and Neck.** At each level, the width, the depth (from front to back), the distance from back central line to a wall, and the height of the body, are measured as shown in Figure 3 (a) and (b). The width and the depth are used to constrain the shape of the cross-section, and the distance to a wall is used to control the shape of a body from the side view. These data comprise a basic set of anthropometric measurement required for the recreation of a torso surface.

Body recreation

The cross-sectional curves of the human body are irregular so that they cannot be expressed in an analytical function of width and depth variables of the cross-section. Therefore a numerical approach has been developed to

cope with this problem and consists of the following three steps:

1. Create and store a set of reference shape vectors of cross-sections.
2. Modify the size and the shape of reference shape vectors using anthropometric data of a body and subsequently a new set of cross-sectional curves can be generated.
3. Create a 3-D surface model of the body using the skinning technique on the basis of cross-sectional curves generated in step 2.

The following two sections focus on the discussion about steps 1 and 2.

The creation of a reference shape vector.

The definition of shape vector. The cross-sectional curve of the human torso can be represented in polar co-ordinate form by radius and angle (r_i, b_i) with their origin at the geometric centre of the curve. Considering that a symmetric model of the human torso is being used in most applications, only 16 pairs of co-ordinates on one half round of a cross section are required, as shown in Figure 4. The co-ordinate system is selected so that r_1 locates at 90 degree and r_{16} at 270 degree. There is an equal angle spacing between two adjacent radii, i.e.

$$b_i = (i-1) \times (180/15) \text{ degree, and } i=1 \dots 16.$$

The **shape vector** of one cross-section of the torso is defined as a vector with 16 elements in which the i th element is a ratio of the i th radius to the first radius corresponding to the polar co-ordinate form of the curve. The reason to take a ratio as an element of the shape vector is to exclude the size factor of curve. The shapes of cross-sections among subjects with different dimensions (width and depth) were found to be highly correlated ($r > 0.9$). Hence the shape vector can be extracted so that only the shape information remains and the comparison of the shape different bodies becomes possible.

Extraction and representation of the shape vector.

The extraction of the shape vector consists of three steps:

1. Fit cross-sectional data precisely;
2. Find out the geometric centre of the cross-sectional curve and sample from the cross-sectional curve using a uniform angle interval (180/15 degree);
3. Calculate 16 radii and normalise them into a shape vector.

Finally the shape vector is represented by:

$$S = \{s_1, s_2, \dots, s_{16}\} \text{ and } s_1 = 1$$

$$\text{and } s_i = r_i / r_1, i = 1, \dots, 16.$$

The **reference shape vector** of a cross-section is defined as an average vector of a group of shape vectors from different bodies. The **reference body** is a set of reference shape vectors corresponding to 9 key cross-sectional levels of the human body (defined in last section).

The recreation of the cross-sectional data

The surface data of a body can be recreated from the reference body. The core of the recreation is to modify the reference shape vectors by the anthropometric data taken from 9 key levels of an individual. If depth D and width W are measured from a cross-section of a subject, according to the representation of a polar co-ordinate of cross-section, we have:

$$D = r_1 + r_b,$$

where r_b is the maximum projection of r_i at 270 degree direction.

Defining r'_i as polar radii of a subject's cross-sectional curve, then from

$$s_i = r_i/r_1 \text{ and } s_b = r_b/r_1,$$

we have approximately

$$r'_1 = D/(s_1 + s_b) = D/(1 + s_b)$$

$$r'_i = r'_1 \times s_i, i = 2 \dots 16.$$

The above derivation assumes that the r_1 is a maximum projection of r_i at 90 degree direction. If it is not true, as happens at the bust section of a female body, particular consideration is needed.

Given r'_i all Cartesian co-ordinate pairs (x_i, y_i) of curve can be calculated from:

$$x_i = r'_i \circ \sin(b_i) = r'_i \circ \sin((i-1)180/15)$$

$$y_i = r'_i \circ \cos(b_i) = r'_i \circ \cos((i-1)180/15)$$

However, the above calculation does not consider the constraint of width, so some modifications are required. The modifying method adopted is based on the ratio of width/depth which gives certain indication about the shape of a cross-section. If w' is the ratio of width/depth of anthropometry and w is of the reference shape vector, then their difference t represents the difference between the shape of cross-section of a subject and that of the reference body. The value t is therefore used to adjust the elements of the shape vector. After modifying all 16 elements of shape vector S , the new cross-sectional data are created by calculating r'_i and/or (x_i, y_i) . At this point, a data refitting module is used to smooth generated cross-sectional shape.

Usually the girth is an important variable in traditional anthropometry. A method to generate the cross-sectional data of the human torso within girth constraint has been reported (West, 1993). However, as shown in Table 1, the current method using only width and depth information can also estimate girth in reasonable accuracy. The method being able to relate the cross-section to any two variables among width, depth and girth is to be explored.

THE DESIGN OF THE SYSTEM

A software system based on the principles and techniques discussed above has been implemented. The program, running on IBM compatible i486DX66 personal computer, provides users with an interactive interface to input anthropometric data, to interrogate body information and to output cross-sectional data.

The design and implementation of the program

Figure 5 shows an overview of the software structure of the system. The programme comprises five main modules: Anthropometry Input, Data Grading, Surface Interpolation, Surface Generating and Output. Designed by structured and object-oriented methods these modules are independent of each other and easily modified.

Of the five main modules, the Data Grading and the Surface Interpolation are the two key modules. The Data Grading module inputs anthropometric data and the reference shape vectors and produces the cross-sections. Its interface has been designed so that it accommodates changes in the method of generating cross-sectional data and changes in anthropometric specifications.

The surface interpolation module interpolates cross-sectional curves and generates control point patches of B-splines. Non-Uniform Rational B-Splines (NURBS) are currently used in this module but other blending functions can be adopted. The advantage of using NURBS is that they provide better parameterization and allow the shape at the base of neck and shoulders to be controlled by adjusting weights.

The system is implemented in Borland C++ and Microsoft Windows 3.1. Multiple processes of the program can be created simultaneously under Windows and this enables the user to observe and compare the shapes of several bodies.

The result of experiment

The system has been tested on 10 male and 15 female subjects who were scanned by LASS. Recreated body data were compared with scanning data and a mean difference between them in 15 women is summed up in table 1:

CONCLUSION

This paper describes a system for modeling the 3-D human torso within anthropometric constraints. The technique of skinning cross-sectional data is used in the recreation of the surface of the human body, which proved to be feasible and effective. The use of the reference shape vectors of the human body facilitates the modification of the cross-sectional shape according to width and depth measurement of a cross-section. Further, it leads to the possibility of classifying the shape of cross sections which is important when establishing a better body surface model. Since the system is implemented on a personal computer, it can be readily used on site and, therefore, can be considered as a vehicle for exchange information between the 3-D scanner, site anthropometric measurements and CAD workstations.

REFERENCES

Dooley, M. 1982 "Anthropometric Modelling Program -- A Survey", *IEEE Computer Graphics and Application*, Vol. 2, No. 9, pp. 17-25.

Farin, G. 1988 *Curves and Surfaces for Computer Aided Geometric Design*, Academic Press, Inc.

Faux, T & Pratt, M. 1979 *Computational Geometry for Design and Manufacture*. Ellis Horwood.

Fetter, W. A. 1980 "Computer graphics human figure application of biosterometrics" *Computer Aided Design* Vol. 12, pp.175-179.

Fetter, W. A. 1982 "A Progression of Human Figures Simulated by Computer Graphics", *IEEE Computer Graphics and Applications*, Vol. 2, No. 9, pp. 9-13.

Jones, P R M, Baker, A J, Hardy, C J and Mowat, A P. . Measurement of body surface area in children with liver disease by a novel 3-D body scanning device. *European Journal of Applied Physiology*. (In press 1993)

Jones, P.R.M, West, G.M., Harris, D.H., and Read, J.B. 1989 "The Loughborough anthropometric Shadow Scanner (LASS)", *Endeavour*, Vol. 13, no 4, pp. 162-168.

Magenat-Thalmann, N., Thalmann, D. 1990 *Computer Animation*, Springer-Verleg

McCartney, J. and Hinds, B.K., 1992. "Computer aided design of garments using digitized three-dimensional surfaces," *Proc. of Institute of Mechanical Engineers Part B: Journal of Engineering Manufacture*, Vol. 206 pp. 199-206.

Nilsson, G. 1994 "On Development of Tools for Ergonomic Simulation and Evaluation in a Computerized Environment," Licnciate degree of Engineering University of Göteborg, Sweden

Piegl, L. 1991 " On NURBS: A Survey," *IEEE Computer Graphics & Application*. Vol. 11, No. 1 pp. 55-71.

Tiller, W. 1983 "Rational B-Spline for Curve and Surface Representation" *IEEE Computer Graphics & Application*. Vol. 3, No. pp 55-71.

West, G. M.1993 Ph.D. Thesis, University of Loughborough, UK.

Woodward, C.D. 1988 "Skinning techniques for interactive B-spline surface interpolation " *Computer Aided Design* Vol. 20, pp. 441-451.

Table 1: Mean and Standard Deviation of Error in Recreated Body Data and Scanned Data in 15 Women (Unit:mm)

Position	Width		Depth		Girth(half)	
	Mean	Std	Mean	Std	Mean	Std
Neck	1.11	0.94	-0.11	0.17	-1.36	3.29
Base of Neck	-3.10	2.85	-0.49	0.58	2.41	2.42
Shoulder	-3.30	1.43	-1.61	3.25	2.61	5.60
Underarm	4.24	0.83	-3.37	3.60	-1.44	3.95
Bust*	0.09	0.18	0.04	1.49	n/a	n/a
Under Bust	-0.63	0.50	-0.37	0.19	-1.51	4.38
Waist	-1.19	0.54	-0.11	0.32	-1.05	4.10
Middle Hips	-0.71	0.50	0.11	0.17	-0.77	3.13
Max. Hips	3.08	0.41	0.65	4.24	4.01	2.97

* Subjects were scanned with tight fitting clothing therefore girth data are not comparable.

$$\begin{bmatrix} (x_{1,1} \ y_{1,1}) & (x_{1,2} \ y_{1,2}) & \dots & (x_{1,16} \ y_{1,16}) & z_1 \\ (x_{2,1} \ y_{2,1}) & (x_{2,2} \ y_{2,2}) & \dots & (x_{2,16} \ y_{2,16}) & z_2 \\ & & \dots & & \\ (x_{32,1} \ y_{32,1}) & (x_{32,2} \ y_{32,2}) & \dots & (x_{32,16} \ y_{32,16}) & z_{32} \end{bmatrix}$$

FIGURE 1, THE STRUCTURE OF THE LASS SHAPE MATRIX

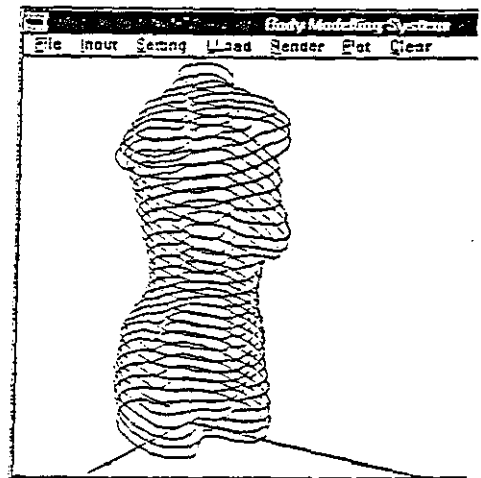


FIGURE 2. WIRE FRAME OF A HUMAN TORSO AFTER SKINNING

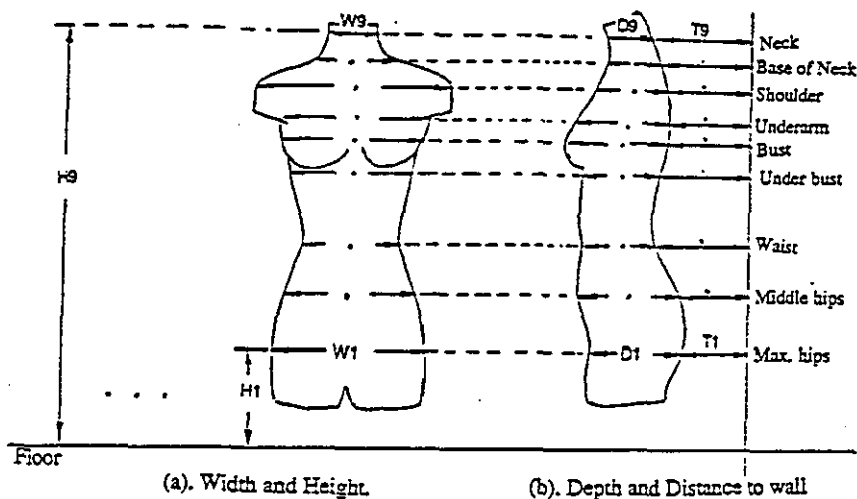


FIGURE 3. THE DEFINITION OF THE ANTHROPOMETRY FOR COMPUTER MODELING

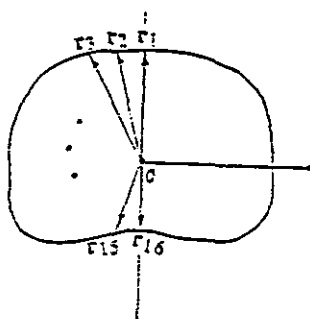


FIGURE 4. SHAPE VECTOR AND ITS LOCATION

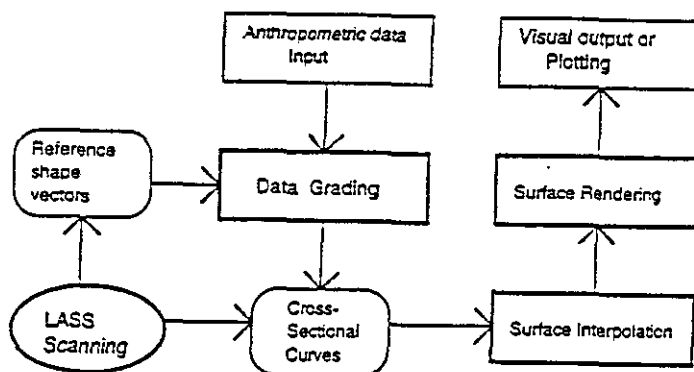


FIGURE 5 SOFTWARE STRUCTURE

Format for human body modelling from 3-D body scanning

Format for
human body
modelling

7

Peter R.M. Jones, Peng Li, Katherine Brooke-Wavell and
Gordon M. West

*HUMAG Research Group, Department of Human Sciences, University
of Loughborough, Loughborough, UK*

Introduction

Computerized three-dimensional (3-D) models of the human body have recently attracted considerable attention in the clothing industry. It has been recognized that the clothing industry needs 3-D human body models to improve the manufacture of design and display stands (manikins) which should represent the average shape and size of the population[1]. The 3-D computer-aided clothing design (CADC) systems, although still in the development stage, require the 3-D body models as a basic element in design and evaluation of clothing[2-4]. Commercial 3-D CADC systems, for example Concept3D (Computer Design Inc., Grand Rapids), require real 3-D body models to enhance their applicability.

The 3-D human body model could be built on the basis of surface data from human beings. However, data collection from the human body surface was a very difficult task before the 3-D body scanner (or digitizer) became available. The 3-D scanner can provide accurate surface co-ordinates of a body in two to three minutes or less and is a novel and useful tool in computer-aided clothing production.

The Loughborough Anthropometric Shadow Scanner (LASS) was developed by our research group to allow digitization of the human body[5]. It is an automated, computerized television 3-D measurement system based on triangulation. The subject being scanned stands on a turnable platform and is rotated through 360 degrees in measured angular increments. A slit of light is projected on to the body in a vertical plane which passes through the centre of rotation. A column of cameras is used to read the image of projected light. From the camera image of the edge of the light slit, the height (h) and horizontal radii (r) of the body at the vertical plane can be easily calculated (as shown in Figure 1). Therefore measured data are 3-D surface co-ordinates of a body in cylinder co-ordinate form. The resolution of measurements in the vertical and the radial

This research was funded by the ACME Directorate of the SERC and by Marks & Spencer plc, Courtaulds (Daintyfit) plc, Kennett & Lindsell Ltd, Fermark, Celestion, Bentwood and Bairdwear. The authors are grateful to Miss Louise M. Deamer for her initial contribution to this work.

*International Journal of Clothing
Science and Technology, Vol. 7
No. 1, 1995, pp. 7-16. © MCS
University Press, 0953-8222*

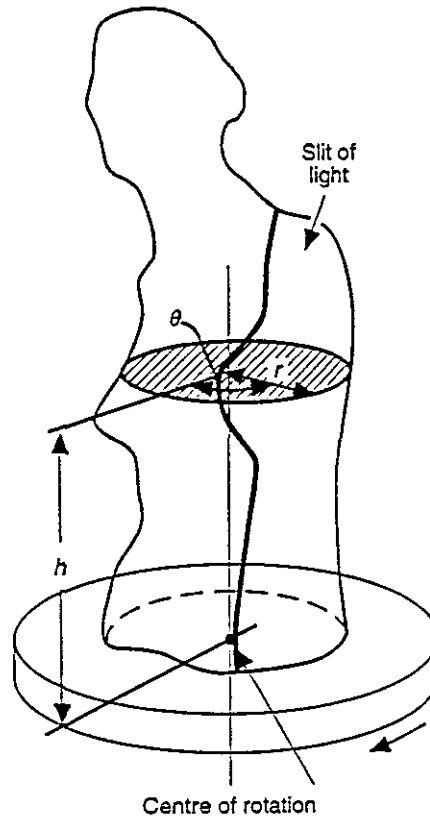


Figure 1.
Principle of LASS
scanner

directions are 1mm and 1.6mm respectively, according to the camera resolution. For a person of average height about 30,000 data points are acquired by LASS after initial data reduction from 315,000 raw data points.

Until recently, only a few commercial automated 3-D body scanners covering the whole body have been reported[6,7]. Although these work on different principles, the amount of data produced by them is also large. Further reduction was required to assemble data into a form suitable for specific applications. This article addresses these issues and their applications in human body modelling for the clothing industry.

Data reduction: LASS shape matrix

Criteria for data reduction

Tasks in body modelling based on 3-D scanned data are basically a surface fitting problem. Usually the objective of data reduction is to achieve an optimal fitting using the smallest number of data points. However, there are some further considerations in practice. For a surface model of the human body to be used in the clothing industry, there are several factors which should be taken into consideration:

-
- Reduced data sets should be easy to output to a geometric modeller for computer-aided design (CAD) systems.
 - Reduced data sets should contain major anthropometric information used in the clothing industry.
 - Reduced data sets from a group of scanned individuals should allow comparison and averaging.

Format for
human body
modelling

9

Data format suitable for CAD packages. Most modern CAD packages can represent a 3-D surface in many data forms, most commonly polygon patches and blend splines. Among different techniques of surface blending, the skinning technique is a suitable candidate for representation of the human body surface since it interpolates a family of cross-sectional curves. Polygon form, if not related to an efficient reconstruction algorithm, would be inaccurate or uneconomic.

The format of the data file for exchange between different hardware and software platforms should be written in plain text. In the CAD domain, for example, two widely used text file formats are Initial Graphics Exchange Specification (IGES) and AutoCAD's DXF. Unfortunately, they represent too many geometric entities and are unnecessarily complicated for our application. The body can be more simply represented using only data for one surface entry and the necessary auxiliary information.

Anthropometric information needed in clothing industry. Anthropometry, as required for clothing design, mainly consists of circumferences, length and width measurements. The circumferences related to the human trunk are usually taken at the levels of hips, waist, underbust, maximum bust, chest and neck[8]. It is desirable that some of the anthropometric measurements can be easily extracted from the data file without interrogating surfaces generated from the data file.

Comparison and averaging of body shapes. Size surveys from sample populations play an important role in obtaining standards for the sizing and the grading of garments. Three-dimensional scanners can now be used to conduct size and shape surveys of sample populations for the clothing industry. However, the data collected would be of limited use as a collection of individual measurements, so some means of describing the shape of the group as a whole is required. This might be achieved by taking an average which describes the size and shape of a particular sample. Calculation of a mean from the raw data is not sensible, as a particular element in the data file is unlikely to correspond to the same anatomical point on different people, because of the biological variation in the anthropometric measurement. To achieve correspondence of data points between files it is necessary to normalize data in such a way that individual anatomical points are coincident from one file to the next, which effectively standardizes for height.

The choice of sections

The cross-sections selected should ideally correspond to major body surface landmarks used in the clothing industry and sample population size surveys.

Moreover, some cross-sections should be located at the peaks and valleys of the body curve, since, if the heights of the sections are selected arbitrarily, some of the detail may be smoothed out in surface interpolation.

It is also desirable for the cross-sectional slices of one body to correspond with those of another. Although proportional heights were generally similar, there are sufficient differences between individuals to indicate that a particular proportional height would not always correspond to the same anatomical site. To ensure that particular sections correspond with major anatomical features, the interactive selection of cross-sections was chosen.

The major cross-sections chosen to represent a human torso are shown in Figure 2. They are at the level of the crotch, hips, waist, underbust, maximum bust, underarm, shoulder, base of neck and neck. Some middle cross-sections, identified by numbers, are inserted between any two major cross-sections in order to improve accuracy. A total of 32 cross-sections are used to describe a human torso. In this way, a particular slice will always correspond with a particular anatomical location; for instance, the underbust slice will always be slice 16 and the underarm slice 24 on every subject. Interpolation from the 32 cross-sections is used to create the 3-D body surface.

Editing and fitting of cross-sectional data

The raw data output from the LASS scanner must be edited and manipulated for the intended applications. For instance, the arms conceal the chest and abdominal region, while many of the required measurements (e.g. chest, waist, hips, etc.) must be measured inside the arms. For some applications, especially in the clothing industry, the shape of the human body is usually required to be

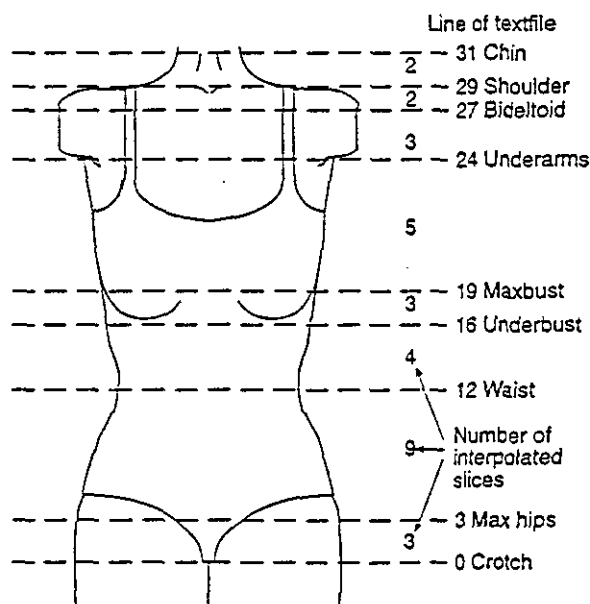


Figure 2.
Arrangement of slices
in the shape matrix file

symmetrical about the vertical axis. The raw data must be edited in some way to remove arms and to achieve symmetry. The editing is performed by fitting cubic splines to horizontal cross-sections. Software has been written to allow semi-automatic cubic spline curve fitting which accurately matches the original data, with the exception of the parts requiring editing, such as the arms. This software allows the manual manipulation of the cubic spline control points, and moves the cubic spline rather like stretching a rubber band. All the 32 cross-sections, as defined previously, may require manipulating in this way.

The choice of the number of control points of the cubic spline is based on a compromise between ease of editing and the accuracy of fitting one slice of the body. As the human body is generally a rounded shape, eight control points were initially tried. Unfortunately these were insufficient to provide the required accuracy. Accordingly, 16 control points were used which satisfactorily defined the cubic spline representing one half of the body's horizontal cross-section. The other half of the cross-section is a mirror image of the first half. It is then possible to create a family of slices where each is described by 16 control points.

Shape matrix

After the fitting of 32 slices, a shape matrix is produced. The shape matrix is a text (ASCII) file containing 16 *x*, 16 *y* and one *z* (height) co-ordinate values on each line. Eight of the 32 lines correspond to the anatomical landmarks as defined, but additional middle lines can be used to improve the accuracy of interpolation. The shape matrix thus contains 512 co-ordinate points to describe a torso. The space occupied by this file is now only 4 per cent of the size of the raw data. The shape matrix can be extended easily to allow representation of the leg, arm or an asymmetric body by adding a header to describe the number of data lines and a format flag. Figure 3 shows the format of the shape matrix.

Uniforming control point spacing and standardizing posture

The control points arising from cubic spline curve fitting do not necessarily occur at equal angles around the vertical axis of the body and their distribution is uneven. This results in distortion in surface interpolation, especially in the longitudinal (vertical) direction where resampling and uniformity of cross-sections are required. Again, the cubic spline is used to fit and to generate a cross-section. Resampling is then automatically performed so that the data points are defined at equal angular spacings around the vertical axis.

Since there are substantial differences in posture between individuals, and the same individual may stand differently between one scan and another, the shape matrix requires further normalization if comparison of bodies is required. This normalization procedure is to remove the effects of posture before comparison. It is achieved by translating the centre of each slice to the geometric centre of *y* (anteroposterio) axis, as shown in Figure 4.

IJCST
7,1

N M RY DX DY

X(1,1) Y(1,1) X(1,2) Y(1,2) • • • X(1,16) Y(1,16) Z(1)

X(2,1) Y(2,1) X(2,2) Y(2,2) • • • X(2,16) Y(2,16) Z(2)

•

•

•

X(N,1) Y(N,1) X(N,2) Y(N,2) • • • X(N,16) Y(N,16) Z(N)

12

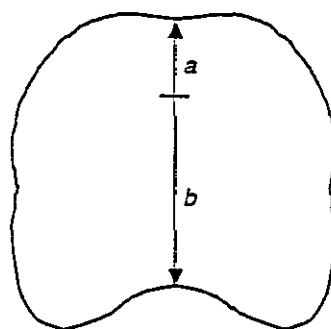
Notes

N = the number of row

M = the mode of file, usual 0

RY, DX and DY = transformation information of cross-section in X-Y plane

Figure 3.
Format of LASS shape
matrix



To recentre the section,
the radius vectors a and
 b are replaced by two
vectors equal to $(a + b)/2$

Figure 4.
Section showing
re-centring methods

The application of LASS shape matrix

3-D surface modelling of the human body

According to the LASS shape matrix, the surface of the human torso can be acquired by surface interpolation. The representation of the surface is based on the tensor-product form of surface[9,10]:

$$S(u, v) = \sum_{i=0}^m \sum_{j=0}^n P_{i,j} \cdot N_{i,p}(u) \cdot N_{j,q}(v) \quad (1)$$

where $0 < u, v < 1$. $N_{i,p}(u)$ and $N_{j,q}(v)$ are basic blending functions of degree p and q in the u and v directions respectively. The vector control points, $P_{i,j}$, contain x , y and z co-ordinate values. With a set of known control points, a complete surface can be generated as parameters u and v vary from 0 to 1.

If the blending functions are uniform degree-3 cubic splines, equation (1) takes its matrix form:

$$S(u,v) = U^T \cdot M^T \cdot P \cdot N \cdot V \quad (2)$$

where $U = [1 \ u \ u^2 \ u^3]$, $V = [1 \ v \ v^2 \ v^3]$

and $P = \begin{bmatrix} p_{i,j} & p_{i,j+1} & p_{i,j+2} & p_{i,j+3} \\ p_{i+1,j} & p_{i+1,j+1} & p_{i+1,j+2} & p_{i+1,j+3} \\ p_{i+2,j} & p_{i+2,j+1} & p_{i+2,j+2} & p_{i+2,j+3} \\ p_{i+3,j} & p_{i+3,j+1} & p_{i+3,j+2} & p_{i+3,j+3} \end{bmatrix} \quad 0 \leq i \leq m-3, \quad 0 \leq j \leq n-3.$

13

Equation (2) presents a sub-surface generated by a 4×4 patch and $U^T \cdot M^T$ and $N \cdot V$ form the blending functions in u and v directions respectively. When some data points of a body surface are given, as in the LASS shape matrix, a complete surface can be regenerated by the surface interpolation, which is a procedure to find out all control points P_{ij} according to known data points. Based on the matrix form (2), if using cardinal splines as the blending functions, the surface of the body can be calculated by taking the LASS shape matrix as control points[11]. For a general blending function, a tensor product interpolant scheme could be used, which involves solving $m+1$ order $(n+1) \times (n+1)$ linear systems and $n+1$ order $(m+1) \times (m+1)$ linear systems[10,12].

A more popular scheme, which is based on non-uniform B-spline, is the skinning interpolation. The skinning method interpolates the surface over a family of cross-sectional data. These data vary at the same parametric direction of equation (1), and therefore are often known as isoparametric curves. Moreover, all isoparametric curves should be normalized so that they have the same number of data points and same parameter distribution. More details about the skinning technique have been described by Woodward[13] and Piegl[14].

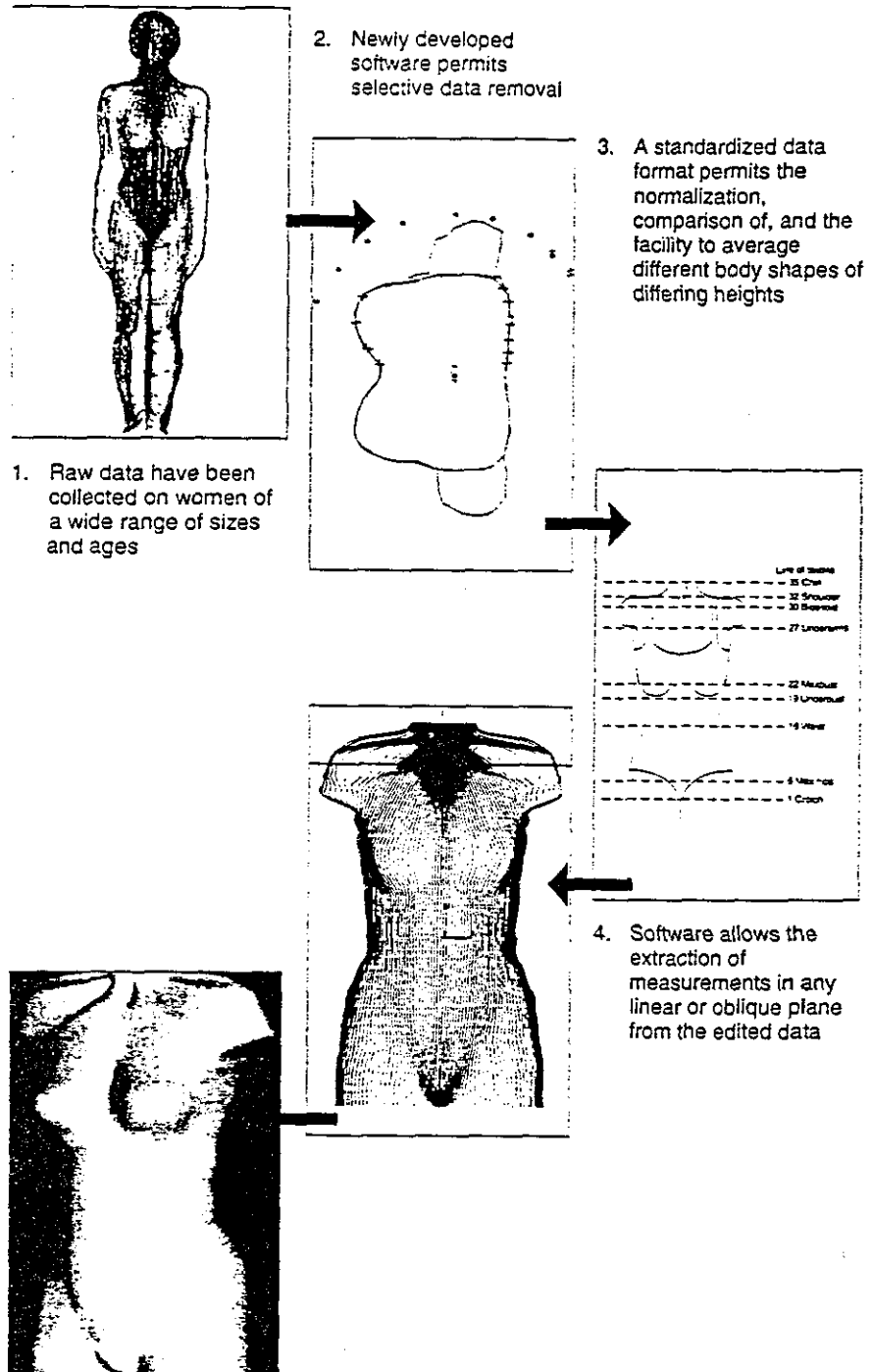
Figure 5 shows a complete flowchart from 3-D scanning to surface regeneration of the human body.

Averaging and comparison of bodies

Average bodies can be created from the normalized shape matrix (with normalized centre points and uniform angle spacing) of a group of subjects. However, a pure mathematical average body is less useful in clothing design. Key anthropometric measurements should be used to control the selection of a sample population. The choice of control variables depends entirely on the application. For example, the circumference of the underbust and maximum bust may be the key measurements for underwear design, and the circumference of waist and hip may be the key measurements for trouser design.

Once the sample population has been selected, an average body can be created by averaging the shape matrices of the sample. By means of surface interpolation, an averaged 3-D body model can be created. This technique thus allows production of averaged 3-D body models for particular garment sizes.

Methodology



Regeneration of a 3-D body shape from anthropometric measurement

There may well be instances where 3-D body shape data are required where there is no access to a whole-body scanner, e.g. for production of bespoke clothing or for manufacture of manikins as fitting stands in realistic shapes to specified measurements. However, with a database of average body shapes, it is possible to create a 3-D body shape from a few simple measurements. This regenerated body could be of a size and shape determined by the measurements, in conjunction with average shapes from the database.

From our research a 3-D database is being assembled which, at present, contains the shape matrices of more than 180 women, aged 16 to 60 years, of a variety of shapes and sizes. A series of average bodies was created, each corresponding to close-fitting garment sizes. These average bodies constitute a shape database which contains a set of eight "masterfiles", each made up from four average bodies in a range of sizes. Eight masterfiles were used to provide information on different bust sizes, as bust size may vary independently from body size. The appropriate masterfile was selected according to the relative size of underbust and maximum bust circumferences. The regenerated body can then be created, by interpolating between average bodies. Further details are reported by West[15].

Discussion

It has been demonstrated that the *shape matrix* is a suitable method for the representation of 3-D shapes of the human torso. An important application of the method is the provision of the ability to reduce data from 3-D scans of a large population to an average body shape. It is also useful to be able to measure changes in a body size and shape when measured at different time intervals even though it was not measured in the same position or posture.

The shape matrix has been used to describe data from surveys of 155 women and 50 children aged three to 14 years. These data have, to date, been used in a range of applications. For example, body surface area of normal and liver-diseased children have been calculated accurately and used for the estimation of drug dosage[16]. Three-dimensional surface distance plots have been produced to allow checking of grading rules for garment manufacture. Manikins have been produced from average bodies, again for applications in the clothing industry[17]. Bespoke manikins of any particular individual's shape can be produced from data from a body scanner. Size and shape of individuals and average shapes have been compared and plots produced which summarize differences.

Data have also been used to create a 3-D body shape to specified anthropometric measurements using different approaches[15,18]. These approaches allow production of 3-D shapes to specified sizes, using average body shapes. Regenerated body shapes may be of use for manufacture of realistically shaped manikins to specified measurements, or for approximation of an individual's shape when a body scanner is not available.

With suitably written computer software it is easy to express data using any number of cross-sections or any number of points to facilitate the transfer of

data. In future it may be possible to integrate digitized 3-D body shapes directly with CAD/CAM systems, to allow automated design and manufacture of garments. This would allow standard sizes and shapes to be represented in shape matrix form, rather than using pattern blocks.

References

1. Taylor, P. and Shoben, M., *Grading for the Fashion Industry: The Theory and Practice*, 2nd ed., Stanley Thornes, Cheltenham, 1990.
2. McCartney, J. and Hinds, B., "Computer-aided design of garments using digitized three-dimensional surfaces", *Proceedings of the Institution of Mechanical Engineers*, Vol. 206, 1992, pp. 199-206.
3. Okabe, H., Imaoka, H., Tomiha, T. and Niwaya, H., "Three-dimensional apparel CAD system", *SIGGRAPH '92, Computer Graphics*, Vol. 26 No. 2, 1992, pp. 105-10.
4. Carignan, M., Yang, Y., Thalmann, N. and Thalmann, D., "Dressing animated synthetic actors with complex deformable clothes", *SIGGRAPH '92, Computer Graphics*, Vol. 26 No. 4, 1992, pp. 99-104.
5. Jones, P., West, G., Harris, D. and Read, J., "The Loughborough Anthropometric Shadow Scanner (LASS)", *Endeavour*, Vol. 13 No. 4, New series, 1989, pp. 164-8.
6. NKK Corporation, *Voxelan 3-D Scanner*, 1992.
7. Cyberware, "3D development", *Cyberware Newsletter*, No. 1, 1993.
8. Jones, P. and Hunt, M., *British Women's Size Survey Age 17 to 69 Years*, HUMAG Research Group, University of Loughborough, Loughborough, 1987.
9. Faux, T. and Pratt, M., *Computational Geometry for Design and Manufacture*, Ellis Horwood, Chichester, 1979.
10. Farin, G., *Curves and Surfaces for Computer-aided Geometric Design*, Academic Press, Boston, MA, 1988.
11. Bartels, R., Beatty, J. and Barsky, B., *An Introduction to Splines for Use in Computer Graphics and Geometric Modelling*, Morgan Kaufmann, Los Altos, CA, 1987.
12. de Boor, C., *A Practical Guide to Splines*, Springer-Verlag, New York, NY, 1978.
13. Woodward, C., "Skinning techniques for interactive B-spline surface interpolation", *Computer Aided Design*, Vol. 20 No. 8, 1988, pp. 441-51.
14. Piegl, L., "On NURBS: a survey", *IEEE Computer Graphics & Application*, Vol. 11 No. 1, 1991, pp. 55-71.
15. West, G.M., "Automated shape anthropometry", PhD Thesis, University of Loughborough, Loughborough, 1993.
16. Jones, P., Baker, A., Hardy, C. and Mowat, A., "Measurement of body surface area in children with liver disease by a novel 3-D body-scanning device", *European Journal of Applied Physiology*, Vol. 68 No. 6, 1994, pp. 514-8.
17. Jones, P., West, G. and Brooke-Wavell, K., "Interrogation of 3D body data for applications in manufacturing industries", in Directorate of the Science and Engineering Research Council, *Application of Computers to Manufacturing Engineering, Research Conference Proceedings*, Sheffield University, 1993, pp. 20-5.
18. Li, P. and Jones, P., "Anthropometry-based surface modelling of the human torso", *Computer in Engineering 1994: Proceedings of the 1994 ASME International Computer in Engineering Conference*, The American Society of Mechanical Engineers, Minneapolis, 1994, pp. 469-74.

Mapping grey-scale image to 3D surface scanning data by ray-tracing

Peng Li*, and Peter R.M. Jones
HUMAG Research Group
Department of Human Sciences
Loughborough University
Loughborough
Leicestershire LE11 3TU
UK.

ABSTRACT

The extraction and location of feature points from range imaging is an important but difficult task in machine vision based measurement systems. There exist some feature points which are not able to be detected from pure geometric characteristics, particularly in those measurement tasks related to the human body. The Loughborough Anthropometric Shadow Scanner (LASS) is a whole body surface scanner based on structured light technique. Certain applications of LASS require accurate location of anthropometric landmarks from the scanned data. This is sometimes impossible from existing raw data because some landmarks do not appear in the scanned data. Identification of these landmarks has to resort to surface texture of the scanned object.

Modifications to LASS were made to allow grey-scale images to be captured before or after the object was scanned. Two-dimensional grey-scale image must be mapped to the scanned data to acquire the 3D co-ordinates of a landmark. The method to map 2D images to the scanned data is based on the collinearity conditions and ray-tracing method. If the camera centre and image co-ordinates are known, the corresponding object point must lie on a ray starting from the camera centre and connecting to the image co-ordinate. By intersecting the ray with the scanned surface of the object, the 3D co-ordinates of a point can be solved. Experimentation has demonstrated the feasibility of the method.

Keywords: 3D surface scanning, ray-tracing, 3D surface anthropometry

1. INTRODUCTION

Acquiring co-ordinates of anthropometric feature points from the human body surface is an essential task in 3D surface anthropometry. There are two types of methods to locate anthropometric feature points. They are geometric reasoning method, based on surface analysis (curvature, normal or continuity, etc.), and artificial marking method. The geometric reasoning method, although it is an automatic method, has limited application in dealing with the human body surface, because many anatomical feature points cannot be identified from the surface geometry of a body. Artificial marking or the operator's observation are normally required to locate the anatomical landmarks. Ferrario *et al* [1] discussed a method in which a number of reflective marks were stuck on 16 landmarks of the subject's face and those marks were measured by infrared photogrammetry. An alternative method used by Vannier *et al.* [2,3] relied on interactive mouse operation to pick feature points from 3-D scanned data.

The existing measurement methods of artificial marks can be roughly grouped into two types: direct co-ordinate measurement without relation to 3-D surface scanned data; and co-ordinate measurement from 3-D surface scanned data. Examples of the first group of methods are:

* This research is funded by Courtaulds Lingerie (Daintifyt), UK.

stereophotogrammetry, 3-D co-ordinate measurement machine *etc.* Because these methods are not related to 3-D scanned data, they are less valuable for a 3-D surface anthropometric task.

The second group methods can be further divided into texture-based or density-based. The texture-based methods identify the artificial marks from an image (RGB or grey-scale) of an object surface and acquires their 3-D co-ordinates by mapping the image onto corresponding 3-D scanned data. This has been a practical method in some colour scanners (for example, Cyberware 3030RGB/PS). The density-based methods exploit the high resolution of a scanner and identify the feature marks according to their geometric feature. These two kinds of methods require a fairly high resolution (say: 2 mm X 2 mm) of the scanner, which is difficult to achieve for a whole body scanner.

A texture-based method was explored by Bhatia *et al.* [6] which automatically identifies cross marks on a scanned body surface. Their method combined digital image processing and optimal estimation to deal with multisensor scanning data. 3-D co-ordinates of a fiducial point was acquired from spatial intersection of multiple rays. Ko *et al.* [7] applied both a texture-based method and a surface analysis method to recognise the feature points from a scanned face. In these work, image data were used to extract feature points of small size, for example, the eyes, and surface analysis was used to identify outstanding feature area, e.g. the nose.

2. MODIFYING LASS SYSTEM TO CAPTURE GREY-SCALE IMAGE

The Loughborough Anthropometric Shadow Scanner (LASS) [4,5] is a whole body scanner developed in the late of 1980s. It adopted seven TV cameras (CCIR non-interlaced format, 312.5 lines/per field) to capture the 3D human body surface up to 2.1 metres high. The system worked on the basis of single beam structured light method. The data resolution is about 1.3 mm in radial direction and 1 mm in height direction, according to current angle set-up of the projectors. However, the data acquisition software reduced the resolution of vertical data to 5 mm. Data resolution in tangential direction of a horizontal slice (cross-section) is a variable of a radius. In the worst situation (maximum object radius 300 mm), the data resolution is 300 (mm) X 0.042 (radian) \approx 12.6 (mm) because the minimum rotation step is 0.04187 radian.

LASS has 150 rotational steps for a complete 360° scan. For each step, data collection time is 14/25 second (14 cameras in serial operation, 25 frame/per second for each camera). This results in the minimum scanning time about 1.5 minute for 150 steps without taking rotation and acceleration/deceleration time of the turntable into account.

The block diagram of the LASS system is shown in Figure 1.

Figure 1. Block diagram of the LASS system.

There are several options available to modify the LASS in order to capture grey-scale images in conjunction with the scanning operation. A simple and feasible modification, which gives the least disturbance to the existing operation of the system, is to use an additional frame grabber to capture the grey-scale picture. To avoid extra calibration work, the existing cameras of LASS are used as input devices for the frame grabber.

To implement this modification, an auxiliary frame grabber (Data Translation's Vision-EZ board) has been selected for image capture, and a 486-Personal Computer (Dell Optiplex 466/MX) is used to interface with the frame grabber and store grey-scale images. The frame grabber is connected with one of the existing cameras in the LASS system by a multiplex switch. Image capture is operated before or after surface scanning. The system block diagram is shown in Figure 2.

Figure 2. An additional imaging system to the LASS.

3. RAY-TRACING METHOD TO MAP 2D POINTS TO 3D SURFACE

This section discusses the method to relate the 2-D image of an object to its 3-D scanned data. The mapping method is based on the principle of projective geometry. It needs to know: 1) the location and orientation of a view point from which the 2D image is taken; 2) the equation of the 3D surface

(analytical or numerical). Two sub-tasks contained in the mapping procedure are: labelling feature points in the 2-D image plane and computing their 3-D co-ordinates. The former is performed by a manual operation on an interactive graphics interface. The latter forms the centre of this section.

Ray/surface intersection problem

From a known 3-D surface and its 2-D visual image, the 2-D to 3-D mapping problem is defined as: given a point in the image plane, to find its corresponding point in the 3-D surface. The problem can be geometrically described as: to find out an intersection of a straight line ray with the 3-D surface. The ray starts from a viewpoint (the exposure station of camera) and passing through an imagery point in the image plane. Hence this is a ray/surface intersection problem as shown in Figure 3.

Figure 3. Ray/surface intersection

Let the viewpoint be located at z_0 plane and its co-ordinates be (x_0, y_0, z_0) . The ray passes through image plane z_p of the camera at point (x_p, y_p, z_p) . Let the intersection of the ray and the surface be (X_i, Y_i, Z_i) . According to the projective geometry, three points (x_0, y_0, z_0) , (x_p, y_p, z_p) and (X_i, Y_i, Z_i) are collinear, namely:

$$\begin{aligned} \frac{Y_i - y_0}{Z_i - z_0} &= \frac{y_p - y_0}{z_p - z_0} \\ \frac{X_i - x_0}{Z_i - z_0} &= \frac{x_p - x_0}{z_p - z_0} \end{aligned} \quad (1)$$

As an alternative, the image plane co-ordinates (x_p, y_p, z_p) can be replaced by the co-ordinates of any 3-D point which is lying on the ray. Therefore the equation (1) is a general collinearity form of three spatial points. From two known points (x_0, y_0, z_0) and (x_p, y_p, z_p) the ray equation can be found, but solution to three unknown values (X_i, Y_i, Z_i) is impossible. If a 3D surface equation is provided, a solution could be found by a ray/surface intersection method.

A 3-D ray equation can be defined by the origin and direction vector of the ray as follows [9]:

Let

$$\begin{aligned} R_{origin} &= R_o = [x_0, y_0, z_0] \\ R_{direction} &= R_d = [x_d, y_d, z_d] \end{aligned} \quad (2)$$

where $x_d^2 + y_d^2 + z_d^2 = 1$ and

$$\begin{aligned} x_d &= \frac{x_p - x_0}{\sqrt{(x_p - x_0)^2 + (y_p - y_0)^2 + (z_p - z_0)^2}} \\ y_d &= \frac{y_p - y_0}{\sqrt{(x_p - x_0)^2 + (y_p - y_0)^2 + (z_p - z_0)^2}} \\ z_d &= \frac{z_p - z_0}{\sqrt{(x_p - x_0)^2 + (y_p - y_0)^2 + (z_p - z_0)^2}} \end{aligned} \quad (3)$$

and a ray is represented by a parametric equation:

$$R(t) = R_o + R_d \cdot t, \text{ where } t > 0 \quad (4a)$$

$$x(t) = x_0 + x_d \cdot t$$

$$\text{or } y(t) = y_0 + y_d \cdot t \quad (4b)$$

$$z(t) = z_0 + z_d \cdot t$$

There are three types of surface representations: implicit surface equation, parametric surface equation and discrete surface meshes. Accordingly, different solving methods are required. The

implicit 3-D surface equation is expressed by $f(x,y,z)=0$. Substituted by (4), the intersection problem is to solve the equation

$$f(x_0 + x_d \cdot t, y_0 + y_d \cdot t, z_0 + z_d \cdot t) = F^*(t) = 0 \quad (5)$$

Except for some simple cases, $F^*(t)=0$ is a higher order non-linear equation. Its roots (zero points) must be solved by a numerical method. The intersection is non-unique since multiple roots may exist, and additional criteria may be required to find the real solution.

When a surface is represented by a parametric equation, for example, bicubic form [8]:

$$\begin{aligned} x &= u^T \cdot M^T \cdot G_x \cdot M \cdot u \\ y &= u^T \cdot M^T \cdot G_y \cdot M \cdot u \\ z &= u^T \cdot M^T \cdot G_z \cdot M \cdot u \end{aligned} \quad (6)$$

the intersection equation is complicated, especially if equation (6) is turned into a implicit surface form [9]. The numerical method, instead of a analytical method, is often used to solve the problem of ray/parametric surface intersection.

When a surface is represented by discrete polygon meshes, each mesh can be finally decomposed into several triangular meshes. A triangular mesh represents a 3-D plane. The ray/surface intersection can be, therefore, solved by computation of ray/plane intersections with the aid of a searching process.

Solution for ray/plane intersection

A normalised plane equation is expressed by

$$A \cdot x + B \cdot y + C \cdot z + D = 0, \text{ where } A^2 + B^2 + C^2 = 1 \quad (7)$$

Given three non-collinear points $p_1 = (x_1, y_1, z_1)$, $p_2 = (x_2, y_2, z_2)$ and $p_3 = (x_3, y_3, z_3)$, A, B, C in Equ. (7) can be computed from:

$$A \cdot i + B \cdot j + C \cdot k = \begin{vmatrix} i & x_2 - x_1 & x_3 - x_1 \\ j & y_2 - y_1 & y_3 - y_1 \\ k & z_2 - z_1 & z_3 - z_1 \end{vmatrix} \quad (8)$$

$$\text{and } D = -(A \cdot x_1 + B \cdot y_1 + C \cdot z_1)$$

Substitute the parametric expression (4) of a ray into Equ. (7), the ray/plane intersection equation is

$$A \cdot (x_0 + x_d t) + B \cdot (y_0 + y_d t) + C \cdot (z_0 + z_d t) + D = 0 \quad (9)$$

This is a single parameter equation and t can be obtained from

$$t = \frac{-(A \cdot x_0 + B \cdot y_0 + C \cdot z_0 + D)}{A \cdot x_d + B \cdot y_d + C \cdot z_d} \quad (10)$$

By substituting t into equation (4), an intersection point which is on the ray can be acquired.

Containment test for ray/triangular mesh intersection

A containment test must be carried out to verify whether the point of intersection is within the area of the triangular mesh. There are several methods available to test if a point is contained in a planar triangle, such as the Jordon curve theorem, area criterion and angle criterion. The angle criterion states:

To connect a point with three vertices of a triangle produces three new triangles. If the point is at interior of a triangle, then the angles of new triangles which have common side with the original triangle are always smaller than their corresponding angles in the original triangle (that is $\text{angle} \langle qab \rangle \leq \text{angle} \langle cab \rangle$, $\text{angle} \langle bcq \rangle \leq \text{angle} \langle bca \rangle$, and so on), as shown in Figure 4.

Figure 4. Containment relationship of a point in a triangular area

Compared with other criteria, the angle theorem can deliver more reliable result and is more suitable for calculation in 3D space. Therefore, it is chosen for the containment test. Computational details are shown as follows: To test if a point q is lying in the triangle (a, b, c) , the angles $\langle qab \rangle$, $\langle qbc \rangle$ and $\langle qca \rangle$ are calculated. If angle qab is smaller than angle cab , qbc is smaller than abc , and qca is smaller than bca , then the point q lies in the triangle (a, b, c) . An angle between three vector points can be calculated by vector dot product:

$$\theta_{qab} = \cos^{-1} \left(\frac{(qa, ab)}{\|qa\| \cdot \|ab\|} \right), \quad (11)$$

where (\bullet, \bullet) denotes a dot product and $\|\bullet\|$ is the two - norm.

Ray/quadrilateral mesh intersection algorithm

The quadrilateral mesh is a frequently used representation form for a scanned surface and a parametric surface. The scanned data of LASS are represented by a quadrilateral mesh form which is a two-dimensional array of heights and rotation angle (steps). The elements of the array are radii of surface points. Four vertices of the i th mesh are $\{ (h_i, \theta_i), (h_{i+1}, \theta_i), (h_{i+1}, \theta_{i+1}), (h_i, \theta_{i+1}) \}$. Similarly, a parametric B-spline surface form is a discrete quadrilateral (u, v) net. Four vertices of a (u, v) mesh are $\{ (u_i, v_j), (u_{i+1}, v_j), (u_{i+1}, v_{j+1}), (u_i, v_{j+1}) \}$. The calculation of ray/quadrilateral mesh intersection is a more sensible approach for a discrete ray/surface intersection problem.

However, four vertices of a quadrilateral mesh are not always co-planar. They must be decomposed into a triangular mesh for the calculation of ray/plane intersection. Let $(p_{i1}, p_{i2}, p_{i3}, p_{i4})$ denote four vertices of a quadrilateral mesh P_i . The mesh P_i can be split into two triangular meshes which consist of (p_{i1}, p_{i2}, p_{i3}) and (p_{i1}, p_{i3}, p_{i4}) respectively, as shown in Figure 5.

Figure 5. Ray/quadrilateral mesh intersection

Searching a solution from a large surface

The algorithm discussed in the last section computes the intersection for one triangular/quadrilateral mesh each time. A searching process is required to deal with a large surface which consists of hundreds and thousands of quadrilateral meshes. The complete solving process for a surface is a two dimensional traversing problem. When the number of meshes is large, it may take considerable time to search a solution in spite of the simplicity of ray/plane intersection algorithm.

Moreover, due to the complex shape of a surface (for example, non-convex surface) multiple intersections may be found during the traversing process and thereby criteria are required to eliminate those inadmissible solutions. Two additional techniques are used to constrain the solving process and to delete inadmissible solutions. One is to constrain the searched space by normal direction of a sub-plane. Only those sub-planes facing the ray need to be searched, namely, the angle between the normal vector of a sub-plane and the direction vector of the ray should be greater than 90 degree. This condition can be described by vector dot product:

$$\mathbf{n} \cdot \mathbf{R}_d < 0 \quad (12)$$

where \mathbf{n} is the normal vector of a plane. This is called as a *visibility test*. The visibility test has been inserted into Algorithm 7-1 in the practical implementation to prevent non-visible intersection from calculation. Figure 6 shows the examples of visible and non-visible intersection.

The second technique adopted to constrain searched space is heuristic. It depends on the knowledge about the relationship between viewpoint position and the surface. A simple pre-estimation of the co-ordinate range to be searched can eliminate many unnecessary effort. Two estimated ranges have been utilised in related to the LASS set-up:

1. Constraint of searching range in height dimension:

The scanned body is located in a central position on the turntable in the LASS system. The maximal radial length of the body surface should be less than 400 mm. Denote h as height and Z as

distance from the centre of turntable. Let h_0 be the intersections of the ray and Z_0 ($Z = 0$) plane, and h_{400} be the intersection of the ray and Z_{400} ($Z = 400$) plane. Then the intersection of ray and body surface must be within h_0 and h_{400} , as illustrated in Figure 7a.

Figure 6. Visible and non-visible intersection

2. Constraint of searching range in angle dimension:

The LASS scanned data are organised by height (h) and angle (θ). The optical axis of the camera is assumed to align with the centre of rotation. The angle range of the scanned data can be divided into the left side and the right side by the position of a feature mark in an imagery plane, i.e. angle searching can only happen in $(0 \sim 180)$ degree or $(180 \sim 360)$ degree range. The searching angle may be further constrained by the intersections of the ray and a 400 mm circle which is assumed a maximum object radius, and the resultant angles are θ_a and θ_b , as illustrated in Figure 7b.

(a) (b)
Figure 7. Search space of a body surface a) height constraint; b) angle constraint

4. CAMERA CALIBRATION AND ERROR ANALYSIS OF THE DIRECT MAPPING METHOD

Camera calibration

The mapping method discussed in the previous section require accurate camera position (x_0, y_0, z_0) and projective co-ordinates (x_p, y_p, z_p) of the object point at a reference for the ray-tracing computation. Although a number of photogrammetric calibration methods can be used to find out the interior and exterior parameters of a camera [10, 11, 12], most of them require accurate 3D control fields, which is difficult to implement in the current set-up of LASS. Moreover, the Newvicon® camera used in LASS is highly sensitive to illumination condition and has severe pixel drift. Therefore two methods are employed for calibration of the co-ordinate mapping method. Firstly, the camera position was measured by using a Leica WILD-T1610 digital theodolite. This procedure can achieve good accuracy for x_0, y_0 . However, because the camera centre is not visible, there is certain error in z_0 (about 10 ~ 20 mm). Secondly, the projective co-ordinates (x_p, y_p, z_p) are calibrated by a linear, finite element mapping procedure [5]. In this procedure, the pixel co-ordinates of the frame grabber are mapped onto the Z_0 plane, where Z_0 is located at the centre of the turntable by a linear equation. To cope with non-linear lens distortions and small camera tilt, the image area is divided into 30 finite element areas in which each area has its own linear mapping equation.

Error analysis

According to Equ. (3), (4) and (10), the co-ordinates of the ray/plane intersection are:

$$\begin{aligned} X_i &= x_0 - \frac{(x_p - x_0) \cdot (Ax_0 + By_0 + Cz_0 + D)}{A(x_p - x_0) + B(y_p - y_0) + C(z_p - z_0)} \\ Y_i &= y_0 - \frac{(y_p - y_0) \cdot (Ax_0 + By_0 + Cz_0 + D)}{A(x_p - x_0) + B(y_p - y_0) + C(z_p - z_0)} \\ Z_i &= z_0 - \frac{(z_p - z_0) \cdot (Ax_0 + By_0 + Cz_0 + D)}{A(x_p - x_0) + B(y_p - y_0) + C(z_p - z_0)} \end{aligned} \quad (13)$$

where the A, B, C are the normal direction of the plane.

Equ. (13) implies that there are three sources of error, namely: camera position error; projected co-ordinate error and plane direction error. The direction of the plane has a complex effect to the error analysis of ray/plane intersection. If the normal of the plane is perpendicular to the ray, the minor perturbation of the ray direction could result in a big error at the intersection (from infinity to finite error or vice versa). In contrast, error of the ray direction has minimum effect to the computation of (X_i, Y_i, Z_i) , if the normal of the plane is parallel to the ray direction. That is the computational error of (X_i, Y_i, Z_i) is a function of the plane direction. To simplify the following error analysis, it is presumed that the plane direction is coincident with the Z plane, i.e. $A=0, B=0, C=1$ and $D = -Cz_p$. This will show clearly the effect of the first two error sources.

Camera position error

Camera position error is the error of viewpoint (x_0, y_0, z_0) . It is caused by a calibration method of the camera system. This section estimates the error magnitude of (X_i, Y_i, Z_i) due to (x_0, y_0, z_0) error. Using the simplified Z plane equation $A=0, B=0, C=1$ and $D = -Cz_p$, the co-ordinates of ray/plane intersection are:

$$\begin{aligned} X_i &= x_0 - (x_p - x_0) \frac{z_0 - Z_i}{z_p - z_0} \\ Y_i &= y_0 - (y_p - y_0) \frac{z_0 - Z_i}{z_p - z_0} \\ Z_i &= z_0 - (z_p - z_0) \frac{z_0 - Z_i}{z_p - z_0} = Z_i \end{aligned} \quad (14)$$

Taking the first order Taylor expansion of (14), we have:

$$\begin{aligned} \Delta X &= \frac{\partial X}{\partial x_0} \Delta x_0 + \frac{\partial X}{\partial y_0} \Delta y_0 + \frac{\partial X}{\partial z_0} \Delta z_0 \\ \Delta Y &= \frac{\partial Y}{\partial x_0} \Delta x_0 + \frac{\partial Y}{\partial y_0} \Delta y_0 + \frac{\partial Y}{\partial z_0} \Delta z_0 \\ \Delta Z &= 0 \end{aligned} \quad (15)$$

where

$$\begin{aligned} \frac{\partial X}{\partial x_0} &= \frac{z_p - Z_i}{z_p - z_0}; \quad \frac{\partial X}{\partial y_0} = 0; \quad \frac{\partial X}{\partial z_0} = -(x_p - x_0) \frac{z_p - Z_i}{(z_p - z_0)^2} \\ \frac{\partial Y}{\partial x_0} &= 0; \quad \frac{\partial Y}{\partial y_0} = \frac{z_p - Z_i}{z_p - z_0}; \quad \frac{\partial Y}{\partial z_0} = -(y_p - y_0) \frac{z_p - Z_i}{(z_p - z_0)^2} \end{aligned} \quad (16)$$

Three conclusions can be obtained from (16):

- 1) X and Y error is proportional to x_0 and y_0 error respectively if the surface plane is perpendicular to the Z axis;
- 2) Errors of X and Y from x_0 and y_0 are independent each other;
- 3) X and Y errors caused by z_0 are inversely proportional to the distance from camera to projective plane.

Taking the set-up of the LASS system as an example, in which $(z_p - z_0) = 3000$ mm and maximum $(z_p - Z_i) = 300$ mm, the X error is 1/10 of x_0 error and 1/17 of z_0 error when $x_p - x_0 = 200$ mm. Table 1 shows the typical errors from the calibration of camera position

Table 1. X error of ray/plane intersection from (x_0, y_0, z_0) error

	Physical calibration by digital theodolite (the estimated worst case)	Maximum X error of physical calibration
Δx_0	2 mm	0.2 mm
Δy_0	2 mm	0
Δz_0	20 mm*	1.18 mm

* the error of distance from a camera centre to the reference plane is caused by the uncertainty of the camera centre. It is difficult from outside of a camera to identify where the camera centre is.

Projected co-ordinate error

Projected co-ordinates (x_p, y_p, z_p) of a image point are obtained from a projective transformation. The projective transformation relies on the calibrated camera parameters. The projection plane could be an arbitrary reference plane in world co-ordinate system or the image plane of a camera. Many 3-D surface scanners were calibrated by projected co-ordinates in one or several reference planes. If the projection plane is the image plane of the camera, the projection error is independent of the camera position but related to the interior parameters of the camera. If the projection plane is a world plane, the exterior parameters of a camera play a crucial role in the error analysis. This suggests that different analysis methods are required for these two cases.

Error analysis related to projected plane method

For simplifying the analysis the projection plane is presumed to be a world plane and parallel to the image plane of the camera system. Based on the computational formula (14), error expression is

$$\begin{aligned}\Delta X &= \frac{\partial X}{\partial x_p} \Delta x_p + \frac{\partial X}{\partial y_p} \Delta y_p + \frac{\partial X}{\partial z_p} \Delta z_p \\ \Delta Y &= \frac{\partial Y}{\partial x_p} \Delta x_p + \frac{\partial Y}{\partial y_p} \Delta y_p + \frac{\partial Y}{\partial z_p} \Delta z_p\end{aligned}\quad (17)$$

$$\Delta Z = 0$$

and

$$\begin{aligned}\frac{\partial X}{\partial x_p} &= -\frac{z_0 - Z_i}{z_p - z_0}; & \frac{\partial X}{\partial y_p} &= 0; & \frac{\partial X}{\partial z_p} &= (x_p - x_0) \frac{z_0 - Z_i}{(z_p - z_0)^2} \\ \frac{\partial Y}{\partial x_p} &= 0; & \frac{\partial Y}{\partial y_p} &= -\frac{z_0 - Z_i}{z_p - z_0}; & \frac{\partial Y}{\partial z_p} &= (y_p - y_0) \frac{z_0 - Z_i}{(z_p - z_0)^2}\end{aligned}\quad (18)$$

Three conclusions which are similar to the camera position error analysis in the previous section can be obtained from Equ. (18),:

- 1) X and Y errors are proportional to projected co-ordinate error x_p and y_p respectively;
- 2) X and Y errors are independent;
- 3) X and Y errors caused by z_p are inversely proportional to the distance from camera to projective plane;

Again, taking the set-up of the LASS system as an example, the X error will be 0.9 times of x_p error and 1/17 of z_p error at $x_p - x_0 \approx 200$ mm. This requires high accuracy co-ordinate mapping between the image (pixel) plane to the reference plane. However, it is difficult to evaluate the co-ordinate mapping accuracy of a calibration method which calculates projected co-ordinates directly. Such a calibration method is usually tested on dimensional measurements of a standard object. If the object plane is close to the reference plane of calibration, the measurement accuracy could be a criterion of the accuracy of the projected co-ordinate. Therefore, according to West [5], the typical measurement error of an object dimension (horizontal direction) of the LASS system is about 2~5 mm in X, Y and Z direction. The distance error from the camera centre to the reference plane, which relies on physical measurement, is less than 20 mm. In the worst case the resultant X errors subjected to x_p, z_p error are about 4.5 mm and 1.18 mm respectively.

5. SUMMARY

This paper presents a ray-tracing method to map grey-scale image to 3D surface scanning data. The method has been used to identify feature points from LASS scanned data in an engineering application. Figure 8a shows the image window and labelled feature marks in the image plane. The 3-D co-ordinates of these feature marks are displayed on the raw scanned data (wireframe surface) in Figure 8b after ray-tracing computation.

The ray-tracing method for mapping grey-scale image to 3D surface scanning data relies on accurate calibration of camera system. This may be difficult in a set-up of a 3D scanner. More rigorous error analysis is required.

(a)

Figure 8. Case of feature point location: (a) labelling of feature marks in the image window; (b) mapped 3-D co-ordinates of the feature marks in the raw scanned surface

(b)

Figure 8. Case of feature point location: (a) labelling of feature marks in the image window; (b) mapped 3-D co-ordinates of the feature marks in the raw scanned surface.

REFERENCES

- [1] Ferrario, V. F., Sforza, C., Miani Jr, A. and Serrao, G., "A three-dimensional evaluation of human facial asymmetry", *Journal of Anatomy*, Vol. 186, pp. 103-110, 1995
- [2] Vannier, M., Pilgram, T., Bhatia, G., Brunnsden, B., Commean, P., "Facial surface scanner", *IEEE Computer Graphics and Application*, pp 72-80, November 1991,.
- [3] Vannier, M., Pilgram, T., Bhatia, G., Brunnsden, B., Nemecek, J., Young, V., "Quantitative three-dimensional assessment of face-lift with an optical facial surface scanner", *Annals of Plastic Surgery*, Vol. 30, No. 3, March 1993
- [4] Jones, P. R. M, West, G, Harris, D. H., Read, J. B., "The Loughborough anthropometric Shadow Scanner (LASS)", *Endeavour*, Vol.13, no 4, pp.162-168, 1989
- [5] West, G., Ph.D. Thesis, *Automated Shape Anthropometry*, Loughborough University, UK, 1994
- [6] Bhatia, G., Godhwani, A., and Vannier, M., "Fiducial point localization in multisensor 3D surface scanning", *Biomedical Image Processing and Three-dimensional Microscopy, Proceedings of SPIE* Vol. 1660, pp 375-386, 1992
- [7] Ko, H., Kim, M-S., Park, H-G., and Kim, S-W., "Face sculpturing robot with recognition capability", *Computer-Aided Design*, Vol. 26, No. 11, pp 814-821, 1994
- [8] Foley, J.D., Van Dam, A., *Computer Graphics: Principles and Practice*, (2nd Edition), Addison-Wesley, 1990
- [9] Hanrahan, P. "A survey of ray-surface intersection algorithms", in Glassner (ed) *An Introduction to Ray-Tracing*, Academic Press, 1993
- [10] American Society of Photogrammetry, *Manual of Photogrammetry*, Fourth Edition, 1980
- [11] Tsai, R. Y., "A versatile camera calibration technique for high-accuracy 3D machine vision metrology using off-the-shelf TV camera and lenses", *IEEE Journal of Robotics and Automation*, Vol. 3, No. 4, pp. 319-344, 1987
- [12] Weng, J., Cohen, P. and Herniou, M. "Camera calibration with distortion models and accuracy evaluation", *IEEE Transactions on Pattern Analysis and Machine Intelligence* Vol.14, No. 10, pp. 965-992, 1992

**TITLE: AUTOMATIC EDITING AND CURVE-FITTING OF 3-D SURFACE
SCANNED DATA OF THE HUMAN BODY**

AUTHORS:

Peng Li & Peter R.M. Jones

HUMAG Research Group

Department of Human Sciences

Loughborough University

Loughborough

Leicestershire LE11 3TU

UK.

Tel: +44 (0)1509 223021

Fax: +44 (0)1509 223941

e-mail: P.Li@lboro.ac.uk; or P.R.M.Jones@lboro.ac.uk

KEY WORDS: 3D surface scanning, curve and surface approximation, B-spline,
Human body modelling

Introduction

Three dimensional (3-D) surface anthropometry is an interdisciplinary technology. Its development has promoted a number of new challenges and requirements to existing data modelling techniques. Since 3-D surface scanned data of the human body are essential data elements of 3-D surface anthropometry, editing and curve-fitting of the scanned data are fundamental functions in a 3-D surface anthropometry environment. For example, to create a torso model of the human body, the arm data must be removed from the whole body scan. This has been the practice with the LASS (Loughborough Anthropometric Shadow Scanner) applications [West 1994, Jones *et al.* 1995]. However, the amount of data from a whole body scanner is huge. Repeated editing and curve-fitting of the scanned data slice by slice is time-consuming and tedious. This paper presents an automatic data editing method to generate a torso model from a body scan. The method can remove the arm data and refill the void by curve and surface approximation.

Automatic data editing: arm trimming

During the scanning process, if a subject adopts a natural standing posture, their arms conceal the profile of the torso and result in an incomplete torso shape from the scanned data. Figure 1a illustrate a cross-sectional slice of the scanned data.

Because of the concavity between the arm and trunk, the cross-sectional data display sharp steps at start and end points of the profile of an arm and form a rising and a falling edge. This feature is utilised to fulfil an edge detecting algorithm. An automatic trimming operation is therefore implemented by taking cross-sectional data between the rising and falling edges of the void.

The step edges can be detected by finite difference of the data and a threshold. The threshold of edge detection can be derived from knowledge about the scanned object. For example, a scanner with a 0.012 radian incremental angle of rotation, assuming the maximum variation of two adjacent points in the radius from a human trunk will be less than 15 mm, then the threshold could be set as $15/0.012=1250$. If the value of the first order difference of data is bigger than the threshold, it could be an edge point. Figure 1b. shows a cross-sectional curve after arm trimming.

Data refilling by curve approximation

Curve approximation by non-uniform B-spline

Given a set of raw data g_i ($i=0, M$) and a non-uniform parametric B-spline function $N_{j,p}(t)$, the approximation problem is defined as: to find a set of control points c_j and parameter t_j to satisfy [de Boor 1978]:

$$\min \sum_{i=0}^M (g_i - \sum_{j=0}^n c_j \cdot N_{j,p}(t_i))^2 \text{ is achieved.} \quad (2)$$

In an approximation problem, the number of raw data is larger than the number of unknown control points. The control points and their parameters are adjusted in such a way that the distance between approximation function and raw data is minimised. The control points c_j , however, are determined by their parameters t_j in a parametric function approximation problem.

The above problem is a least square approximation problem in the form

$$e^2(x) = \|g - A \cdot c\|^2. \quad (3)$$

where A is a $(M+1) \times (n+1)$ matrix with elements

$$\begin{bmatrix} N_{0,p}(t_0) & N_{1,p}(t_0) & \dots & N_{n,p}(t_0) \\ N_{0,p}(t_1) & N_{1,p}(t_1) & \dots & N_{n,p}(t_1) \\ \vdots & \vdots & \ddots & \vdots \\ N_{0,p}(t_M) & N_{1,p}(t_M) & \dots & N_{n,p}(t_M) \end{bmatrix} \quad (4)$$

The function $e(\cdot)$ is called residual sum of squares and $r = g - Ac$ is called the *residual vector*. Equ. (3) can be solved by QR factorisation [Stewart 1973].

Refilling data gap in raw scanned data after arm trimming by curve approximation:

Refilling of the data gap after the trimming process can be treated as an approximation process. However, because the gap is big, the approximate function can take any value to fill the gap without losing accuracy at existing data points. Hence, some constraints must be applied to the approximate process. A solution is to give some guess data which bridge the gap so that the approximate function does not generate an oscillation.

A set of support data to bridge the gap is constructed by inserting a number of middle points into the gap. However, less attention should be given to these data during the approximate process. In mathematical term, they should be given a lower weighting. A weighted least square approximate method based on non-uniform B-spline is used to refill the gap.

The refilling process of the arm gap can be described as follows:

1. insert linearly some points between the gap;
2. calculate parametric vector from the revised data set;
3. calculate the knot vector from the parametric vector ;
4. calculate the matrix A and multiple A by a weight vector;
5. apply the least square method to compute the control points of the B-spline;
6. generate the B-spline curve and fill the gap.

Figure 2a and b show a shaded body before arm trimming and after this refilling gap operation. The raw scanned data were acquired from the CYBERWARE 3030RGB/PS scanner.

Data refilling by surface approximation

Surface approximating by tensor-product representation

Similarly, a surface approximation problem can be defined as

$$\min \sum_{i=0}^M \sum_{j=0}^N (g_{i,j} - S(u_i, v_j))^2 = \min \sum_{i=0}^M \sum_{j=0}^N (g_{i,j} - \sum_{l=0}^m \sum_{k=0}^n c_{l,k} \cdot N_{l,p}(u_i) \cdot N_{k,q}(v_j))^2 \quad (5) \quad \text{The}$$

residual sum of square is a function of control points c , parameters u and v

$$e^2(c, u, v) = \sum_{i=0}^M \sum_{j=0}^N (g_{i,j} - \sum_{l=0}^m \sum_{k=0}^n c_{l,k} \cdot N_{l,p}(u_i) \cdot N_{k,q}(v_j))^2 \quad (6)$$

Therefore, there are $(M+1) \times (N+1)$ raw data (known vector) and $(m+1) \times (n+1)$ unknown elements in the above surface approximation problem. If we define two B-spline matrix U and V as follows:

$$\begin{aligned} U &= \{N_{l,p}(u_i)\} \quad i = 0 \dots M, \quad l = 0 \dots m \\ V &= \{N_{k,q}(v_j)\} \quad j = 0 \dots N, \quad k = 0 \dots n \end{aligned} \quad (7)$$

then U is a $(M+1) \times (m+1)$ matrix and V is a $(N+1) \times (n+1)$ matrix. The matrix A for the least square approximation is

$$A = U \otimes V \quad \text{here } \otimes \text{ is Kronecker product of two matrices}$$

and the dimension of matrix A is $(M+1) \times (N+1) \times (m+1) \times (n+1)$. It is clear that the solution is not feasible if Equ. (5) is directly applied to the raw data set of 3-D scan (imagining $M = 300$, $N = 200$, $m=10$ and $n=10$ so that the matrix A contains 6,000,000 elements).

In order to overcome the problem of large matrix dimension, a two-step solving strategy is proposed which is based on the structure of the tensor-product of Equ. (5). In the first step, a series of curve approximations are performed on the raw data (provided such curves can be identified from the raw data). These curves are isoparametric curves with the same parametric direction (say u direction). The resultant output of the approximation is an array of control points of the curves. If m control points are selected, then the amount of the data is reduced to m/M of the original raw data. If there are N slices data to be approximated, total amount of control points is $(N \times m)$.

In the second step, the curve approximation is used to fit the control points produced from the first step. This time the approximation is performed at v direction and n control points are used to approximate N data points (there are control points for u curves). There are m slices data to be approximated here and the resultant control points comprise the control points of a surface. The number of final control points is $(n \times m)$.

At the second step, there are several possible alternatives: it is possible to use interpolation instead approximation to fit the control points of u curves, or perform a surface interpolation to these data picked from u curves.

Conclusion

In order to facilitate data modelling and interrogation in 3-D surface anthropometry, an automatic editing and fitting method of the raw scanned data of the human body is necessary. This paper reports a method to trim arm data to acquire a smooth torso model. The method is applied to raw scanned data from the CYBERWARE scanner, but can be applied to other data formats as well.

References

- de Boor, A *Practical Guide to Spline*, Springer-Verlag, New York, 1978
- Jones, P.R.M, Li, P., Brook-Wavell, K., West, G, 'Format for human body modelling from 3-D body scanning', *International Journal of Clothing Sciences and Technology*, Vol. 7, No. 1, pp. 7-16, 1995
- Stewart, G.W., *Introduction to Matrix Computations*, Academic Press, Inc. 1973
- West, G., Ph.D. Thesis, *Automated Shape Anthropometry*, University of Loughborough, 1994, UK

Appendix C. Evaluation and comparison of calibration methods

This section presents test results of three camera calibration methods, namely: the non-linear method, the RDO methods and Tsai method. The default values of exterior and interior parameters of the camera are listed in Table C-1 unless stated otherwise. In noise tests, a uniform distribution random noise is added on the observed image co-ordinates in order to simulate the different error sources.

Table C-1. Default camera parameters

Interior parameters:

fx (mm)	fy (mm)	u0 (pixel)	v0 (pixel)	k ₁	p1 (default)	p2 (default)
-4240.000	-4136.747	384	256	varied	0.00000000	0.00000000

Exterior parameters:

omega (rad)	phi (rad)	kappa (rad)	Xc (mm)	Yc (mm)	Zc (mm)
0.0000	0.0000	0.0000	0.000	0.000	1100.000

C-1. Effect of lens distortion and initial value conditions

a) Test under different lens distortion

Table C- 2 Two tests of non-linear method under different p1, p2 and with k1 varies
Test 1: p1=0.00001, p2=0.00002.

Interior parameters								
k1	prjerr	fx	fy	u0	v0	k1(est.)	p1(est.)	p2(est.)
5.00E-08	0.06289	-4239.50	-4134.52	380.021	256.510	5.3E-08	1E-05	2.03E-05
1.00E-07	0.09504	-4239.84	-4135.62	381.231	254.880	1.05E-07	1.01E-05	2.06E-05
2.00E-07	0.22462	-4243.70	-4139.20	381.754	255.560	2.17E-07	1.04E-05	2.14E-05
3.00E-07	0.44983	-4252.82	-4149.64	384.659	252.640	3.38E-07	1.16E-05	2.12E-05
Exterior parameters								
k1		omega	phi	kappa	Xc	Yc	Zc	
5.00E-08		0.000139	0.000924	-1.9E-05	-0.018	-0.021	1099.627	
1.00E-07		-0.00025	0.000655	-4E-06	-0.001	-0.025	1099.673	
2.00E-07		-0.0001	0.000589	0.000004	0.062	-0.012	1100.452	
3.00E-07		-0.00082	-2.2E-05	0.000027	0.141	0.000	1102.410	

Test 2: $p_1=0.00002$, $p_2=0.00001$

Interior parameters								
k1	prjerr	fx	fy	u0	v0	k1(est)	p1(est.)	p2(est.)
5.00E-08	0.1054	-4245.20	-4140.48	377.888	255.064	5.6E-08	2.02E-05	1.01E-05
1.00E-07	0.1616	-4249.36	-4143.89	376.944	255.779	1.09E-07	2.03E-05	1.03E-05
2.00E-07	0.3407	-4257.07	-4153.24	381.037	255.226	2.22E-07	2.15E-05	1.04E-05
3.00E-07	0.5790	-4263.05	-4164.46	393.027	251.715	3.44E-07	2.62E-05	9.51E-06
Exterior parameters								
k1		omega	phi	kappa	Xc	Yc	Zc	
5.00E-08		-0.0002	0.0015	0.0000	0.032	0.023	1100.648	
1.00E-07		-0.0001	0.0017	0.0000	0.077	0.024	1101.504	
2.00E-07		-0.0002	0.0009	0.0000	0.188	0.024	1103.838	
3.00E-07		-0.0011	-0.0018	0.0000	0.327	0.025	1106.724	

Table C- 3 Test of the RDO method via. different k_1

a). Interior parameters

k1	prjerr	fx	fy	u0	v0	k1(est)
0	0.003376	-4239.54	-4136.18	384.2744	256.2742	0
1E-08	0.003805	-4240.4	-4136.96	383.6092	255.1493	1E-08
5E-08	0.0107	-4240.09	-4136.67	383.9502	256.0378	5.1E-08
1E-07	0.041287	-4242.05	-4138.56	383.7279	256.6134	1.04E-07
1.5E-07	0.094204	-4242.97	-4139.49	383.3742	256.799	1.59E-07
2E-07	0.1708	-4246.04	-4142.46	383.3008	257.02	2.16E-07
2.5E-07	0.272101	-4248.15	-4144.54	383.1755	257.2479	2.75E-07
3E-07	0.399341	-4251.88	-4148.18	383.02	257.4869	3.37E-07
3.5E-07	0.555295	-4255.43	-4151.62	382.8697	257.7031	4.01E-07
4E-07	0.785688	-4269.7	-4165.8	383.0633	256.2144	4.71E-07
4.5E-07	1.016176	-4278.02	-4173.93	382.9499	256.2313	5.41E-07
5E-07	1.283061	-4287.18	-4182.96	382.8478	256.2551	6.14E-07

a). Exterior parameters

k1	omega	phi	kappa	Xc	Yc	Zc
0	0.000063	-6.3E-05	0.000004	0.00	0.00	1099.88
1E-08	-0.0002	0.000095	-2E-06	0.00	0.00	1100.11
5E-08	0.000011	0.000014	-2E-06	0.00	0.00	1100.00
1E-07	0.000146	0.000064	0.000004	0.00	0.00	1100.45
1.5E-07	0.000195	0.000154	0.000007	0.01	0.00	1100.58
2E-07	0.000253	0.000172	0.000017	0.01	-0.01	1101.20
2.5E-07	0.000321	0.000212	0.000024	0.02	-0.02	1101.53
3E-07	0.000385	0.00025	0.000035	0.02	-0.03	1102.24
3.5E-07	0.000452	0.000291	0.000045	0.02	-0.04	1102.80
4E-07	-3E-06	0.000443	-9E-06	0.25	0.07	1106.01
4.5E-07	-1.8E-05	0.00053	-1.8E-05	0.32	0.09	1107.70
5E-07	-3.8E-05	0.000631	-1.7E-05	0.41	0.12	1109.53

Table C- 4. Test of Tsai's method with different k_1

a). Interior parameters

k_1	pr_{err}	f_x	f_y	u_0	v_0	k_1 (est)
0	0.010044	-4239.05	-4135.74	384	256	0
1E-08	0.012578	-4239.87	-4136.66			-1E-08
5E-08	0.038076	-4239.57	-4135.44			-5.2E-08
1E-07	0.045549	-4241.05	-4137.51			-1.1E-07
1.5E-07	0.098597	-4241.18	-4137.72			-1.6E-07
2E-07	0.173018	-4244.45	-4140.9			-2.2E-07
2.5E-07	0.275011	-4245.91	-4142.31			-2.8E-07
3E-07	0.411534	-4248.83	-4145			-3.4E-07
3.5E-07	0.561832	-4250.39	-4146.51			-4.1E-07
4E-07	0.791879	-4282.15	-4177.75			-4.7E-07
4.5E-07	1.021805	-4294.45	-4189.05			-5.4E-07
5E-07	1.289946	-4303.77	-4199.36			-6.1E-07

a). Exterior parameters

k_1	w	q	k	X_c	Y_c	Z_c
0	-0.00004	0.00001	-0.00004	0.016	0.045	1099.728
1E-08	0.00007	0.00005	-0.00003	0.062	-0.077	1100.039
5E-08	-0.00019	-0.00017	0.00011	-0.204	0.225	1099.544
1E-07	-0.00008	0.00002	-0.00009	0.019	0.098	1100.095
1.5E-07	-0.00012	0.00002	-0.00014	0.021	0.146	1099.979
2E-07	-0.0001	-0.00001	-0.0001	-0.004	0.118	1100.663
2.5E-07	0.00004	-0.00001	0.00004	-0.01	-0.046	1100.874
3E-07	0.00033	-0.00003	0.00037	-0.043	-0.395	1101.491
3.5E-07	0.00004	0	0.00003	-0.004	-0.041	1101.283
4E-07	0.00016	0.00014	-0.00009	0.166	-0.196	1109.682
4.5E-07	0.00004	0.00004	-0.00003	0.044	-0.053	1112.265
5E-07	0.00042	0.00038	-0.00024	0.454	-0.499	1114.719

Tsai's method requires the principal point co-ordinates (image centre). They are assigned at the ideal image centre where the co-ordinates are (384, 256). Table C-3 and C-4 show:

- 1) Three methods demonstrate similar performance with noise-free test data, according to the RMS residuals and estimated parameter values;
- 2) Increasing k_1 always causes an over-estimated k_1 and object distance Z_c ;
- 3) There is a link between Z_c and f_x, f_y . An increase in estimated Z_c leads to increases in both f_x, f_y .

b) Test of initial value condition of non-linear method

It has been argued that good initial estimated values of unknown parameters are critical to the non-linear optimisation method [Weng *et al* 1992; Shih, Hung and Lin 1995]. No report is available to discuss this problem further. Tests carried out in this section examine the effect of initial stimated values on parameter evaluation. Table C-5 gives test results of the non-linear method with noise-free data. Table C-6 presents test results for the RDO method with 0.5 pixel noise level.

Table C-5. Initial value conditions of the non-linear method
k1=0.0000001 (noise-free)

		Test 1		Test 2		Test 3	
Real parameters		Initial guess	Estimated results	Initial guess	Estimated results	Initial guess	Estimated results
fx	-4240.000	-5200.000	-4239.842	-5555.556	-4239.841	-2800.000	-4239.838
fy	-4136.747	-5073.171	-4135.614	-5371.901	-4135.618	-2731.707	-4134.610
u0	384.000	330.000	381.22	500.000	381.226	300.000	381.205
v0	256.000	200.000	254.903	200.000	254.893	200.000	254.927
k1	1.0xE-7	0.1xE-7	1.05xE-7	0.1xE-7	1.10xE-7	0.1xE-7	1.05xE-7
p1	0.0000100	0.000000	0.0000101	0.000000	0.0000101	0.000000	0.0000101
p2	0.0000200	0.000000	0.0000206	0.000000	0.0000206	0.000000	0.0000206
omega	0.0000	-0.01	-0.000247	-0.0100	-0.000250	-0.01	-0.00024
phi	0.0000	0.01	0.000657	0.0100	0.000656	0.01	0.00066
kappa	0.0000	0.01	-0.000004	0.0100	-0.000004	0.01	0.00000
Xc	0.000	-80.000	-0.0007	-80.000	-0.0007	-80.000	-0.001
Yc	0.000	10.000	-0.0253	100.000	-0.0253	100.000	-0.025
Zc	1100.000	1400.000	1099.673	2600.000	1099.673	600.000	1099.674
prjerr		0.09504		0.09490		0.09426	

Table C-6. Initial value conditions of the RDO method (k1=0.0000001 and noise level =0.5 pixel)
Note: The position of the camera is altered to (-8, 10, 1100).

		Test 1		Test 2		Test 3	
Real parameters		Initial guess	Estimated results	Initial guess	Estimated results	Initial guess	Estimated results
fx	-4240.000	-5200.000	-4269.834	-2800.000	-4269.808	-2800.000	-4269.792
fy	-4136.747	-5073.170	-4163.519	-2731.707	-4163.486	-2731.707	-4163.470
u0	384.000	330.000	384.709	300.000	384.702	300.000	384.710
v0	256.000	200.000	251.531	400.000	251.481	400.000	251.469
k1	1.0xE-7	0.1xE-7	1.2xE-7	1.0xE-7	1.2xE-7	0.1xE-7	1.2xE-7
omega	0.0000	-0.01	-0.000989	-0.0100	-0.0010	-0.01	-0.00103
phi	0.0000	-0.01	-0.000741	-0.0100	-0.00074	0.01	-0.00074
kappa	0.0000	0.01	-0.000058	0.0100	-0.000058	0.01	-0.000058
Xc	-8.000	40.000	-8.666	40.000	-8.667	-80.000	-8.667
Yc	10.000	-60.000	9.890	-60.000	9.889	100.000	9.889
Zc	1100.000	600.000	1105.996	600.000	1105.986	1600.000	1105.981
prjerr		0.33548		0.33549		0.33549	

Yc	10.000	-60.000	9.890	-60.000	9.889	100.000	9.889
Zc	1100.000	600.000	1105.996	600.000	1105.986	1600.000	1105.981
prjerr		0.33548		0.33549		0.33549	

Table C-5 and C-6 shows:

1) The non-linear method always converges to real values despite large variation of initial estimated values under noise free condition;

2) The RDO method is robust when data are corrupted by 0.5 pixel noise. Estimated parameters always converge from the different initial value to the same values within very good precision. This reveals that the discrepancy of estimated values and real values is basically caused by noise, rather than the variation of initial estimated values of the camera parameters.

c) Effect of principal point displacement to Tsai's method

Tsai's method requires the principal point co-ordinates (u_0, v_0) as known parameters. However, the determination of the principal point co-ordinates is difficult. Ten or more pixels displacement is not unusual [Tsai, 1987, Willson & Shafer, 1994]. The performance of Tsai's method under different principal point positions, with noise-free and 0.5 pixel noise level cases are presented in Table C-7.

Table C- 7. Tsai's method under variation of principle points u_0, v_0

a) noise=0, with different image centre u_0, v_0 (camera position at (-8, 10, 1100))

prjerr	fx	fy	k1	u0	v0
0.05361	-4241.39	-4137.92	1.05E-07	384	256
0.20822	-4244.89	-4146.26	8.9E-08	403	285
0.09728	-4247.56	-4142.58	1.11E-07	393	245
0.18305	-4247.26	-4139.43	1E-07	363	235
0.23558	-4243.36	-4142.18	7.8E-08	353	285
w	q	k	Xc	Yc	Zc
0	0	0	-7.995	9.998	1100.207
0.00702	-0.00442	0.00024	-7.918	10.018	1102.741
-0.00257	-0.002	0.0001	-7.85	9.89	1101.329
-0.00515	0.0048	-0.00017	-8.2	10.049	1101.559
0.00676	0.00695	-0.00039	-8.435	10.31	1102.611

b) noise=0.5, with different image centre u_0, v_0 . (camera position at (-8, 10, 1100))

prjerr	fx	fy	k1	u0	v0
0.38105	-4272.12	-4163.24	1.2E-07	384	256
0.46443	-4274.72	-4171.04	1.08E-07	403	285

w	q	k	Xc	Yc	Zc
0.00006	-0.00048	-0.00035	-8.595	9.915	1106.061
0.00668	-0.00507	-0.00042	-8.727	10.359	1108.349
-0.00253	-0.0025	-0.00016	-8.466	9.808	1097.938
-0.00475	0.00459	-0.00039	-8.461	9.593	1106.235
0.00686	0.00664	-0.00127	-8.678	10.07	1121.081

It can be concluded from these tests that:

1) The estimation of camera parameters and projection error are not sensitive to the variation of the image centre (even more than 30 pixels drift). This might explain why many researchers take the frame centre as the principal point position without loss of projection precision.

2) The major source of error is the noise level rather than the position variation of the principal point.

C-2. Robust test under different noise conditions

a) Effect of noise level

Table C-8. Response of the non-linear method to different noise levels

a) $k=0$, $p_1=0$, $p_2=0$

noise	prierr	omega	phi	kappa	Xc	Yc	Zc
0	0.00337	-0.00008	0.00007	0	0.0005	0.001	1099.951
0.1	0.05029	0.00525	0.00379	0.00004	0.018	0.002	1100.534
0.5	0.24914	0.02865	0.02002	-0.00003	0.068	-0.041	1101.484
1	0.50186	0.05738	0.04108	-0.00065	0.178	-0.162	1099.547
1.5	0.75844	0.08412	0.06115	-0.00176	0.341	-0.339	1094.859
2	1.0215	0.10848	0.07797	-0.00312	0.529	-0.543	1086.75
2.5	1.55768	0.14854	0.11682	-0.00611	0.615	-0.64	1075.923
3	3.61601	0.12358	0.05488	-0.00038	0.944	-0.53	1059.151
noise	fx	fy	xp	yp	k1	p1	p2
0	-4239.85	-4136.47	383.711	255.664	0	1.2E-08	3E-09
0.1	-4242.59	-4139.09	367.957	277.72	2E-09	2.4E-07	-7E-08
0.5	-4247.85	-4143.1	299.137	374.581	7E-09	8.56E-07	-8.9E-08
1	-4240.27	-4132.34	210.383	492.606	1E-08	1.27E-06	2.05E-07
1.5	-4220.5	-4108.25	126.971	600.546	1.1E-08	1.63E-06	4.32E-07
2	-4186.79	-4070.2	59.075	695.923	1.2E-08	1.87E-06	6.37E-07
2.5	-4146.83	-4001.13	-98.798	851.127	2.4E-08	7.82E-07	5.34E-06
3	-4096.34	-3975.85	164.085	742.257	1.3E-08	6.37E-06	-1.2E-06

b) $k=0.0000001$, $p1=0$, $p2=0$

noise	prjerr	omega	phi	kappa	Xc	Yc	Zc
0	0.04128	-0.00057	0.00053	0	-0.0005	0.0013	1100.473
0.1	0.06604	0.00447	-0.0011	0.00006	0.024	0.003	1101.143
0.5	0.25288	0.02451	-0.00227	0.00035	0.056	-0.03	1102.842
1	0.50624	0.06222	-0.0023	0.00072	0.093	-0.057	1102.984
1.5	3.49448	0.13841	0.00188	0.00088	0.047	0.111	1104.288
2	45.61543	0.20383	0.07488	-0.00451	1.034	-1.141	1097.167
2.5	23.85552	0.19666	0.04869	-0.00314	0.902	-1.597	1083.186
3	15.41326	0.1913	0.01904	-0.00033	0.43	-1.809	1066.086
noise	fx	fy	xp	yp	k1	p1	p2
0	-4242.14	-4138.63	381.734	253.628	1.04E-07	-1.7E-07	-2.5E-07
0.1	-4245.18	-4141.3	388.743	274.543	1.06E-07	3.76E-07	1.94E-06
0.5	-4248.42	-4134.78	393.763	357.513	1.13E-07	6.29E-07	1.11E-05
1	-4220.58	-4052.14	394.103	511.961	1.22E-07	4.88E-07	2.93E-05
1.5	-4098.15	-3675.83	378.751	806.327	1.36E-07	-5.2E-07	6.84E-05
2	-4151.41	-4025.32	77.177	1087.323	4.8E-08	-8.4E-06	3.15E-05
2.5	-4088.11	-3995.78	190.246	1047.422	3E-08	4.95E-06	2.05E-05
3	-4012.53	-3954.99	314.427	1013.997	2.1E-08	1.96E-05	1.16E-05

c) $k=0.0000002$, $p1=0$, $p2=0$

noise	prjerr	omega	phi	kappa	Xc	Yc	Zc
0	0.16612	-0.00219	0.00236	0.00001	0.005	-0.014	1101.307
0.1	0.14447	0.00483	0.00221	0.00007	0.064	0.012	1102.249
0.5	0.28865	0.02884	-0.00142	0.00035	0.094	-0.009	1104.361
1	1.12716	0.08321	-0.0008	0.0007	0.145	0.068	1106.942
1.5	2.4373	0.05854	0.01175	0.00069	0.089	0.29	1097.469
2	28.38882	0.21602	0.009	0.00092	0.205	0.829	1113.024
2.5	56.86967	0.24664	-0.02327	0.00369	0.114	2.064	1119.163
3	112.9496	0.27143	-0.03185	0.00564	-0.122	-4.827	1116.412
noise	fx	fy	xp	yp	k1	p1	p2
0	-4246.36	-4142.61	373.998	246.887	2.16E-07	-1.8E-06	-2E-06
0.1	-4251.63	-4146.94	374.81	276.059	2.19E-07	-1.8E-06	4.29E-06
0.5	-4247.4	-4117.23	390.262	375.415	2.25E-07	1.08E-06	2.61E-05
1	-4157.95	-3849.1	387.992	593.612	2.29E-07	4.18E-07	7.37E-05
1.5	-4218.1	-4058.19	335.326	497.814	2.44E-07	-7.1E-06	4.66E-05
2	-3818.95	-2719.89	350.974	1007.805	2.28E-07	-8.5E-06	0.000163
2.5	-3503.58	-2233.7	497.873	981.253	2.13E-07	1.96E-05	0.000158
3	-3184.09	-1263.73	539.57	760.186	2.37E-07	2.18E-06	0.000245

d) $k1=0.0000001$, $p1=0.00002$, $p2=0.00001$

noise	prjerr	omega	phi	kappa	Xc	Yc	Zc
0	0.16268	-0.00002	0.00172	-0.00001	0.077	0.024	1101.51
0.1	0.18283	0.00267	0.00692	-0.00008	0.038	0.044	1098.906
0.5	0.37516	0.00981	0.02085	-0.00037	-0.106	0.095	1086.212
1	0.70187	0.02438	0.03726	-0.00107	-0.259	0.13	1065.781
1.5	1.8967	-0.02353	0.18418	0.00076	-0.529	0.143	1027.072
noise	fx	fy	xp	yp	k1	p1	p2
0	-4249.19	-4144.05	377.03	256.036	1.09E-07	2.03E-05	1.03E-05
0.1	-4249.24	-4135.11	354.856	267.183	1.08E-07	1.84E-05	1.1E-05
0.5	-4223.81	-4091.51	296.014	296.353	1.02E-07	1.36E-05	1.22E-05
1	-4158.73	-4005.66	228.77	353.953	9.6E-08	8.86E-06	1.44E-05
1.5	-3781.72	-3794.25	-351.319	163.566	1.12E-07	-4.5E-05	-3.6E-06

Table C-9. Response of the RDO method to different noise levels

a). $k1=0.00000020$

noise	prjerr	omega	phi	kappa	Xc	Yc	Zc
0.1	0.18973	-0.0004	0.0001	0.0001	0.085	0.024	1101.891
0.5	0.32403	-0.0019	-0.0002	0.0003	0.158	-0.002	1101.595
1	0.56035	-0.0034	-0.0005	0.0006	0.274	-0.058	1097.705
1.5	0.81576	-0.0046	-0.0008	0.0009	0.392	-0.143	1089.79
2	1.07877	-0.0054	-0.0012	0.0012	0.52	-0.277	1077.685
2.5	1.34877	-0.006	-0.0014	0.0015	0.678	-0.415	1062.496
3	1.62649	-0.0064	-0.0017	0.0017	0.816	-0.583	1043.568
noise	fx	fy	u0	v0	k1		
0.1	-4249.5	-4145.85	383.8	254.338	2.19E-07		
0.5	-4251.47	-4147.86	385.168	248.198	2.27E-07		
1	-4241.33	-4138.04	386.902	241.844	2.38E-07		
1.5	-4216.52	-4114.03	388.581	236.799	2.49E-07		
2	-4176.47	-4075.25	390.199	233.191	2.61E-07		
2.5	-4125.1	-4025.36	391.783	230.528	2.74E-07		
3	-4060.03	-3962.03	393.28	228.822	2.87E-07		

b) $k_1=0.00000010$

noise	prjerr	omega	phi	kappa	Xc	Yc	Zc
0.1	0.069	-0.0009	-0.0001	0.0001	0.031	0	1100.6
0.5	0.26571	-0.0038	-0.0008	0.0003	0.109	-0.027	1100.015
1	0.52626	-0.0065	-0.0016	0.0006	0.211	-0.089	1095.931
1.5	0.78956	-0.0084	-0.0022	0.0009	0.329	-0.177	1087.718
2	1.05585	-0.0097	-0.0028	0.0012	0.44	-0.305	1076.071
2.5	1.32881	-0.0104	-0.0033	0.0015	0.569	-0.453	1060.858
3	1.60715	-0.0108	-0.0038	0.0018	0.711	-0.622	1042.235
noise		fx	fy	u0	v0	k1	
0.1		-4243.36	-4139.89	384.499	252.44	1.06E-07	
0.5		-4244.36	-4140.95	387.64	240.164	1.14E-07	
1		-4233.65	-4130.77	391.085	229.021	1.25E-07	
1.5		-4207.91	-4106.07	394.093	221.073	1.36E-07	
2		-4169.63	-4069.12	396.797	215.847	1.47E-07	
2.5		-4118.27	-4019.35	399.134	212.849	1.6E-07	
3		-4054.31	-3957.11	401.181	211.566	1.72E-07	

c) $k_1=0.000000000$

noise	prjerr	omega	phi	kappa	Xc	Yc	Zc
0.1	0.05056	0.0045	0.0009	0	0.021	0.005	1100.631
0.5	0.25155	0.0273	0.0054	0.0002	0.113	-0.011	1101.416
1	0.50981	0.0563	0.0149	0	0.304	-0.101	1097.597
1.5	0.77367	0.0897	0.0639	-0.0021	0.395	-0.33	1085.371
2	1.07805	-0.0263	-0.0124	0.0012	0.256	-0.349	1066.803
2.5	1.34744	-0.026	-0.0123	0.0015	0.373	-0.511	1053.12
3	1.62349	-0.0244	-0.012	0.0018	0.513	-0.682	1035.459
noise		fx	fy	u0	v0	k1	
0.1		-4242.94	-4139.42	380.395	274.796	2E-09	
0.5		-4246.88	-4142.81	361.487	368.888	8E-09	
1		-4231.24	-4127.36	321.954	488.172	1.1E-08	
1.5		-4182.34	-4082.41	117.79	620.992	1.6E-08	
2		-4140.07	-4041	435.771	148.785	5.4E-08	
2.5		-4093.96	-3996.62	434.9	150.376	6.4E-08	
3		-4033.49	-3937.75	433.141	157.609	7.6E-08	

Table C-10. Response of Tsai's method to different noise levelsa) $k_1=0.00000020$

noise	prjerr	fx	fy	k1	u0*	v0*
0.1	0.68475	-4222.98	-4131.01	-2E-07	384	256
0.5	2.57099	-3968.52	-3916.88	-1.7E-07	384	256
1	5.10917	-3390.49	-3386.4	-1.6E-07	384	256
1.5	7.82072	-2766.14	-2796.71	-1.6E-07	384	256
noise	w	q	k	Xc	Yc	Zc
0.1	0.00258	0.0022	-0.00151	2.58	-3.04	1098.466
0.5	0.01074	0.00922	-0.00642	10.197	-12.022	1038.492
1	0.02131	0.01838	-0.0128	17.451	-20.656	887.741
1.5	0.0317	0.0275	-0.01918	21.401	-25.406	719.751

b) $k_1=0.00000010$

noise	prjerr	fx	fy	k1	u0*	v0*
0.1	0.54250	-4220.91	-4127.66	-9.2E-08	384	256
0.5	2.52938	-3965.73	-3913.74	-6E-08	384	256
1	5.11684	-3382.99	-3378.86	-4.5E-08	384	256
1.5	7.81966	-2766.36	-2796.4	-4.9E-08	384	256
noise	w	q	k	Xc	Yc	Zc
0.1	0.00221	0.00188	-0.0013	2.208	-2.605	1097.767
0.5	0.01065	0.00915	-0.00636	10.117	-11.919	1037.917
1	0.02127	0.01841	-0.01278	17.449	-20.576	885.836
1.5	0.03146	0.02743	-0.01907	21.352	-25.215	719.783

c) $k_1=0.000000000$

noise	prjerr	fx	fy	k1	u0*	v0*
0.1	0.55804	-4216.93	-4124.29	1.3E-08	384	256
0.5	2.48150	-3974.21	-3920.95	4.3E-08	384	256
1	5.07861	-3396.48	-3391.06	5.7E-08	384	256
1.5	7.80003	-2777.82	-2806.88	5.4E-08	384	256
noise	w	q	k	Xc	Yc	Zc
0.1	0.00231	0.00201	-0.00136	2.35	-2.725	1096.963
0.5	0.01034	0.00895	-0.00619	9.918	-11.596	1040.02
1	0.02089	0.01816	-0.0126	17.279	-20.281	889.324
1.5	0.03108	0.02719	-0.01886	21.257	-24.996	722.723

* assigned principal point co-ordinates

It can be concluded from these test results:

- 1) Noise causes deterioration of parameter estimation in three methods. The most significantly affected parameters in the non-linear optimisation method are the principal point position (u_0, v_0) and Z_c (Note: the variations of f_x, f_y are associated with Z_c 's variation). For Tsai's method, the most affected parameter is Z_c because the principal point position is fixed.
- 2) The non-linear method is obviously superior to Tsai's method with respect to the RMS error and discrepancy of estimated parameters. When the noise level is bigger than 1.5 pixel, Tsai's method is not applicable.
- 3) The RMS projection error is nearly 1/2 of the noise level for the RDO method.

b) Effect of noise distribution

The noise with uniform distribution is generated from random number series. Generation of random number by the computer is a determinate process. The series of random number is fixed if the seed for a random number generator is not changed. A bias may be caused if such a random number series is added to image co-ordinates. Tests conducted in this section explore the effect of different random number series to the calibration result. Each test uses a new random number series which is generated by altering the seeds for the random number generator. (Note: the random number generator is a library function of C language).

Table C-11. Effect of noise distribution at 0.5 pixel level to the RDO method
(camera position at (-8, 10, 1100))

Interior parameters						
Prjerr	f_x	f_y	u_0	v_0	k_1	
0.05329	-4240.40	-4136.96	383.79	256.09	1.04E-07	(noise free)
0.3101	-4211.19	-4104.11	367.52	258.30	9.4E-08	
0.32913	-4223.00	-4120.19	389.54	266.83	1.07E-07	
0.34422	-4198.94	-4094.38	389.50	248.65	1.25E-07	
0.32871	-4224.81	-4120.21	374.33	258.04	9.3E-08	
0.35844	-4235.79	-4128.77	391.30	245.11	1.21E-07	

Exterior parameters					
omega	phi	kappa	Xc	Yc	Zc
0.0000	0.0001	0.0000	-8.00	10.00	1099.99 (noise free)
0.0003	0.0040	0.0000	-7.95	10.35	1092.27
0.0023	-0.0013	0.0000	-7.96	10.44	1095.32
-0.0018	-0.0010	0.0002	-7.62	10.05	1086.99
0.0009	0.0021	0.0003	-8.30	9.54	1096.55
-0.0027	-0.0020	0.0002	-8.28	10.06	1096.92

Table C-12. Effect of noise distribution at 0.5 pixel level to Tsai's method
(camera position at (-8, 10, 1100))

Variation of noise distribution only					
prjerr	fx	fy	k1	u0	v0
0.05361	-4241.39	-4137.92	1.05E-07	384	256 (noise-free)
0.43995	-4226.37	-4122.89	8.8E-08	384	256
0.29098	-4193.74	-4090.76	1.08E-07	384	256
0.36059	-4233.9	-4131.8	1E-07	384	256
0.38209	-4290.44	-4183.65	9.7E-08	384	256
w	q	k	Xc	Yc	Zc
0	0	0	-7.995	9.998	1100.207 (noise-free)
-0.00095	-0.00101	0.00083	-9.191	11.117	1097.555
-0.00009	-0.00089	-0.0004	-9.021	10.107	1087.22
-0.00007	-0.00022	-0.00071	-8.246	10.072	1098.783
-0.00017	0.00055	-0.00078	-7.356	10.184	1113.196

It is observed that the distribution of noise has a significant effect on the estimation of camera parameters in both methods, though the effects on RMS is relatively smaller.

c) Effect of control point distribution

It is believed that the distribution of control points could affect the calibration result. This test is designed to generate different distributions of control points and to observe their effects on results of calibration. The generation of control points is implemented by randomly selecting 3D points from volume of the control field. As mentioned earlier, the randomisation relies on the generation of random number series. Different distributions of control points can be acquired, if the seed for random number generation is altered. Table

C-13 and C-14 presents the calibration results for the RDO method and Tsai’s method under noise-free and 0.5 pixel noise level.

Table C- 13. Effect of control point distribution to the RDO method (camera position at (-8, 10, 1100))

(a) Noise-free

	prjerr	omega	phi	kappa	Xc	Yc	Zc
Test1	0.04704	-6E-06	0.000033	0.000001	-8.009	10.011	1100.129
Test2	0.0422	-1.1E-05	-5.2E-05	0.000001	-8	9.988	1100.126
Test3	0.03786	-0.00013	0.000095	-6E-06	-7.996	10.004	1099.848
Test4	0.03717	0.000013	-3.2E-05	0.000003	-7.998	10.001	1099.924
	fx	fy	u0	v0	k1	p1	p2
Test1	-4240.95	-4137.52	383.828	256.014	1.04E-07	0	0
Test2	-4240.91	-4137.44	384.218	255.91	1.04E-07	0	0
Test3	-4239.74	-4136.36	383.613	255.47	1.03E-07	0	0
Test4	-4240.17	-4136.77	384.141	256.056	1.04E-07	0	0

(b) Noise level = 0.5 pixel

	prjerr	omega	phi	kappa	Xc	Yc	Zc
Test1	0.32011	0.003788	-0.0004	-0.0002	-8.403	10.351	1088.772
Test2	0.32683	0.004451	0.003231	0.000249	-7.948	10.044	1099.343
Test3	0.33971	-0.00309	-0.00019	-0.00018	-7.797	10.067	1100.382
Test4	0.28394	0.004948	0.001964	-0.00026	-8.819	9.174	1088.716
	fx	fy	u0	v0	k1	p1	p2
Test1	-4200.75	-4101.21	384.126	272.606	1.07E-07	0	0
Test2	-4237.73	-4134.58	370.538	274.393	9.5E-08	0	0
Test3	-4245.19	-4141.55	385.517	243.431	1.17E-07	0	0
Test4	-4202.77	-4101.95	372.761	273.193	1.09E-07	0	0

Table C- 14. Effect of control point distribution to Tsai’s method (camera position at (-8, 10, 1100))

(a) Noise-free

prjerr	fx	fy	k1	u0*	v0*
0.0479	-4241.43	-4138.01	1.04E-07	384	256
0.04188	-4240.75	-4137.28	1.04E-07	384	256
0.03905	-4240.15	-4136.78	1.04E-07	384	256
0.04065	-4240.36	-4136.94	1.04E-07	384	256
0.03805	-4240.57	-4137.17	1.04E-07	384	256
w	q	k	Xc	Yc	Zc
0	-0.00001	0	-8.012	9.999	1100.264
0	0	-0.00001	-8.003	10.001	1100.085
0	0	-0.00002	-7.998	9.999	1099.955
0	0.00001	0.00001	-7.991	10.001	1099.995
0	-0.00001	0	-8.011	10.006	1100.029

* assigned principal point co-ordinates

(b) Noise level = 0.5 pixel

prjerr	fx	fy	k1	u0*	v0*	
0.05361	-4241.39	-4137.92	1.05E-07	384	256	(noise-free)
0.36818	-4258.46	-4151.27	1.2E-07	384	256	
0.3643	-4196.4	-4098	1.18E-07	384	256	
0.537	-4235.21	-4127.84	1E-07	384	256	
0.48261	-4212.16	-4111.97	1.07E-07	384	256	
w	q	k	XL	YL	ZL	
0	0	0	-7.995	9.998	1100.207	(noise-free)
0.0003	-0.00045	0.00032	-8.496	9.679	1103.347	
0.00031	-0.00025	0.00022	-8.271	9.65	1088.092	
-0.00016	-0.00182	-0.00134	-9.974	10.18	1097.529	
-0.00004	-0.00047	-0.00112	-8.499	10.005	1092.237	

* assigned principal point co-ordinates

Conclusions can be drawn from these test:

1) If noise exist in the observed data, the distribution of control points can affect the calibration result in both methods. However, methods show similar stability under different distributions of control points.

2) Without noise, the distribution of control points has no significant effect to the tested calibration methods.

C-3. Effect of camera orientation

It is mentioned that there is a coupling between the estimations of camera centre (principal point position) and rotation angles of the camera which can lead to ill-conditioning normal equations for the least-squares method [ASP 1980]. A test is carried out to examine the effect of camera orientation to the estimated camera parameters, with noise-free and noise level at 0.5 pixel.

Table C- 15. Effect of camera orientation for the RDO method

(a) noise-free

w	prjerr	u0	v0	fx	fy	k1
0.01	0.00004	384.001	256.011	-4240.01	-4136.59	0
0.05	0.00004	384.004	256.006	-4240	-4136.58	0
0.1	0.00003	383.996	255.717	-4240.03	-4136.62	0
0.3	0.00321	383.895	256.459	-4239.67	-4136.24	0
0.5	0.0034	383.436	255.871	-4239.55	-4136.18	0
w	w	q	k	Xc	Yc	Zc
0.01	0.01	0	0	7	0	1100.001
0.05	0.05	0	0	7	0	1100
0.1	0.09993	0	0	7	0	1100.003
0.3	0.30012	0.00002	0	6.991	-324.987	1099.904
0.5	0.49997	0.00014	-0.00001	7.006	-526.936	1099.867

(b) noise=0.5

w	prjerr	u0	v0	fx	fy	k1
0	0.25058	372.936	366.05	-4248.15	-4143.94	7E-09
0.01	0.25085	374.674	371.798	-4248.09	-4143.13	6E-09
0.05	0.29873	345.787	328.653	-4254.18	-4145.56	-1E-09
0.1	0.25175	378.759	375.825	-4238.5	-4133.41	5E-09
0.3	0.27587	393.006	432.817	-4213.88	-4107.52	7E-09
0.5	0.30333	488.048	631.691	-4194.71	-4073.29	7E-09
w	w	q	k	Xc	Yc	Zc
0	0.02658	0.00268	0.00015	7.113	-0.027	1101.743
0.01	0.03795	0.00229	0.00013	7.136	-0.032	1102.138
0.05	0.06755	0.00911	0.0002	7.173	-0.237	1104.642
0.1	0.12899	0.00136	0.00014	7.164	-99.986	1099.693
0.3	0.34348	-0.00207	0.00005	7.096	-323.609	1093.717
0.5	0.59303	-0.02396	0.00226	7.713	-525.401	1095.047

Table C-15 shows that the orientation of the camera has negligible effects in a noise-free condition to the estimation of camera parameter. However, it does have a certain effect when noise exist. Nevertheless, the estimated parameters further corrupts, if noise presents.

C-4. Effect of object distance : the thin lens formula

The lens distortion is related to the object distance for a close range application [ASP 1980]. Brown [1971] and Abdel-Aziz [1973] have investigated the changes of the lens distortion with object distance. They derived formulas to predict the lens distortion at object distance s with two known lens distortion equations at object distances of s' and s'' . In their interpolation equation, the thin lens formula [Wolf, 1983] play a key role to decide the interpolation coefficients. It is difficult to simulate and verify Brown's or Abdel-Aziz's formula, because there is no facility available to decide lens distortion equations accurately. Instead, a revision is therefore introduced to calculate the projection equation (5-32). New simulation data are generated according to the thin lens formula. The camera model uses Table 6-2 parameters with $k_1=0.0000005$ and a focal length of 53 mm. However the image distance varies with the distances of control points according to

$$f_e = \frac{f \cdot Z}{Z - f} \quad \text{here } Z \text{ is the camera distance to the object plane}$$

and the equivalent focal length is uncertain. Noise-free and 0.5 pixel noise level cases are examined and the estimated results of three methods are summarised in Table C-16.

Table C- 16. Calibration results using data from the thin lens formula

(a) noise free

Parameters of camera-frame grabber system		Complete non-linear method	Radial distortion only (RDO) non-linear method	Tsai method
u0	384.000	430.696	382.994	384.000*
v0	256.000	260.103	256.162	256.000*
fx	-4240.000	-4479.795	-4495.555	-4473.863
fy	-4136.175	-4382.032	-4386.283	-4402.269
k1	0.0000005	0.000000608	0.000000611	0.00000062
p1	0	0.00002801	n/a	n/a
p2	0	0.000002285	n/a	n/a
ω	0	0.00089	-0.00007	-0.00021
ϕ	0	-0.0101	0.00058	-0.00021
κ	0	0.00007	-0.00002	0.00012
Xc	0	0.360	0.432	-0.257
Yc	0	0.065	0.132	0.271
Zc	1100	1178.117	1177.534	1182.228
prj-err		1.09667	1.20854	2.48612

* assigned image centre.

(b) noise=0.5

Parameters of camera-frame grabber system		Complete non-linear method	Radial distortion only (RDO) non-linear method	Tsai method
u0	384.000	389.909	385.617	384.000*
v0	256.000	385.350	253.002	256.000*
fx	-4240.000	-4470.090	-4500.103	-4146.445
fy	-4136.175	-4274.297	-4390.578	-4129.452
k1	0.0000005	0.000000611	0.000000623	0.000000569
p1	0	0.000003493	n/a	n/a
p2	0	0.0000785	n/a	n/a
ω	0	0.029	-0.00080	0.01099
ϕ	0	-0.00078	0.00052	0.00926
κ	0	0.00042	0.00029	-0.00651
Xc	0	0.460	0.564	10.865
Yc	0	0.125	0.123	-13.049
Zc	1100	1181.530	1177.611	1105.972
prj-err		0.74104	1.27207	4.12338

* assigned image centre.

It has been found out from these tests that the lens formula in a close range application can give a significant effect on the estimation of equivalent focal length and camera distance. The thin lens formula affects the estimated result in two ways:

- 1) It elongates the camera-object plane distance because the equivalent focal length changes.
- 2) It causes a tangential distortion effect to the non-linear method for 13 parameters and results in estimating error in principal point position.

